UNIVERSITY OF SOUTHAMPTON

Faculty of Engineering and Physical Sciences
School of Engineering

Synthetic cone penetrometer test (CPT) data for geotechnical design: Evaluating the impact of resolution

DOI: 10.5258/SOTON/PG/T189

by

Chrysoula Anastassopoulos

MEng

ORCiD: 0009-0008-3912-7806

A thesis for the degree of
Doctor of Philosophy

May 2026

University of Southampton

Abstract

Faculty of Engineering and Physical Sciences
School of Engineering

Doctor of Philosophy

Synthetic cone penetrometer test (CPT) data for geotechnical design: Evaluating the impact of resolution

by Chrysoula Anastassopoulos

The emerging technology of synthetic cone penetrometer tests (CPT) offers the potential for profiles of geotechnical resistance to be derived from two or three-dimensional geophysical seismic survey data at any location across a wind farm site, alleviating dependence on in situ geotechnical CPT testing and interpolation between test locations. However, the lower vertical resolution of synthetic CPT data compared with in situ geotechnical CPT data introduces uncertainty in design outcomes. In this thesis, the effect of CPT resolution on lateral pile performance is explored to inform on the minimum resolution of synthetic CPT profiles for design. Geotechnical CPT profiles from a case study site are systematically reduced in resolution from the field resolution of 0.01 m to a minimum resolution (i.e. maximum data interval) of 2.5 m. Use of artificially reduced resolution geotechnical CPT data as a proxy for synthetic CPT data enables comparative assessment of predicted pile volume and capacity in the same deposit at multiple resolutions. Results show increased variation in predicted pile volume as CPT resolution decreases, and hence data interval increases. Predicted minimum required pile volume remains within 3 % of, but consistently below, that predicted with the full resolution geotechnical CPT, translating to a reduction in pile capacity of the same order of magnitude. The effect on design outcomes is expanded further to include comparison between co-located in situ geotechnical and geophysical data from another wind farm site investigation. This has demonstrated that, with synthetic CPTs, it is possible to obtain minimum monopile dimensions within 2 % of those calculated with the in situ geotechnical CPT, corresponding to within 5 % of the required capacity. The application of time series complexity measures to CPT profiles has revealed that resolution is not the driving factor behind complexity but more to do with the soil type and the multi-faceted geotechnical design concept. The results from this research highlight the potential for the use of synthetic CPTs in pile design to facilitate the expansion of offshore wind by reducing the time required for geotechnical site investigations and uncertainty in design outcome from interpolating between in situ geotechnical CPTs.

Contents

List of Figures

List of Tables

Declaration of Authorship

I declare that this thesis and the work presented in it is my own and has been generated by me as the result of my own original research.

I confirm that:

1. This work was done wholly or mainly while in candidature for a research degree at this University;
2. Where any part of this thesis has previously been submitted for a degree or any other qualification at this University or any other institution, this has been clearly stated;
3. Where I have consulted the published work of others, this is always clearly attributed;
4. Where I have quoted from the work of others, the source is always given. With the exception of such quotations, this thesis is entirely my own work;
5. I have acknowledged all main sources of help;
6. Where the thesis is based on work done by myself jointly with others, I have made clear exactly what was done by others and what I have contributed myself;
7. Parts of this work have been published as:

   Anastassopoulos, C., Charles, J., & Gourvenec, S. (2023). Effect of CPT profile resolution on minimum required size of monopile for ultimate limit state design. In *9th International SUT Offshore Site Investigation Geotechnics Conference Proceedings* (pp. 393–400).: Society of Underwater Technology. https://doi.org/10.3723/IPLP6449.

   Anastassopoulos, C., Charles, J., Crispin, J., Henstock, T., Vardy, M., & Gourvenec, S. (2025a). Understanding the effect of CPT resolution on calculated lateral pile resistance to assist adoption of synthetic CPTs in geotechnical design. *Geoenergy*, https://doi.org/10.1144/geoenergy2025-022.

   Anastassopoulos, C., Crispin, J., Vardy, M., Henstock, T., & Gourvenec, S. (2025b). Assessment of Synthetic CPTs in Monopile Design for Offshore Wind Turbines: A Case Study. In *Sixth EAGE Global Energy Transition Conference & Exhibition (GET 2025)* (pp. 1–5). Rotterdam, Netherlands,: European Association of Geoscientists & Engineers. https://doi.org/10.3997/2214-4609.202521144.

Signed:..... Date:.....

Acknowledgements

I would like to thank my supervisors Prof. Susan Gourvenec, Dr. Jamie Crispin, Dr. Jared Charles and Prof. Timothy Henstock for their continuous guidance and support throughout my studies. I would also like to thank Dr. Mark Vardy who provided me with valuable data and scientific and practical insights into this research.

This work forms part of the activities of the Royal Academy of Engineering Chair in Emerging Technologies Centre of Excellence for Intelligent and Resilient Ocean Engineering (IROE). This research was funded by the Southampton Marine and Maritime Institute and the School of Engineering. I am grateful for this opportunity enabling me to continue my academic studies in pursuit of this PhD.

I am thankful to all my friends and colleagues at Boldrewood campus who provided an enjoyable environment in which to work. A final thank you goes to my family for their support.

I dedicate this PhD to my father

List of Symbols

Latin

B	Number of segments in time series
B_q	Excess pore water pressure ratio
D	Diameter
D_F	Fractal dimension
D_r	Relative density
E_{py}	Spring stiffness
F	Fluctuation function
F_k	Fluctuation function of segment
F_q	Generalised fluctuation function
F_r	Normalised friction ratio
f_s	Sleeve friction
G_0	Small strain stiffness
H	Horizontal load
H_e	Hurst exponent
H_q	Generalised Hurst exponent
h	Height above seabed
I_c	Soil Behaviour Type Index
I_r	Rigidity index
i	Position in time series
k	Segment number in time series
L	Length
M	Moment
M_p	Moment capacity
N_{kt}	Cone factor
n	Length of time series
n_τ	Segment length of time series
P_k	Fitted polynomial of segment
p_a	Atmospheric pressure
p_u	Ultimate lateral soil resistance

Q_t	Normalised cone resistance
q	Order of fluctuation function
q_c	Measured cone penetration resistance
q_{net}	Net cone penetration resistance
q_t	Corrected cone penetration resistance
R	Range
S	Standard deviation
S_k	Standard deviation of segment
s_u	Undrained shear strength
t	Thickness
u	in situ pore water pressure
u_2	Pore water pressure at the cone shoulder
V	Volume
V_s	Shear wave velocity
W_k	Detrended fluctuation of segment
y	Lateral displacement
z	Depth below seabed

Greek

α	Net area ratio
α_{DFA}	DFA exponent
γ'	Soil effective unit weight
γ	Soil unit weight
μ	Mean
μ_k	Mean of segment
ρ	Bulk density
σ'_v	in situ vertical effective stress
σ_v	in situ vertical total stress
σ_y	Yield stress
τ_k	Segment in time series

List of Acronyms

ApEn	Approximate Entropy
COP	Conference of the Parties
CPT	Cone Penetrometer Test
DFA	Detrended Fluctuation Analysis
FE	Finite Element
FuzzEn	Fuzzy Entropy
K2En	Kolmogorov Entropy
LRFD	Load and Resistance Factors Design
MF-DFA	Multifractal Detrended Fluctuation Analysis
PermEn	Permutation Entropy
PISA	Pile Soil Analysis
R/S	Rescaled Range
RPDE	Resolution-induced Pile Design Error
SampEn	Sample Entropy
SLS	Serviceability Limit State
SpecEn	Spectral Entropy
TNW	Ten Noorden van de Waddeneilanden
UK	United Kingdom
ULS	Ultimate Limit State
WSD	Working Stress Design

Chapter 1

Introduction

1.1 Motivation, purpose and scope

Climate change, resulting from anthropogenic greenhouse gas emissions, poses a significant threat globally (Ritchie et al., 2023). The majority of anthropogenic greenhouse gas emissions, 92 % (Andrew and Peters, 2021; Friedlingstein et al., 2022), are generated due to burning fossil fuels for energy. In total, this amounts to 35 billion tonnes of carbon dioxide emitted each year (Andrew and Peters, 2021; Friedlingstein et al., 2022); the fuel types contributing the most being coal, oil, and gas. The carbon dioxide concentration in the atmosphere has now reached 426 parts per million, an increase of over 25 % from the atmospheric concentration of 338 parts per million in 1980 (Lan et al., 2025). These large volumes of carbon dioxide in the atmosphere form almost 75 % of global greenhouse gas emissions, with the remaining 25 % consisting of methane, nitrous oxide and small amounts of fluorinated gases (Ge and Friedrich, 2024), and are causing the rise in average global temperatures (Lacis et al., 2010). Increased average global temperatures will cause extreme weather events to become more frequent and severe (UNEP, 2022; IPCC, 2023), increasing risks of both river and coastal flooding, heatwaves, forest fires, hurricanes, etc. (IPCC, 2014; Ritchie et al., 2023).

To mitigate climate change and the resulting consequences, the United Nations' Conference of the Parties (COP) has taken place annually for almost three decades (COP, 2021). At COP21, held in Paris in 2015, the Paris Agreement was established and signed by 195 countries (COP, 2015). This stated that the average global temperature must be kept below 1.5 $^{\circ}C$ above pre-industrial levels (COP, 2015; National Grid ESO, 2021). As of 2021, the global temperature has risen to 1.2 $^{\circ}C$ above pre-industrial levels, and is increasing by about 0.25 $^{\circ}C$ per decade as a result of human-induced warming (CCC, 2021). Without further international action, at such a rate, the 1.5 $^{\circ}C$ limit will be exceeded by the early 2030s (CCC, 2021; COP, 2021).

Therefore, to limit global warming to 1.5 $^{\circ}C$ by 2100, governments worldwide have adopted plans to reach net zero carbon emissions by 2050 (IRENA and GWEC, 2021; IPCC, 2023). This requires a complete shift away from energy production by fossil fuels (CCC, 2021; National Grid ESO, 2021; Supergen ORE, 2021), and highlights the demand for alternative renewable energy methods. The transition away from fossil fuels is expected to be largely driven by the wind industry and increasingly so by offshore wind (GWEC, 2022). Global offshore wind had its second largest annual increase of 10.8 *GW* in 2023, 24 % higher than that in 2022, taking the total capacity to 75.2 *GW* (GWEC, 2024). However, offshore wind must provide 2000 *GW* of energy capacity globally by 2050 (IRENA and GWEC, 2021).

The UK has pledged to completely decarbonise its electricity system by 2035 through the implementation of carbon capture technology for all fossil fuel generation and the increase in renewable energy resources (Supergen ORE, 2021), with 50 *GW* of offshore wind by 2030 (HM Government, 2022). The geographical location of the UK as an island nation with strong winds and shallow seas means it is ideally situated to further develop offshore wind through construction of additional and increasingly larger wind farms (CORE, 2015). The placement of wind turbines offshore, rather than onshore, has both the advantage of higher wind speeds and less turbulent wind, and is less likely to be opposed by people living nearby (Houlsby, 2016). Such factors are desirable in enhancing the amount of power generated.

The ambitious targets for offshore wind will require the design and construction of wind turbines at 6.5 times the rate that has been achieved in recent years (GWEC, 2024). To accommodate the seabed space needed for offshore wind developments (Putuhena et al., 2023a), wind farms will not only increase in size but will also have to extend into more challenging environmental and geotechnical areas (Supergen ORE, 2021). These large areas of seabed must be characterised, typically through geotechnical in situ cone penetrometer tests (CPTs), to acquire the soil parameters for the design of the wind farm foundations. CPTs are performed at discrete locations across a wind farm site and therefore will not be able to keep up with the pace and scale of site characterisation, since larger sites would require more CPTs and make site investigations even longer. Furthermore, turbine locations are not always known a priori to the site investigation, leading to the need for interpolation between tests. With more complex sites, seabed properties can vary significantly over short distances and introduce greater uncertainty.

Achieving and maintaining this rate of installation requires innovative site investigation methods, alongside innovation across design methods, manufacture, installation, operation and decommissioning (Tapoglou et al., 2023; Gourvenec, 2024). An emerging technique in site characterisation is the synthetic CPT, which involves deriving a one-dimensional profile of CPT resistance from inverted geophysical seismic survey data (Vardy et al., 2015; Forsberg et al., 2017; Provenzano et al., 2017; Vardy et al., 2017; Vardy and Pinson, 2018; Sauvin et al., 2019; Carpentier et al., 2021; Chen et al., 2021;

Peuchen et al., 2022b; Sauvin et al., 2022; Shoukat et al., 2023; Cox et al., 2024; Klinkvort et al., 2024; Siemann et al., 2024; Stuyts, 2024; Bolève et al., 2025). Geophysical data is continuous laterally, meaning synthetic CPTs can be generated at any location within a wind farm site. This allows for the construction of a site wide ground model that enables design of wind turbine foundations from a synthetic CPT profile at any point on the site. However, synthetic CPTs have a lower vertical resolution than geotechnical CPTs which could affect geotechnical design outcomes, potentially resulting in under or over-design. This lack of knowledge has prevented synthetic CPTs from being implemented on a large scale and means they are not currently approved by certification bodies, despite having the potential to transform site investigations.

Therefore, investigation into the requirements of synthetic CPT data will be carried out in terms of resolution, with results being judged by foundation sizing accuracy. Examples of synthetic CPT data will be included in the analysis, from which piles are to be designed and compared to those derived from co-located in situ geotechnical CPT profiles, to determine the extent to which synthetic CPTs actually affect design outcomes. An assessment into the effect of CPT profile complexity on resolution will be performed to provide guidance on the use of synthetic CPTs in design. This research will help bridge the gap between the theory and practice of synthetic CPTs, building the evidence base to enable greater reliance on synthetic CPTs for geotechnical design.

1.2 Aim and research objectives

The overall aim of this PhD is to advance the implementation of synthetic CPTs in the design of offshore wind turbine monopile foundations. This will be achieved through the following three research objectives, with further information provided in Section 2.7:

RO1 Evaluate the impact of using reduced resolution CPT data on the design of monopile foundations for offshore wind turbines.

RO2 Evaluate the impact of using synthetic CPT data on the design of monopile foundations for offshore wind turbines.

RO3 Evaluate the application of time series complexity measures on CPT profiles and determine their relationships with pile design outcomes.

1.3 Novelty

The novelty of this research lies in bridging the gap between the theory of synthetic CPTs and their use in practice for the design of offshore wind turbine foundations. There have been several studies on the different ways in which synthetic CPTs can be derived from geophysical site data and the extent to which the actual CPT profile can be predicted. However, the impact of using these synthetic CPT profiles in pile design has not been assessed. By first investigating the effect of CPT profile resolution on pile design outcomes, this research can be applicable to any synthetic CPT method and provides information on minimum resolution, below which design alters.

It has only been recently that synthetic CPTs have been generated alongside CPTs in a comparable form, and the data has become more readily available. Furthermore, any comparison that has been performed remains limited to the profiles of cone penetration resistance, rather than how this translates into pile design. Therefore, this research is novel in the way it analyses the practical consequences of designing piles from synthetic CPT data and installing them into the 'actual' soil.

There is expansive knowledge on time series analysis and a vast range of methods of measuring the complexity of a time series. Such methods are utilised on a daily basis across several disciplines, from medicine to finance, forming a whole field in itself of information theory. The consistent nature of CPT profiles, with readings at approximately equal increments in depth, means it can be modelled as a time series. However, such a concept has not been well-used in geotechnical engineering. This research applies a large selection of complexity measures to CPT profiles in order to assess whether complexity of the profile can capture minimum allowable resolution and inform on overall design guidance.

1.4 Publications

The following publications form a part of this research:

- **Anastassopoulos, C.**, Charles, J.A. and Gourvenec, S. (2023). Effect of CPT profile resolution on minimum required size of monopile for ultimate limit state design. In *9th International SUT Offshore Site Investigation Geotechnics Conference Proceedings*, pages 393–400. Society of Underwater Technology. https://doi.org/10.3723/IPLP6449
- **Anastassopoulos, C.**, Charles, J.A., Crispin, J.J., Henstock, T.J., Vardy, M.E. and Gourvenec, S. (2025a). Understanding the effect of CPT resolution on calculated lateral pile resistance to assist adoption of synthetic CPTs in geotechnical design. *Geoenergy*. https://doi.org/10.1144/geoenergy2025-022

- **Anastassopoulos, C.**, Crispin, J.J., Vardy, M.E., Henstock, T.J. and Gourvenec, S. (2025b). Assessment of Synthetic CPTs in Monopile Design for Offshore Wind Turbines: A Case Study. In *Sixth EAGE Global Energy Transition Conference & Exhibition (GET 2025)*, pages 1–5, Rotterdam, Netherlands, European Association of Geoscientists & Engineers. https://doi.org/10.3997/2214-4609.202521144

1.5 Thesis structure

This thesis comprises of six chapters in total, with this first chapter providing the motivation for the research and setting out the desired outcomes. Chapter 2 presents a critical literature review of existing research and background knowledge to concepts that are used later on in the thesis. The following three chapters form the main body of research in accordance to each of the three research objectives outlined in Section 1.2. Chapter 3 focusses on actual CPT data from the Burbo Bank Extension offshore wind farm site, Liverpool Bay, UK, to assess how reduced resolution CPT profiles affect pile design outcomes. Chapter 4 moves on to another case study site: Ten Noorden de Waddeneilanden wind farm zone in the Dutch Sector of the North Sea, where site investigations involved the derivation of synthetic CPTs alongside standard geotechnical ones, allowing direct comparison of pile design outcomes between synthetic and geotechnical CPTs. Both sites comprise interbedded sands and lightly overconsolidated, low plasticity clay that are highly heterogenous with depth and laterally. Chapter 5 uses time series analysis methods to model CPT profiles as a function of depth, to investigate whether the complexity of a profile is linked to variation in pile design outcomes. Finally, Chapter 6 ties the research all together in terms of guidance to design, giving details of future work and conclusions to this thesis.

Chapter 2

Literature review

2.1 Introduction

A critical evaluation of currently available literature has been performed to set out the existing state of the art and identify the areas where knowledge is limited. This begins with an overview of foundations for offshore wind turbines, focussing on the geotechnical design of monopiles. Design of offshore wind turbine foundations requires extensive site investigations in order to gain an understanding of soil conditions beneath the seafloor and obtain specific parameters. Cone penetrometer tests (CPTs) are a key component, however, to keep up with the demand for increasing offshore wind, the potential of synthetic CPTs are explored as an innovative method that seeks to combine geophysical data with geotechnical. In order to evaluate the effect of lower resolution synthetic CPTs in design, the subsequent sections move on to address the interpretation of CPT data and how it can be used to derive soil parameters, from which both concepts inform lateral pile design methods. Finally, an investigation of time series analysis complexity measures is set out.

2.2 Foundations for offshore wind turbines

Foundations for offshore wind turbines provide support for the wind turbine structure by transferring the loads, derived from the wind, waves and currents, to the seabed. The foundation design then ensures that the unit is sufficient to withstand the loads within ultimate and serviceability limits (Bhattacharya, 2014). They also form a substantial proportion of the total cost of an offshore wind farm project, between 15 and 35 % (Bhattacharya, 2019). Due to the large size of wind turbine structures and the harsh metocean conditions experienced out at sea, these foundations must be able to withstand significant forces (O'Kelly and Arshad, 2016). The exact configuration of the

loads and how the structure behaves under loading is governed by the water depth, geographic location and type of foundation. Foundation type installed depends on several different aspects such as seabed, site conditions, size of wind turbine and loading (Bhattacharya, 2019), as well as the depth of the water at the location of the wind turbine: ranging from fixed bottom structures in shallower waters to floating platforms with anchors and moorings in water depths greater than 50 m (GWEC, 2024). The extent of the variation in foundations as water depth increases is portrayed in Figure 2.1.

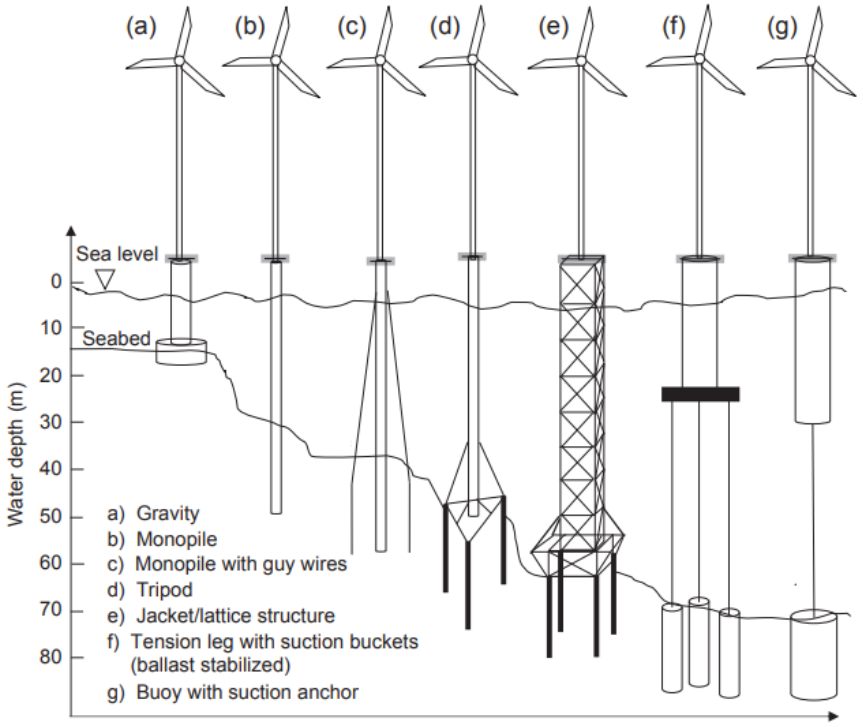

FIGURE 2.1: Types of foundations for offshore wind turbines (O'Kelly and Arshad, 2016)

The most commonly used type of foundations for offshore wind are monopiles (Figure 2.1(b)), making up 70 % of all offshore wind turbine foundations globally by the end of 2022 (GWEC, 2024). Therefore, the focus of this work is on monopile foundations.

2.2.1 Monopiles

Monopiles are a steel hollow tube, as displayed in Figure 2.2, with outer diameters between 4 and 12 m and lengths between 20 and 40 m (Wu et al., 2019). Their popularity in the use of offshore wind turbine foundations comes from the fact that they are versatile in different seabed sediments (Malhotra, 2009). The low length to diameter ratio of less than five (Houlsby, 2016), typical of monopiles for offshore wind turbines, gives them a high stiffness. As a result, the monopile acts as a rigid structure, rotating about a

pivot point within the pile, under lateral loading (O'Kelly and Arshad, 2016; Wu et al., 2019). The forces which cause the lateral loading on an offshore wind turbine monopile foundation is addressed in the following section (Section 2.2.2), and highlights why this mechanism is most critical.

FIGURE 2.2: A 7.5 m diameter monopile foundation for an offshore wind turbine (Kallehave et al., 2015)

2.2.2 Loading on monopiles

The loads acting on an offshore wind turbine with a monopile foundation can be seen in Figure 2.3. This includes the lateral loads from the wind and waves and the vertical self-weight of the wind turbine structure. The combined environmental loading of the wind and waves can be modelled as an instantaneous static horizontal load (H) (Alexander and Bhattacharya, 2011), acting at the midpoint of the load distribution and applied to the wind turbine structure at this height (h) above the seafloor (see Figure 2.4). A substantial overturning moment, as indicated in Figure 2.3, is induced by the lateral wind and wave loads (Byrne et al., 2015), making the vertical load small in comparison (Ahayan et al., 2019; Byrne and Houlsby, 2003). As such, it is this lateral loading that governs the design of monopile foundations for offshore wind turbines.

Figure 2.4 also demonstrates how the lateral loads can be directly applied to the monopile. This is through a horizontal force of equal magnitude to the combined wind and wave loading and a moment (M) of this force multiplied by the height of its midpoint above the ground surface, acting on the pile head at seafloor level.

The wind and wave loads are dynamic as their magnitude depends on the turbulent wind speed, and wave height and wave period, respectively (Bhattacharya, 2019).

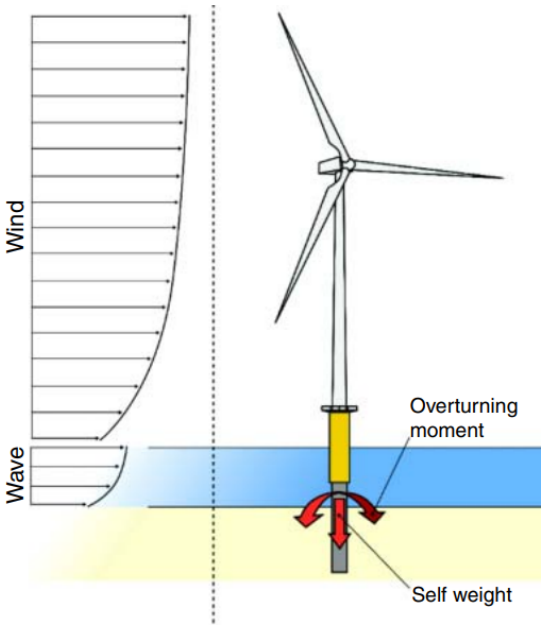

FIGURE 2.3: Loading on an offshore wind turbine with a monopile foundation (Bhattacharya, 2019)

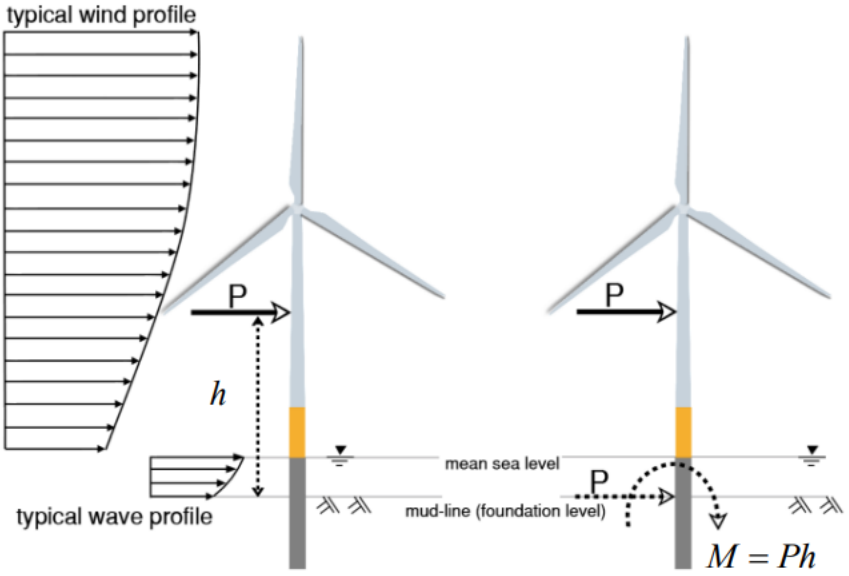

FIGURE 2.4: Simplified lateral loading on a monopile foundation for an offshore wind turbine (Alexander and Bhattacharya, 2011)

Therefore, the monopile must be able to resist the greatest combined load on its structure. This is when both the wind and waves act in the same direction. Although most extreme wave conditions and highest wind speeds usually occur at the same time, this is not when their individual maximum impact on the structure is greatest as the turbines shut down above a certain wind speed threshold (Arany et al., 2017). The rotor-thrust reaction of the wind on an idle turbine is much less than that in normal operating conditions, so loading will be dominated by the waves (Arany et al., 2017). The extent to which the monopile is considered to withstand these lateral loads depends on the design criteria.

2.2.3 Design criteria

The design criteria of a monopile foundation for an offshore wind turbine under lateral loading specify the horizontal load applied to the structure that the structure must resist without exceeding ultimate limit state and serviceability limit state principles, which focus on the capacity and deflection of a structure respectively. A limit state marks a condition beyond which a structure is no longer able to satisfy the specified performance requirements (Bhattacharya, 2019). The design of a monopile is governed through the minimum dimensions of diameter, length and thickness it must have in order to meet the limit states (Bhattacharya, 2019). Although serviceability limit state typically governs the design for offshore wind, in this thesis, ultimate limit state allows for optimised pile dimensions of diameter and length to the nearest 0.1 m, without an extensive amount of computational time to provide proof-of-concept.

2.2.3.1 Ultimate limit state

Ultimate limit state (ULS) is defined as the point beyond which the monopile foundation can no longer resist the loads applied to it, resulting in collapse of the soil, usually accompanied by a catastrophic collapse of the structure. It has already been explained in Section 2.2.2 that the lateral loading is much more significant than the vertical loading, therefore, the ultimate lateral capacity governs design. Due to the rotational mechanism of an offshore wind turbine monopile as a rigid structure about a pivot point within the pile (see Section 2.2.1), ultimate limit state is when the net lateral force acting on the monopile is equal to the maximum lateral resistance of the soil (Randolph and Gourvenec, 2011). Therefore, failure of the soil takes place. Figure 2.5 portrays this failure mechanism, along with graphs demonstrating the soil resistance, which acts in the opposite direction to the applied lateral load on the wind turbines when acting above the pivot depth. In engineering practice, ULS utilises factors of safety in order to accommodate for uncertainties in soil parameters and design method. These can either be applied as partial factors to both the soil properties and loads, to artificially reduce

soil strength and increase loads, or as a global factor of safety to the calculated horizontal capacity (Atkinson, 2007). The necessary soil parameters to determine the lateral resistance of the soil are soil strength, unit weight, pore water pressure and vertical total stress. These are obtained through site investigations (see Section 2.3).

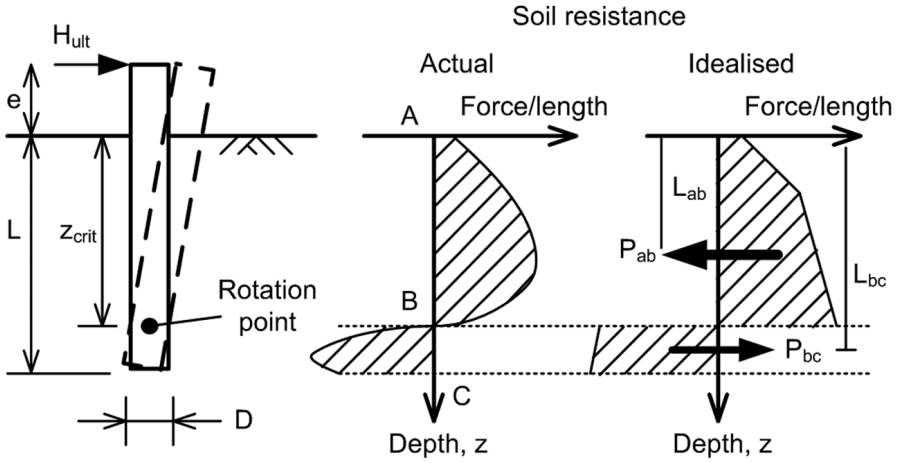

FIGURE 2.5: Failure mechanism of monopile for offshore wind turbine under lateral loads (Randolph and Gourvenec, 2011)

2.2.3.2 Serviceability limit state

Serviceability limit state (SLS) is based on displacement tolerances: allowable deflection and rotation, of the wind turbine so that it can operate properly (Bhattacharya, 2014). The magnitude of any displacement or deformation are turbine specific, depending on the turbine size and hub height, and are typically specified by the turbine manufacturer. Design codes also offer advice on limits of rotation, with the DNV stating that the maximum allowance of rotation at the nacelle (centre of rotation of turbine blades) is 0.25 degrees from the vertical (Bhattacharya, 2014, 2019). It is the lateral displacement of the monopile that is most critical, as opposed to the vertical, due to the lateral loads from the wind and waves governing design, as mentioned in Section 2.2.2. These displacement tolerances of deflection and rotation are demonstrated in Figure 2.6.

In the same way as for ultimate limit state, serviceability limit state geotechnical design depends on the lateral resistance of the soil, but the stiffness of the wind turbine structure also plays a crucial role. The dynamic sensitivity of offshore wind turbine structures means the natural frequency of the structure is very close to the frequencies from the waves and rotor forces (Bhattacharya, 2019), and therefore must ensure resonance, which is dependent on stiffness, does not occur.

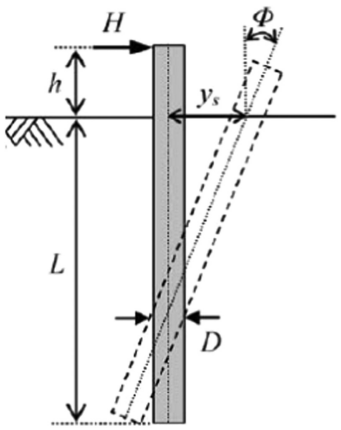

FIGURE 2.6: Rotation of monopile under static lateral wind and wave loading (Wu et al., 2019)

2.3 Offshore site investigation

Site investigation is required to provide the properties of the soil in which offshore wind turbine monopiles are to be designed and later installed. Such properties include soil resistance, unit weight, pore water pressure, and vertical total stress, as were introduced in Sections 2.2.3.1 and 2.2.3.2 in order to obtain soil lateral resistance. In foundation design, there are two main components of the site investigation: geophysical (Section 2.3.1) and geotechnical (Section 2.3.2). The combination of data from both the geophysical and geotechnical site investigations allows for an integrated ground model (Section 2.3.3); the benefits of which are significant. From the integrated ground model, innovative tools can be implemented, such as synthetic CPTs (Section 2.3.4). These could potentially have an important role to play in the development of current and future offshore wind farms.

2.3.1 Geophysical investigation

The geophysical investigation involves the collection of data through non-invasive methods (Audibert and Huang, 2005), predominantly seismic surveys, to evaluate the geology and the variation in the physical properties of the seafloor and seabed (Tyler et al., 2017). The indirect inference of the soil properties comes from the fact that geophysical surveying approaches are carried out using sensors that operate remotely, rather than based on tests carried out on physical soil (Audibert and Huang, 2005; Silva et al., 2021). This enables a large range of data to be collected over an extensive area (Silva et al., 2021). The information provided by geophysical surveying is either surface data, referring to that obtained from above and along the seafloor, or subsurface, which comes from beneath the seafloor (Audibert and Huang, 2005).

Surface surveying techniques are varied, with acoustic methods commonly adopted for geophysical investigations for site characterisation (Audibert and Huang, 2005). Bathymetric mapping using echo sounding technology enables a three-dimensional map of the seafloor to be produced (Randolph and Gourvenec, 2011). It picks up features of the seafloor and its slope through determination of the water depth (Tyler et al., 2017). This includes geological features, slope failures and obstructions along the seafloor (Audibert and Huang, 2005). Seafloor mapping using side-scan sonar systems also provides information on the seafloor by transmitting narrow beams of acoustic energy from either a towed device or a remotely operated vehicle (Randolph and Gourvenec, 2011). The sound is reflected off the seafloor or any other underwater object, generating a two or three-dimensional image of seafloor topography (Bai and Bai, 2019).

Seismic profiling is the method used to investigate the subsurface properties of the soil beneath the seafloor, based on the reflected and refracted waves from an acoustic energy source (Randolph and Gourvenec, 2011). The signal picked up by the receiver is affected by the media through which the generated pulse of energy passes (Audibert and Huang, 2005). In seismic reflection surveying, energy will be reflected at the interface between two different media as a result of their difference in properties, such as at the boundaries between different soil strata or at the water-seafloor interface. The amount of energy reflected back depends on the acoustic impedance of the soil layers, which is a function of the compressional velocity multiplied by the density (Onajite, 2014). This reflected energy shows up as dark zones on the recorder display, where the lighter zones indicate the energy has been transmitted further into the seabed (Randolph and Gourvenec, 2011). Whilst stronger, more dense soil layers will cause a greater loss of energy through reflection, so would the presence of multiple soil layers. This would then decrease the resolution of the signal and reduce the penetration depth of the signal. However, the attenuation of the energy as a result of the soil acoustic impedance, enables the visual representation of the subsurface layers within the seabed (Micallef, 2011).

Seismic refraction surveying utilises the fact that sound waves travel faster through denser materials, causing them to refract when crossing boundaries between different sediment layers (Audibert and Huang, 2005). A pressure wave generated by a seismic source on the seafloor propagates through the seabed, refracting along the interfaces between soil layers. These refracted signals are captured by hydrophones; their travel times plotted against distance to determine compression wave velocities. By inverting these velocities, a subsurface model can be constructed, offering insights into soil composition and mechanical properties (Tyler et al., 2017). This inversion process, frequently employed in both seismic reflection and refraction methods, is referred to as seismic inversion (Silva et al., 2021).

Seismic inversion is the process of constructing and optimising a seismic ground model that closely predicts the observed seismic reflection and refraction data (Provenzano

et al., 2018; Silva et al., 2021; Vardy et al., 2017). In this way, the reflected and refracted signals, denoting changes in soil boundaries and stratification, have been converted into three-dimensional profiles of soil properties (Sokolov et al., 2021). However, limitations of the seismic inversion process mean there are numerous possible seismic ground models that predict seismic reflection and refraction signals despite differing soil properties (Silva et al., 2021).

Geophysical surveying is beneficial as it is able to provide information on the seabed characteristics and properties without the need for invasive data collection methods. However, the most significant benefit of the data from geophysical surveying is that it is continuous laterally, since it can be collected over the entire site, as opposed to geotechnical investigations which are performed at discrete locations.

2.3.2 Geotechnical investigation

The geotechnical investigation involves analysis of the soil beneath the seafloor of the site through invasive methods, including in situ tests or laboratory testing of retrieved samples. This enables the engineering soil properties to be determined, providing the fundamental geotechnical parameters required for the engineering design of offshore foundations (Randolph and Gourvenec, 2011).

In situ tests are performed on the soil in the field. Examples include cone penetrometer tests (CPTs), flowaround penetrometers and vane shear tests. CPTs are an ubiquitous in situ geotechnical testing protocol both onshore and offshore, involving penetration of a metal rod vertically into the soil through a drilling rig or seabed frame (Briaud, 2013), typically at a fixed rate of penetration of 2 cm/s (Robertson and Cabal, 2015). CPTs feature a cone tip, connected to a metal rod which is pushed into the ground through a drilling rig or seabed frame (Briaud, 2013). Figure 2.7 demonstrates the CPT equipment for an offshore site, highlighting the shape of the cone.

CPTs are equipped with sensors, providing one-dimensional profiles with depth of cone penetration resistance, sleeve friction, and commonly pore water pressure at the shoulder of the cone. Example profiles obtained directly from the CPT are shown in Figure 2.8. CPT data is widely used to estimate sediment type visually via charts of absolute or normalised cone resistance, sleeve friction and pore water pressure (e.g., Robertson, 1990) or by the Soil Behaviour Type Index (Robertson and Wride, 1998). CPT data is also directly used in geotechnical design methods (e.g., Atkinson, 2007; Robertson, 2009b; Moshfeghi and Eslami, 2016; Lehane, 2019). These methods of soil classification and pile design are discussed in Sections 2.4.2 and 2.5.2, respectively. While CPT data is essentially continuous with depth, each test provides a profile at a discrete location, with tests for offshore wind applications typically carried out at proposed turbine locations.

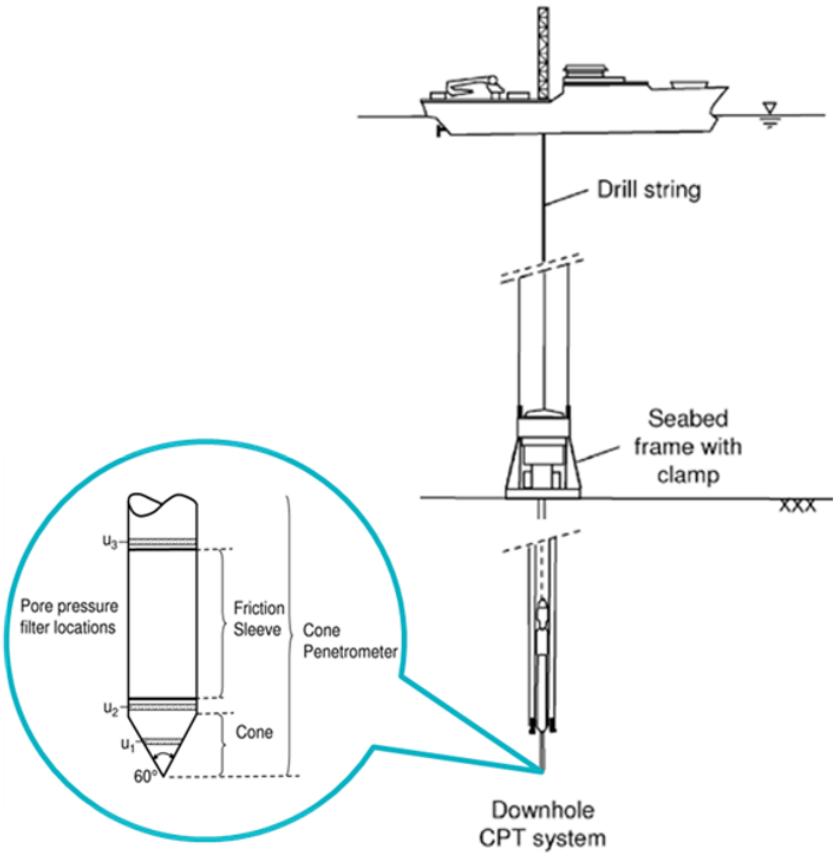

FIGURE 2.7: CPT equipment for an offshore site, featuring a zoom in of the cone tip (after Randolph and Gourvenec (2011))

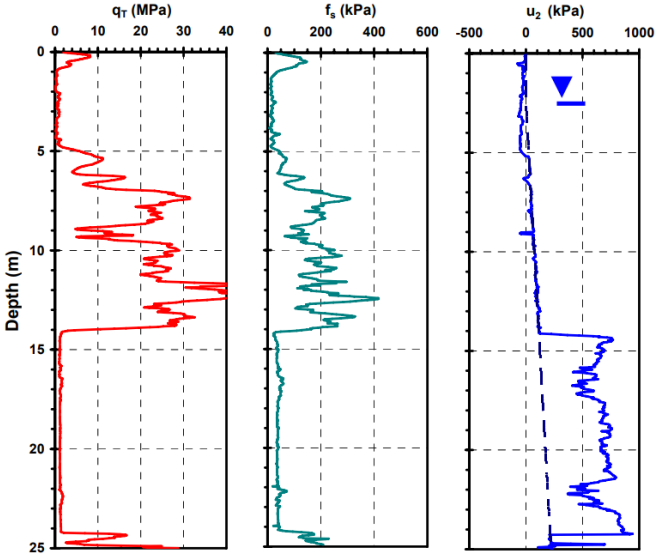

FIGURE 2.8: CPT profiles of cone penetration resistance (q_c), sleeve friction (f_S) and pore water pressure (u_2) with depth (Mayne, 2007)

Although CPTs do not retrieve samples of the soil, the pushing equipment can be used in a separate location nearby to collect samples (Robertson, 2009a). Soil samples obtained during offshore geotechnical site investigations are brought onshore to be analysed in the laboratory. Several tests can be performed on the samples, ranging from soil classification to deriving the stress and strain behaviour of the soil through element testing. Classification testing can consist of taking x-rays of the samples to enable the visualisation of the internal structure in order to assess the degree of disturbance and the soil stratification (Audibert and Huang, 2005; Randolph and Gourvenec, 2011). The fabric of the soil can be observed through a scanning electronic microscope, provided that the sample has remained undisturbed (Randolph and Gourvenec, 2011). Analysis of the soil sample grain size, as well as the grading and uniformity, takes the form of a particle size distribution study, which can either be performed by sieving or by a hydrometer (Randolph and Gourvenec, 2011; Briaud, 2013).

Element testing determines the mechanical properties of a soil, without the need for reference points or boundary conditions, when a sample of it undergoes uniform changes in stress or strain. These tests enable monotonic and cyclic stress paths to be simulated on the soil specimen and its response to be observed, which will be used to inform the foundation design. The main element tests that are often carried out on soil samples in the laboratory include consolidation tests for determination of the one-dimensional compression behaviour and preconsolidation pressure of the soil through oedometer equipment; direct shear tests for determination of the shear stress-strain behaviour and the shear strength of the soil; and triaxial tests, involving the shearing of the sample following a specified stress path (total or effective) under replicated in situ conditions (Randolph and Gourvenec, 2011).

Both in situ testing and sampling with laboratory testing have their own benefits. A significant attribute of in situ testing is that the physical properties of the soil can be investigated in its natural state. This function is invaluable in cohesionless soils as it is the only possible way to determine certain parameters, such as the relative density. Furthermore, in situ tests enable the soil to be analysed without disturbance of the material, which leads to a better evaluation of the soil stratification (Audibert and Huang, 2005; Patel, 2019). Without the need for laboratory tests in order to obtain results, in situ tests generate data immediately, saving time (Patel, 2019). Both testing methods enable the determination of soil parameters, including the undrained shear strength and the friction angle of the soil, however, lab tests allow the exploration of more complex stress paths (Patel, 2019). Therefore, in a geotechnical site investigation it is important to balance in situ tests and laboratory tests on retrieved samples.

The geotechnical investigation provides detailed, high resolution information on the vertical profile of the soil beneath the seafloor, from which the soil stratification and engineering parameters can be generated. This forms an essential part in the design process of offshore wind turbine foundations, since their dimensions are directly based

on the engineering characteristics of the surrounding seabed soil. However, geotechnical investigations only provide sparse data in the lateral direction, leading to uncertainties in the soil characteristics between in situ tests or the boreholes of the testing locations. The final wind turbine locations are not always known prior to the site investigation, so wind turbines may end up being designed using the approximation of soil conditions interpolated between CPTs. The trend in developing increasingly larger wind farms, as mentioned in Section 1.1, would either increase the distance between CPTs, leading to greater uncertainties in the soil conditions, or require an expensive and time-consuming geotechnical investigation with many CPTs per campaign and repeated campaigns to accommodate changes in layout. Furthermore, there are not sufficient quantities of vessels, equipment and personnel to perform such site investigations at the pace and scale required to reach net zero by 2050. This highlights the need for an integrated ground model.

2.3.3 Integrated ground model

An integrated ground model is a structured, three-dimensional representation of the surface and subsurface that compiles site-specific data (SUT, 2022; Vanneste et al., 2022), including both the geophysical and geotechnical data in Sections 2.3.1 and 2.3.2, respectively. It provides a spatial understanding of the conditions at a site (Vanneste et al., 2022) to identify hazards, direct site investigations and inform on foundation design (SUT, 2022). An important feature is that it is dynamic, always continuously evolving throughout a project, from early development to decommissioning, as more data becomes available (Vanneste et al., 2022).

Traditional ground models did not integrate geophysical and geotechnical data, but rather performed these as separate site investigations. The seismic data from geophysical surveys was often acquired before geotechnical investigations which resulted in interpretations that lacked calibration and ground-truthing (Vanneste et al., 2022). Furthermore, the correlation between seismic data and soil properties of geotechnical tests is complex, since the different methods do not respond to the same subsurface characteristics. Therefore, to extract the maximum information from the data obtained through geophysical and geotechnical site investigations, an integrated ground model is essential. The laterally continuous nature of the geophysical data (Section 2.3.1) can be used to deduce the variations in soil conditions between the high resolution boreholes and CPTs (Section 2.3.2) in order to obtain the soil properties and stratification at any position through synthetic CPTs.

2.3.4 Synthetic CPTs

Synthetic CPTs are the derivation of one-dimensional profiles of CPT properties, such as soil resistance, from inverted geophysical seismic survey data. Synthetic CPTs can address significant challenges for site investigation for offshore wind:

1. The large area of seabed and number of locations that need to be characterised to acquire the engineering parameters required for geotechnical design of monopile foundations or anchors for mooring systems, with each 2 GW farm occupying an area of seabed of approximately 500 km^2 with 150-200 offshore wind turbine locations depending on turbine size (Putuhena et al., 2023b).
2. The scale disparity between a CPT instrument (0.037 m diameter) and an offshore foundation, which can be 10 m or more in diameter, such that a geotechnical CPT profile only represents the soil profile over a small portion of the foundation footprint.
3. The uncertainty of final location of foundations or anchors ahead of the geotechnical survey since geotechnical parameters for design may not be acquired at the exact location of the foundation.

Reducing the number of CPTs across a site, extending coverage of CPT profile to foundation footprint, and changing layout or micro siting of turbines lead to the need for interpolation between in situ tests that can introduce uncertainty into design outcomes. These challenges are particularly relevant in complex ground conditions where seabed properties can vary significantly over short lateral or vertical distances. Therefore, this section outlines methods of determining synthetic CPTs and the accuracy in which these synthetic CPTs compare to the actual CPT profile.

Various statistical methods or machine learning approaches are used to combine 'real' one-dimensional geotechnical CPT profiles at discrete locations with continuous two or three-dimensional seismic profiles of geophysical data acquired as close as possible to the geotechnical CPT location (Vardy et al., 2015; Forsberg et al., 2017; Provenzano et al., 2017; Vardy et al., 2017; Vardy and Pinson, 2018; Sauvin et al., 2019; Carpentier et al., 2021; Chen et al., 2021; Peuchen et al., 2022b; Sauvin et al., 2022; Shoukat et al., 2023; Cox et al., 2024; Klinkvort et al., 2024; Siemann et al., 2024; Stuyts, 2024; Bolève et al., 2025). Synthetic CPT approaches have been shown to be able to capture real CPT profiles with high fidelity, although typically have lower resolutions (data intervals ranging from decimetres to metres) when compared with geotechnical CPT data (data intervals of 1-2 centimetres) (e.g., Chen et al., 2021; Peuchen et al., 2022b). In some conditions, particularly in locations with many fine layers, the resolution may not be able to capture stratigraphic boundaries that traditional CPTs could (Vardy et al., 2015; Siemann et al.,

2024); and where acoustic impedance between two geotechnically different materials is similar, the interface will not be visible from the inverted seismic data.

Examples of a synthetic CPT profile from statistical methods and a machine learning approach are illustrated in Figure 2.9 (with synthetic CPT profiles shown in black), overlaid on the real co-located geotechnical CPT profiles (shown in red) (after (Sauvin et al. (2019)), to give an indication of the achievable agreement. Figure 2.9(a) illustrates a geometric-geostatistical approach in which seismic data guides the prediction of geotechnical properties within a geometric model (Forsberg et al., 2017). Figure 2.9(b) illustrates co-kriging, an interpolation method that uses multiple correlated variables simultaneously to improve overall estimation, to build upon the first method by also incorporating seismic velocities to guide the predictions of the geotechnical properties (Myers, 1984). Figure 2.9(c) illustrates a machine learning approach in the form of an artificial neural network to carry out multi-attribute regression between the various quantitative seismic features (Vardy et al., 2017, 2018). The geometric-geostatistical approach provides a coarse fit, the co-kriging and machine learning methods generate higher fidelity fits at least over the top 10 m of seabed, with the machine learning method capturing the form of the real CPT data at highest vertical resolution.

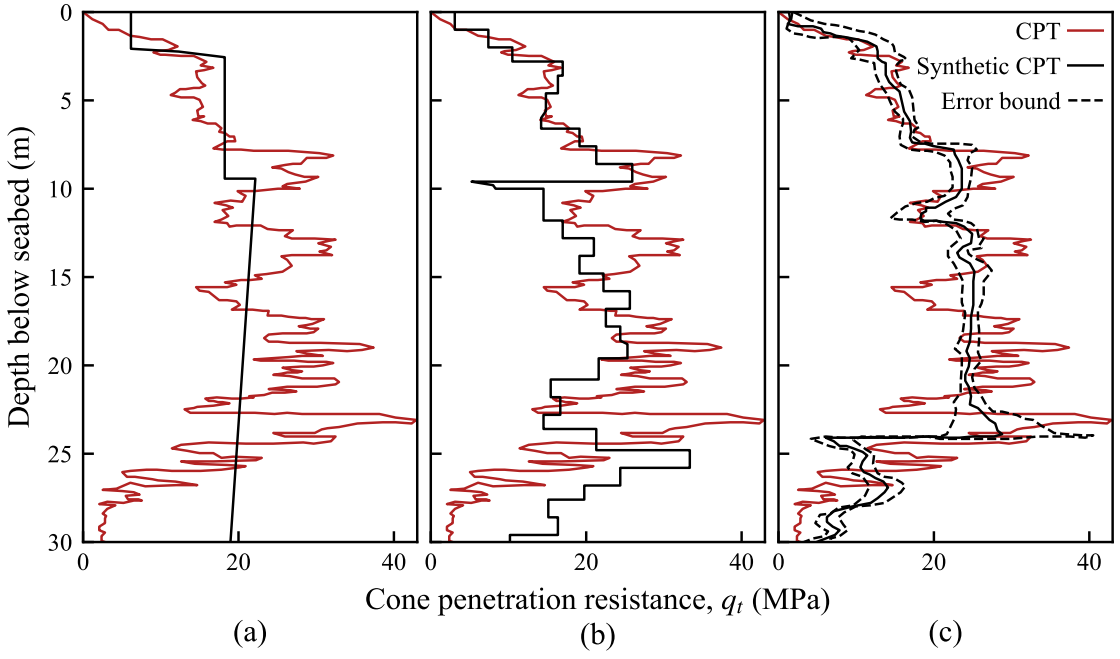

FIGURE 2.9: Synthetic CPT profiles from (a) geometric-geostatistic approach (b) co-kriging and (c) machine learning (after Sauvin et al. (2019))

Synthetic CPTs are a potentially transformational site investigation innovation, however, uptake is currently limited by uncertainty regarding the effect of the lower resolution profiles of soil resistance on design outcome (Sauvin et al., 2024). With a view to improving understanding of the effect of lower resolution of synthetic CPT profiles

on resulting geotechnical design outcomes, to move the approach towards wider acceptance by industry and regulators, this research systematically investigates the effect of CPT profile resolution on minimum required monopile size for ULS and SLS design under lateral loading.

2.4 Interpretation of a CPT

CPTs, as introduced in Section 2.3.2, measure cone penetration resistance (q_c), sleeve friction (f_s) and pore water pressure (u_2) with depth at the location of testing; a useful tool in soil profiling. It is common practice to pre-process cone penetration resistance data to incorporate corrections to pore water pressure and overburden that the equipment is unable to factor for (Section 2.4.1). Subsequent processing of the CPT data involves various methods of soil classification (Section 2.4.2) and the determination of additional soil parameters often utilised in pile design (Section 2.4.3).

2.4.1 Pre-processing

Pre-processing of the CPT data involves a few adjustments made to the measured parameters to take into consideration the pore water pressure and overburden effects. The pore pressure correction factor accounts for the water pressure acting on the back face of the porous disc in the cone shoulder (Campanella et al., 1982), allowing calculation of corrected cone penetration resistance (q_t) through Equation 2.1 (Robertson, 1990):

$$q_t = q_c + u_2(1 - \alpha) \tag{2.1}$$

where q_c is measured cone penetration resistance (MPa), u_2 is pore water pressure acting on the shoulder of the cone (MPa) and α is the net area ratio, which depends on the dimensions of the cone. α is typically provided by the cone manufacturer and is usually around 0.6 (Robertson and Campanella, 1983).

A pore pressure correction factor is sometimes also applied to the sleeve friction data through subtraction. As is the case for cone penetration resistance data, the value depends on the cone dimensions, but tends to be much smaller in magnitude. Pore pressure correction is important in clayey soils since excess pore pressure is high, whereas in granular soils pore water dissipates sufficiently quickly to be approximately hydrostatic during cone penetration.

The overburden correction enables calculation of net cone penetration resistance (q_{net}), removing the component of cone resistance caused by the pressure of the overlying

soil, as shown in Equation 2.2 (Robertson, 1990; Randolph and Gourvenec, 2011):

$$q_{net} = q_t - \sigma_v \tag{2.2}$$

where q_t is corrected cone penetration resistance (MPa) as given by Equation 2.1, and σ_v is the overburden at depth z below the seafloor, i.e. the in situ vertical total stress (MPa), given by:

$$\sigma_v = \gamma z \tag{2.3}$$

where γ is soil unit weight (kN/m^3) and z is depth below seafloor (m).

2.4.2 Soil classification

After the measured CPT data has been pre-processed, the corrected cone penetration resistance and sleeve friction parameters can be used to derive the type of soil. Differing levels of cone penetration resistance and sleeve friction are observed depending on the soil type (Bhattacharya, 2019). For example, coarse-grained soils typically exhibit higher cone penetration resistance and lower sleeve friction, whereas fine-grained soils tend to show the opposite behaviour, with elevated sleeve friction values and reduced resistance. As a result, several classification charts have been established which correlate these CPT properties to the type of soil.

One of the first classification charts to gain popularity was proposed by Robertson et al. (1986). This chart directly used the CPT parameters of corrected cone penetration resistance and sleeve friction to determine the friction ratio (R_f):

$$R_f = \frac{f_s}{q_t} \tag{2.4}$$

where f_s is sleeve friction (MPa) and q_t is corrected cone penetration resistance (MPa). Plotting corrected cone penetration resistance with friction ratio, expressed as a percentage, generated Figure 2.10, with the soil categorised into twelve regions.

However, due to the overburden of overlying soil, which was introduced in Section 2.4.1 and required correction through Equation 2.2, a normalised classification chart was developed (Robertson, 1990). This defined normalised cone resistance (Q_t) and normalised friction ratio (F_r) by normalising net cone resistance by vertical effective stress (Equation 2.5), and friction ratio by net cone resistance (Equation 2.7), respectively:

$$Q_t = \frac{q_{net}}{\sigma'_v} \tag{2.5}$$

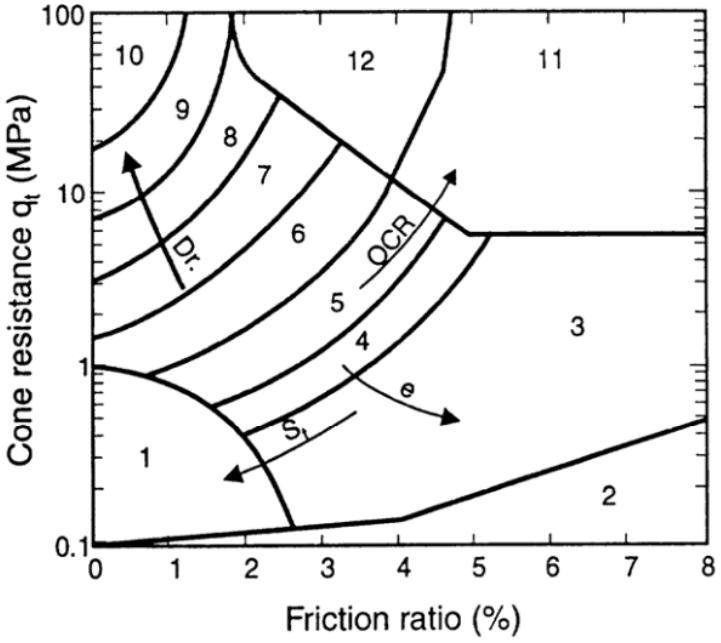

Zone	*Soil Behavior Type*
1	*Sensitive fine grained*
2	*Organic material*
3	*Clay*
4	*Silty Clay to clay*
5	*Clayey silt to silty clay*
6	*Sandy silt to clayey silt*
7	*Silty sand to sandy silt*
8	*Sand to silty sand*
9	*Sand*
10	*Gravelly sand to sand*
11	*Very stiff fine grained**
12	*Sand to clayey sand**

** Overconsolidated or cemented*

FIGURE 2.10: CPT-based soil classification chart (Robertson et al., 1986; Robertson, 2010)

where q_{net} is net cone penetration resistance (MPa), as given by Equation 2.2, and σ'_v is in situ vertical effective stress (MPa), found with Equation 2.6:

$$\sigma'_v = \sigma_v - u \tag{2.6}$$

where σ_v is in situ vertical total stress (MPa), as given by Equation 2.3, and u is the in situ pore water pressure at depth z below seafloor (m), given by u_2. Normalised friction ratio (expressed as a percentage) is given by:

$$F_r = \frac{f_s}{q_{net}} \tag{2.7}$$

where f_s is sleeve friction (MPa) and q_{net} is net cone penetration resistance (MPa).

The normalised soil classification chart can be seen in Figure 2.11, with only nine distinct soil regions. An updated version of the non-normalised Robertson et al. (1986) classification chart reduced the original twelve soil categories to match the nine in the normalised chart, as well as dividing the cone penetration resistance by an atmospheric pressure of 100 kPa in order to make both parameters dimensionless (Robertson, 2010; Robertson and Cabal, 2015). These CPT-based classification charts are advantageous in the way the cone responds to the in situ mechanical properties of the soil, predictive of Soil Behaviour Type, rather than classification in accordance to grain-size distribution and plasticity (Robertson, 2010). Overall, the normalised classification charts are more reliable at identifying Soil Behaviour Type since the normalisation reduces the influence of overburden effects, although differences between the two are small for in situ vertical effective stresses in the range of 50 to 150 kPa (Robertson, 1990, 2010).

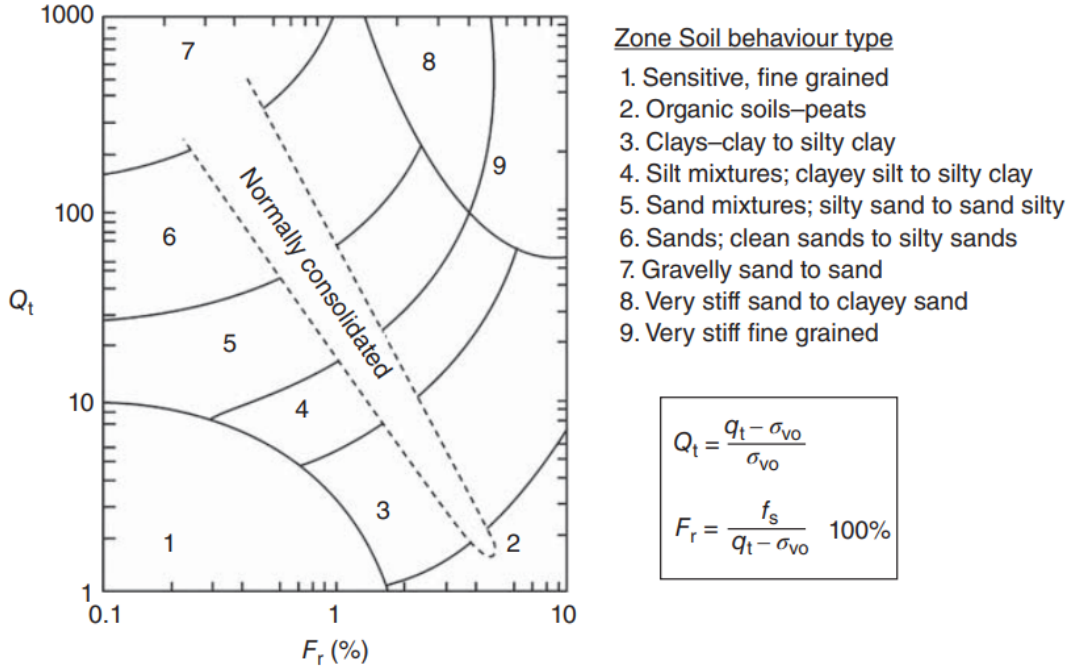

FIGURE 2.11: Normalised $Q_t - F_r$ soil classification chart (Robertson, 1990; Bhattacharya, 2019)

Whilst the pore water pressure measurements enable the measured cone penetration resistance to be corrected for the unequal end area effects of the CPT cone through Equation 2.1 (see Section 2.4.1), they can also aide in the identification of soil type (Randolph and Gourvenec, 2011). Excess pore water pressure (Δu_2) can be calculated:

$$\Delta u_2 = u_2 - u_0 \tag{2.8}$$

where u_2 is pore water pressure acting on the shoulder of the cone (MPa) and u_0 is in situ equilibrium pore water pressure (MPa). In the same way that corrected cone penetration resistance and sleeve friction were normalised, the excess pore water pressure

ratio (B_q) was derived:

$$B_q = \frac{\Delta u_2}{q_{net}} \tag{2.9}$$

where Δu_2 is excess pore water pressure (MPa) and q_{net} is net cone penetration resistance (MPa), as given by Equation 2.2. The normalised cone resistance is then plotted with excess pore pressure ratio to denote the soil type regions (Figure 2.12), with the numbers referring to the corresponding zones. Figure 2.12 can be used in addition to the $Q_t - F_r$ chart from Figure 2.11 to ensure that the same soil type zones are predicted for each pair of parameters. However, the $Q_t - F_r$ chart has proven to be more reliable (Robertson, 2009b).

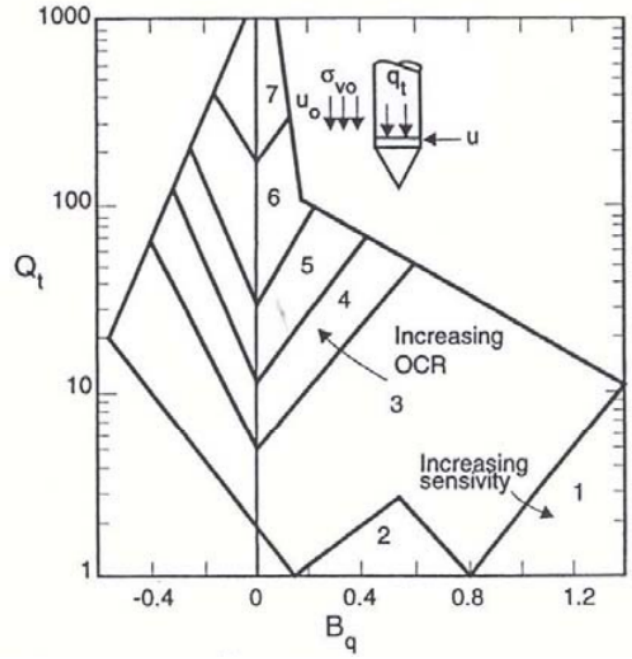

FIGURE 2.12: Normalised $Q_t - B_q$ soil classification chart (Robertson, 1990; Robertson and Cabal, 2015)

Instead of plotting on the Soil Behaviour Type charts to obtain soil type, the normalised cone resistance and normalised friction ratio were combined into a single value of Soil Behaviour Type Index (I_c) (Jefferies and Davies, 1993; Robertson and Wride, 1998):

$$I_c = \left((3.47 - \log Q_t)^2 + (\log F_r + 1.22)^2 \right)^{0.5} \tag{2.10}$$

where Q_t is normalised cone resistance and F_r is normalised friction ratio. The Soil Behaviour Type Index is the radius of concentric circles that represent the boundaries of the Soil Behaviour Type zones in the $Q_t - F_r$ chart (Figure 2.11) (Robertson, 2009b; Robertson and Cabal, 2015). Contours of I_c are shown in Figure 2.13, along with the values of the Soil Behaviour Type Index that denote each soil type zone within the $Q_t - F_r$ chart. The simplicity of directly inputting the parameters to an equation makes the soil classification based on the Soil Behaviour Type Index most convenient.

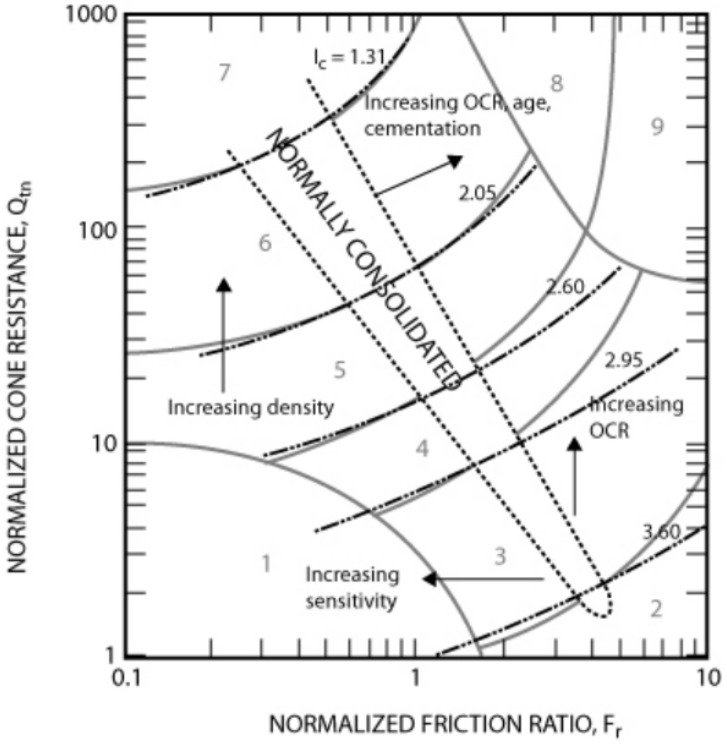

Zone	*Soil Behavior Type*	I_c
1	*Sensitive, fine grained*	N/A
2	*Organic soils – clay*	> 3.6
3	*Clays – silty clay to clay*	2.95 – 3.6
4	*Silt mixtures – clayey silt to silty clay*	2.60 – 2.95
5	*Sand mixtures – silty sand to sandy silt*	2.05 – 2.6
6	*Sands – clean sand to silty sand*	1.31 – 2.05
7	*Gravelly sand to dense sand*	< 1.31
8	*Very stiff sand to clayey sand**	N/A
9	*Very stiff, fine grained**	N/A

** Heavily overconsolidated or cemented*

FIGURE 2.13: Contours of Soil Behaviour Type Index on normalised $Q_t - F_r$ soil classification chart (Robertson et al., 1986; Robertson and Cabal, 2015)

The soil classification into either clay or sand governs which lateral resistance equation is to be used in pile design (see Section 2.5).

2.4.3 Soil parameters

There are several empirical correlations estimating geotechnical soil parameters from CPT data. This section focusses on three of the most commonly used parameters in lateral design of monopile foundations for offshore wind farm turbines: undrained shear strength of fine-grained soils (Section 2.4.3.1), relative density of coarse-grained soils (Section 2.4.3.2), and small strain shear stiffness of both fine and coarse-grained soils (Section 2.4.3.3).

2.4.3.1 Undrained shear strength

The undrained shear strength (s_u) is an indicator of the strength of fine-grained soils when they are loaded quickly and no time is allowed for drainage (Mayne, 2007). Its value varies based on the specific design problem since the response of the soil depends on the direction of loading, soil anisotropy, strain rate and stress history (Robertson and Cabal, 2015). The cone penetration resistance can be related to the undrained shear strength through empirical correlations, as portrayed in Equation 2.11:

$$s_u = \frac{q_t - \sigma_v}{N_{kt}} \tag{2.11}$$

where q_t is corrected cone penetration resistance (kPa) as given by Equation 2.1, σ_v is the in situ vertical total stress (kPa), and N_{kt} is a cone factor with a value generally between 11.5 and 15.5 for lightly overconsolidated clays (Randolph and Gourvenec, 2011). The numerator of this equation can be simplified to the net cone penetration resistance, in accordance with Equation 2.2.

2.4.3.2 Relative density

Relative density (D_r) is a measure of the compressibility of coarse-grained soils (Mayne, 2007), usually determined through values of void ratio. However, this requires laboratory analysis of disturbed samples and highlights the benefit of empirical correlations to derive relative density of sands from measured in situ CPT data (Jamiolkowski et al., 2003). CPT cone penetration resistance is affected by the compressibility of a sand, which in turn is influenced by grain characteristics (Robertson and Cabal, 2015). The greater the compressibility of a sand, the lower the cone penetration resistance for a

given relative density. Such a correlation can be expressed in the form of Equation 2.12:

$$D_r = D + Elog\left(\frac{q_c}{\sigma_v'^{0.5}}\right) \tag{2.12}$$

where D and E are constants, q_c is measured cone penetration resistance (kPa) since correction for pore water pressure is unnecessary in sands (see Section 2.4.1), and σ_v' is the in situ vertical effective stress (kPa). If a database is available, D and E can take values in accordance with the line of best-fit, however, for a sand of average compressibility, values of -1.21 and 0.584 can be assumed, respectively (Knappett and Craig, 2020).

2.4.3.3 Small strain stiffness

The small strain stiffness (G_0) of a soil governs the lateral response of a monopile foundation for an offshore wind turbine (Stuyts, 2024). This is the elastic stiffness of a soil at shear strains of less than 10^{-6} (Robertson and Cabal, 2015). The small strain stiffness can be calculated directly from the shear wave velocity through Equation 2.13 or by correlation to the cone penetration resistance measured in a CPT.

$$G_0 = \rho V_s^2 \tag{2.13}$$

where ρ is bulk density of the soil (derived from saturated unit weight) (kg/m^3) and V_s is shear wave velocity (m/s).

Whilst various methods exist to measure shear wave velocity either in situ or in the laboratory, the relatively high cost typically restricts their application to select foundation locations (Stuyts, 2024). However, accurate soil stiffness profiles are required at every wind turbine location to allow for soil-structure interaction analyses, including SLS design and natural frequency assessments (see Section 2.5.3) (Byrne et al., 2015). Therefore, using empirical correlations to derive the small strain stiffness from CPT data is desirable.

A critical difference between CPT and small strain stiffness measurements is the scale on which the strains occur: CPTs induce large strains in the soil, whereas small strain stiffness concern small strain conditions (Stuyts, 2024). Despite the challenge this poses in terms of obtaining an appropriate correlation, Mayne and Rix (1993) and Rix and Stokoe (1991) developed Equations 2.14 and 2.15 for clays and sands, respectively.

For clay:

$$G_0 = 2.78(q_t)^{1.335} \tag{2.14}$$

where q_t is corrected cone penetration resistance (kPa).

For sand:

$$G_0 = 1634(q_c)^{0.25}(\sigma_v')^{0.375} \tag{2.15}$$

where q_c is measured cone penetration resistance (kPa) since correction for pore water pressure is unnecessary in sands (see Section 2.4.1), and σ'_v is vertical effective stress (kPa).

These equations were based on calibration chamber tests and have been used as the basis of extended correlations, such as combining the single small strain stiffness of clays and sands into a single correlation expression (Peuchen et al., 2022a).

2.5 Monopile design

From the soil profiles gathered through CPTs at the desired locations of monopile foundations for offshore wind turbines, the monopiles are designed to have sufficient dimensions that they can withstand the design loads applied to the structure and under certain conditions. Design will focus on lateral resistance of the soil in opposition to the large horizontal forces of the wind and waves acting on the monopile foundation in accordance with the most critical failure mechanism (see Sections 2.2.2 and 2.2.3 for loading on monopiles and design criteria, respectively). This is usually assessed in terms of capacity and deflection. Capacity of the monopile is the maximum lateral load it can resist before failure, whereas deflection is the limiting displacement and rotation of the monopile.

The overall behaviour of laterally loaded monopiles for offshore wind turbine foundations is commonly based on a Winkler modelling approach, known as the $p-y$ method (Byrne et al., 2015). This consists of modelling the pile as a beam and the soil as a series of independent, nonlinear springs. Each spring is defined as a $p-y$ curve, where p is the reaction of the soil on the pile, and y is the resulting lateral displacement of the pile at a given depth (Ahayan et al., 2019). Figure 2.14 demonstrates this $p-y$ model for a monopile split into four depth segments of soil, each represented by their own reaction curve with spring stiffness (E_{py}), defined as the secant modulus of the curve. Both capacity and deflection criteria can be identified through points on the $p-y$ curve. Sections 2.2.3.1 and 2.2.3.2 referred to these design criteria as ULS and SLS. The following sections will compare different monopile design methods of ultimate lateral resistance and $p-y$ curves.

2.5.1 Original methods

The ultimate lateral resistance of a clay soil can be linked to the undrained shear strength of the soil, with the governing failure mechanisms varying significantly with depth. Near the ground surface, failure is characterised by the formation of a conical soil wedge that is displaced upward. This wedge of soil failing in front of the monopile

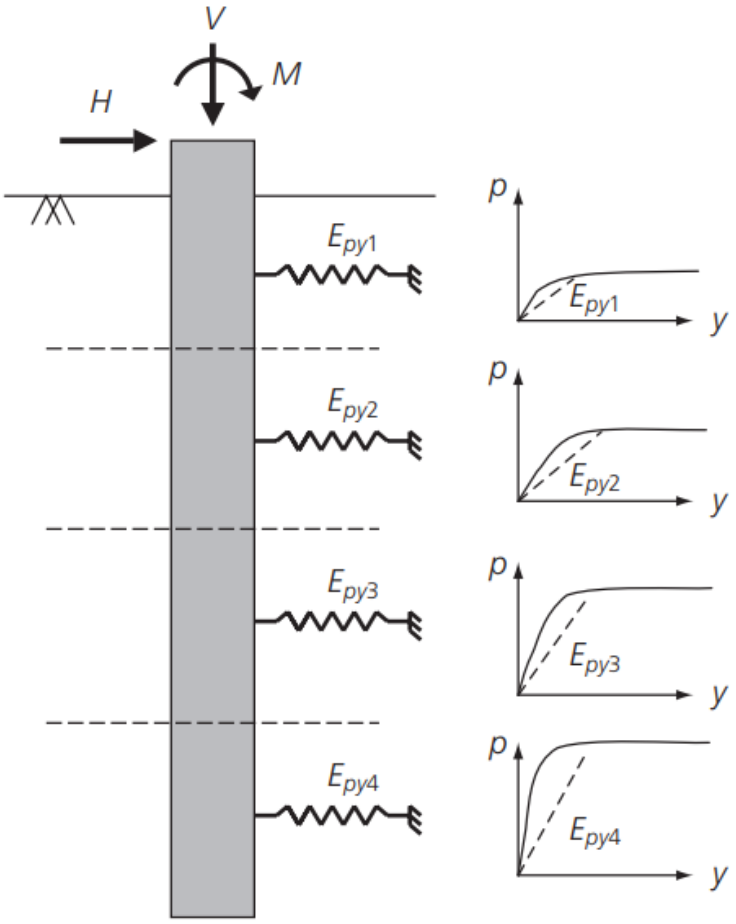

FIGURE 2.14: $p - y$ model based on Winkler approach (Doherty and Gavin, 2012)

forms a gap behind the pile, which reduces the ultimate lateral resistance of the soil with depth. The mechanism is resisted by a combination of shaft friction, internal soil shear, and the self-weight of the displaced wedge (Randolph and Gourvenec, 2011), as indicated in Figure 2.15. Beyond a depth of reduced resistance, failure involves the flow of soil in a horizontal plane around the pile shaft.

Matlock (1970) proposed a non-dimensional ultimate resistance factor as a function of the depth to diameter ratio within the monopile. For cylindrical piles, this has a minimum value of three at the surface, increasing with depth to a limiting value of nine at the point of reduced resistance (Matlock, 1970). Beyond this depth, the soil resistance can be conservatively assumed to remain this value (Matlock, 1970), although it has been shown to slightly increase with the roughness of the interfaces between flow around regions (Murff and Hamilton, 1993).

The accompanying $p - y$ curves were compiled through piecewise functions, with the ultimate lateral resistance equation forming the last segment where the curve becomes a horizontal line (Figure 2.16 Point e). Due to the non-dimensional form of the $p - y$ curves, the lateral resistance is normalised through division of the static ultimate lateral

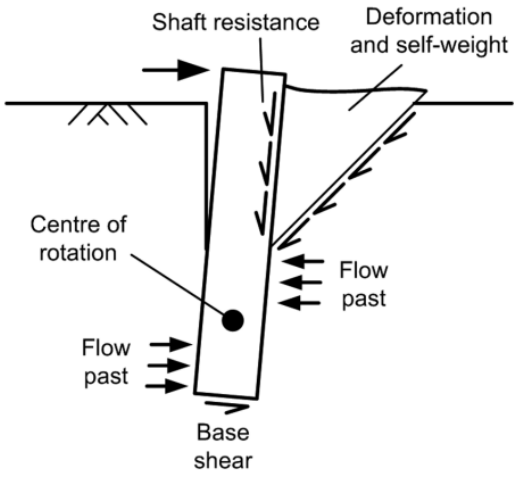

FIGURE 2.15: Lateral resistance in clay close to ground surface (Randolph and Gourvenec, 2011)

resistance, therefore, this final segment plots at a vertical coordinate of one. Normalisation of pile deflection, plotted on the horizontal axis, involves division by the deflection where the static lateral resistance is half of the ultimate value (Figure 2.16 Point c). The first segment of the $p - y$ curve, up to Point c, estimates the short-term load-settlement characteristics, based on elastic theory, ultimate strength and laboratory soil properties (Matlock, 1970). Connecting these first and last segments is the middle section between Points c and e. This represents the preplastic portion of the static resistance curve, where the $p - y$ behaviour is modelled through a cubic root function (to the power of 1/3), and therefore, always intercepts with the last segment at a normalised pile deflection of eight (Matlock, 1970). Alterations to the functions of the $p - y$ curve shown in Figure 2.16 can be made to allow for cyclic loading and reloading (Matlock, 1970).

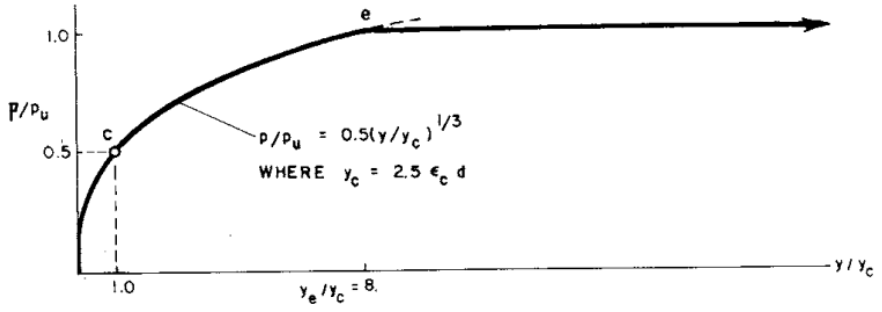

FIGURE 2.16: Matlock (1970) normalised $p - y$ curve

In terms of sand, the ultimate lateral resistance also depends on the depth of the failure mechanism, with separate expressions for shallow and deep depths. The one that governs is the minimum of the two. However, the more complex interactions between the soil self-weight and stresses from the pile load mean straightforward mechanisms, such as the wedge and flow around failure of clays, cannot be constructed (Randolph and Gourvenec, 2011). This means that the variation of the ultimate lateral resistance

with depth must be established empirically and checked against field or model test data (Randolph and Gourvenec, 2011). Reese et al. (1974) proposed empirical coefficients based on the density and friction angle of the sand to determine the ultimate lateral resistance at shallow and deep depths. The $p-y$ curves consist of an initial portion that is essentially a straight line, representing linear elastic behaviour, with a slope defined through the initial stiffness of the soil (Reese et al., 1974). In a similar way to Matlock (1970) for clay, the ultimate lateral resistance defines the final horizontal segment of the curve. However, the overall shape can be modelled by a *tanh*-shaped curve which approximates the initial and final sections, whilst capturing the non-linear soil behaviour of the middle section (Reese et al., 1974).

However, the methods of Matlock (1970) and Reese et al. (1974) were derived especially for the long, slender piles of offshore oil and gas structures, which are significantly different to the design of monopiles for offshore wind turbines. Whilst offshore oil and gas piles have lengths ranging from 30 to 100 m with diameters no greater than 2 m, monopiles for offshore wind turbines do not tend to exceed 30 m in length but have much greater diameters of up to 10 m with the potential to be increased further (Houlsby, 2016). The difference in length to diameter ratio results in the stiff behaviour in bending of monopiles for offshore wind turbines (see Section 2.2.1), as opposed to the flexible nature of offshore oil and gas piles (Leblanc et al., 2010). The requirement for much stiffer monopiles for offshore wind turbines is attributed to the fact that oil and gas used jacket structures supported on piles, whilst the wind turbine mast is a single slender structure (Randolph and Gourvenec, 2011). As a result, such $p-y$ methods are not appropriate for the use in monopiles for offshore wind turbine foundations.

2.5.2 CPT-based methods

2.5.2.1 Clay

There has been the development of CPT-based equations to derive the lateral pile response directly from CPT profiles of cone penetration resistance parameters. This is beneficial since the estimation of undrained shear strength for clay soils is difficult due to the influence of rate dependencies and anisotropy, as well as being derived from disturbed samples that do not accurately represent in situ conditions (Guo et al., 2014; Truong and Lehane, 2014). The study of Truong and Lehane (2014), involved the numerical derivation of $p-y$ curves in clay from correlations with net cone penetration resistance. A linear elastic perfectly plastic soil was modelled through three-dimensional finite element (FE) analyses to predict the behaviour of piles under lateral loading (Truong and Lehane, 2014). The lateral pile displacements were read directly from the FE model for each increment of applied load, with the soil lateral resistance

determined by double differentiation of the bending moment diagrams. The relationship between the ultimate lateral resistance of the soil (p_u) and the net cone penetration resistance was found to be governed by a resistance factor as a function of depth to diameter ratio and rigidity index. Whilst the resistance factor is responsible for how much soil strength, through the CPT data, translates into soil lateral resistance, the diameter of the pile scales this resistance. Therefore, the ultimate lateral resistance is expressed (Truong and Lehane, 2014):

$$p_u = Dq_{net}\left(\left(\frac{3}{4.7+1.6\ln I_r}\right)+(1.5-0.14\ln I_r)\tanh\left(\frac{0.65\,z}{D}\right)\right) \tag{2.16}$$

where D is diameter (m), q_{net} is net cone penetration resistance (MPa), I_r is rigidity index, which is the ratio between shear modulus and undrained shear strength of a soil (Randolph and Gourvenec, 2011), and z is depth below seafloor (m).

To obtain the $p-y$ curves from the FE model, the extracted lateral displacements and corresponding lateral resistances were normalised to allow comparison across different pile dimensions and soil strengths. Normalisation of displacement involved dividing by pile diameter, whereas lateral resistance was normalised by division of the ultimate lateral resistance. The plotted normalised $p-y$ curves are displayed in Figure 2.17 for a constant rigidity index of 200 and various depth to diameter ratios. Regression analyses of these normalised curves led to the $p-y$ equation (Truong and Lehane, 2014):

$$\frac{p}{p_u}=\begin{cases}\tanh\left((0.26I_r+3.98)\left(\frac{y}{D}\right)^{0.85}\left(\frac{z}{D}\right)^{-0.5}\right) & \text{for } \frac{z}{D}<3\\[2ex] \tanh\left((0.15I_r+2.3)\left(\frac{y}{D}\right)^{0.85}\right) & \text{for } \frac{z}{D}\geq 3\end{cases} \tag{2.17}$$

The $p-y$ curves in Figure 2.17 show that the slope of the curve reduces as the depth to diameter ratio increases, but only up to a value of three. This change in dependency on diameter to depth ratio is a result of the failure mechanism moving from shallow to deep soil. At a diameter to depth ratio of three, failure of the soil occurs by flow around the pile, however, below this depth, wedge failure dominates (Truong and Lehane, 2014). Therefore, $p-y$ curves are not unique for all depth to diameter ratios, as was believed from earlier methods such as Matlock (1970). Comparison of the resistance factors between Matlock (1970) and (Truong and Lehane, 2014) has also revealed that Matlock (1970) underpredicts lateral resistance by 20 %. In terms of rigidity index, its effect on the shape of the $p-y$ curve is concentrated in the initial slope, at the early stages of loading where deflections remain small.

Centrifuge tests on open-ended piles in kaolin clay were also performed in a related study (Guo et al., 2014) which verified the results from Truong and Lehane (2014). Overall, Truong and Lehane (2014) demonstrate an improvement to Matlock (1970)

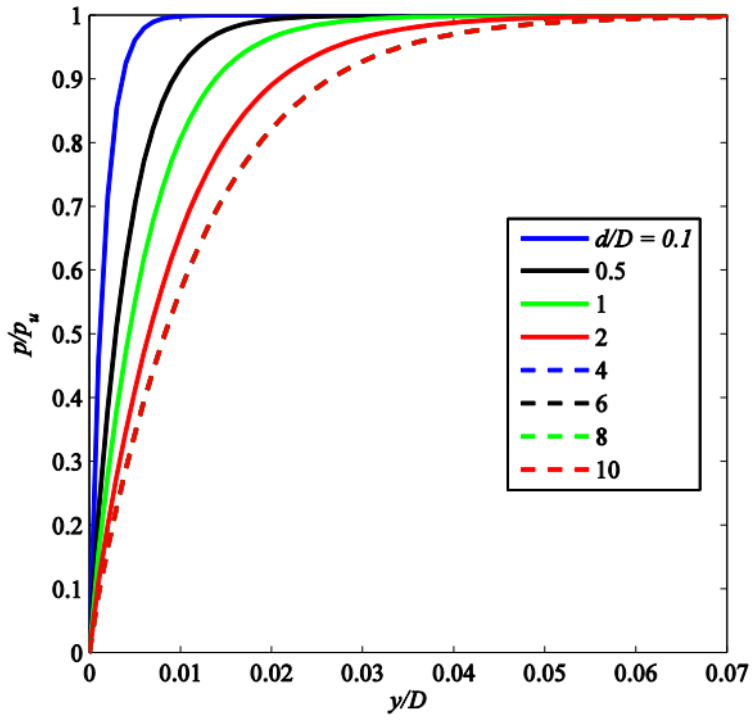

FIGURE 2.17: Truong and Lehane (2014) normalised $p - y$ curve (Doherty, 2020)

in predicting the lateral behaviour of piles in clay soils. A key development is the applicability of Truong and Lehane (2014) to monopiles for offshore wind turbines, since the piles tested had a much lower length to diameter ratio than those used in Matlock (1970). Furthermore, the length to diameter ratio of the piles was limited to ensure capacity was controlled by soil strength so that failure would occur by rigid rotation of the pile about a pivot point (Guo et al., 2014). As was mentioned in Section 2.2.1, this is the behaviour typical of offshore wind turbine monopile foundations under lateral loading.

2.5.2.2 Sand

Soil parameters that affect the lateral resistance of sands, including density and friction angle, can be related to the cone penetration resistance from CPTs. A numerical correlation between $p - y$ curves and cone penetration resistance in sands has been derived through FE analyses (Suryasentana and Lehane, 2014). The sand was modelled as a non-linear elasto-plastic material with a fully rough interface with the pile (Suryasentana and Lehane, 2014). A range of pile diameters in several different types of sand were subjected to increasing lateral loads, from which their behaviour could be assessed. The profiles of cone penetration resistance in these different soils were simulated and then related to the lateral pile behaviour. An exponential expression was

found to best model the $p-y$ response, especially to limit the tendency of overpredictions of lateral resistance at large displacements (Suryasentana and Lehane, 2014):

$$p = 2.4\,\sigma'_v\,D\left(\frac{q_c}{\sigma'_v}\right)^{0.67}\left(\frac{z}{D}\right)^{0.75}\left\{1-\exp\left[-6.2\left(\frac{z}{D}\right)^{-1.2}\left(\frac{y}{D}\right)^{0.89}\right]\right\} \tag{2.18}$$

where σ'_v is vertical effective stress (kPa), D is diameter (m), q_c is measured cone penetration resistance (MPa) since correction for pore water pressure is unnecessary in sands (see Section 2.4.1), z is depth below seafloor (m), and y is lateral displacement of pile at seafloor (m). Ultimate lateral resistance then simplifies to Equation 2.19 with the normalised $p-y$ curves given through Equation 2.20.

$$p_u = 2.4\,\sigma'_v\,D\left(\frac{q_c}{\sigma'_v}\right)^{0.67}\left(\frac{z}{D}\right)^{0.75} \tag{2.19}$$

$$\frac{p}{p_u} = 1-\exp\left[-6.2\left(\frac{z}{D}\right)^{-1.2}\left(\frac{y}{D}\right)^{0.89}\right] \tag{2.20}$$

The $p-y$ curves are plotted in Figure 2.18 for a range of depth to diameter ratios. As depth to diameter ratio increases, the $p-y$ curve becomes flatter, due to the decrease in the exponential term of the expression. This means the rate of mobilisation of resistance is slower. A deeper embedment depth increases the ultimate lateral capacity of the pile, therefore a larger displacement is required to mobilise it.

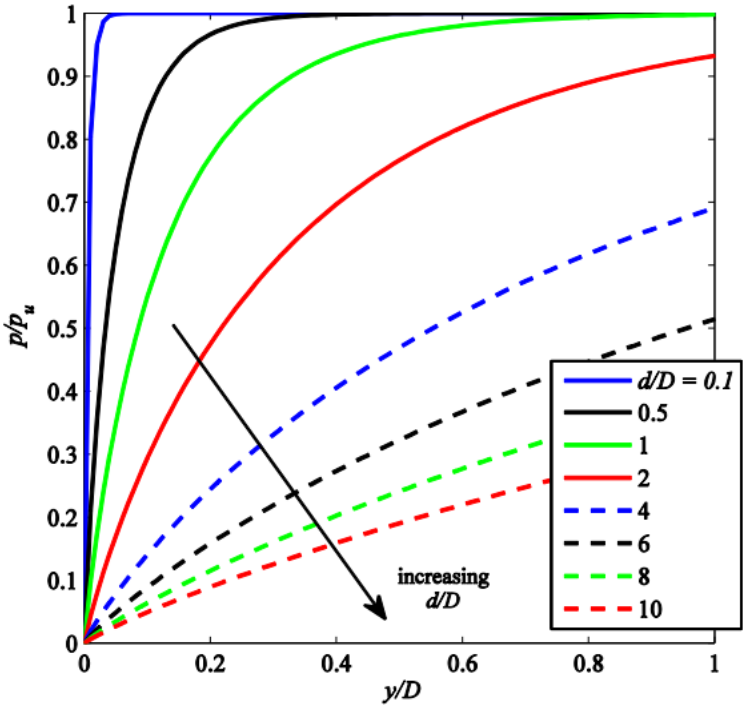

FIGURE 2.18: Suryasentana and Lehane (2014) normalised $p-y$ curve (Doherty, 2020)

However, from Figure 2.18 it can be seen that most of the $p-y$ curves do not fully

mobilise the ultimate lateral resistance of the soil, even at large displacements equal to the pile diameter. As a result, piles designed using Equation 2.19 for ultimate limit state design would have dimensions much too small for any realistic serviceability limit state. Furthermore, data used to derive Equation 2.19 was limited to y/D ratios of less than or equal to 0.1 so predictions for values larger than 0.1 are not validated. A solution for this is to use the full exponential form of Equation 2.18 for ultimate lateral resistance with the y/D parameter set to 0.1:

$$p_u = 2.4\,\sigma'_v\,D\left(\frac{q_c}{\sigma'_v}\right)^{0.67}\left(\frac{z}{D}\right)^{0.75}\left\{1-\exp\left[-6.2\left(\frac{z}{D}\right)^{-1.2}(0.1)^{0.89}\right]\right\} \tag{2.21}$$

This sets a limit of deflection of 10 % of the pile diameter, normally considered the point at which pile capacity has been reached (Lehane, 2019) and therefore the pile failed.

Another similar expression for the lateral resistance of monopiles in sand which has the same dependence on the cone penetration resistance is Equation 2.22 (Wang et al., 2022), which was developed for use as a $p-y$ curve calibrated against CPT data:

$$p = \sigma'_v D\left[\frac{2.7q_c}{\sqrt{\sigma'_v p_a}}\right]^{0.7}\tanh\left[5\left(\frac{y}{D}\right)^{0.55}\right] \tag{2.22}$$

where σ'_v is vertical effective stress (kPa), D is diameter (m), q_c is measured cone penetration resistance (MPa) since correction for pore water pressure is unnecessary in sands (see Section 2.4.1), p_a is atmospheric pressure (= 100 kPa), z is depth below seafloor (m), and y is lateral displacement of pile at seafloor (m). For large displacements, the *tanh* component approaches one, so the ultimate lateral resistance can be obtained:

$$p_u = 2.0\,\sigma'_v D\left(\frac{q_c}{\sigma'_v}\right)^{0.7}\left(\frac{\sigma'_v}{p_a}\right)^{0.35} \tag{2.23}$$

The σ'_v/p_a term can then be expressed in terms of pile diameter and normalised depth, z/D, to allow direct comparison to Equation 2.21:

$$p_u = 2.0\,\sigma'_v D\left(\frac{q_c}{\sigma'_v}\right)^{0.7}\left(\frac{z}{D}\right)^{0.35}\left(\frac{\gamma' D}{p_a}\right)^{0.35} \tag{2.24}$$

where γ' is the soil effective unit weight (kPa). Since the submerged unit weight of sand is typically about 10 kN/m^3, and the typical order of magnitude of monopile diameters for offshore wind turbines is 10 m, the $\gamma' D/p_a$ ratio is approximately equal to one. The three Equations of 2.19, 2.21 and 2.24 can now be compared for various depth to diameter (Figure 2.19) and cone penetration resistance to vertical effective stress (Figure 2.20) ratios.

Plotting normalised ultimate lateral resistance with normalised cone penetration resistance in Figure 2.19 demonstrates that normalised ultimate lateral resistance increases with normalised cone penetration resistance at a decreasing rate for all three equations

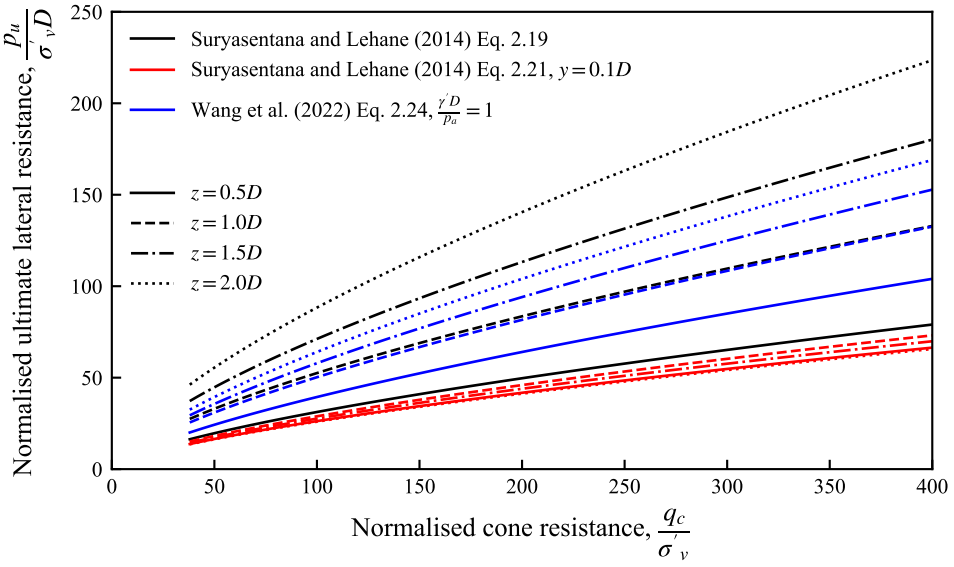

FIGURE 2.19: Comparison of different normalised ultimate lateral resistance expressions with normalised cone resistance for a range of depths

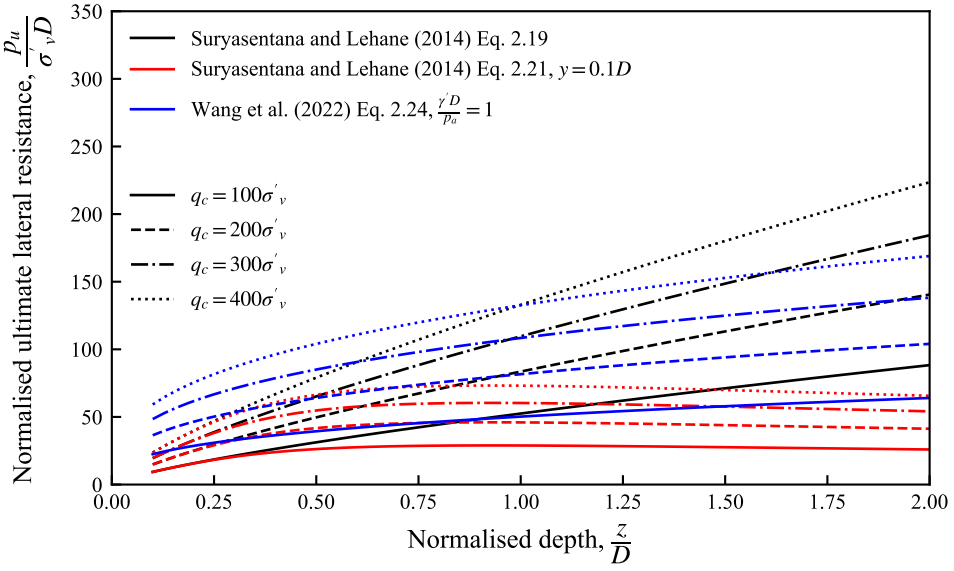

FIGURE 2.20: Comparison of different normalised ultimate lateral resistance expressions with normalised depth for a range of cone penetration resistances

but the rate at which this occurs depends on the specific method. Equation 2.21 shows the smallest amount of increase in normalised ultimate lateral resistance as normalised cone penetration resistance increases, with varying depth to diameter ratios having very little effect on the $p - y$ curve. The steepness of the curves for the other two methods is much more dependent on the depth to diameter ratio. Equation 2.19 exhibits the greatest increase in steepness with increasing depth to diameter ratio. For an increase in normalised cone penetration resistance from 100 to 200, normalised ultimate lateral resistance increases by 25 at $z/D = 0.5$, but by double this amount at $z/D = 2$. The behaviour of the $p - y$ curves from Equation 2.24 displays behaviour somewhere between

the other two.

In Figure 2.20, where normalised ultimate lateral resistance is plotted against normalised depth (depth to diameter ratio), the curves do not exhibit the same overall shapes. Equation 2.19 shows an almost linear increase in normalised ultimate resistance with normalised depth, the gradient of the line a function of the cone penetration resistance to vertical effective stress ratio. For all three methods, increasing the cone penetration resistance to vertical effective stress ratio increases the normalised ultimate lateral resistance. The other two Equations of 2.24 and 2.21 reveal that there is a point at which increasing normalised depth no longer causes an increase in normalised ultimate lateral resistance. Whilst normalised ultimate lateral resistance plateaus for Equation 2.24, a decrease is observed for Equation 2.21. Combined with the very shallow steepness of the $p - y$ curve at $q_c/\sigma'_v = 400$, the normalised depth barely impacts the value of normalised ultimate lateral resistance.

Overall, Figures 2.19 and 2.20 demonstrate that Equation 2.21 has the least variation in $p - y$ curves and, most crucially, is much less dependent on depth to diameter ratio than Equations 2.19 and 2.24. In comparison to earlier methods such as Reese et al. (1974), the $p - y$ curve of Suryasentana and Lehane (2014) also shows good agreement with the observed load displacement response, whereas Reese et al. (1974) predicts a much stiffer load displacement result. This can be attributed to the fact that Suryasentana and Lehane (2014) takes into consideration much smaller length to diameter ratios, making it more appropriate in predicting the lateral behaviour of monopiles for offshore wind turbines. Therefore, in this work, the modified Equation of 2.21, will be used to limit the ultimate lateral resistance of the Suryasentana and Lehane (2014) $p - y$ curves to within more representative lateral displacements of pile design of offshore wind turbines.

2.5.3 PISA method

The Pile Soil Analysis (PISA) method was developed to address the limitations of traditional $p - y$ curve approaches (Section 2.5.1) which were originally calibrated for slender, flexible piles. These conventional methods often underpredict the lateral stiffness and capacity of large-diameter monopiles used in offshore wind turbine foundations. The PISA project introduced a more advanced framework by calibrating a one-dimensional Winkler-type model using results from three-dimensional FE analyses (Byrne et al., 2015, 2019). It still kept the basis of the $p - y$ method, modelling the pile and soil in the same way as previous methods, but added additional soil reactions which become important for monopiles with low length to diameter ratios. In total there are four components of soil reactions taken to act on the monopile. Besides the distributed lateral load (p), a distributed moment (m) is included, as a result of the vertical tractions induced on the perimeter of the pile when there are vertical displacements at the pile-soil interface. The final two soil reactions are the lateral force (H_B)

and moment (M_B) on the pile base (Byrne et al., 2015, 2019). An idealisation of these soil reaction components acting on the pile is portrayed in Figure 2.21, alongside the corresponding one-dimensional FE model. The pile is modelled as a Timoshenko beam in order to include shear strain effects (Byrne et al., 2015). Each soil reaction component is related to the local lateral displacement or rotation through a calibrated parametric function of a soil reaction curve (Byrne et al., 2019). These curves are formulated using dimensionless variables, which allows for the development of standardised curve shapes that can be efficiently scaled to represent soil reactions at any depth along the pile during numerical implementation (Burd et al., 2020; Byrne et al., 2020). The dimensionless forms are given in Table 2.1.

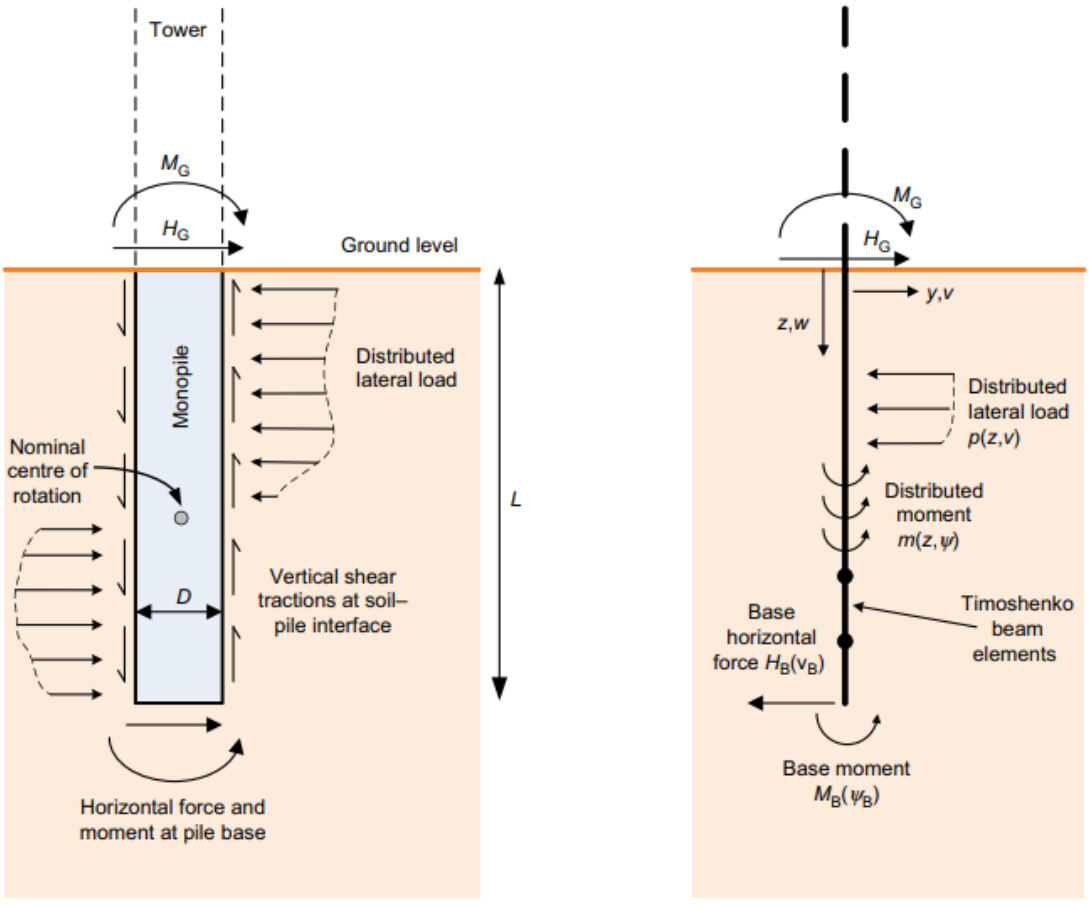

FIGURE 2.21: PISA design model (Burd et al., 2020; Byrne et al., 2015, 2020)

The soil reaction curves are represented in the one-dimensional model based on the four-parameter conic function (Burd et al., 2020; Byrne et al., 2020):

$$-n\left(\frac{\bar{y}}{\bar{y}_u}-\frac{\bar{x}}{\bar{x}_u}\right)^2+(1-n)\left(\frac{\bar{y}}{\bar{y}_u}-\frac{\bar{x}k}{\bar{y}_u}\right)\left(\frac{\bar{y}}{\bar{y}_u}-1\right)=0 \tag{2.25}$$

where $\bar{x}$ is normalised displacement or rotation, $\bar{y}$ is the corresponding normalised load or moment, $\bar{x}_u$ is normalised ultimate displacement, $\bar{y}_u$ is normalised ultimate load, k is

TABLE 2.1: Dimensionless groups for soil reaction curves (Burd et al., 2020; Byrne et al., 2020)

Normalised variable	**Non-dimensional form**	
	Clay	**Sand**
Distributed load, $\bar{p}$	$\frac{p}{s_u D}$	$\frac{p}{\sigma'_{vi} D}$
Lateral displacement, $\bar{v}$	$\frac{v G_0}{D s_u}$	$\frac{v G_0}{D \sigma'_{vi}}$
Distributed moment, $\bar{m}$	$\frac{m}{s_u D^2}$	$\frac{m}{\lvert p \rvert D}$
Pile cross-section rotation, $\bar{\psi}$	$\frac{\psi G_0}{s_u}$	$\frac{\psi G_0}{\sigma'_{vi}}$
Base horizontal force, $\bar{H}_B$	$\frac{H_B}{s_u D^2}$	$\frac{H_B}{\sigma'_{vi} D^2}$
Base moment, $\bar{M}_B$	$\frac{M_B}{s_u D^3}$	$\frac{M_B}{\sigma'_{vi} D^3}$

initial stiffness where $\bar{x}_u > \bar{y}_u / k$, and n is the curvature parameter with values between zero and one. The conic form of this function is displayed graphically in Figure 2.22.

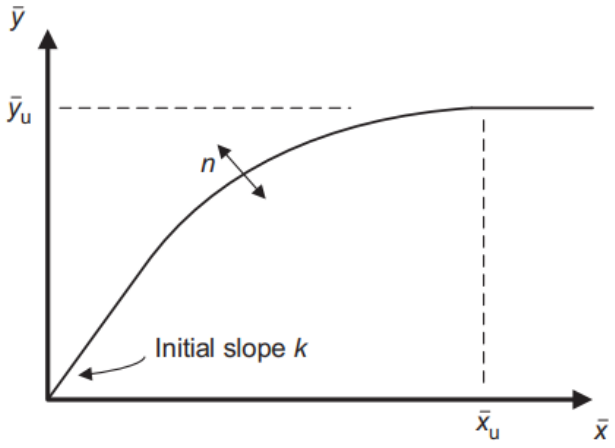

FIGURE 2.22: Conic form of the function used to represent the PISA soil reaction curves (Burd et al., 2020; Byrne et al., 2020)

The normalised soil reactions are determined through (Burd et al., 2020; Byrne et al., 2020):

$$\frac{\bar{y}}{\bar{y}_u} = \begin{cases} \dfrac{2c}{-b + \sqrt{b^2 - 4ac}}; & \bar{x} \leq \bar{x}_u \\ 1; & \bar{x} > \bar{x}_u \end{cases} \tag{2.26}$$

where a, b and c are parameters obtained through Equations 2.27, 2.28 and 2.29, respectively (Burd et al., 2020; Byrne et al., 2020).

$$a = 1 - 2n \tag{2.27}$$

$$b = 2n\frac{\bar{x}}{\bar{x}_u} - (1-n)\left(1 + \frac{\bar{x}k}{\bar{y}_u}\right) \tag{2.28}$$

$$c = \frac{\bar{x}k}{\bar{y}_u}(1-n) - n\frac{\bar{x}^2}{\bar{x}_u^2} \tag{2.29}$$

The dimensionless data in Table 2.1 is calibrated to the mathematical conic function of Equation 2.25 for each site through three-dimensional FE analyses with a range of pile dimensions and soil parameters to find the best fit. The PISA method then effectively interpolates the response of these three-dimensional FE analyses. In the PISA project, calibration involved field tests from two onshore sites: Cowden and Dukirk for clay and sand, respectively, with the resulting parameters detailed in Tables 2.2 and 2.3.

The PISA method offers two approaches for developing soil reaction curves. The rule-based method is typically used during concept design when detailed soil behaviour data is not available. This approach relies on basic strength and stiffness parameters, obtained from desk studies or preliminary site investigations, and applies pre-defined soil reaction functions based on soil type (Byrne et al., 2015), such as those from Cowden or Dunkirk. The numerical-based method is used for detailed design and involves comprehensive site investigations and laboratory testing to determine site-specific soil properties. Three-dimensional FE analyses are performed on representative monopile configurations, tailored to local soil conditions and pile dimensions. The resulting soil reaction curves are then extracted from the simulation results and incorporated into the one-dimensional PISA model, enabling efficient evaluation of different foundation layouts and locations (Byrne et al., 2015).

Overall, the PISA method enables more accurate and efficient design for offshore wind monopiles than traditional $p-y$ methods, such as those of Matlock (1970) and Reese et al. (1974), as it is specifically calibrated for large-diameter, short piles using advanced three-dimensional simulations and site-specific data. This leads to better material optimisation and more reliable predictions of lateral stiffness and capacity. However, the calibration of the model to specific sites requires high quality field tests. In comparison to CPT-based methods, the PISA method includes the resistance of the pile base, which can generate a much more significant proportion of the overall lateral resistance in monopiles for offshore wind turbines. While both PISA and CPT-based methods can be derived directly from CPT data, PISA requires the conversion of the CPT parameters into different soil properties of undrained shear strength, relative density and small strain stiffness.

TABLE 2.2: Soil reaction curve parameters for clay (Byrne et al., 2020)

Soil reaction component	**Parameter**	**Depth variation functions**
Distributed lateral load, p	Ultimate displacement, $\bar{v}_{pu}$	241.4
	Initial stiffness, k_p	$10.60 - 1.650\frac{z}{D}$
	Curvature, n_p	$0.9390 - 0.03345\frac{z}{D}$
	Ultimate reaction, $\bar{p}_u$	$10.70 - 7.101e^{-0.3085\frac{z}{D}}$
Distributed moment, m	Ultimate rotation, $\bar{\psi}_{mu}$	Given by $\bar{m}_u/k_m$
	Initial stiffness, k_m	$1.420 - 0.09643\frac{z}{D}$
	Curvature, n_m	0.0
	Ultimate moment, $\bar{m}_u$	$0.2899 - 0.04775\frac{z}{D}$
Base horizontal force, H_B	Ultimate displacement, $\bar{v}_{Hu}$	235.7
	Initial stiffness, k_H	$2.717 - 0.3575\frac{L}{D}$
	Curvature, n_H	$0.8793 - 0.03150\frac{L}{D}$
	Ultimate reaction, $\bar{H}_{Bu}$	$0.4038 + 0.04812\frac{L}{D}$
Base moment M_B	Ultimate rotation, $\bar{\psi}_{Mu}$	173.1
	Initial stiffness, k_M	$0.2146 - 0.002132\frac{L}{D}$
	Curvature, n_M	$1.079 - 0.1087\frac{L}{D}$
	Ultimate reaction, $\bar{M}_{Bu}$	$0.8192 - 0.08588\frac{L}{D}$

TABLE 2.3: Soil reaction curve parameters for sand (Burd et al., 2020)

Soil reaction component	**Parameter**	**Depth variation functions**
Distributed lateral load, p	Ultimate displacement, $\bar{v}_{pu}$	$146.1 - 92.11D_r$
	Initial stiffness, k_p	$(8.731 - 0.6982D_r) - 0.9178\frac{z}{D}$
	Curvature, n_p	$0.917 + 0.06193D_r$
	Ultimate reaction, $\bar{p}_u$	$(0.3667 + 25.89D_r) + (0.3375 - 8.900D_r)\frac{z}{L}$
Distributed moment, m	Ultimate rotation, $\bar{\psi}_{mu}$	Given by $\bar{m}_u/k_m$
	Initial stiffness, k_m	17.00
	Curvature, n_m	0.0
	Ultimate moment, $\bar{m}_u$	$0.2605 - (0.1989 - 0.2019D_r)\frac{z}{L}$
Base horizontal force, H_B	Ultimate displacement, $\bar{v}_{Hu}$	$(0.5150 + 2.883D_r) + (0.1695 - 0.7018D_r)\frac{L}{D}$
	Initial stiffness, k_H	$(6.505 - 2.985D_r) - (0.007969 + 0.4299D_r)\frac{L}{D}$
	Curvature, n_H	$(0.09978 + 0.7974D_r) + (0.004994 - 0.07005D_r)\frac{L}{D}$
	Ultimate reaction, $\bar{H}_{Bu}$	$(0.09952 + 0.7796D_r) + (0.03988 - 0.1606D_r)\frac{L}{D}$
Base moment, M_B	Ultimate rotation, $\bar{\psi}_{Mu}$	44.89
	Initial stiffness, k_M	0.3515
	Curvature, n_M	$0.300 + 0.4986D_r$
	Ultimate reaction, $\bar{M}_{Bu}$	$(0.09981 + 0.3710D_r) + (0.01998 - 0.09041D_r)\frac{L}{D}$

2.6 Complexity assessment

To assess whether a synthetic CPT has a suitable level of resolution to be used in the design of offshore wind turbine foundations, there needs to be some sort of comparable measure that takes into consideration the variability in soil properties with depth and across a site. This is because sites with greater soil variability are more prone to the omission of peaks and troughs under lower resolutions, and therefore are anticipated to require a higher resolution in order to not significantly alter the pile design from an actual CPT profile. Soil variability can be identified through the shape of a CPT profile, where a more 'complex' profile indicates changes in soil properties with depth. As such, a 'complex' CPT profile will be sensitive to reductions in resolution. Therefore, it must be ascertained whether a CPT profile is 'complex' or not and to what extent it is. The fact that CPTs collect data at approximately constant intervals in depth, means that time series measures of complexity can be applied to CPT profiles, unlocking an existing body of research in application to this problem. The following sections look into the characteristics of a time series (Section 2.6.1), how the complexity of time series can be defined (Section 2.6.2), and the ways in which complexity are measured (Section 2.6.3).

2.6.1 Characteristics of a time series

To model the depth series of a CPT profile as a time series, it is first important to establish the characteristics of a time series. A time series is a set of observations made sequentially in time (Chatfield, 2003; Box et al., 2015; Brockwell and Davis, 2016). This can be either continuous, if a data point exists for any moment in time, or discrete, if data points only exist at certain time intervals (Chatfield, 2003). Although a CPT profile has been described previously as continuous with depth, in the context of time series analysis, it is a discrete time series formed by sampling a continuous time series. This is because it is possible to measure the soil properties at any depth, however the CPT only takes readings at approximately equal intervals in depth.

If future values in a time series can be determined exactly through a mathematical function, the time series is defined as deterministic (Box et al., 2015). In practice, most time series are stochastic, meaning future values can only be partly determined using past values and are based on probability distributions (Chatfield, 2003). Another key characteristic of a time series is whether it is stationary or nonstationary. A stationary time series is a process that remains in statistical equilibrium with probabilistic properties that remain constant over time (Box et al., 2015). This can be split into strictly stationary and weakly stationary. Strictly stationary is when the joint distribution of a set of observations is not affected by a shift in time (Chatfield, 2003), whereas weakly stationary is when the mean and variance do not change in time but the autocovariance, i.e.

the relationship between an observation and its past values, depends only on the time difference between observations (Box et al., 2015). If a time series is nonstationary, then its properties do not remain constant in time.

A summarised list of key characteristics are detailed below:

- Stochasticity: unpredictability
- Stationarity: statistical properties remain constant over time
- Linearity: future values can be expressed as a linear function of past values
- Chaoticity: sensitivity to initial conditions
- Fractality: self-similarity of a structure
- Memorability: influence of past states on future states in the short and long-term
- Regularity: consistent pattern
- Cyclicity: fluctuations that occur over long, non-fixed periods
- Seasonality: regular and predictable patterns that repeat over fixed intervals

Complexity is an important measure of time series data as it is interlinked with several of the other features. The measure of complexity can also determine the behaviour of internal factors and how they interact with each other within a system. Lower complexity indicates regular factors have a greater influence in shaping the overall data dynamics.

2.6.2 Complexity definition

Complexity has a multitude of different definitions depending on the type of measure it is describing and the context to which it applies. In this work, a mathematical concept of complexity of a time series is used to ascertain whether these measures can be used for CPT profiles. In turn, more complex profiles would require a higher resolution of synthetic CPTs. In this way, the minimum resolution of synthetic CPTs for their use in design can be quantified according to the complexity of a CPT profile performed at the site. To understand how a CPT profile can be measured in terms of complexity, a review of existing complexity measures was carried out. First an understanding of what defines complexity is needed, before attributing it to features of a time series. Measuring the complexity of a time series forms a large field in information theory and has applications across vast disciplines, from brain signals and ECGs in medicine, to stock markets in finance. Meaning it could be applied to CPT profiles with depth in the same way as with time.

2.6.3 Measures of complexity

Several methods of measuring complexity of time series data exist, which can be grouped into three categories: fractality, methods derived from nonlinear dynamics, and entropy (Tang et al., 2015). These three domains have been defined by the different approaches they take at measuring complexity, with each explained in the following sections. Fractality through self-similarity (2.6.3.1), methods derived from nonlinear dynamics through the attractor in phase space (2.6.3.2), and entropy through disorder state (2.6.3.3). Further classifications can be made within each category, in which a range of techniques of measuring the complexity exist through the associated features. This structure, connecting the types of complexity measures to the specific methods of measuring the complexity, is portrayed in Figure 2.23. A selection of the methods used in this work are detailed in Chapter 5, Section 5.2.

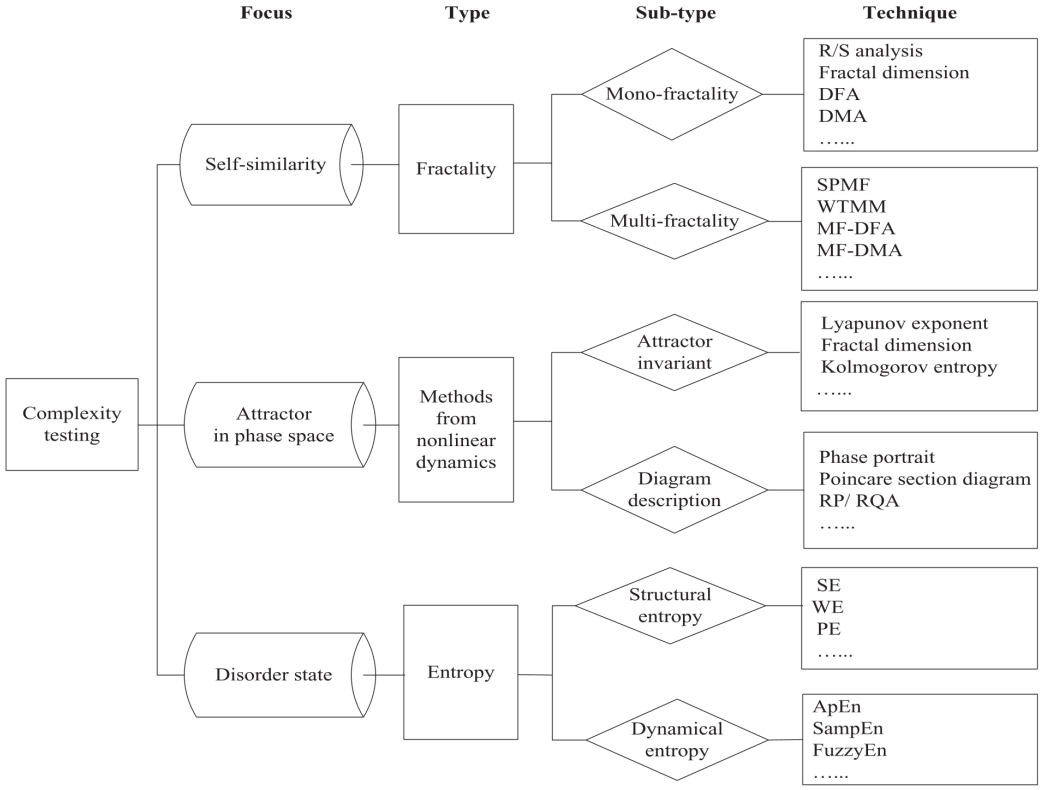

FIGURE 2.23: Complexity measures (reproduced from Tang et al. (2015))

2.6.3.1 Fractality

Fractality, as defined in Section 2.6.1, refers to how much the structure exhibits similar patterns at different scales of magnitude. This idea is based on fractal geometry, in which the Hausdorff dimension strictly exceeds the topological dimension (Mandelbrot, 1977). The Hausdorff dimension is a term for the fractal dimension and measures

the roughness of a surface (Gneiting et al., 2012). When a surface is smooth, the fractal dimension is equal to the topological dimension, giving a line, square and cube its dimensions of one, two, and three, respectively. For fractals, the fractal dimension becomes non-integer to allow for the fine details in the structure that make it fill more space, giving it a greater complexity than what the topological dimension would suggest (Gneiting et al., 2012; Mandelbrot, 1977).

In terms of complexity, fractality can examine the metric scaling behaviour of a data system (Sun et al., 2006). This is how measurements vary with scale. For example, the length of a coastline increases with increasing scale as the more detailed the length measurements become (Lopes and Betrouni, 2009). Fractality can also describe the relationship between the partial components and the whole system by revealing how structures or patterns repeat across different scales (Song et al., 2005). In time series analysis, the fact that fractal behaviour means patterns at small time scales resemble those at larger time scales enables the memorability of a system to be evaluated through its scaling behaviour, in particular long-term persistence (Tang et al., 2015).

Fractality can be analysed through both mono-fractality and multi-fractality approaches. Mono-fractality analysis explores the global structure of time series data by investigating its scaling behaviour using a single statistic to measure long-term dependencies (Tang et al., 2015). This is often quantified by the Hurst exponent, which can be estimated through the rescaled range analysis and is implemented in Section 5.2.2.1. Another method is detrended fluctuation analysis (Section 5.2.2.2). These measures are appropriate when the entire system can be described using one scaling exponent. On the other hand, multi-fractality analysis involves introducing an order parameter into the fluctuation function to discover local scaling behaviours using multiple exponents. This is because different segments of the structure follow different scaling behaviour (Tang et al., 2015). Building upon the mono-fractality measure of the detrended fluctuation analysis is the multifractal detrended fluctuation analysis and applies to multi-fractality analysis, as detailed in Section 5.2.2.3.

Fractality analysis considers two key factors: the detrending approach and the scaling exponent. The detrending approach removes the non-fractal long-term trends from a time series so that the fractal behaviour with regards to self-similarity can be quantified through the scaling exponent. Trends from external influences would otherwise hide the scaling properties of intrinsic fluctuations. By employing different detrending approaches, various fractality testing methods can be formulated (Tang et al., 2015).

2.6.3.2 Methods derived from nonlinear dynamics

Nonlinear dynamics involves the study of systems in which the output is not proportional to the input (Lipsitz and Goldberger, 1992). Methods derived from nonlinear

dynamics analyse time series data through chaos theory (Tang et al., 2015). Chaos is defined as seemingly unpredictable behaviour, as a result of the interactions between internal factors (Lipsitz and Goldberger, 1992). These factors follow some level of order by adhering to internal rules (Raubitzek and Neubauer, 2021) but are sensitive to initial conditions (Tang et al., 2015). This means chaotic behaviour can be predictable in the short term but unpredictable in the long term (Li and Yorke, 1975).

Testing for chaoticity in time series data investigates the attractor in phase space through phase-space reconstruction (Tang et al., 2015). Phase space is a mathematical space where each possible state of a system is represented by a point. From a single point in phase space, the underlying dynamics of a system can be reconstructed using phase-space reconstruction. This enables analysis of the attractor: a specific set of points that the states of a system will converge to over time. It can be considered as the system's final destination, attracting trajectories from all possible initial conditions (Tang et al., 2015). The structure of the attractor provides information on the chaoticity of a system. A fixed point indicates a deterministic non-chaotic system whilst a periodic system and quasi-periodic system are represented by a limit cycle and a limit torus, respectively. If no attractor can be found, the system is random (Sharma, 2009). These shapes are diagram descriptions which utilise graphical measures to represent the complexity of a system. For a measure of complexity as a numerical output, there are attractor invariants. Attractor invariants can investigate attractor properties through the exponential divergence of nearby trajectories or the loss of information (Tang et al., 2015). An example is Kolmogorov entropy (Section 5.2.3.1).

2.6.3.3 Entropy

Entropy is a statistical measure in thermodynamics that characterises the disorder of a system. Several entropies have been developed within complexity testing to assess the disorder state of data dynamics. A higher value of entropy indicates a more complex system in a greater state of disorder. There are two main categories of entropies: structural and dynamical. Structural entropies measure the complexity of a system's structure in terms of power concentration, through conversion of data from the time domain into the frequency or time-frequency domain. The method of transformation between domains governs the type of structural entropy obtained. Dynamical entropies investigate the complexity of a system by examining how the similarity between inner patterns in data dynamics changes. This analysis is based on the conditional probability that two sequences in the phase space remain similar to each other as the embedding dimension increases (Tang et al., 2015).

2.7 Research gap and alignment with research objectives

In summary, engineering parameters with depth, achieved through CPTs, are essential for the design of offshore wind turbine foundations. Monopile foundations, in particular, require soil properties at frequent intervals at significant depths below the seafloor. Currently, site investigations for offshore wind farms involve performing a number of CPTs across a proposed wind farm. These provide soil properties with depth at high resolution but only at discrete locations. On the other hand, geophysical data is continuous laterally and therefore can be used to generate synthetic CPTs at any desired location within a site. This is a significant advantage, as turbine location is not fixed prior to site investigation, reducing the need to interpolate between CPT locations. The aim of this research is to:

> Advance the implementation of synthetic CPTs in the design of offshore wind turbine monopile foundations.

Synthetic CPTs have a lower vertical resolution than actual CPTs, which could affect the design of offshore monopile foundations. No significant studies into the effect of this reduced resolution have been found. Therefore, the first research objective of this thesis is to:

RO1 Evaluate the impact of using reduced resolution CPT data on the design of monopile foundations for offshore wind turbines.

This will be achieved through artificial and systematic resolution reduction of real geotechnical CPT profiles from the Burbo Bank Extension offshore wind farm site at Liverpool Bay, UK, enabling a comparison of design outcomes between the reduced resolution profiles and the actual full resolution soil data. Three different methods of resolution reduction will be tested with a sample of the data before implementing the one most suitable and representative of synthetic CPTs on a selection of CPTs. The effect of using reduced resolution profiles to inform on ultimate limit state (ULS) pile design under lateral loading will be assessed through minimising pile volume. The real full resolution CPT profile will enable a benchmark pile design to be determined and then compared to those predicted under the reduced resolution profiles. By evaluating the change in output minimum pile volume with reducing CPT profile resolution, the minimum resolution can be found. This is the point at which the resolution begins to have significant effects on pile design. However, the minimum required resolution is likely to be site specific, depending on the soil conditions and the variability across a site.

A second case study site of Ten Noorden de Waddeneilanden wind farm zone in the Dutch Sector of the North Sea, will be introduced, providing synthetic CPTs alongside co-located standard geotechnical ones. Therefore, the second objective of this research is to:

RO2 Evaluate the impact of using synthetic CPT data on the design of monopile foundations for offshore wind turbines.

The same analysis as that carried out for **RO1** will be implemented, as well as a direct comparison between pile outcomes from the synthetic and in situ CPT profiles. An assessment into the effect of the resultant ULS optimal pile dimensions under serviceability limit state will also be performed, from which lateral deformations can be compared.

Finally, this research will look into ways in which the complexity of a site can be quantified by applying time series complexity measures to the depth series of CPT profiles. Therefore, the third objective of this research is to:

RO3 Evaluate the application of time series complexity measures on CPT profiles and determine their relationships with pile design outcomes.

The concept of complexity in terms of CPT profiles will need to be explored in order to identify appropriate complexity measures, before applying these on CPT profiles at the Burbo Bank Extension wind farm site. This will be carried out for both the full and reduced resolution profiles from **RO1**. Whether the complexity of a CPT profile is able to capture minimum allowable resolution and inform on overall design guidance will be investigated.

Chapter 3

Effect of CPT resolution on design outcome

3.1 Introduction

The effect of cone penetrometer test (CPT) resolution is considered by systematically reducing the resolution of geotechnical CPT profiles from an offshore wind farm site and, for each reduced resolution, predicting the resulting minimum required monopile diameter, length, and thickness for a given offshore wind farm design scenario for ultimate limit state (ULS) under lateral load. The effect on capacity of the predicted required pile size when installed in the real, full resolution, soil profile is also assessed. The reduced resolution CPT profiles are intended to represent synthetic CPT profiles with the variation in resolution representing what might be derived with a range of geophysical survey methods in a range of sediment types. The process allows for a systematic quantitative analysis to be made across different CPT resolutions and provide insight on minimum synthetic CPT resolution to use in geotechnical design.

3.2 Case study: Burbo Bank Extension offshore wind farm site

Open access geotechnical CPT data from the Burbo Bank Extension offshore wind farm, situated in a shallow water site off the coast of Liverpool, UK (Ørsted, 2020), was used as a case study site for this work, accessed via the Marine Data Exchange (Marine Data Exchange, 2014). The site consists of interbedded sands and lightly overconsolidated, low plasticity clay (DONG Energy, 2013). The site investigation included 41 CPTs within an area of 40 km^2 and distributed over the site as shown in Figure 3.1 (DONG Energy, 2014). A subset of nine CPTs were selected for use in this work, chosen to ensure a range of different CPT profile shapes. The selection was made by visual

inspection of the CPT profiles supported by time series analysis demonstrating quantitative assessment of ground variability across the Burbo Bank Extension (Charles et al., 2023). As such, the selected CPTs are representative of the range of soil types observed within the site. The CPTs used in this study are highlighted with solid markers in Figure 3.1, annotated with their identification number in the original site investigation report (DONG Energy, 2014), which are used throughout this thesis as reference. Figure 3.2 shows the cone penetration resistance and sleeve friction profiles with depth for the nine selected CPTs.

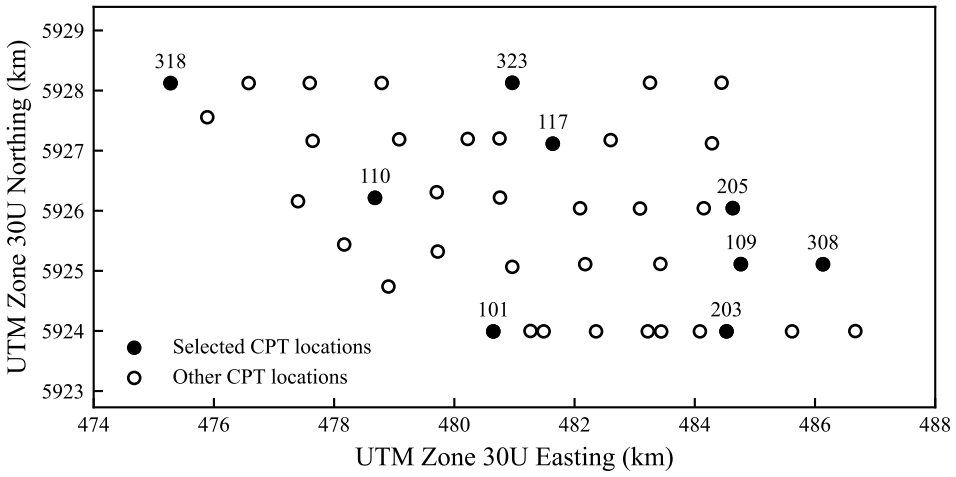

FIGURE 3.1: Locations of geotechnical CPTs within the Burbo Bank Extension offshore wind farm site (DONG Energy (2014) via the Crown Estate Marine Data Exchange)

3.3 Loading scenario

A single horizontal load of 16 MN acting at a height of 35 m above the seafloor, indicative of the loading on a 5 MW wind turbine, with hub-height of 95 m and rotor diameter of 125 m, in the North Sea (Lesny and Wiemann, 2005) was adopted. A global factor of safety of three was applied to the horizontal load, giving a design load of 48 MN. The global factor of safety working stress design (WSD) approach was selected as opposed to a partial factor approach with separate load and resistance factors design (LRFD) for simplicity so as not to adjust the CPT profiles from the publicly available data. An LRFD approach would be equally applicable. Application of a factor of safety (either WSD or LRFD) is industry standard for ULS design and as such was applied in this analysis in order to achieve pile dimensions comparable with those that would be achieved in an industry standard design. The exact selection of loading magnitude is not relevant, since the focus of this study is on the trends between the different pile designs as a function of the CPT resolution, which would be expected to scale with applied load. ULS is considered for this proof-of-concept approach, although the general framework is equally applicable to serviceability limit state design.

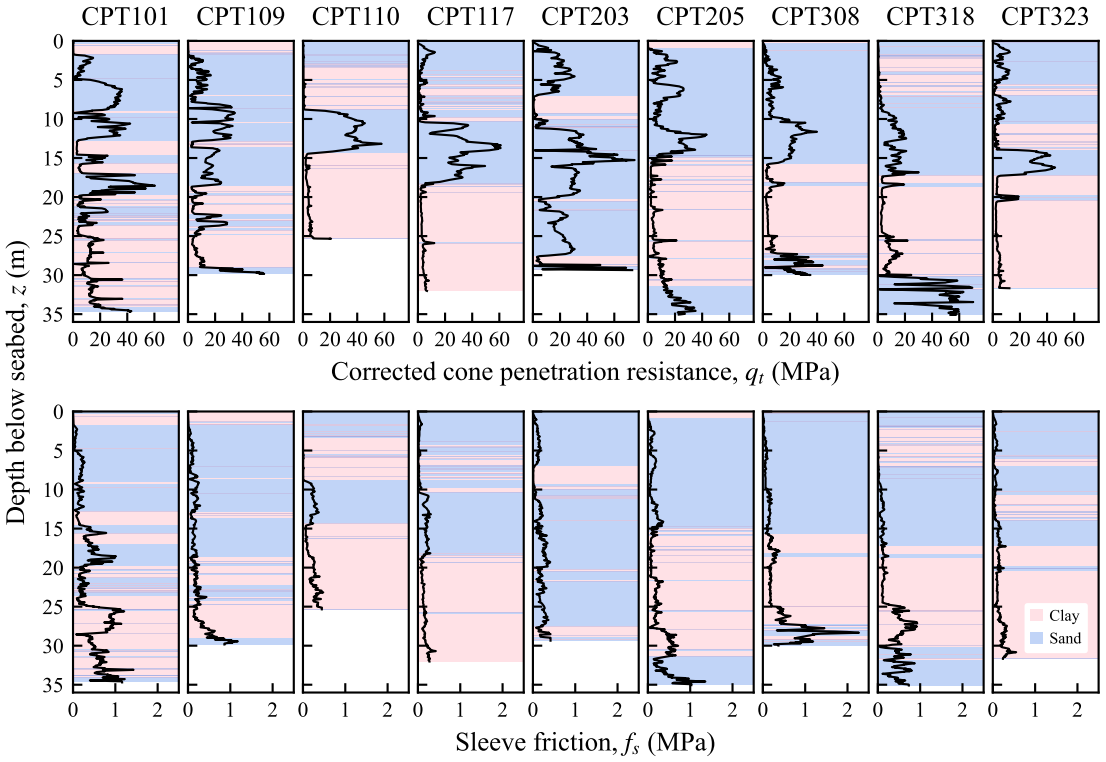

FIGURE 3.2: CPT profiles of corrected cone penetration resistance (q_t) and sleeve friction (f_s) with depth for the nine selected tests from Burbo Bank Extension offshore wind farm site

3.4 Methodology: Lateral pile design from a CPT

The workflow of the method developed for this study consists of six main steps. Once the CPT data has been acquired for a selected location (Section 3.4.1), the full resolution CPT data is processed in line with conventional geotechnical practice, i.e. adjusting for pore water pressure and overburden (Section 3.4.1.1). The resolution of the CPT profile is then systematically reduced by increasing the data interval between readings in increments of 0.1 m up to a maximum interval of 2.5 m (Section 3.4.1.2). Using the reduced resolution CPT profile, each depth corresponding to a data point is classified as either clay or sand (Section 3.4.2) in order to apply the appropriate equation to calculate the lateral resistance. An initial pile diameter is specified to apply the pile lateral resistance equations (Section 3.4.3) and to find the corresponding minimum length. The process is repeated for piles of reducing diameter, with a specified increment of 0.1 m in this case (Section 3.4.4). For each optimal diameter and length pair, the minimum thickness is calculated to ensure rigid body rotation (i.e. no formation of plastic hinge (Section 3.4.5)), from which the minimum pile volume is determined (Section 3.4.6). The process can then be repeated for any number of additional CPT locations. These steps are outlined in more detail below.

3.4.1 Step 1: Acquire full resolution CPT data

Acquire cone penetration resistance, sleeve friction and pore water pressure data, at near constant increments of depth, starting at the seafloor and terminating at some depth within the seabed. Seabed conditions can affect the drive rate, resulting in depth increments not necessarily being at exact regular intervals, in which case raw data should be interpolated to ensure that each data point corresponds to an exact interval. Soil unit weight to calculate the vertical stress profile, and the net cone area ratio must also be known for the corrections to the raw data applied in Section 3.4.1.1.

3.4.1.1 Step 1(a): Process full resolution CPT data

Adjust measured cone penetration resistance with pore water pressure and overburden corrections (Section 2.4.1). Calculate corrected cone penetration resistance (q_t) and correct for overburden through Equations 2.1 (reproduced as Equation 3.1) (Robertson, 1990) and 2.2 (reproduced as Equation 3.2) (Robertson, 1990; Randolph and Gourvenec, 2011), respectively:

$$q_t = q_c + u_2(1 - \alpha) \tag{3.1}$$

where q_c is measured cone penetration resistance (MPa), u_2 is pore water pressure acting on the shoulder of the cone (MPa) and α is the net area ratio. For the CPTs at the Burbo Bank Extension site, various cone sizes were used depending on the type of test, however, a review of the α values for the CPTs selected in Figure 3.1 gave either 0.59 or 0.6 (DONG Energy, 2014). As such, taking α as 0.6 to one decimal place was deemed sufficient for all CPTs.

$$q_{net} = q_t - \sigma_v \tag{3.2}$$

where q_t is corrected cone penetration resistance (MPa) as given by Equation 2.1 (reproduced as Equation 3.1), and σ_v is the in situ vertical total stress (MPa), given by Equation 2.3 (reproduced as Equation 3.3):

$$\sigma_v = \gamma z \tag{3.3}$$

where γ is soil unit weight (kN/m^3) and z is depth below seafloor (m).

Pore pressure correction is only necessary for clays, as opposed to sands, but for simplicity, the correction was applied to all readings regardless of soil classification. As expected, the correction was trivial for cone penetration resistance readings in sandy sediments. A pore pressure correction factor is sometimes also applied to the sleeve friction data through subtraction. As is the case for cone penetration resistance data, the value depends on the cone dimensions, but tends to be much smaller in magnitude.

Where the site investigation reports of the Burbo Bank Extension include a sleeve friction correction factor, the value was no greater than 0.02 (DONG Energy, 2014). Therefore, it was assumed to have a negligible effect and excluded from the pre-processing of the CPT data.

3.4.1.2 Step 1(b): Reduce resolution of CPT data

An idealised profile with a 10 mm data interval, the depth between consecutive readings, is defined as the 'full resolution' profile in this work. Resolution herein refers to the density of data points in the CPT profile.

Reduce resolution of CPT data by increasing the data interval between readings in increments of 0.1 m up to a maximum data interval of 2.5 m via three different approaches: reducing sampling rate, single averaging interval, and double averaging interval. These are detailed in Section 3.5.

3.4.2 Step 2: Classify soil type

Assign a soil type to each of the data points using the Soil Behaviour Type Index (Ic) through Equation 2.10 (reproduced as Equation 3.4) (Robertson and Wride, 1998) in order to apply the appropriate ultimate lateral resistance equation in Section 3.4.3. For this work, a simplistic approach was taken in which the soil classification was binary and defined as either clay or sand. Soils with an index of less than 2.6 were classified as sand, while higher values were classified as clay (Robertson and Cabal, 2015).

$$I_c = \left((3.47 - \log Q_t)^2 + (\log F_r + 1.22)^2 \right)^{0.5} \tag{3.4}$$

where Q_t is normalised cone resistance and F_r is normalised friction ratio, defined by normalising net cone resistance by vertical effective stress (Equation 2.5 (reproduced as Equation 3.5)), and friction ratio by net cone resistance (Equation 2.7 (reproduced as Equation 3.7)):

$$Q_t = \frac{q_{net}}{\sigma'_v} \tag{3.5}$$

where q_{net} is net cone penetration resistance (MPa), as given by Equation 2.2 (reproduced as Equation 3.2), and σ'_v is in situ vertical effective stress (MPa), found with Equation 2.6 (reproduced as Equation 3.6):

$$\sigma'_v = \sigma_v - u \tag{3.6}$$

where σ_v is in situ vertical total stress (MPa), as given by Equation 2.3 (reproduced as Equation 3.3), and u is the in situ pore water pressure at depth z below seafloor (m).

Normalised friction ratio (expressed as a percentage):

$$F_r = \frac{f_s}{q_{net}} \tag{3.7}$$

where f_s is sleeve friction (MPa) and q_{net} is net cone penetration resistance (MPa).

3.4.3 Step 3: Apply pile design equation for an initial set of pile diameter and length

Calculate lateral resistance at each data point for a pair of pile diameter and length dimensions. Although an iterative process is used to consider many pairs of diameter and length (see Section 3.4.4), this section will describe the design methodology for an individual dimension set. The ultimate lateral resistance of the soil per unit depth (p_u), i.e. the maximum horizontal load that the soil can withstand before it fails, can be determined from well-established CPT based methods, available for both clay and sand. In this work, Equation 2.16 (reproduced as Equation 3.8) (Truong and Lehane, 2014) and Equation 2.21 (reproduced as Equation 3.9) (Suryasentana and Lehane, 2014) were applied to acquire the ultimate lateral resistance per unit depth for clay and sand, respectively.

For clay:

$$p_u = D q_{net} \left(\left(\frac{3}{4.7 + 1.6 \ln I_r} \right) + (1.5 - 0.14 \ln I_r) \tanh \left(\frac{0.65\, z}{D} \right) \right) \tag{3.8}$$

where D is diameter (m), q_{net} is net cone penetration resistance (MPa), I_r is rigidity index, which is the ratio between shear modulus and undrained shear strength of a soil (Randolph and Gourvenec, 2011) and z is depth below seafloor (m). A value of rigidity index of 125 was selected in accordance with a lightly overconsolidated, low plasticity clay (Keaveny, 1985; Mayne, 2007) at the case study site.

For sand:

$$p_u = 2.4\, \sigma'_v\, D \left(\frac{q_c}{\sigma'_v} \right)^{0.67} \left(\frac{z}{D} \right)^{0.75} \left\{ 1 - \exp \left[-6.2 \left(\frac{z}{D} \right)^{-1.2} (0.1)^{0.89} \right] \right\} \tag{3.9}$$

where σ'_v is vertical effective stress (kPa), D is diameter (m), q_c is cone penetration resistance (MPa), and z is depth below seafloor (m). The lateral displacement of the pile at seafloor has been limited to 10 % of the pile diameter to ensure that the predicted pile capacity does not require unrealistic displacements to mobilise.

The point about which the pile pivots is identified by iterating the moment contribution of each increment along the length of the pile, (i.e. lateral resistance per unit length, multiplied by the length over which it applies, multiplied by the lever arm), to find

the location where the sum of the resisting moment is in equilibrium with the moment caused by the applied load. It is possible that no pivot point can be found, in which the pile is unstable for the selected pile diameter and length pair. Horizontal equilibrium was also checked, meaning that the soil pressure acting in front of the pile is equal to the combined force of the soil pressure acting behind the pile and the applied lateral load.

Note that more rigorous PISA-type methods (e.g., Burd et al., 2020) include additional soil reactions (e.g. a base shear term) which are particularly relevant for the low length to diameter ratios obtained in this analysis. If added, these terms would reduce the required pile volume. However, for the purposes of this work, a simple shaft lateral resistance solution is suitable to capture the impact of changes to a CPT profile on the design pile dimensions.

3.4.4 Step 4: Optimise pile diameter and length by iteration

Iterate through pairs of pile diameter and length in Equations 2.16 and 2.19 to identify minimum pairs to satisfy the ULS under lateral load. As diameter is used as an input in the lateral resistance equations, it is most efficient to initially define diameter and iterate through reducing pile lengths until ultimate lateral resistance is less than the applied load, i.e. failure is reached, or a minimum specified length is reached. The process is repeated for decrements of diameter until failure of the pile is calculated or a limiting minimum diameter is reached.

In this work, an initial upper limit of pile diameter of 15 m (Byrne et al., 2015) and a length of 40 m below the seafloor (DONG Energy, 2014) were specified. For those CPT profiles that did not extend to such a depth, the initial pile length was set equal to the maximum depth of the selected CPT. To enable small changes in pile size to be distinguished, both the diameter and length were reduced in intervals of 0.1 m. Limiting minimum pile length of 1.0 m and diameter of 0.5 m were specified.

3.4.5 Step 5: Minimise thickness

Determine minimum thickness for each optimised diameter and length pair to prevent formation of a plastic hinge under the maximum applied moment. In this work, this is represented by the following equation to approximate the thickness (t) required (Randolph and Gourvenec, 2011):

$$t = \frac{M_p}{D^2 \sigma_y} \tag{3.10}$$

where M_p is moment capacity of the pile (MNm), D is diameter (m) and σ_y is yield stress (MPa) of steel. Yield stress depends on the type of steel used in the pile, which

was assumed to be 250 MPa in this work (American Institute of Steel Construction, 2017). In the case that no possible thickness passed the criterion, i.e. a physically impossible value greater than $D/2$ was calculated, the length and diameter combination were considered impermissible. A minimum thickness threshold was also enforced, defined by diameter to thickness ratio of at least 110, a value taken from design guidelines (Burd et al., 2020).

3.4.6 Step 6: Output minimum pile volume

Calculate pile volume for each set of optimal pile diameter, length, and thickness (from steps in Sections 3.4.4 and 3.4.5) to identify the minimum volume of steel in the pile. The minimum pile volume predicted with the reduced resolution CPT profile can then be compared to the pile design from the full resolution CPT profile, enabling the effect of reduced CPT resolution on pile volume to be assessed.

3.5 Methods of reducing CPT profile resolution

CPT profile resolution, in this work, refers to the density of data points in the profile and can be defined through the data interval between CPT readings. As mentioned in Section 2.3.2, CPTs are pushed into the ground at a constant rate, meaning data should theoretically be collected at small, regular intervals. However, seabed conditions can affect the drive rate so that the depth increments of actual CPT data are not always consistent. To avoid any discrepancies in this work, an idealised profile with a 10 mm data interval, the depth between consecutive readings, was defined as the 'full resolution' profile. Therefore, interpolation was carried out between CPT readings to ensure that each data point corresponded to an exact interval of 10 mm.

The resolution of a CPT profile was systematically reduced by increasing the data interval between readings in increments of 0.1 m, from 0.1 m (maximum reduced resolution) to 2.5 m (minimum resolution) (Section 3.4.1.2). Various methods were considered for resolution reduction, three of which were implemented in this work: reducing sampling rate, single averaging interval, and double averaging interval. All three methods intend to represent synthetic CPT profiles, which likely lay somewhere between the reducing sampling rate and averaging methods, to assess the effect of using reduced resolution profiles in pile design. Example results using CPT203: the CPT profile that reaches the greatest value of corrected cone penetration resistance out of all the selected CPTs, showing large variation in its profile, are presented for each method before refining and selecting the best method of resolution reduction for which the full results are analysed in Section 3.6.

3.5.1 Reducing sampling rate

The first method of reducing the CPT profile resolution was through simply reducing the sampling rate. This involved selecting the corrected cone penetration resistance data point from the full resolution profile at intervals relevant to the desired reduced resolution (Figure 3.3). Linear interpolation was used when the required depth did not match exactly with a full resolution depth increment. However, the final data point of the full resolution CPT profile was always carried over to the reduced resolution profiles to consistently mark the bottom of the CPT profiles. From the reduced resolution profiles for corrected cone penetration resistance and sleeve friction in Figures 3.4(a) and (b), respectively, it can be seen that each data point in the reduced resolution profiles lies on the full resolution profile. However, as the sampling rate is reduced, the data interval between data points increases, increasing the tendency for omission of peaks and troughs within the full resolution profile. This is evident at a data interval of 2.5 m, where the lack of peaks and troughs in the reduced resolution profile makes it difficult to establish a connection to the full resolution profile, i.e. the reduced resolution CPT profile could represent many different profiles.

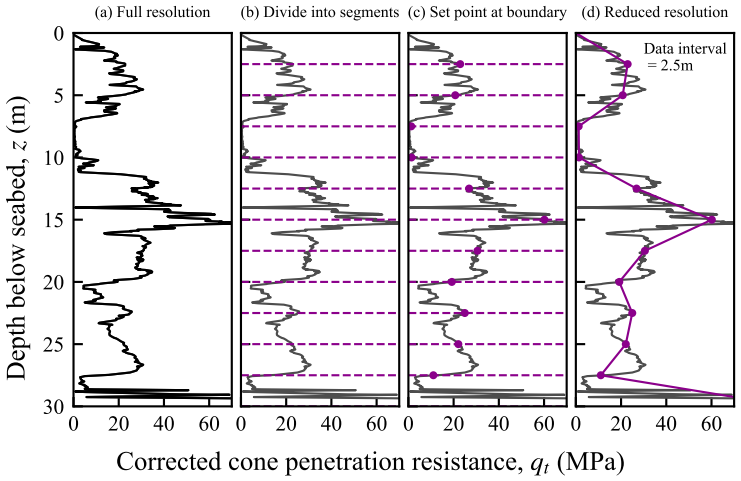

FIGURE 3.3: Process of reducing the CPT profile resolution by reducing the sampling rate for a specified data interval of 2.5 m

3.5.1.1 Minimum pile volume

Minimum monopile dimensions for ULS design were calculated as per the methodology set out in Section 3.4 for CPT203. Results for the subset of data intervals portrayed in Figure 3.4 are presented in Table 3.1. A pile of the same dimensions as the full resolution pile is predicted for an increased data interval of 0.1 m, suggesting the CPT resolution has not affected the pile design. At a data interval of 0.5 m, pile length has decreased, causing a small decrease in pile volume to the smallest value observed out of this set of data intervals. Pile diameter then decreases by 0.1 m for the largest data

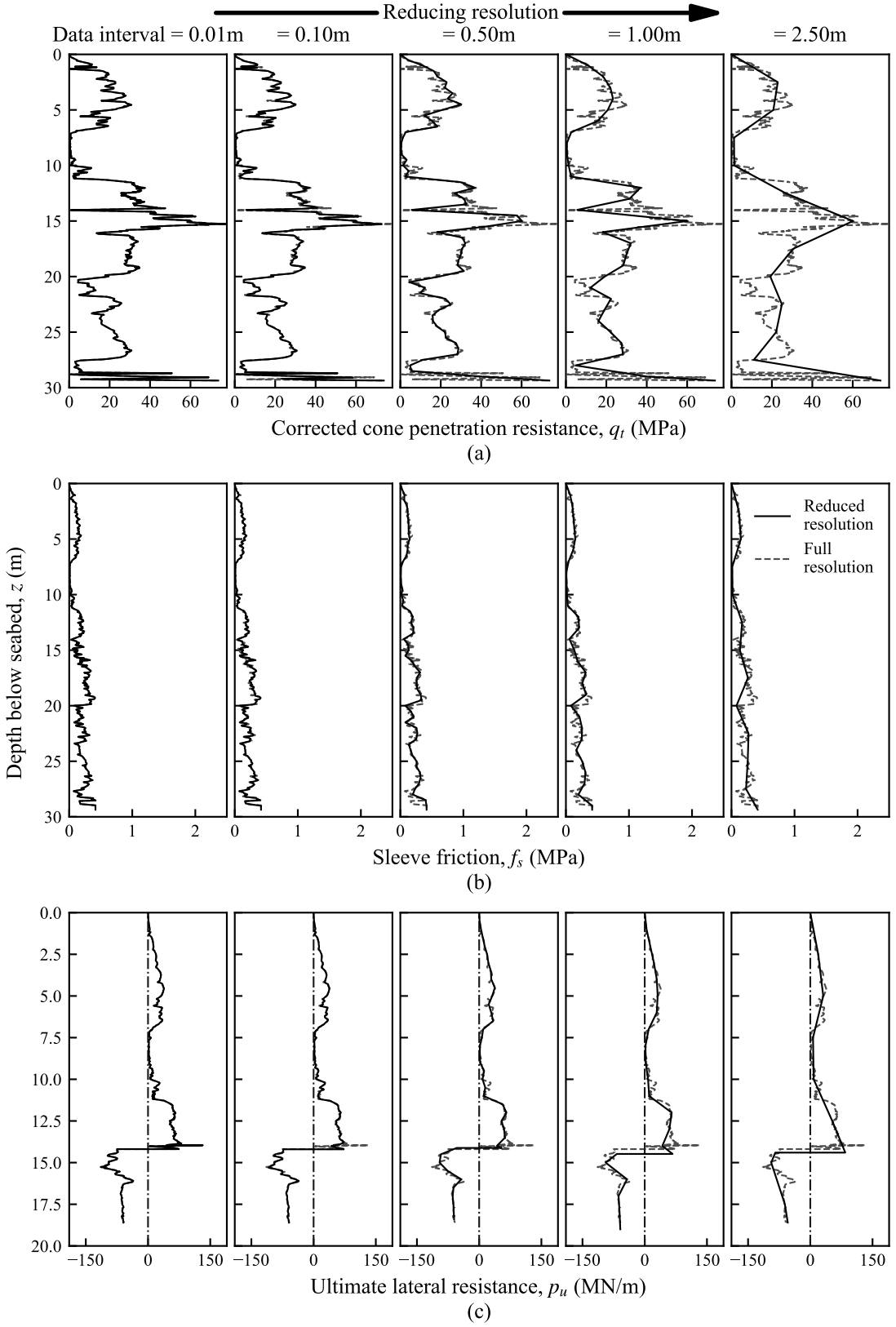

FIGURE 3.4: Effect of reducing resolution on profiles of (a) corrected cone penetration resistance, (b) sleeve friction, and (c) ultimate lateral resistance under optimal pile dimensions for example CPT (CPT203)

intervals of 1.0 and 2.5 m, however, pile volume has still increased compared to that of the 0.5 m data interval through increasing length. The greatest pile volume is that at a data interval of 1.0 m, with the volume at a data interval of 2.5 m actually being less than the full resolution pile. This can be explained through a comparison of the corrected cone penetration resistance plots in Figure 3.4(a) over the optimal pile depth (i.e. approximately 18-19 m). For a data interval of 0.5 m, soil resistance is overpredicted in the first 5 m, enabling sufficient resistance to be reached at a shorter depth. Meanwhile, at a data interval of 1.0 m, soil resistance is generally under predicted so the pile has to extend deeper to obtain the necessary resistance. Overall, the variation in pile volume across these data intervals demonstrates that it is simply an artefact of the interval selected, and the depth and cone penetration resistance of the first point considered for presentation in the table.

TABLE 3.1: Dimensions of the minimum volume pile for CPT203 at data intervals of 0.01, 0.1, 0.5, 1.0 and 2.5 m under reducing sampling rate method

Data interval (m)	Diameter (m)	Length (m)	Thickness (mm)	Volume (m^3)
0.01	9.3	18.6	84.7	45.60
0.1	9.3	18.6	84.5	45.53
0.5	9.3	18.4	84.5	45.04
1.0	9.2	19.0	85.3	46.43
2.5	9.2	18.6	84.8	45.15

The variation in minimum pile volume for CPT203, normalised by that of the full resolution, was plotted in Figure 3.5 for the whole range of data intervals tested. As the data interval is increased, Figure 3.5 shows increased variation in pile volume from the full resolution case, either under or overpredicting the pile design. Since lateral soil resistance is entirely dependent on the cone penetration resistance reading at a specified depth, the omission or inclusion of peaks and troughs will be amplified at lower resolutions. The pseudorandom nature of reducing the resolution of cone penetration resistance through changing the sampling rate means it is not possible to predict whether the reduced resolution pile will be either over or underdesigned. If, by chance, the sample point happens to be on a peak, then significantly higher soil strength will be recorded than if the peak is missed, with the opposite true in the case of troughs.

The reduced resolution corrected cone penetration resistance profiles corresponding to the extreme high (data interval of 1.4 m) and extreme low (data interval of 1.9 m) pile volumes found in Figure 3.5 are presented in Figure 3.6, with the optimal pile length for the specific data interval plotted as a horizontal line. At a data interval of 1.4 m, the reduced resolution profile tends to underpredict the soil resistance for the majority of the profile, up to 16 m. A significant underprediction occurs at a depth of 14 m, where the data point lies on a large trough in the profile, lowering the predicted values of soil resistance either side. Although there is an overprediction at 17 m which allows the

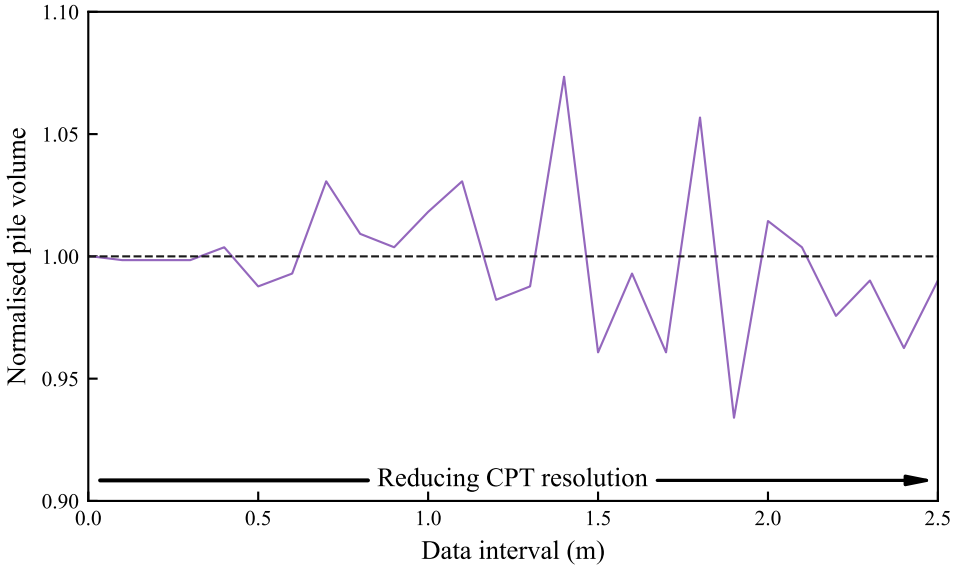

FIGURE 3.5: Effect of CPT resolution under reducing sampling rate method on minimum required pile volume for CPT203 within the Burbo Bank Extension offshore wind farm

required soil resistance to be reached by 20 m, this is 1.4 m longer than that designed under the full resolution profile. In contrast, at a data interval of 1.9 m, the reduced resolution profile generally overpredicts the soil resistance up to its optimal length of 17.4 m by capturing most of the peaks in the full resolution profile and none of the troughs.

The greatest continuous decrease in pile volume occurs between data intervals of 1.8 and 1.9 m. The reduced resolution corrected cone penetration resistance profile for the 1.8 m data interval is also included in Figure 3.6. The reduction in CPT profile resolution, which causes differences in the corrected cone penetration resistance readings that form the reduced profiles, results in the predicted minimum pile volume decreasing from 48.19 to 42.59 m^3.

3.5.1.2 Area under CPT profile up to optimal pile length

Section 3.5.1.1 has revealed that the minimum pile volume depends on the amount of smoothening of the peaks and troughs in the reduced resolution corrected cone penetration resistance profile. Therefore, this effect can be measured quantitatively by integrating the CPT curve of the reduced resolution corrected cone penetration resistance up to the optimal pile length for that resolution. The area measurements for every data interval were normalised by dividing by the area under the full resolution profile up to the optimal pile length of the full resolution design. Plotting this with data interval in Figure 3.7, alongside the minimum normalised pile volume from Figure 3.5, reveals that the integral of the CPT curve up to the optimal pile length for a given resolution

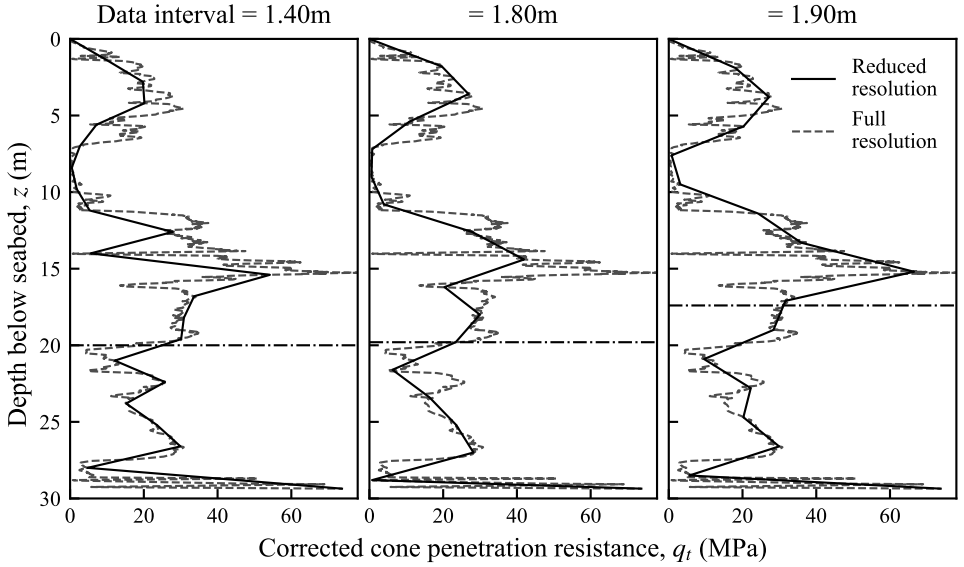

FIGURE 3.6: CPT203 reduced resolution corrected cone penetration resistance profiles for data intervals of 1.4, 1.8 and 1.9 *m*; horizontal dashed line indicates optimal pile length

appears to be inversely proportional to minimum pile volume. Peaks in the normalised pile volume line correspond almost exactly to inverse peaks in the normalised area under the CPT curve line. A larger normalised area means greater soil lateral resistance, which in turn, enables the pile to be designed with smaller dimensions.

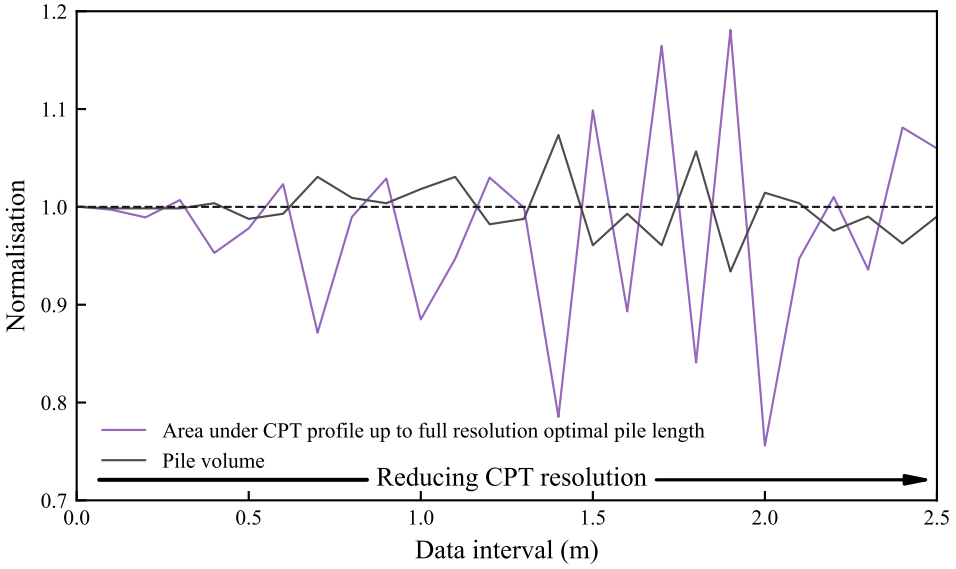

FIGURE 3.7: Effect of CPT resolution under reducing sampling rate method on area under CPT curve up to optimal pile length and minimum required pile volume for CPT203 within the Burbo Bank Extension offshore wind farm

3.5.1.3 Offsetting

This method exhibits a degree of pseudorandomness, in that significant changes in pile volume are possible by adjusting the sampled depth by a single increment. Therefore, the effect of the initial data point on the resulting reduced resolution profiles, and in turn minimum pile volume, was assessed through offsetting. Offsetting involved starting the analysis at a depth below the seafloor, equal to a percentage of the specified data interval (0, 10, 20 and 30 % was used in this work), and then adding on the depth of that data interval.

Figure 3.8(a) plots the corrected cone penetration resistance for CPT203 at a data interval of 2.0 m for 0, 10, 20 and 30 % offsets, against the original full resolution profile. This corresponds to first data points at depths of 0, 0.2, 0.4 and 0.6 m below the seafloor, respectively. Data points are then plotted at every 2.0 m data interval, i.e. the second data points are at depths of 2.0, 2.2, 2.4 and 2.6 m below the seafloor, respectively. It should be noted that for simplicity, in this work, all offset curves still originate from seafloor level, therefore assuming the same corrected cone penetration resistance as the 0 % offset curve at the seafloor, before connecting up with the first data points in their corresponding offsets. The different offset curves demonstrate large variations in corrected cone penetration resistance, with the greatest disparity observed between 14 and 16 m. This is due to the random way in which the reducing sampling method selects the corrected cone penetration resistances for the reduced resolution profiles.

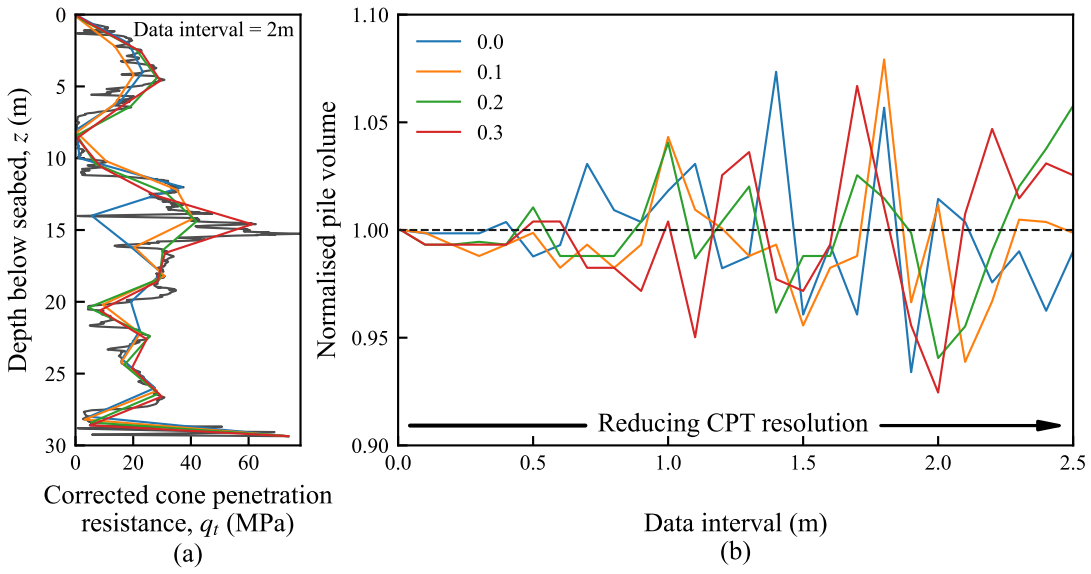

FIGURE 3.8: Effect of offsetting under reduced sampling rate method on q_t profile and minimum pile volume for CPT203 within the Burbo Bank Extension offshore wind farm

The effect of using the offset curves in pile design, such as those portrayed for CPT203 at a data interval of 2.0 m in Figure 3.8(a), can be evaluated through Figure 3.8(b). Each line plotted represents normalised optimal pile volume with increasing data interval

for a given offset (expressed as either 0, 10, 20 or 30 % of the data interval), all using CPT203 to enable comparison of the results. The overall trend is in accordance with that observed in Figure 3.5, showing increased variance in minimum pile volume as the data interval increases with reducing resolution. However, different minimum pile volumes are predicted depending on the amount of offset from the depth below the seafloor. At a data interval of 1.4 m, the influence of the offset profile from Figure 3.8(a) is evident, with the 0 % offset curve overpredicting the pile volume by 7.5 % whilst the other curves all underpredict pile volume, up to almost 4 % for the 20 % offset curve.

3.5.1.4 Summary

Overall, artificial resolution reduction through reducing the sampling rate has demonstrated dependency of minimum pile volume on the first data points below the seafloor. Furthermore, the randomness associated with the way in which corrected cone penetration resistance is selected means it cannot be known whether piles are under or overdesigned. Therefore, to overcome such limitations, reducing the CPT profile resolution through averaging was implemented.

3.5.2 Single averaging interval

In the single averaging interval method, the full resolution CPT profile (Figure 3.9(a)) was split into intervals of the desired data interval (Figure 3.9(b)), with a single average value calculated over the interval, plotted at the midpoint depths of each interval (Figure 3.9(c)). The average values were then connected together to form the reduced resolution profile (Figure 3.9(d)), at a data interval of 2.5 m for this example. Since the depth of the CPT profile was very unlikely to be equally divisible by the specified data interval, the remaining depths at the bottom of the profile were averaged over their own smaller interval and plotted at the corresponding midpoint. The final data point of the full resolution CPT profile was then carried over to the reduced resolution profiles in the same way as in the reducing sampling rate method. Under the single averaging interval method, the reduced resolution profiles for corrected cone penetration resistance, sleeve friction and ultimate lateral resistance of the soil in Figures 3.10(a), (b) and (c), respectively, were more representative of the full resolution profile than those generated from the reducing sampling rate for CPT203 (see Figure 3.4).

3.5.2.1 Minimum pile volume

Reducing the CPT profile resolution by averaging over the depth interval shows increased variation in normalised pile volume with increasing data interval. However, this variation is significantly less than that observed for the reduced sampling method

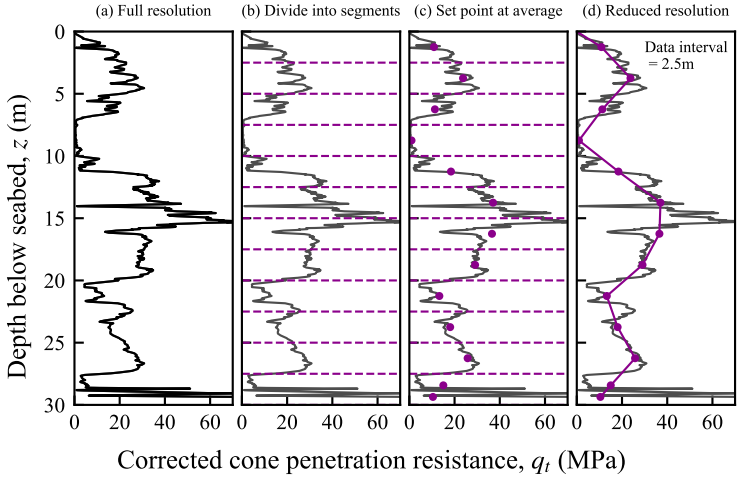

FIGURE 3.9: Process of reducing the CPT profile resolution by averaging over the specified data interval of 2.5 m

(see Section 3.5.1) and consistently tends to underdesign pile dimensions, compared to the full resolution design, as is evident by the downward trend plotted in Figure 3.11. The reducing sampling rate method is indicated by the dotted line to facilitate comparison between the two methods. This observation can be attributed to an increase in available soil lateral resistance. Using this design methodology, the single averaging interval method of artificial resolution reduction leads to potentially unconservative design.

3.5.2.2 Area under CPT profile up to full resolution optimal pile length

The averaging method should theoretically result in no change in area under the CPT curve for a given pile length. Plotting normalised area, through division by the area under the full resolution profile up to the optimal pile length of the full resolution design, with data interval, alongside normalised pile volume, can be seen in Figure 3.12. The almost horizontal line demonstrates that the area under the CPT curve has remained constant.

3.5.2.3 Offsetting

The purpose of developing the single averaging method was to reduce the effect of offsetting under the reducing sampling rate method in Section 3.5.1.3. In Figure 3.13, the impact of offsetting can be seen to be much smaller for the single averaging interval method. The greater the offset applied, the greater the difference between the offset curves. The variation in pile volume is mostly consistent regardless of minor adjustments to the initial incremental depth below the seafloor, with the lines starting

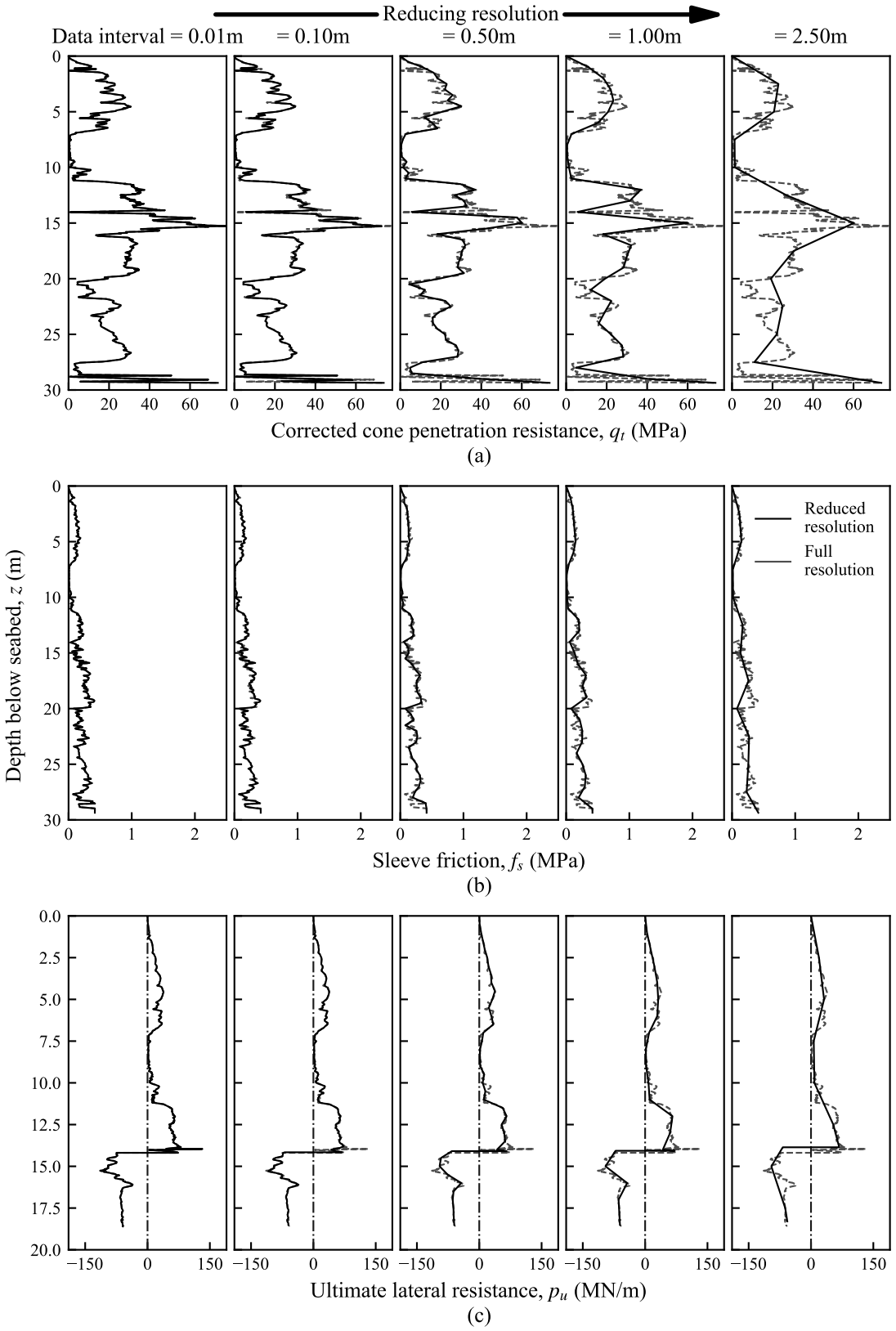

FIGURE 3.10: Effect of reducing resolution on profiles of (a) corrected cone penetration resistance, (b) sleeve friction, and (c) ultimate lateral resistance under optimal pile dimensions for example CPT (CPT203)

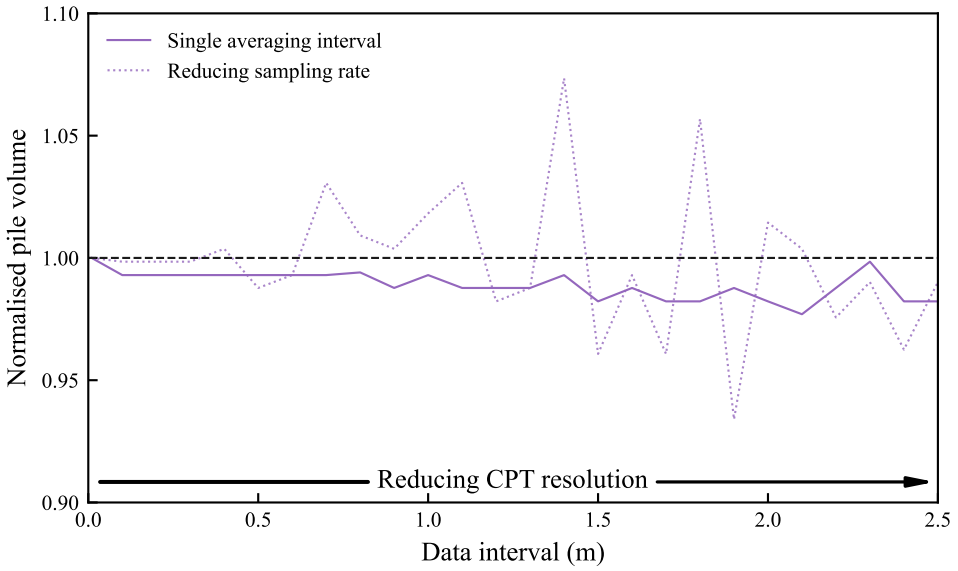

FIGURE 3.11: Effect of CPT resolution under single averaging interval method on minimum required pile volume for CPT203 within the Burbo Bank Extension offshore wind farm

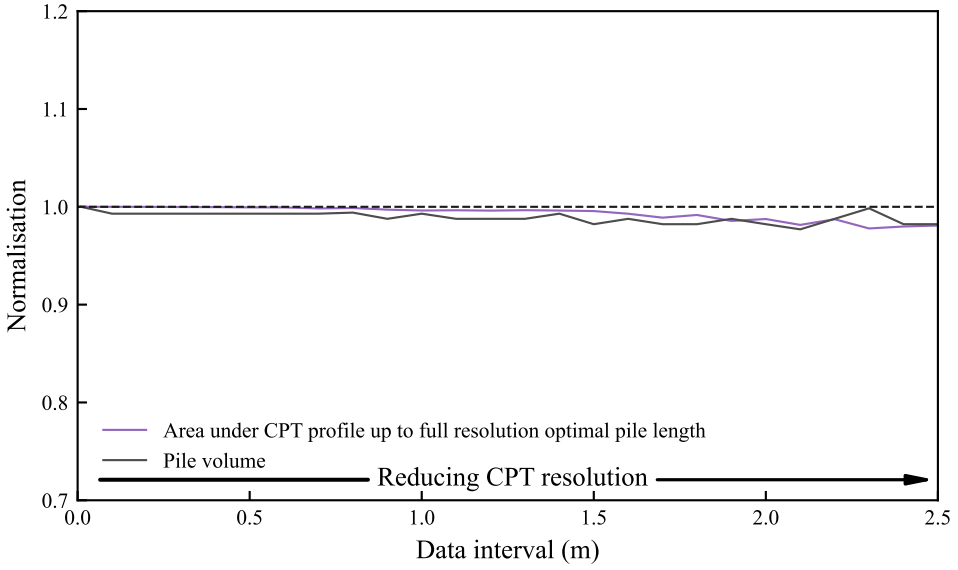

FIGURE 3.12: Effect of CPT resolution under single averaging interval method on area under CPT curve up to full resolution optimal pile length and minimum required pile volume for CPT203 within the Burbo Bank Extension offshore wind farm

to diverge more at larger data intervals. The randomness observed in the selected corrected cone penetration resistances profiles in offsetting under the reducing sampling rate has been reduced through the averaging method, with the discrepancy between the offset profiles being almost negligible.

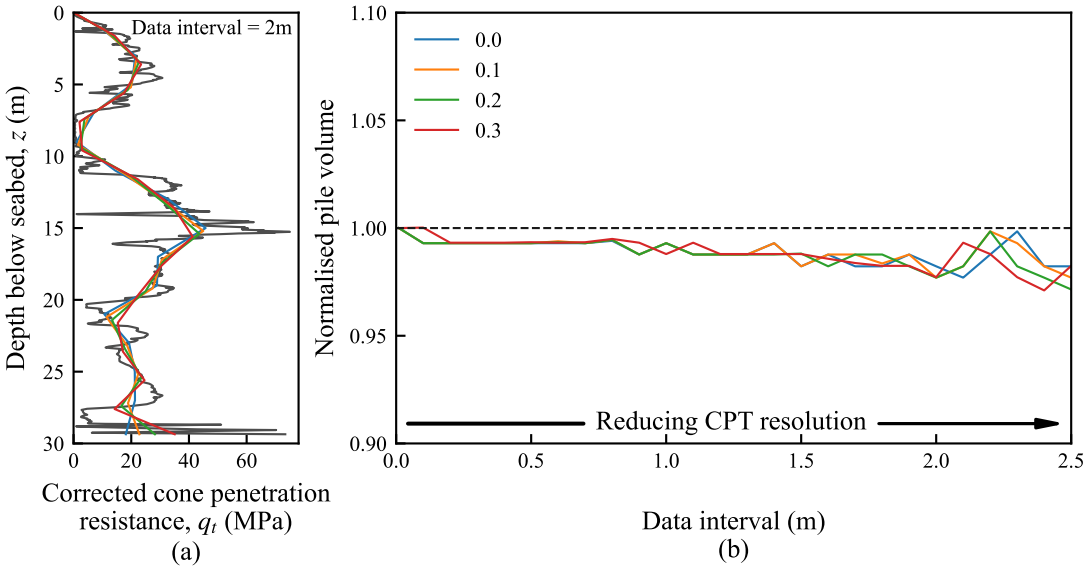

FIGURE 3.13: Effect of offsetting under single averaging interval method on q_t profile and minimum pile volume for CPT203 within the Burbo Bank Extension offshore wind farm

3.5.2.4 Summary

Whilst averaging has removed the randomness associated with the reducing sampling rate, only averaging over a single interval could lead to aliasing of the results. This is a phenomenon in which the sampling rate is too low to capture an accurate signal so it appears distorted. To prevent aliasing the Nyquist-Shannon sampling theorem states that the sampling rate should be at least twice the highest frequency.

3.5.3 Double averaging interval

The full resolution CPT (Figure 3.14(a)) was split into intervals of twice the desired data interval (Figure 3.14(b)), with a single average value calculated over the interval, plotted at the midpoint depths of each interval (Figure 3.14(c)). This process was repeated for the full resolution CPT at an offset of half the data interval below its starting depth (Figures 3.14(d) and (e)). The two sets of average values were then combined to produce a reduced resolution CPT with the desired data interval between points (Figure 3.14(f)).

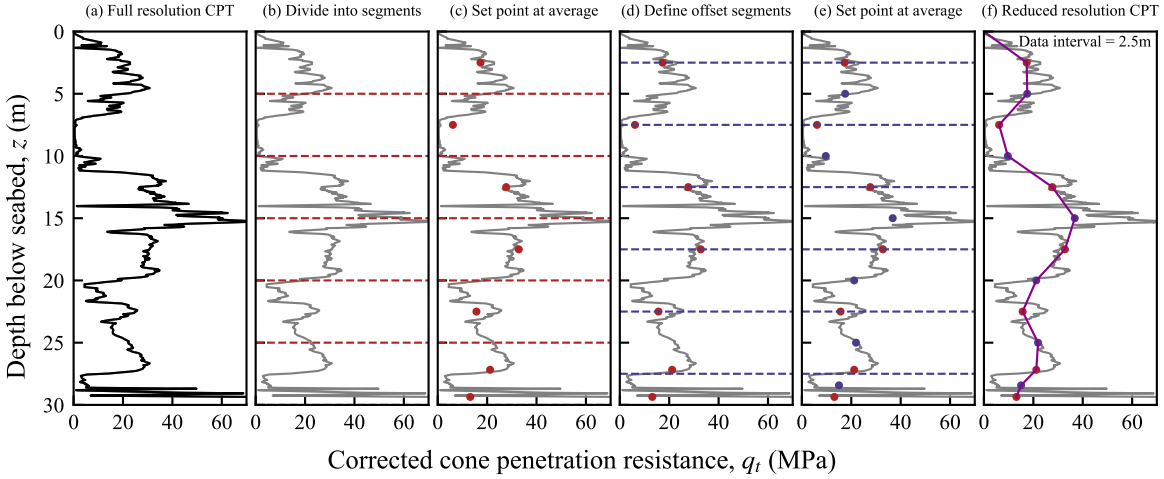

FIGURE 3.14: Process of reducing the CPT profile resolution by averaging over double the specified data interval of 2.5 *m*

Full resolution profiles (i.e. data interval of 0.01 *m*) of corrected cone penetration resistance and sleeve friction for CPT203 are shown in Figures 3.15(a) and (b) compared to reduced resolution profiles with data intervals of 0.1, 0.5, 1.0 and 2.5 *m* over the full depth of the CPT. The reduced resolution profile is shown as a solid line and the full resolution profile is shown by the dashed line in each plot. The background colour indicates the soil type classification for each depth interval, as associated to the averaged data point of that layer; pink for clay and blue for sand. It can be seen that as the resolution of the CPT profile decreases, the profile begins to lose its resemblence to the original full resolution profile. Furthermore, layers of clay are omitted from the profile with reducing resolution, starting with just the very thin layers of a few centimeters in depth at a 0.5 *m* data interval, but then extending to those of a couple of metres by a 2.5 *m* data interval.

To demonstrate the process by which the optimal pile dimensions were found through moment equilibrium about a pivot point within the pile, mobilised lateral resistance is plotted over the derived optimal pile depth (Figure 3.15(c)). The pivot point is identifiable as the depth at which the lateral resistance transitions from positive to negative, although remains equal in magnitude. Up to a data interval of 0.5 *m*, the lateral resistance profile closely follows that of the full resolution indicating pivot depth and pile length are unaffected. However, as the data interval is increased further, and the soil type classification is affected, lateral resistance is overpredicted between depths of 7 and 11 *m*, resulting in a decrease in optimal pile length (observed through the shorter lateral resistance profiles).

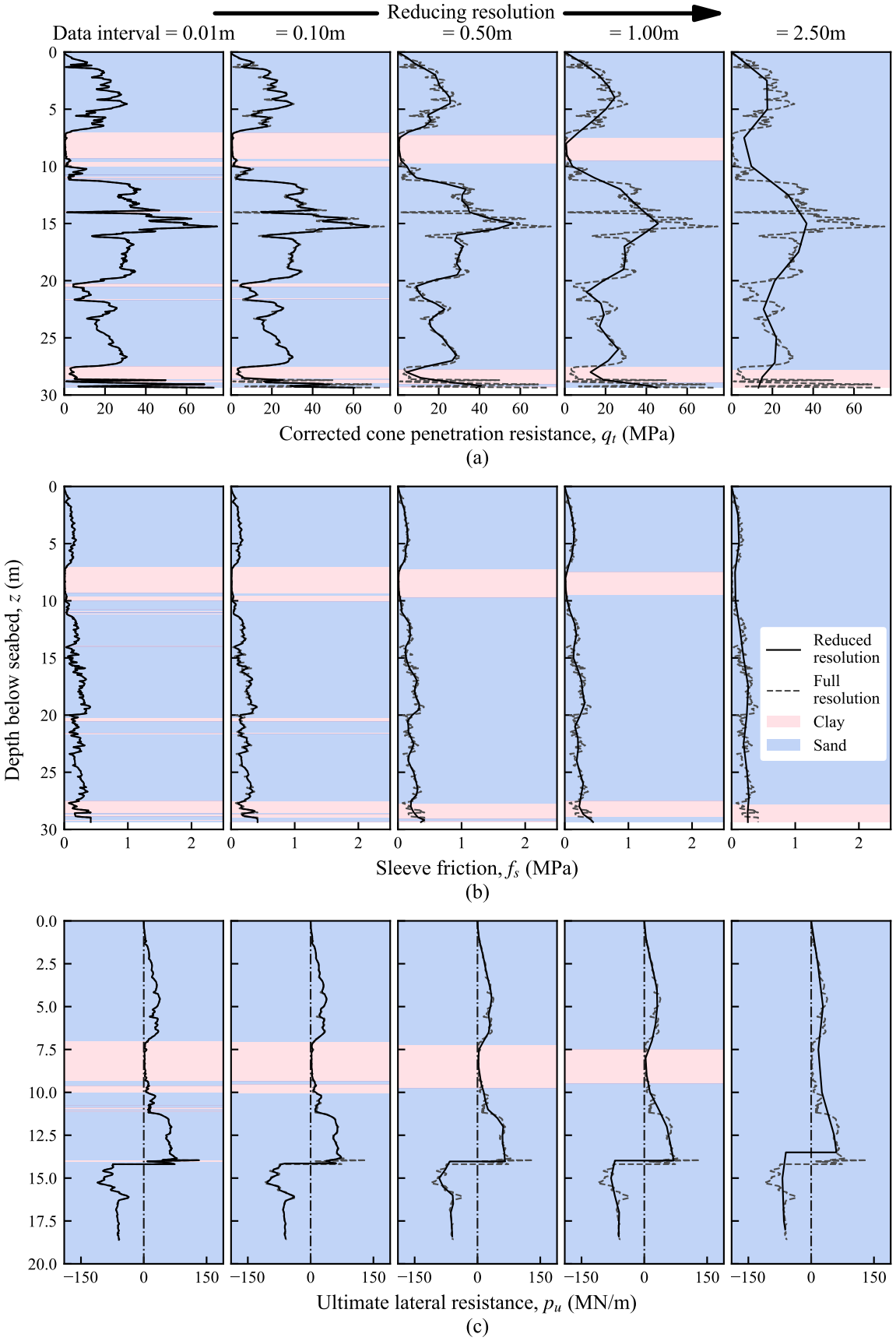

FIGURE 3.15: Effect of reducing resolution on profiles of (a) corrected cone penetration resistance, (b) sleeve friction, and (c) ultimate lateral resistance under optimal pile dimensions for example CPT (CPT203); soil type classification for clay and sand superimposed

3.5.3.1 Minimum pile volume

The downward trend exhibited for minimum normalised pile volume with increasing data interval for the single averaging interval method was also evident for the double averaging interval method, as plotted in Figure 3.16. Although for all three methods there is increased variation between the full resolution and reduced resolution designs at increasing data intervals, fluctuations in pile design between subsequent data intervals have been reduced under the double averaging interval method. This demonstrates that, for the purpose of this work, the double averaging interval method minimises the effect of the reducing resolution method on the output results, making it most suitable in this analysis.

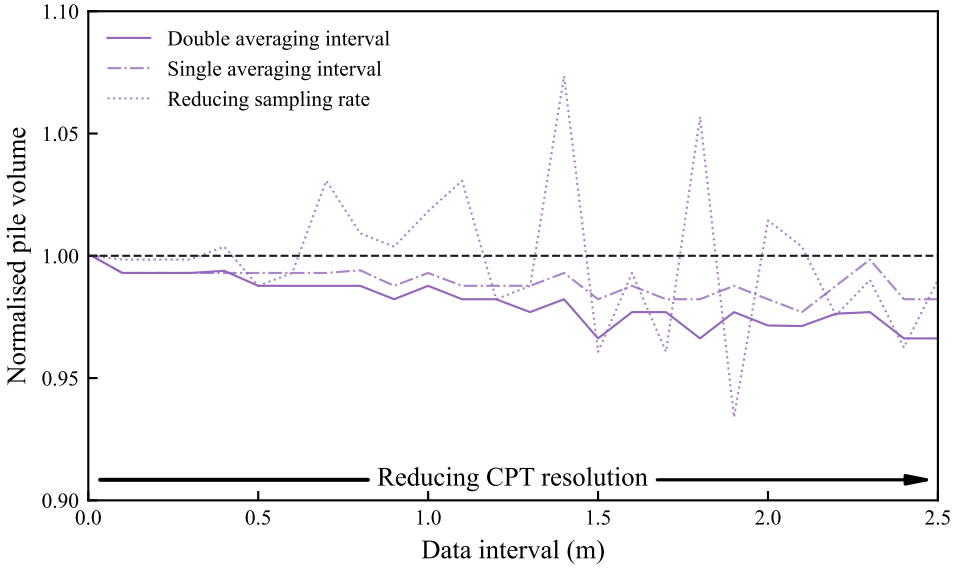

FIGURE 3.16: Effect of CPT resolution under double averaging interval method on minimum required pile volume for CPT203 within the Burbo Bank Extension offshore wind farm

3.5.3.2 Summary

Resolution reduction through averaging was selected to represent the nature of a synthetic CPT profile, which represents an average of the acoustic response through the sediment over the vertical resolution of the geophysical data. Further, using an averaging interval that is double the specified data interval avoids aliasing according to the Nyquist-Shannon sampling theorem, which dictates that the sampling rate must be at least twice the bandwidth of the signal.

3.6 Results

3.6.1 Minimum pile volume

Figure 3.17 demonstrates the influence of reduced CPT resolution on minimum required pile volume, where predicted pile volume at each CPT resolution is normalised by the pile volume predicted by the full resolution CPT profile. For the trialled CPT profiles, a general trend of decreasing normalised pile volume is observed with reducing CPT resolution (i.e. increasing CPT data interval), along with increasing variation in normalised pile volume. For the nine selected CPTs, for data intervals of up to 0.5 *m*, predicted pile volume falls within 3 % of that with the full resolution CPT. This reduction in predicted required volume increases up to 11 % at a data interval of 2.5 m. These resolutions are comparable with what can be achieved by machine learning based synthetic CPT methodologies (e.g., Sauvin et al., 2019; Chen et al., 2021).

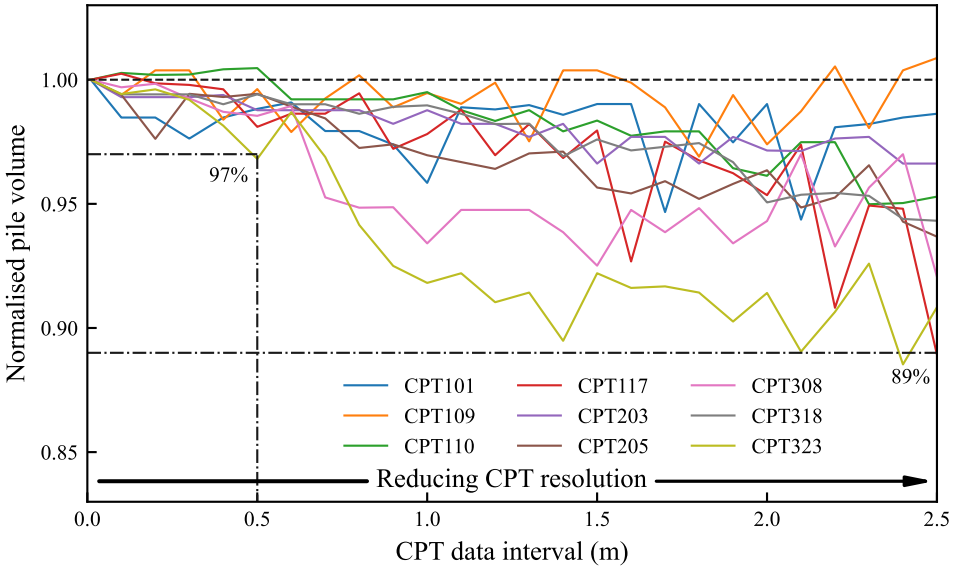

FIGURE 3.17: Effect of CPT resolution on minimum required pile volume for selected CPTs within the Burbo Bank Extension offshore wind farm

The consistent underprediction of pile volume with reduced CPT resolution can be explained by increasing omission of clay layers as resolution decreases (as illustrated in Figure 3.15), resulting in continuous sand layers with higher strength than interbedded sand and clay layers.

3.6.2 Area under curves

Further insight can be gained by examining the CPT profiles. Since the method by which CPT profile resolution was reduced involved averaging over specified depth intervals, the area under the CPT curve is independent of resolution for a given pile

length. The depth-integrated CPT resistance for CP203 at various resolutions (i.e. data intervals), calculated using the trapezium rule at the corresponding data interval, is plotted in Figure 3.18(a), and as expected, all the lines are essentially coincident. Any slight discrepancies between the lines can be attributed to the fact that data points are not plotted at the same depths and, for the larger data intervals of 1.0 and 2.5 m, points are linearly connected.

As per the lateral resistance equations and the design methodology adopted, it follows that the integral of the CPT cone penetration resistance profile is inversely proportional to some function of the required pile volume, i.e., more resistance will result in smaller piles. It is not possible to quantify this proportionality directly due to the range of influential variables, including soil classification, the different lateral resistance equations used, and distance to the pivot. For example, soil resistance further from the pivot depth has a greater effect on the pile resistance due to the larger lever arm.

While this observation is potentially specific to the lateral resistance equations chosen, it is likely that similar reductions in required pile volume with reducing resolution would be observed for other design methodologies where the lateral resistance equations used involve nonlinear relations to geotechnical parameter profiles. This trend likely extends to full $p - y$ curve analyses and more rigorous PISA-type design methods (e.g., Burd et al., 2020). It should also be noted that in the case study used, the soil is mostly sandy, with thin clay layers being eliminated through the resolution reduction process. Where the soil is mostly clayey with thin layers of sand, with the lateral resistance equations for clay lacking this nonlinearity, it is possible that this observation would not apply.

The trend of decrease in pile volume with reducing resolution is a result of an increase in available soil lateral resistance. To demonstrate this, the depth-integrated absolute lateral resistance profile, as portrayed in Figure 3.15(c), is plotted along the depth of optimal pile length for CPT203 at various data intervals (Figure 3.18(b)). Further, the depth-integrated absolute lateral resistance was divided by the cumulative area under the corresponding CPT profile up to the optimal pile depth, as illustrated in Figure 3.18(c). As the cumulative area under the CPT profile is approximately constant for different resolutions (see Figure 3.18(a)), Figure 3.18(c) demonstrates that the cumulative area under the lateral resistance profile increases with decreasing resolution for a given depth. This increase in lateral resistance would then result in the decrease in minimum pile volume for lower resolutions, supporting the trend observed in Figure 3.18(b). It should be noted that Figures 3.18(b) and (c) are specific to CPT203 and the selected resolutions. As such, the purpose of Figure 3.18(c) is to highlight the general trend of lateral resistance being overpredicted as resolution reduces in support of the trends of reducing minimum required pile volume observed in Figure 3.17 and the discussion regarding the influence of the lateral resistance equations.

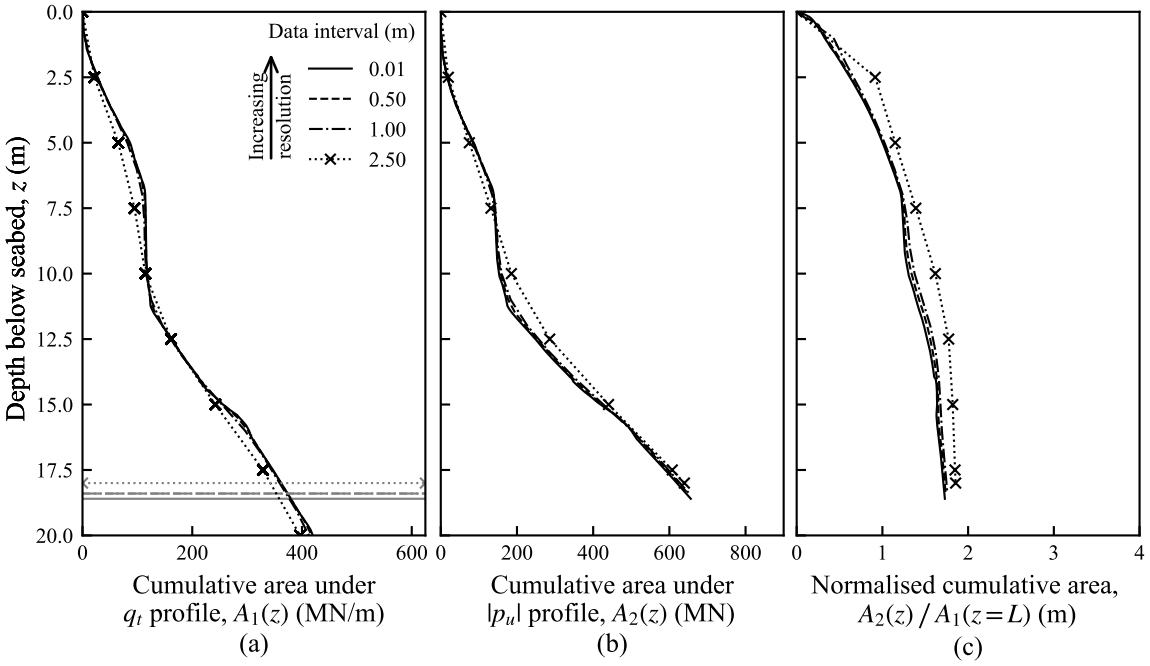

FIGURE 3.18: Effect of reducing CPT resolution on cumulative areas under (a) cone penetration resistance profile, (b) absolute lateral resistance profile up to optimal pile length, and (c) normalisation ((b)/(a)) up to optimal pile length, for example CPT (CPT203)

3.6.3 Pile capacity

Having established that reducing resolution of CPT data leads to a divergence of minimum predicted pile volume compared to that for the full resolution soil profile, it is necessary to quantify the impact of this on pile capacity. For each CPT resolution considered, a pile with dimensions equal to the optimal pile diameter and length for the given resolution was analysed as if it were installed in the full resolution CPT soil profile – representing a pile designed with low resolution ground data being installed in the actual ground. The maximum horizontal load that the reduced resolution piles were able to withstand before ULS failure was calculated, and normalised by the capacity of the full resolution pile. Figure 3.19 demonstrates that normalised lateral pile capacity decreases with reducing CPT resolution, and the variation increases with reducing resolution, as was also observed for pile volume (Figure 3.17). Lateral pile capacity falls to 93 % of its full CPT resolution capacity for data intervals less than 0.5 m. The reduction in capacity increases up to 15 % at a data interval of 1.0 m. A maximum reduction in pile capacity of 21 % is observed at a data interval of 2.5 m.

Since smaller piles generally have lower capacity, a similar trend was to be expected and is in accordance with Figure 3.17. However, comparison between Figure 3.17 and Figure 3.19 indicate that the correlation between pile capacity and volume is not always one-to-one, and the difference becomes more pronounced with reducing resolution (i.e. increasing data interval). At a data interval of 2.5 m, the percentage loss in capacity can

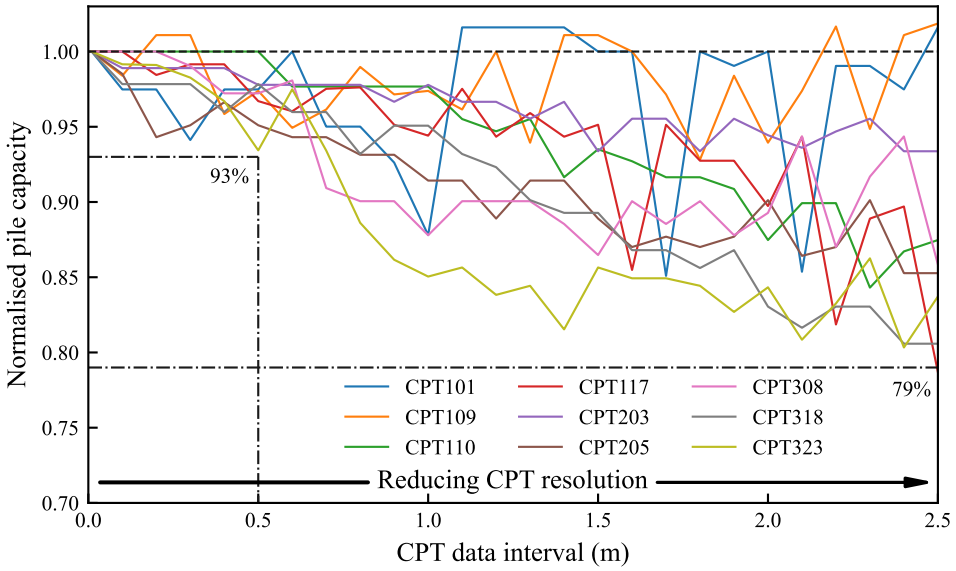

FIGURE 3.19: Effect of reducing CPT resolution on lateral pile capacity for selected CPTs within the Burbo Bank Extension offshore wind farm

be twice the corresponding percentage loss in pile volume: e.g., a pile volume decrease of just over 10 % causes just over a 20 % decrease in capacity for CPT117. Nonetheless, at resolutions achievable with synthetic CPTs, where the data interval remains less than 1 m, the reduction in capacity is relatively minor.

Figure 3.20 illustrates this variation by plotting normalised lateral pile capacity against normalised pile volume for every data interval trialled and for each of the nine selected CPTs. Marker edges are coloured to represent each CPT, with shading of the marker face representing magnitude of data interval. The correlation between capacity and volume is evident, with slight variation in gradient for different CPT profiles. Irrespective of the CPT location, and therefore the ratio between capacity and volume, the higher the resolution, the closer the point to coordinates (1, 1) and the smaller the decrease in pile capacity and volume. The overall trend that reducing the CPT profile resolution (i.e. increasing the data interval), results in increased variation in decreases in pile volume and capacity, is further reinforced.

3.6.4 Comparison with lateral interpolation between CPTs

To demonstrate the potential of synthetic CPTs in pile design, a comparison is made between a pile design from a reduced resolution CPT at the desired location (representing a synthetic CPT derived from available geophysical survey data), and a soil profile acquired by linear interpolation between adjacent full resolution geotechnical CPTs. To illustrate this point, the location at CPT109 is selected for a pile design, using (i) interpolation between CPT203 and CPT205 that lie either side of CPT109, and

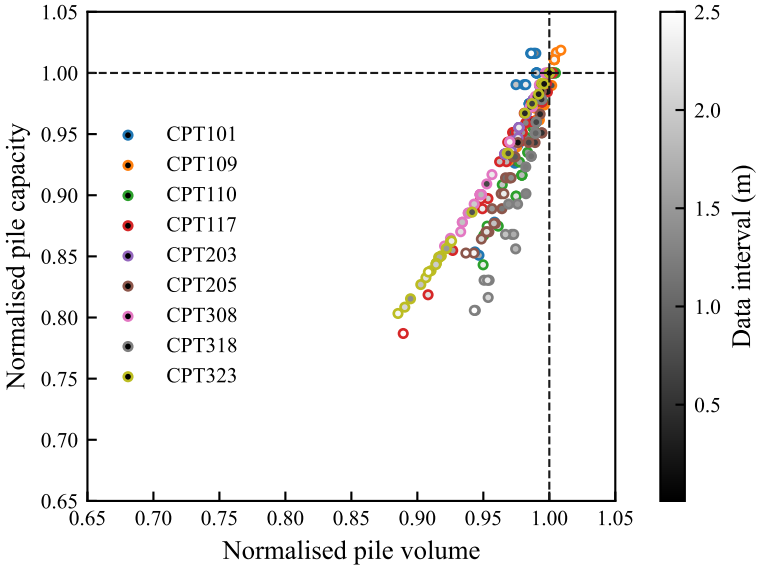

FIGURE 3.20: Variation in correlation between normalised pile volume, normalised pile capacity and CPT resolution, shown through data interval, for nine selected CPTs within the Burbo Bank Extension offshore wind farm

(ii) reduced resolution CPT profile from CPT109 location (see Figure 3.2 for CPT locations across the area). Figure 3.21 shows the area of the location of the three selected CPTs (Figure 3.21(a)), the CPT corrected cone penetration resistance profiles at each location (Figures 3.21(b) and (c)), and the interpolated and reduced resolution profiles at location CPT109 (Figures 3.21(d) and (e)). This interpolation method is a simplified example of design practice when a CPT has not been performed at the desired location of an offshore wind turbine foundation.

It can be seen that the soil conditions indicated by the CPT profiles can vary considerably at some depths between locations: CPTs 203 and 205 (Figures 3.21(b) and (c), respectively), and as such the interpolated CPT profile differs considerably from the actual profile of CPT109 (Figure 3.21(d)). By contrast, the reduced resolution profiles of CPT 109 - even at the largest data interval of 2.5 m - capture the key form of the profile (Figure 3.21(e)). The effect of the approximations in the cone penetration resistance profile, either by interpolation or reducing resolution, is assessed here by comparing the required pile volume to resist ULS under lateral load. Use of the full resolution CPT109 profile - which we assume is not available to the designer in this example - leads to prediction of an optimal pile volume of 40.39 m^3, compared to 37.33 m^3 predicted from the linearly interpolated profile from adjacent CPTs 203 and 205: a difference of 8 %. By contrast using a reduced resolution profile from the actual location (representing a synthetic CPT at location 109), predicts an optimal pile volume of 38.9 m^3 even for the largest data interval of 2.5 m: a difference of less than 4 % compared to the predicted optimal pile volume with the full resolution CPT at that location. Although simple, and only illustrative, this example shows that adopting a significantly reduced resolution

CPT profile can provide a better measure of the actual pile volume, than by interpolating a high resolution CPT soil profile from adjacent locations, particularly in highly heterogenous seabeds.

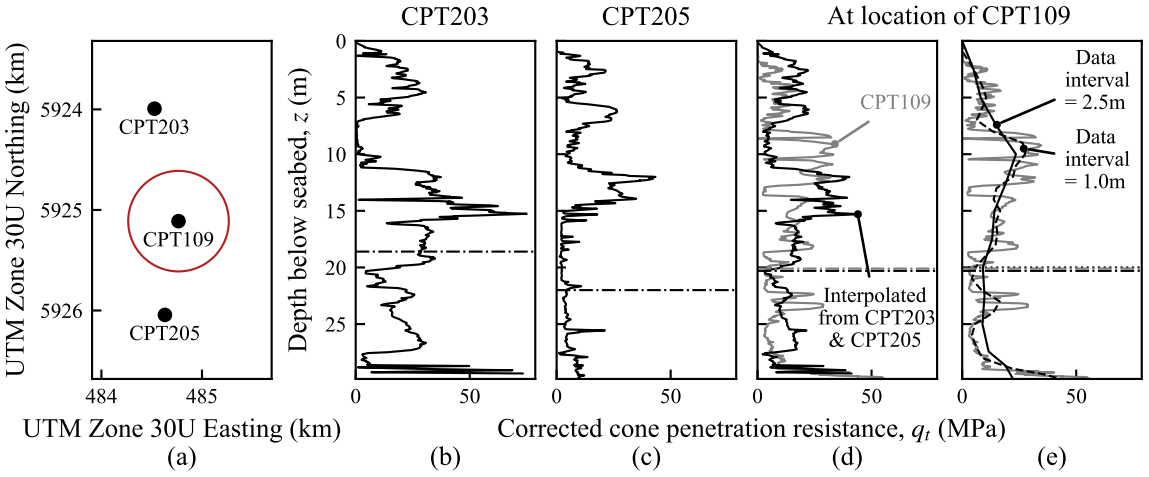

FIGURE 3.21: (a) Cluster of adjacent CPTs used for example; (b) Full resolution q_t profile of CPT203; (c) Full resolution q_t profile of CPT205; (d) Interpolated profile between CPTs 203 and 205 with full resolution q_t profile of CPT109; (e) Reduced resolution q_t profiles of CPT109 with full resolution q_t profile of CPT109 (optimal pile length indicated by horizontal broken lines)

3.7 Summary

This chapter has set about narrowing the gap between the theory of synthetic CPTs and their use in practice in the design of offshore wind turbine monopile foundations. The actual effect of reduced resolution CPT profiles on design outcomes has been evaluated, in accordance with **RO1**, by artificially reducing the resolution of geotechnical CPT profiles at the Burbo Bank Extension offshore wind farm, from which minimum pile dimensions were calculated under ultimate limit state. Different ways of reducing CPT profile resolution were assessed in Section 3.5 before the double averaging interval method was deemed most suitable since it had the least impact on pile dimensions (Figure 3.16). Whilst averaging over the reduced resolution data interval removed the randomness in whether the pile was to be over or underdesigned, as well as dependency on starting depth of the CPT profile, following the Nyquist-Shannon sampling theorem of an averaging window at least twice the sampling rate ensured there was no aliasing of the results.

The effect of using reduced resolution CPT profiles on minimum pile dimensions was an overall decrease with reducing resolution for all nine of the selected CPTs at the Burbo Bank Extension wind farm site (Figure 3.17). This decrease in minimum pile volume is due to an increase in available soil lateral resistance in the reduced resolution

CPT profiles, which has been associated with the omission of weaker clay layers in CPT203 (Figure 3.15).

In this work, it was observed that CPT resolution could be reduced to a data interval of 0.5 m, with predicted pile volume decreasing by no more than 3 % (Figure 3.17) of a pile designed using the full resolution profile (with resolution of 0.01 m). This corresponded to a reduction in pile capacity, when installed in the full resolution soil, of up to 7 % (Figure 3.19), as the relationship between pile volume and capacity was found to not necessarily be one-to-one (Figure 3.20).

Using reduced resolution CPT profiles was also found to be an improvement to interpolation between geotechnical CPT locations for the determination of soil properties not at a CPT location. A reduced resolution profile with the largest tested data interval of 2.5 m halved the discrepancy between the actual and predicted optimal pile volumes from 8 % under interpolation to 4 % (Figure 3.21).

Overall, the work in this chapter has demonstrated that accurate pile design can be achieved with reduced resolution CPT profiles, especially for data intervals up to 0.5 m which can be achieved or surpassed with state-of-the-art geophysical acquisition equipment and machine learning based synthetic CPT methods. It is also possible that simpler CPT profiles, i.e. from a site with less complex ground conditions than in the case study area considered here, would be even less sensitive to reduction in resolution.

Further research is required to assess the effect of CPT resolution on a range of foundations, anchors, loading conditions, limit states and seabed conditions to generalise recommendations, and the specific thresholds identified from the analysis presented in this work should not be directly applied to another site, another foundation or anchor type, or failure criterion. The work presented here is intended as a proof-of-concept workflow that could be applied to other foundation and anchor systems, design criteria and seabed conditions.

Chapter 4

Effect of using synthetic CPTs on design outcome

4.1 Introduction

Synthetic CPTs offer immense potential for offshore site characterisation, but the lower vertical resolution of synthetic CPTs compared to in situ geotechnical CPTs, poses questions as to the consequent effect on design outcome. To contribute to an evidence base to address this question, this work compares a monopile design based on co-located in situ geotechnical and synthetic CPTs.

4.2 Case study: TNW offshore wind farm site

The Ten Noorden de Waddeneilanden (TNW) wind farm zone in the Dutch Sector of the North Sea was selected as a case study area, due to the availability of both geothechnical and synthetic CPTS. Geotechnical CPT data (Fugro, 2020) as well as two and three-dimensional ultra high resolution seismic data (MMT, 2020) made available by RVO, the Netherlands Enterprise Agency, were used. The geotechnical CPTs were processed according to standardised procedures (see Section 2.4) (Robertson, 1990, 2009b). The synthetic CPT predictions were produced using a two-stage process (NGI, 2022; Vardy et al., 2023a). Firstly, the geophysical data were inverted to derive a range of bulk physical parameters (e.g. P-wave velocity, Q-factor, acoustic impedance), including estimates of uncertainty. Secondly, an artificial neural network was trained to predict the CPT cone penetration resistance, sleeve friction and pore pressure response based on the inverted geophysical parameters. This machine learning prediction was validated using a series of leave-one-out predictions, where the CPT parameters were blindly

predicted at each CPT location in turn and the results used to statistically analyse performance (Vardy et al., 2023a,b).

4.3 Discrepancy between in situ and synthetic CPT profiles

The 116 CPT locations across the zone are displayed in Figure 4.1, of which a subset of nine locations were selected for further analysis. These were chosen to provide a good spatial coverage across the site as well as a cone penetration depth of at least 20 m (suitably deep for pile design). To ensure the fit of the nine synthetic CPT profiles to the corresponding geotechnical profiles captured the range of variability observed within the site, a discrepancy of the cone penetration resistance was calculated. This was determined from the absolute difference in the area under the geotechnical and synthetic CPT cone penetration resistance curves up to the maximum depth of the geotechnical profile, since the synthetic data always extended much deeper, for the 60 CPTs at each location that were deeper than 15 m. Including those up to 15 m in depth, enabled a ranking to be assigned which was a better representative of the whole site. Figure 4.2 plots this measure of discrepancy, expressed as a percentage of the area under the geotechnical curve, with CPT number, keeping the labelling the same as specified in the site investigation reports (Fugro, 2020). The red markers depict the nine CPTs that were ultimately selected, demonstrating that both well matched in situ and synthetic CPTs, and the worst fit of TNW051 have been included in the analysis. Overall, Figure 4.2 shows that the synthetic CPTs do enable a good prediction of the in situ geotechnical cone penetration resistance profiles for the full 60 CPTs, generally within 1 %, but with a maximum discrepancy of just over 2 %.

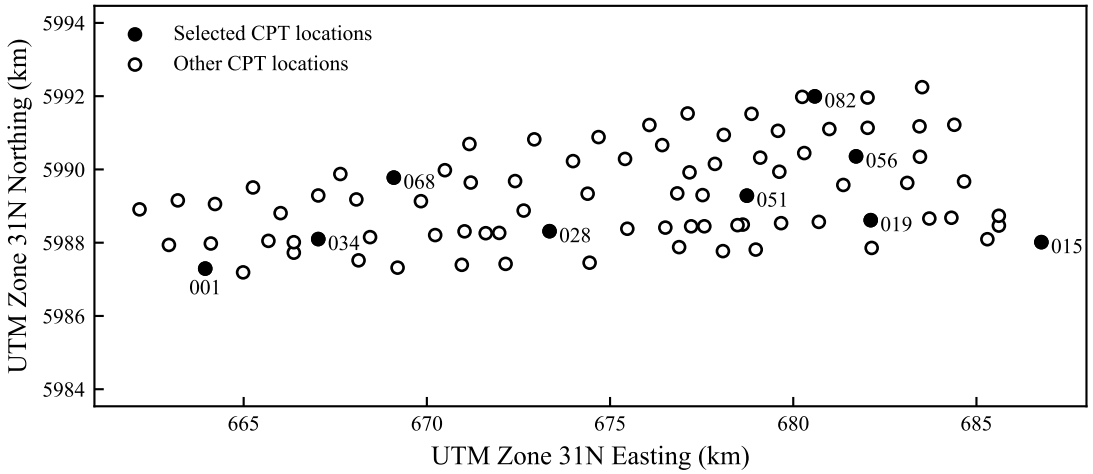

FIGURE 4.1: Locations of geotechnical CPTs within the TNW site

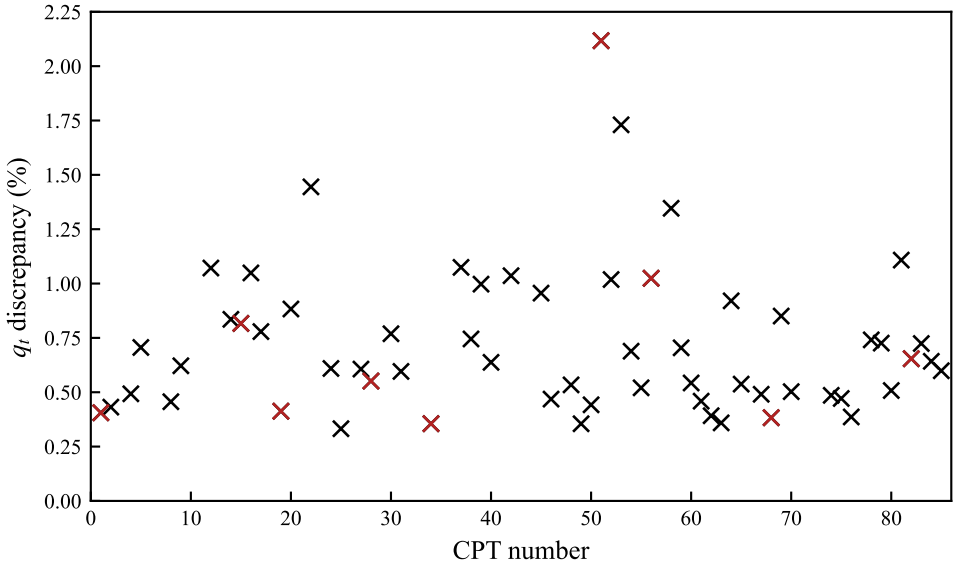

FIGURE 4.2: Discrepancy between the in situ and synthetic cone penetration resistance (q_t) profiles of the 60 CPT locations to depths of at least 15 m at the TNW offshore wind farm site, with the nine selected CPT locations shown in red

The co-located in situ and synthetic profiles of cone penetration resistance and sleeve friction are shown in Figure 4.3 in rank order by cone penetration resistance discrepancy. The synthetic CPT profiles follow the trends of the in situ CPTs although reduced vertical resolution in the synthetic profiles is evident. An equivalent measure of discrepancy could also be applied to the sleeve friction profiles for the same 60 CPTs greater than 15 m. Ranking according to the position of the sleeve friction profile gives the values on the sleeve friction plots in Figure 4.3. In general, these exhibit slightly larger differences between in situ and synthetic profiles, but less variation between CPTs.

4.4 Resolution of synthetic CPT profile

The resolution of a CPT profile has been defined as the data interval between cone penetration resistance readings. For the geotechnical CPTs in Chapter 3 at the Burbo Bank Extension wind farm site, this was 0.01 m. The resolution was then artificially reduced to a maximum data interval of 2.5 m. In comparison, the in situ CPTs at the TNW offshore wind farm zone have a very similar resolution of 0.02 m. This level of resolution is what would be expected from CPTs (Chen et al., 2021; Peuchen et al., 2022b). However, to determine the resolution of the synthetic CPTs, it is not as straightforward as calculating the average data interval between readings, 0.1 m for the TNW case study, due to the increased sampling rate. Whilst in geotechnical CPTs, the sampling rate governs the data interval, the synthetic data has been generated to provide a given sampling rate from the geophysical data which requires interpolation between the actual data

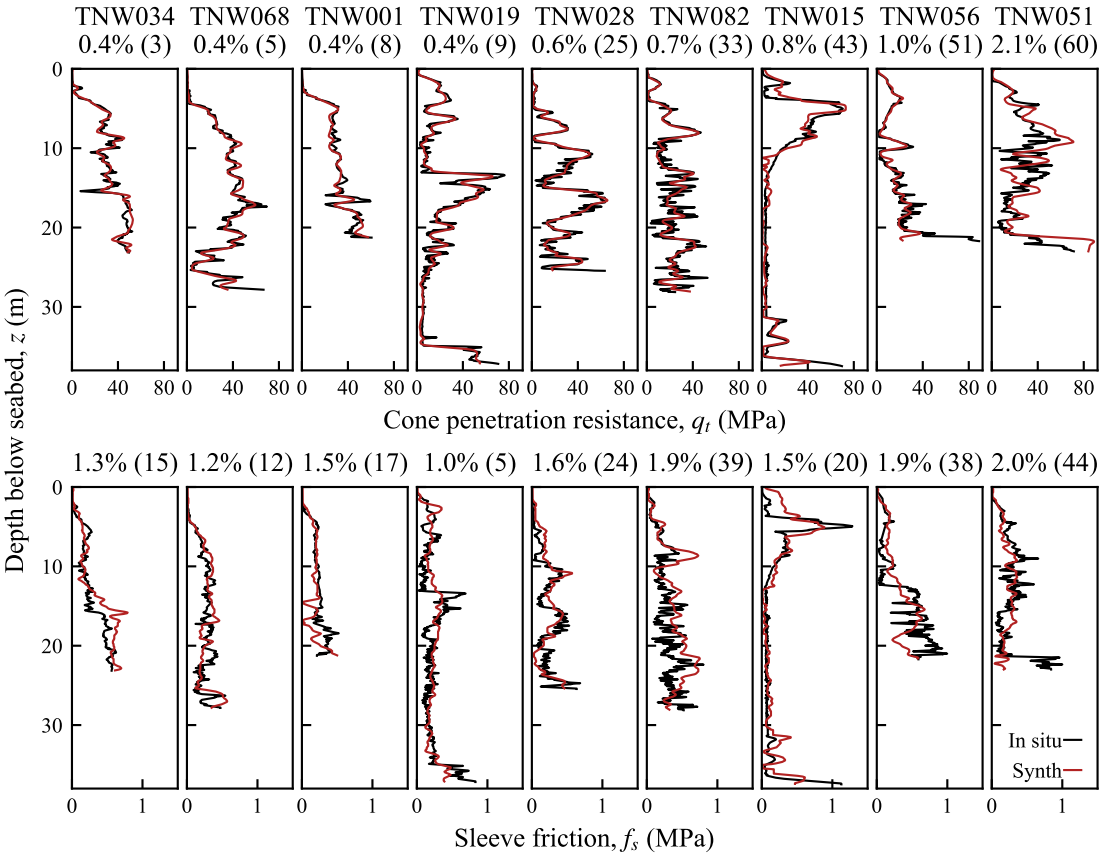

FIGURE 4.3: Geotechnical (black) and synthetic (red) CPT profiles for the selected locations, shown in ranked order for cone penetration discrepancy. % indicates absolute variation in area under geotechnical and synthetic profiles.

intervals. This is because the resolution of geophysical data decreases with depth (Audibert and Huang, 2005), making it difficult to provide a single value of resolution for a synthetic CPT.

In order to establish a resolution of synthetic CPT profiles which could be compared to the range of artificially reduced resolutions of the in situ geotechnical CPT, changes in the synthetic cone penetration resistance profiles were assessed by eye. From Figure 4.3, there appear to be sharp changes in value, which do not signify linear interpolation, every 1 m in depth, on average. This suggests that assuming a resolution of 1 m across the whole length of a synthetic CPT profile is reasonable and is in accordance with the resolution of the geophysical data (MMT, 2020) used to create them.

4.5 Soil classification

From the cone penetration resistance and sleeve friction profiles in Figure 4.3, the soil type for each depth increment can be derived according to the Soil Behaviour Type Index (see Section 3.4.2). Applying the same pile design calculations as in Section 3.4.3,

the ultimate lateral resistance of the soil for the optimal pile dimensions is plotted in Figure 4.4, with soil type indicated by the background colour. Clay is depicted in pale pink, whilst sand is in pale blue. To portray the differences in soil classification from the synthetic CPTs, as opposed to the in situ geotechnical ones, and therefore be deemed as incorrect predictions, the pink and blue colours have been highlighted. A dark pink indicates the synthetic CPT has predicted a clay when it is actually a sand in the in situ CPT, whereas a dark blue marks the opposite: the synthetic CPT predicts a sand when it is a clay in the in situ CPT.

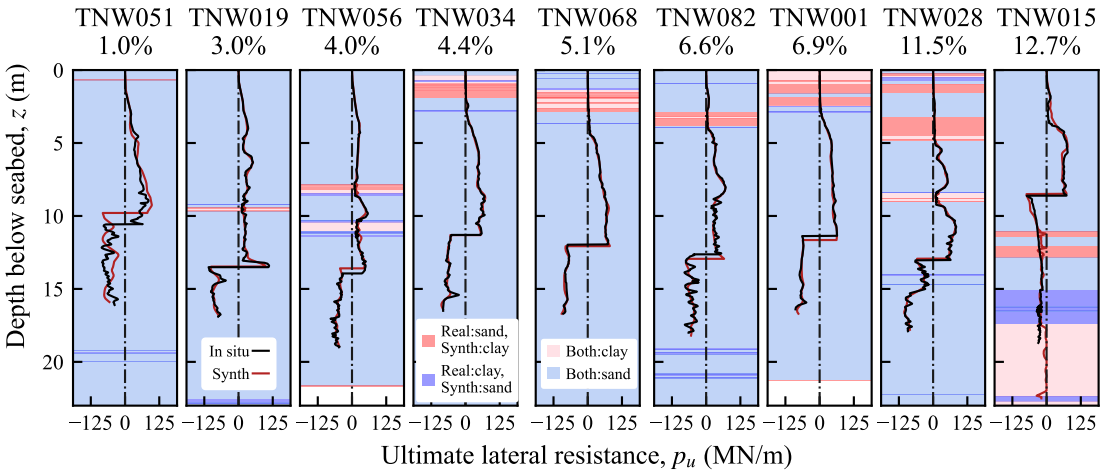

FIGURE 4.4: Geotechnical (black) and synthetic (red) CPT ultimate lateral resistance (p_u) profiles for the selected locations, shown in ranked order for percentage of incorrect soil type. Soil type classification for clay and sand superimposed with incorrect predictions highlighted.

The ultimate soil lateral resistance profiles in Figure 4.4 for the nine selected CPTs at the TNW site have been ordered according to the percentage of incorrect soil type. This involved comparing the soil type between the in situ and synthetic CPTs at each depth increment over the whole in situ CPT length, to identify where they did not match up, as a proportion of the total soil classifications. It should be noted that the profiles in Figure 4.4 have only been plotted up to a maximum depth of 23 m, even though some CPTs extended far deeper, to focus on the depths relevant to pile design. This means the ranking of a CPT may appear to be lower, i.e. have a smaller proportion of incorrect soil, than its position suggests, if this occurs below the depth of the pile. However, in general, any incorrect soil at depths greater than 23 m have not caused significant change to the order.

Figure 4.4 demonstrates accurate classification is achieved with synthetic CPTs, with the percentage of incorrect soil for the majority of CPTs being less than 10 % but no larger than 13 %. The incorrect layers of soil tend to consist of thicknesses in the order of magnitude of tens of centimetres, with the greatest two layers both just over a metre in TNW028 and TNW015. Comparing the ranking of CPT profiles in Figure 4.4 to that in Figure 4.3 for the discrepancy in cone penetration resistance, shows distinct differences.

The CPT with the largest cone penetration discrepancy is TNW051, whereas it exhibits the least proportion of incorrect soil type. The ultimate lateral resistance profile of the synthetic CPT does vary the most to the in situ profile, in accordance with the discrepancy, resulting in a pivot depth most noticeably above that of the pile designed using the in situ CPT. However, this overprediction in soil ultimate lateral resistance in the first 10 m happens to be cancelled out by the underprediction between 13 and 14 m. The final result is a pile of similar length under both the in situ and synthetic CPTs. The incorrect soil layer at just under one metre does not affect the pile design from the synthetic CPT as it occurs near the top of the seabed where lateral resistance is small, regardless of clay or sand. This also applies to the other CPT profiles where the soil is incorrectly predicted closely below the seafloor.

The effect of discrepancy and incorrect soil type on optimal pile design will be analysed through pile volume and capacity in Sections 4.6.3 and 4.6.4. As yet, there does not seem to be a correlation between discrepancy of cone penetration resistance, or sleeve friction, and percentage of incorrect soil type, and if one plays a larger role in affecting pile design. However, TNW015 ranks near the high end of cone penetration resistance discrepancy and has the largest percentage of incorrect soil. It can be seen from Figure 4.4 that the pile designed from the synthetic CPT has to be about 4 m longer than that designed from the in situ CPT. There is a section of incorrect soil between 15 and 17 m where the synthetic CPT predicts it as a sand, before correctly identifying the thick clay layer below, although underpredicting it to be almost zero tip resistance. This lack of resistance means the pile under the synthetic CPT has to extend significantly longer to provide the needed resistance. The cone penetration resistance profile in Figure 4.3 for TNW015 also portrays this underprediction in resistance in the synthetic CPT. The issue is exacerbated by the fact that there is a large decrease in resistance from a depth of 15 m in the in situ CPT which is predicted as almost zero in the synthetic CPT. Therefore the proportion of underprediction is amplified but the discrepancy remains small since the values are close together.

4.6 Lateral pile design by capacity

4.6.1 Minimum pile volume

Minimum pile dimensions were determined for both the in situ and synthetic CPT profiles following the CPT-based equations that were used in the Burbo Bank Extension analysis in Section 3.4.3, according to the type of soil at each depth increment. Furthermore, pile volume was also minimised for reduction in resolution of the in situ CPT profiles from a minimum increased data interval of 0.1 m to a maximum data interval of 2.5 m at intervals of 0.1 m (see Section 3.4.1.2). This meant the effect of using synthetic CPTs on output optimal pile dimensions could be assessed in relation to the effect of

the artificial resolution reduction method (double averaging interval method in Section 3.5.3) on pile design.

The pile volume for each reduced resolution in situ CPT profile was normalised by dividing by the pile volume obtained from the full resolution in situ CPT. Plotting this normalised pile volume for the range of increased data intervals, produced Figure 4.5. The trend of an overall decrease in normalised pile volume with reducing CPT resolution (i.e. increasing CPT data interval), as was observed from the Burbo Bank Extension CPTs in Figure 3.17, can be seen. For data intervals of up to 0.5 m, predicted pile volume remains within 2 % of that with the full resolution CPT. A maximum reduction in pile volume of 5 % is reached for data intervals of up to 2.5 m, and therefore implies that reasonable pile dimensions can still be achieved for low resolutions. Comparing this to the normalised pile volumes of the synthetic CPTs, which have been plotted at a data interval of 1 m in accordance with the approximate resolution of a synthetic CPT at the TNW site (see Setion 4.4), any reduction in pile volume falls within that of the reduced resolution in situ CPTs. The synthetic CPTs of TNW019, TNW028, TNW034 and TNW051 all match up to their corresponding minimum volume pile, designed from the 1 m reduced resolution in situ CPT profile. TNW056 also closely predicts pile dimensions, although in this instance, the reduced resolution pile happens to be the same as that of the full resolution. The remaining CPTs of TNW001, TNW015, TNW068 and TNW082, generate piles of increased volume under the synthetic profiles, greater than the piles from any of the reduced resolution in situ CPT profiles. However, with the exception of TNW015, these overpredictions are very small: no larger than 3 % of the full resolution in situ pile design.

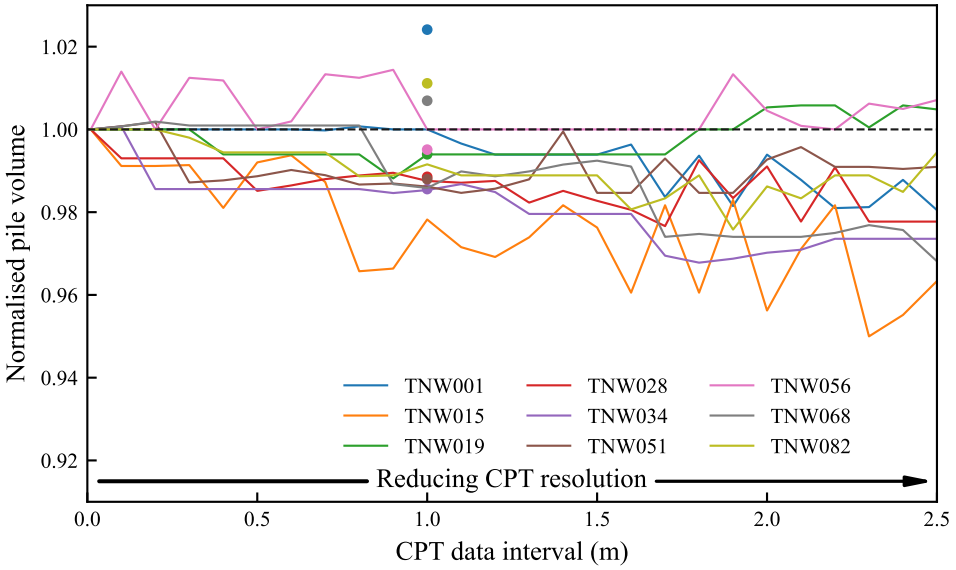

FIGURE 4.5: Effect of CPT resolution on minimum required pile volume for selected CPTs within the TNW offshore wind farm

The normalised pile volume for the synthetic CPT of TNW015 has not been included in Figure 4.5, since it is an outlier result with a 20 % increase in pile volume compared to that of the full in situ resolution. This can be attributed to the fact that the pile has to be 4 m longer, as mentioned in Section 4.5, due to the lack of soil resistance in both the in situ and synthetic cone penetration resistance profiles between depths of 15 and 30 m (see Figure 4.3). Although the difference in cone penetration resistance values between the in situ and synthetic CPTs for this range of depths is not large, the synthetic values as a proportion of those of the in situ are significantly less by a factor of 10. Therefore, the pile must be made longer when designed from the synthetic CPT, however there is barely any resistance from the soil until at least a depth of 22 m.

4.6.2 Pile capacity

The effect of CPT profile resolution on pile capacity was assessed as if a pile of reduced resolution optimal pile dimensions was installed in the full resolution soil, from which the ultimate applied lateral load on the pile for ULS design was found. Normalising this maximum horizontal load by dividing by that of the full resolution pile in the full resolution soil, and plotting for each in situ reduced resolution CPT profile produced the solid lines in Figure 4.6. An overall decrease in normalised pile capacity with reducing resolution can be observed. As is most evident for TNW015, the variation in normalised capacity also tends to increase. For data intervals of up to 0.5 m, lateral pile capacity falls within 3 % of its in situ full resolution capacity. This range can increase to almost 9 % for data intervals of up to 2.5 m, although most do not exceed the 5 % limit. Comparing to the trend of decreasing pile volume with reducing resolution for the in situ CPTs in Figure 4.5, generates similar reductions with capacity falling at a slightly greater rate at the higher data intervals. Nevertheless, the effect on pile design remains relatively small.

Calculating the normalised capacity of the synthetic CPTs in the same way as the in situ reduced resolution CPTs and adding them as marker points at their approximate data interval of 1 m, can also be seen in Figure 4.6. The order of the synthetic CPTs follows that in Figure 4.5, which is to be expected since changes in pile volume have a direct impact on the pile capacity, however, not always one-to-one. This is demonstrated by the increase in gaps between adjacent markers. The synthetic CPT of TNW015 has once again been omitted from the plot due to the outlier nature of the profile, as mentioned in Section 4.5 and reiterated in Section 4.6.1, which causes an excessive increase in pile length and a resulting capacity of over 50 % that of the full in situ resolution. Despite this, the majority of synthetic CPTs have a capacity very close to that of the equivalent reduced resolution profile, with small increases in capacity for TNW068 and TNW082, and a slightly larger one for TNW001.

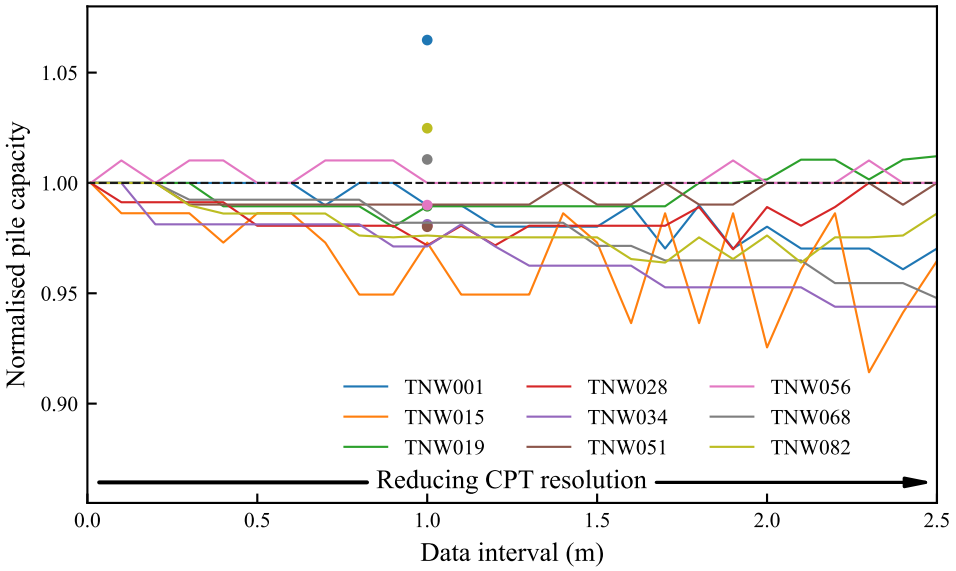

FIGURE 4.6: Effect of CPT resolution on lateral pile capacity for selected CPTs within the TNW offshore wind farm

4.6.3 Effect of cone penetration resistance discrepancy

The effect of discrepancy between the cone penetration resistance in situ and synthetic CPT profiles on pile design was assessed through normalisation of the synthetic minimum pile volume and capacity by dividing by the in situ full resolution minimum pile volume and capacity, respectively. Figure 4.7(a) plots this for both normalised pile volume (solid markers) and normalised pile capacity (hollow markers). In accordance with Figures 4.5 and 4.6, pile volume predicted using the synthetic CPTs varies from the optimal design based on the in situ CPT by less than 3 %, whilst capacity is affected by similarly small amounts of up to 7 %. Both can be either over or under predicted. It is important to note that TNW015 has been excluded from the plot to enable any trend between the other CPTs to be distinguished without a skew towards the outlier behaviour of TNW015, which has been discussed in previous sections. Additionally, TNW015 does not exhibit the greatest discrepancy (see Figure 4.3) which could otherwise have been attributed to the large difference in pile volumes derived from the in situ and synthetic CPTs. Instead, the largest discrepancy of cone penetration resistance is observed in TNW051, for which deviations of normalised pile volume and capacity from unity are minimal: within 1 % and 2 %, respectively. The greatest change in both normalised pile volume and capacity that was plotted in Figure 4.7(a), is for TNW001, but the discrepancy between its in situ and synthetic cone penetration resistance profiles is less than 0.5 %. Therefore, the extent of variance in pile volume or capacity is not reflected in the rank order based on similarity of in situ and synthetic cone penetration resistance profiles.

Variations in capacity are non-linearly related to those in pile volume, as capacity is

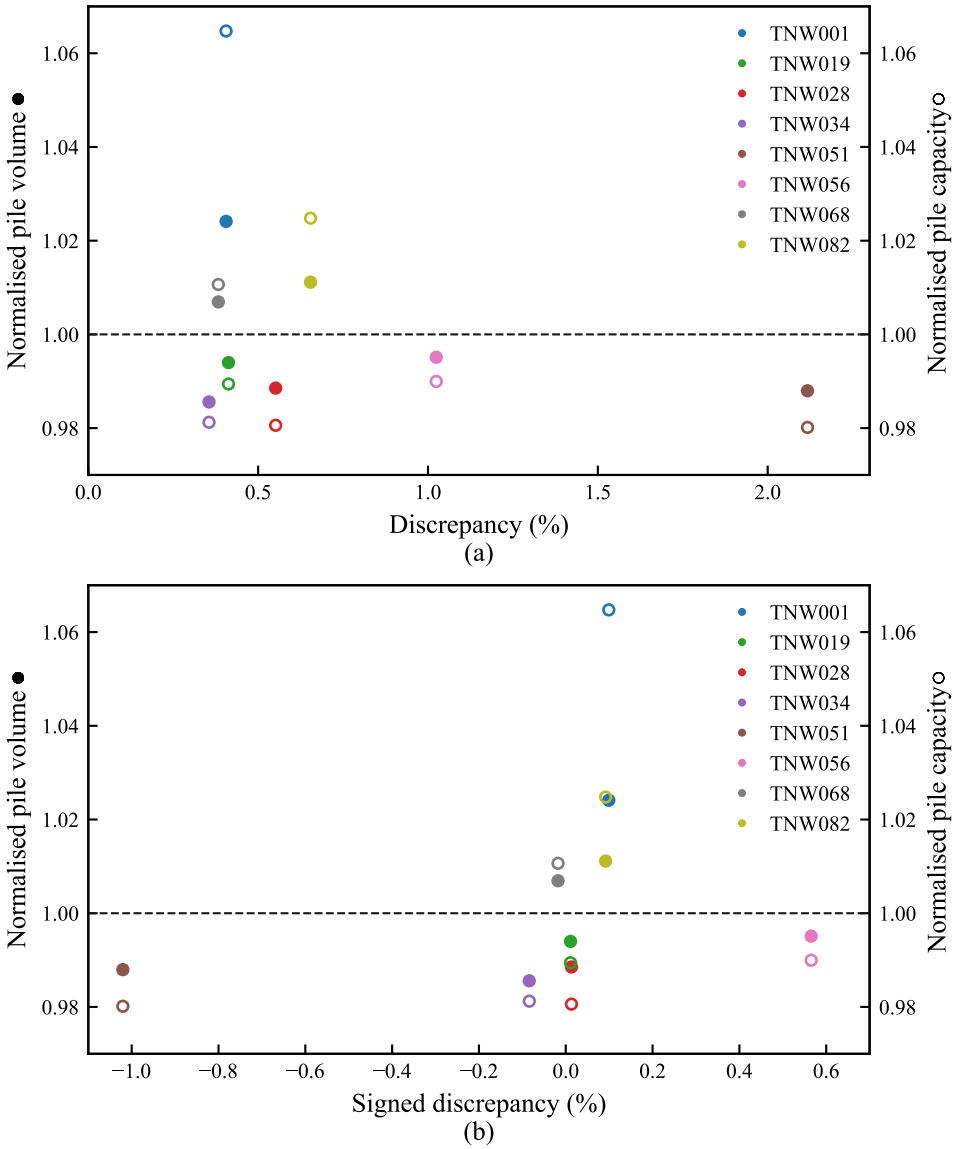

FIGURE 4.7: Variation in predicted optimal pile volume and resulting pile capacity for synthetic CPTs compared to design from in situ CPT, presented in order of cone penetration resistance discrepancy and signed discrepancy

influenced by the lateral resistance profile mobilised along the length of the pile, which is a function of soil type classification (clay or sand) – see Figure 4.4. The distance of certain soil layers from the pivot point also impacts the amount of resistance available, as soil further away has a greater lever arm and hence greater effect on pile resistance. This means, for example, that, while the variation in optimal pile volume predicted by the synthetic CPTs of least and greatest cone penetration resistance discrepancy: TNW034 and TNW051, respectively, vary by a similar amount compared to the design based on their respective in situ CPTs, the effect on pile capacity is lesser for TNW034.

Normalised pile volume and capacity is also plotted with signed discrepancy in Figure 4.7(b), to take into consideration whether the corrected cone penetration resistance

of the synthetic CPT over or underpredicts that of the in situ. Most CPTs are clustered around a signed discrepancy of 0 %, but the two extremes both result in underpredicted pile dimensions. This implies the over or underprediction of pile design cannot be attributed to the sign of the discrepancy measure. Furthermore, this clustering about 0 % suggests that, for the selected CPTs, the double averaging interval method of artificially reducing the resolution of the in situ CPTs corresponds well to the synthetic profiles.

4.6.4 Effect of incorrect soil type

Rearranging the ordering of the TNW CPTs plotted in Figure 4.7 so that they are ranked according to incorrect soil type, rather than cone penetration resistance discrepancy between the in situ and synthetic CPT profiles, generates the plot in Figure 4.8(a). The evidence of a trend in the data has become more pronounced, as both normalised pile volume and capacity tend to increase with increasing incorrect soil type. For the four CPTs with an incorrect soil type of less than 5 %, predicted pile volume under the synthetic CPT is very close to that under the in situ CPT, but is always less. This implies that the these synthetic profiles have very slightly overpredicted the strength of the soil. At larger proportions of incorrect soil type, greater than 5 %, predicted pile volume exceeds that of the actual design, firstly by only 1 % but then in increasing amounts. Whilst predicted capacity follows the same trajectory as predicted volume, the change in volume is amplified in the capacity reading. Therefore, reductions in pile volume result in piles of smaller capacity, whereas increases in pile volume lead to increasingly greater pile capacity. The exception to the trend, is TNW028, as even the excessive overprediction of dimensions for TNW015 occur in line with it having the largest proportion of incorrect soil type. The decrease in both pile volume and capacity for TNW028 is representative of those CPTs that almost have no incorrect soil types in their profiles.

The effect of soil type classification on normalised pile volume and capacity can be incorporated through the signed discrepancy between the synthetic and in situ ultimate lateral resistance profiles. This has been plotted in Figure 4.8(b). Both normalised pile volume and capacity are overpredicted for negative signed discrepancies, but by smaller amounts as the signed discrepancy approaches 0 %. This downward trend continues for positive signed discrepancies, which result in underpredicted normalised pile volume and capacity. Therefore, a pile could be predicted to be either under or overdesigned depending on the signed discrepancy between the ultimate lateral resistance profiles. However, errors from misclassifying soil type have already been introduced into the analysis, further highlighting the importance of correctly identifying the soil before applying the corresponding lateral resistance equation.

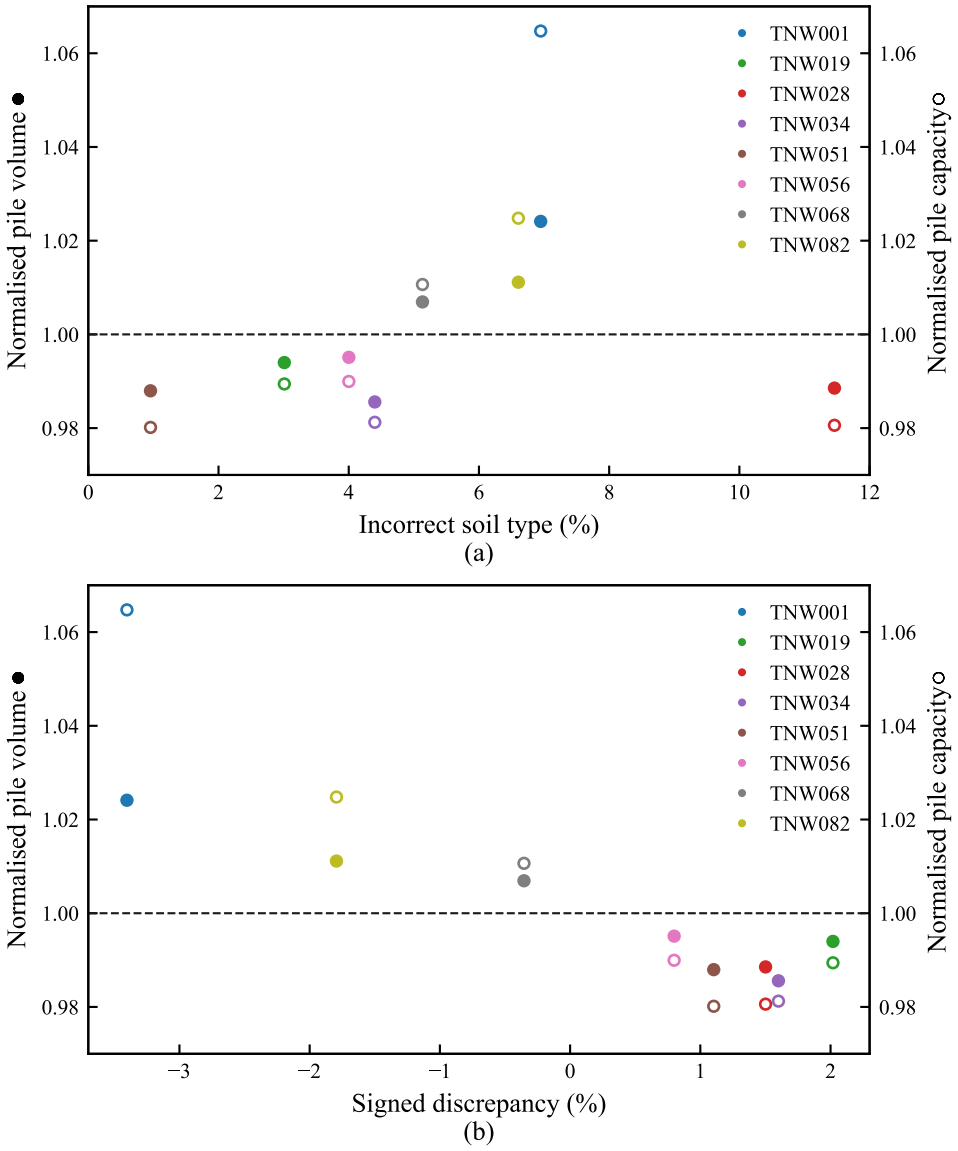

FIGURE 4.8: Variation in predicted optimal pile volume and resulting pile capacity for synthetic CPTs compared to design from in situ CPT, presented in order of incorrect soil type and ultimate lateral resistance signed discrepancy

4.6.5 Summary

This work has shown for the conditions at the TNW site and with the synthetic CPT profiles that were obtained, for pile design under ULS lateral loading, predicted optimal pile volume is within 3 % of the design based on in situ geotechnical CPTs. The resulting capacity from installing the piles designed with synthetic CPTs in the real site conditions is within 7 % of the required design capacity. Pile volume and capacity tend to increase with the proportion of incorrect soil type in the synthetic profile. It is possible that with different seabed conditions, synthetic CPT algorithms, and foundation or anchor types, outcomes may differ, and further research is required. Nonetheless,

this study demonstrates promising insights into the effect of lower vertical resolution of synthetic CPTs on design outcomes.

4.7 Methodology: Predicting lateral deflections

The workflow of the method developed for this study consists of six main steps. Once the in situ geotechnical and synthetic CPT data has been acquired for a selected location (Section 4.7.1), the CPT data is processed in line with conventional geotechnical practice (Section 4.7.1.1). Each depth corresponding to a data point is classified as either clay or sand (Section 4.7.2) and necessary soil parameters are derived (Section 4.7.3). The corresponding soil reaction curves for either clay or sand are implemented (Section 4.7.4) for two pile design methods: CPT-based (Section 4.7.4.1) and PISA (Section 4.7.4.2). A finite element analysis is performed (Section 4.7.5) for a specified applied load (Section 4.7.6) from which pile deflections can be obtained.

4.7.1 Step 1: Acquire in situ and synthetic CPT data

Acquire in situ cone penetration resistance, sleeve friction and pore water pressure data, at near constant increments of depth, starting at the seafloor and terminating at some depth below the seabed. Seabed conditions can affect the drive rate, resulting in depth increments not necessarily being at exact regular intervals, in which case raw data should be interpolated to ensure that each data point corresponds to an exact interval. Soil unit weight to calculate the vertical stress profile, and the net cone area ratio must also be known for the corrections to the in situ geotechnical raw data applied in Section 4.7.1.1.

4.7.1.1 Step 1(a): Process in situ and synthetic CPT data

Adjust in situ measured cone penetration resistance with pore water pressure, and overburden corrections for both in situ and synthetic data (Section 2.4.1). Calculate in situ corrected cone penetration resistance (q_t) and correct for overburden through Equations 2.1 (reproduced as Equation 4.1) (Robertson, 1990) and 2.2 (reproduced as Equation 4.2) (Robertson, 1990; Randolph and Gourvenec, 2011), respectively.

$$q_t = q_c + u_2(1 - \alpha) \tag{4.1}$$

where q_c is measured cone penetration resistance (MPa), u_2 is pore water pressure acting on the shoulder of the cone (MPa) and α is the net area ratio.

$$q_{net} = q_t - \sigma_v \tag{4.2}$$

where q_t is corrected cone penetration resistance (MPa) as given by Equation 2.1 (reproduced as Equation 4.1), and σ_v is the in situ vertical total stress (MPa), given by Equation 2.3 (reproduced as Equation 4.3):

$$\sigma_v = \gamma z \tag{4.3}$$

where γ is soil unit weight (kN/m^3) and z is depth below seafloor (m).

Pore pressure correction for in situ measured cone penetration resistance is only necessary for clays, as opposed to sands, but for simplicity, the correction was applied to all readings regardless of soil classification. As expected, the correction was trivial for cone penetration resistance readings in sandy sediments. The synthetic cone penetration resistance does not need to be corrected for the pore water pressure because this physical aspect is not present in the geophysical data.

4.7.2 Step 2: Classify soil type

Assign a soil type to each of the data points using the Soil Behaviour Type Index (Ic) through Equation 2.10 (reproduced as Equation 4.4) (Robertson and Wride, 1998) in order to apply the appropriate ultimate lateral resistance equation in Section 3.4.3. For this work, a simplistic approach was taken in which the soil classification was binary and defined as either clay or sand. Soils with an index of less than 2.6 were classified as sand, while higher values were classified as clay (Robertson and Cabal, 2015).

$$I_c = \left((3.47 - \log Q_t)^2 + (\log F_r + 1.22)^2 \right)^{0.5} \tag{4.4}$$

where Q_t is normalised cone resistance and F_r is normalised friction ratio, defined by normalising net cone resistance by vertical effective stress (Equation 2.5 (reproduced as Equation 4.5)), and friction ratio by net cone resistance (Equation 2.7 (reproduced as Equation 4.7)):

$$Q_t = \frac{q_{net}}{\sigma'_v} \tag{4.5}$$

where q_{net} is net cone penetration resistance (MPa), as given by Equation 2.2 (reproduced as Equation 4.2), and σ'_v is in situ vertical effective stress (MPa), found with Equation 2.6 (reproduced as Equation 4.6):

$$\sigma'_v = \sigma_v - u \tag{4.6}$$

where σ_v is in situ vertical total stress (MPa), as given by Equation 2.3 (reproduced as Equation 4.3), and u is the in situ pore water pressure at depth z below seafloor (m),

given by u_2. Normalised friction ratio (expressed as a percentage):

$$F_r = \frac{f_s}{q_{net}} \tag{4.7}$$

where f_s is sleeve friction (MPa) and q_{net} is net cone penetration resistance (MPa).

4.7.3 Step 3: Obtain soil parameters

Calculate necessary soil parameters for use in pile design methods, such as PISA in Section 4.7.4.2, from the CPT data. In this work, the following parameters were calculated: undrained shear strength (s_u) in clays (Equation 2.11 (reproduced as Equation 4.8)), relative density (D_r) in sands (Equation 2.12 (reproduced as Equation 4.9)), and small strain stiffness (G_0) in both clays (Equation 2.14 (reproduced as Equation 4.10)) and sands (Equation 2.15 (reproduced as Equation 4.11)).

$$s_u = \frac{q_t - \sigma_v}{N_{kt}} \tag{4.8}$$

where q_t is corrected cone penetration resistance (kPa) as given by Equation 2.1 (reproduced as Equation 4.1), σ_v is the in situ vertical total stress (kPa), and N_{kt} is a cone factor. For the lightly overconsolidated clays at the TNW site, a value of 13.5 was assummed (Randolph and Gourvenec, 2011). The numerator of this equation can be simplified to the net cone penetration resistance, in accordance with Equation 2.2 (reproduced as Equation 4.2).

$$D_r = D_c + E_c log\left(\frac{q_c}{{\sigma'_v}^{0.5}}\right) \tag{4.9}$$

where D_c and E_c are constants, q_c is measured cone penetration resistance (kPa) since correction for pore water pressure is unnecessary in sands (see Section 2.4.1), and σ'_v is the in situ vertical effective stress (kPa). For sands of average compressibility, values of -1.21 and 0.584 can be assumed, respectively (Knappett and Craig, 2020).

For clay:

$$G_0 = 2.78(q_t)^{1.335} \tag{4.10}$$

where q_t is corrected cone penetration resistance (kPa).

For sand:

$$G_0 = 1634(q_c)^{0.25}(\sigma'_v)^{0.375} \tag{4.11}$$

where q_c is measured cone penetration resistance (kPa) since correction for pore water pressure is unnecessary in sands (see Section 2.4.1), and σ_v is vertical effective stress (kPa).

4.7.4 Step 4: Define soil reaction curves

In this work, two families of soil reaction curves were compared, the CPT-based method (Truong and Lehane, 2014; Suryasentana and Lehane, 2014) in Section 4.7.4.1, which combines $p-y$ curves for both clay and sand calibrated against CPT parameters; and the PISA method (Burd et al., 2020; Byrne et al., 2020) in Section 4.7.4.2, which employs four soil reaction curves calibrated against finite element (FE) analysis. These resulting $p-y$, $m-\psi$ and base curves are functions of the soil parameters obtained in Section 4.7.3.

4.7.4.1 Step 4(a): CPT-based method

The CPT-based $p-y$ curves implemented in this work are Equation 2.17 (reproduced as Equation 4.12) for clay (Truong and Lehane, 2014) and Equation 2.18 (reproduced as Equation 4.14) for sand (Suryasentana and Lehane, 2014):

$$\frac{p}{p_u} = \begin{cases} \tanh\left((0.26I_r + 3.98)\left(\frac{y}{D}\right)^{0.85}\left(\frac{z}{D}\right)^{-0.5}\right) & \text{for } \frac{z}{D} < 3 \\ \tanh\left((0.15I_r + 2.3)\left(\frac{y}{D}\right)^{0.85}\right) & \text{for } \frac{z}{D} \geq 3 \end{cases} \tag{4.12}$$

where I_r is rigidity index, y is lateral displacement of pile at seafloor (m), D is pile diameter (m), z is depth below seafloor (m), and p_u is ultimate lateral resistance (MPa) expressed through Equation 2.16 (reproduced as Equation 4.13):

$$p_u = Dq_{net}\left(\left(\frac{3}{4.7 + 1.6\ln I_r}\right) + (1.5 - 0.14\ln I_r)\tanh\left(\frac{0.65\,z}{D}\right)\right) \tag{4.13}$$

where q_{net} is net cone penetration resistance (MPa) as given by Equation 2.2 (reproduced as Equation 4.2).

$$p = 2.4\,\sigma'_v\,D\left(\frac{q_c}{\sigma'_v}\right)^{0.67}\left(\frac{z}{D}\right)^{0.75}\left\{1 - \exp\left[-6.2\left(\frac{z}{D}\right)^{-1.2}\left(\frac{y}{D}\right)^{0.89}\right]\right\} \tag{4.14}$$

where σ'_v is vertical effective stress (kPa), D is pile diameter (m), q_c is measured cone penetration resistance (MPa) since correction for pore water pressure is unnecessary in sands (see Section 2.4.1), z is depth below seafloor (m), and y is lateral displacement of pile at seafloor (m).

4.7.4.2 Step 4(b): PISA method

In this work, the rule-based method has been employed with the normalised soil reaction curves calibrated against Cowden Clay and Dunkirk Sand. In practice, this method

is best calibrated for the soil conditions found on the design site by extracting relevant data from three-dimensional FE analyses conducted for a range of pile dimensions and soil properties. However, for the purposes of assessing the sensitivity of the analysis method to employing synthetic CPTs, using the existing curves as part of a rule-based approach is suitable.

All four normalised soil reactions take the generalised form (Burd et al., 2020; Byrne et al., 2020):

$$\frac{\bar{y}}{\bar{y}_u} = \begin{cases} \dfrac{2c}{-b + \sqrt{b^2 - 4ac}}; & \bar{x} \leq \bar{x}_u \\ 1; & \bar{x} > \bar{x}_u \end{cases} \tag{4.15}$$

where a, b and c are parameters obtained through Equations 2.27 (reproduced as Equation 4.16), 2.28 (reproduced as Equation 4.17) and 2.29 (reproduced as Equation 4.18), respectively (Burd et al., 2020; Byrne et al., 2020).

$$a = 1 - 2n \tag{4.16}$$

$$b = 2n\frac{\bar{x}}{\bar{x}_u} - (1 - n)\left(1 + \frac{\bar{x}k}{\bar{y}_u}\right) \tag{4.17}$$

$$c = \frac{\overline{x}k}{\overline{y}_u}(1 - n) - n\frac{\overline{x}^2}{\overline{x}_u^2} \tag{4.18}$$

The curve parameters $\overline{x}_u$, $\overline{y}_u$, k and n for each soil reaction curve are obtained in dimensionless form from Tables 2.2 and 2.3 for clays and sands, respectively. These are related to the soil properties obtained in Section 4.7.3 using the relationships given in Table 2.1.

4.7.5 Step 5: Build one-dimensional finite element (FE) model

To create an FE model, the problem must be split into elements. In general, this is done in consideration of identified soil layers. In this work, in order to reduce the impact of resolution on the results, elements with a constant element size of 0.1 m were chosen, each consisting of five gauss points. This correlates to having a gauss point, at which the pile design calculation is carried out, at least every 0.027 m. In comparison, the full resolution of the CPTs at the TNW site is 0.02 m, therefore the distance between gauss points is generally smaller than this full resolution, enabling the interval between gauss points to be small enough that there is always at least a CPT reading, but not too small that computation time is significantly large.

Each element consisted of a Timoshenko beam element alongside a soil element describing the soil reaction curves applied. For the base curves in the PISA model, an additional 'lumped spring' element was added at the pile base to model both base curves.

The values of the soil reaction curve and soil parameters were linearly interpolated at each gauss point using the values calculated at each depth of the CPT.

It is necessary for each element to consist of the same soil type because of the binary nature of the pile design equations into either clay or sand. This was achieved by taking the soil type that most data points within the CPT profile of an element were assigned to. However, in the case that there were an even number of data points which were equally split between the two, the average of the soil classification indices was obtained and the soil of the element assigned based on the value in relation to the 2.6 boundary between clays and sand (see Section 4.7.2).

The larger data intervals between readings of the synthetic CPT profiles meant that there were occasions where an element had no data points. To allow for such an occurrence, the element was assigned the properties of the closest reading, which could be either in the previous or the following element. This ensured that every element had suitable soil parameters in order to perform the analysis. On the other hand, where elements only consisted of a single data point, soil type was straightforward to assign to the whole element, compared to that involved for the in situ CPTs.

Above the ground surface, a single Timoshenko beam element was used with the same parameters as the pile to model the load eccentricity.

4.7.6 Step 6: Apply load and extract deflection

In this work, a total load of 48 MN was applied over 100 steps. This is to incorporate the factored load from the ULS capacity design based on a deflection of one pile diameter into the model. However, the deflection is extracted for the unfactored load of 16 MN, in accordance with serviceability limit state (SLS) design. Having 100 steps ensures that the load is increased frequently enough to capture smooth behaviour of the $p - y$ curves whilst not requiring excessive computational time for the analysis to be performed.

4.8 Results

The FE model was run for the nine selected CPT locations within the TNW wind farm zone in Figure 4.1 according to the steps detailed in Section 4.7 under three different scenarios. This included various combinations of the ULS optimised pile dimensions from Section 4.6, as derived from either the corresponding in situ geotechnical or synthetic CPT profile, and assessing the predicted pile deflection within either the in situ geotechnical or synthetic soil. The three different pile dimensions and soil combinations implemented were as follows:

- In situ geotechnical pile dimensions in in situ geotechnical CPT soil (*gDgCPT*)
- Synthetic pile dimensions in in situ geotechnical CPT soil (*sDgCPT*)
- Synthetic pile dimensions in synthetic CPT soil (*sDsCPT*)

4.8.1 Response at ground surface

The two output parameters of ground displacement and rotation have been plotted in Figure 4.9 with the discrepancy measure of cone penetration resistance that was introduced in Section 4.3. It is important to note the way in which these parameters have been normalised as each combination of cases portrays a different narrative. Here, the predicted displacement, at ground level, of a pile with dimensions from the synthetic CPT (*sDgCPT*) inserted in the in situ geotechnical soil has been divided by that of a pile from the in situ geotechnical CPT in the in situ soil (*gDgCPT*). The same is true for the ground rotation. Therefore, this plot is a measure of how much the synthetic pile dimensions affect the predicted ground deflection and rotation. Another useful normalisation configuration is that of different soils, i.e., one of the in situ and the other the synthetic, which is compared in Section 4.8.4. At this point in the analysis, Figure 4.9 demonstrates that plotting displacement or rotation does not impact the trend in the data, just that ground rotation has a slightly greater magnitude. For this reason, only ground rotation has been included on the y-axis of subsequent plots, avoiding excessive data markers when it is known that displacement follows the same findings as rotation.

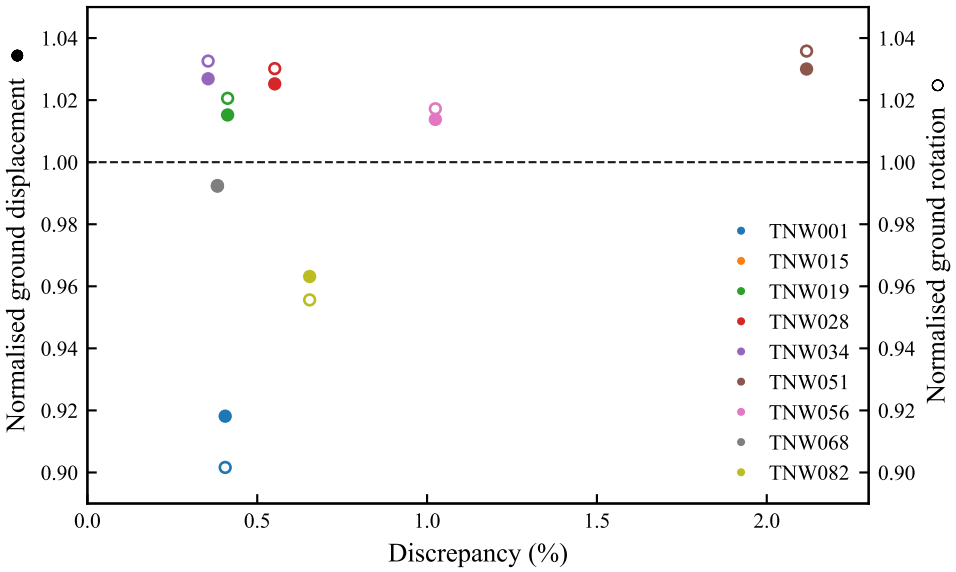

FIGURE 4.9: Comparison of normalised ground displacements and rotations with discrepancy

4.8.2 Effect of method type

The prediction of deflections for the given optimised pile dimensions found for ULS design in Section 4.6, was undertaken according to both a CPT-based method and the PISA method (see Sections 4.7.4.1 and 4.7.4.2, respectively). This enabled a comparison between the different methods to determine whether they are in agreement with each other. The predicted ground rotation of a pile of synthetic dimensions compared to one of in situ dimensions, inserted in the in situ geotechnical soil (*sDgCPT*/*gDgCPT* normalisation) varies within a few percent between the CPT-based and PISA methods. The magnitude of the change in ground rotation under the PISA method tends to be larger than that under the CPT-based method, but the overall consistency between these two methods means only the CPT-based method will be plotted subsequently, for the same reason as omitting deflection.

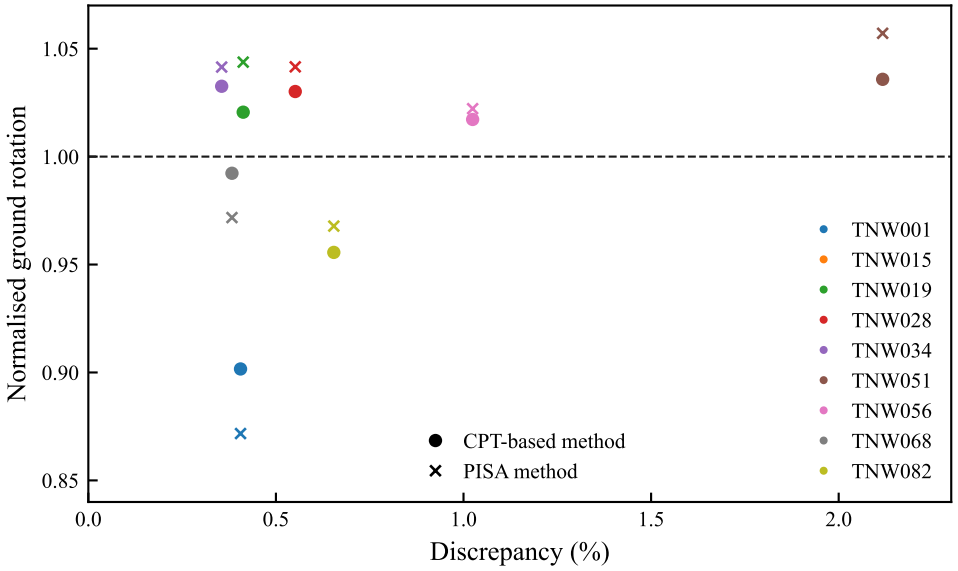

FIGURE 4.10: Comparison of normalised ground rotations under CPT-based and PISA design methods with discrepancy

4.8.3 Effect of using synthetic dimensions

The actual effect of the scenario *sDgCPT*/*gDgCPT* on discrepancy, which was used for the comparisons in Sections 4.8.1 and 4.8.2 can now be evaluated directly through Figure 4.11. This involves determination of the predicted ground rotation through the CPT-based method when a pile of synthetic dimensions is installed in the in situ geotechnical soil and an unfactored lateral load of 16 *MN* applied, normalised by the predicted ground rotation for a pile with in situ dimensions in the in situ soil. Therefore, for the CPTs where ground rotation is greater than one, the pile of synthetic dimensions is rotating more than the in situ dimensions pile. This is because the synthetic dimensions derived by the synthetic CPT for ULS design, for these CPTs: TNW019,

TNW028, TNW034, TNW051, and TNW056, have been underpredicted. To summarise, a pile of smaller volume (i.e., dimensions) will experience greater deflection for a given lateral load than a larger one, since increases in volume have been governed by increasing pile length, rather than diameter. As a result, the slenderness (L/D) of a smaller volume pile is generally greater.

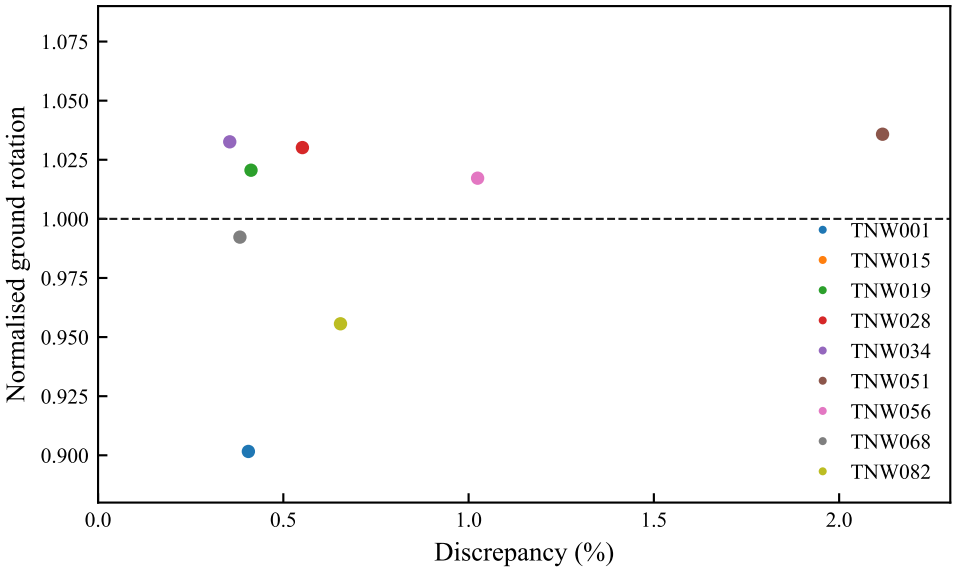

FIGURE 4.11: Normalised ground rotations under CPT-based design methods with discrepancy

On the other hand, the CPTs that have a normalised ground rotation of less than one in Figure 4.11 (TNW001, TNW068, TNW082, as well as TNW015) have synthetic piles of overpredicted dimensions so undergo less rotation than their corresponding in situ piles. Therefore, the predicted deflections of the optimised synthetic piles designed in Section 4.6, according to ULS design, can be either over or underpredicted, compared to the in situ geotechnical piles. However, this is the opposite of what was observed in normalised pile volume in Figure 4.7. For example, the increase in pile volume of TNW001 in Figure 4.7, demonstrating the synthetic pile has overpredicted the dimensions of the in situ pile, is accompanied by a decrease in predicted ground rotation of the synthetic pile in Figure 4.11, underpredicting the rotation of the in situ pile. It should be noted that the amount of overprediction in pile volume does not necessarily correspond to the amount of underprediction in pile rotation, and vice versa.

The ground rotations plotted in Figure 4.11 have been reordered according to the incorrect soil type, as opposed to cone penetration resistance which again did not demonstrate any clear trend, as was discussed in Section 4.6.3. This can be seen in Figure 4.12, where normalised ground rotation reduces at an increasing rate as the proportion of incorrect soil type increases. This is in agreement with the finding that the change in synthetic pile volume is inversely reflected in the change in synthetic pile rotation, since the opposite was observed in Figure 4.8. Both Figures 4.8 and 4.12 demonstrate

that incorrect soil type is a more suitable measure of ranking the CPTs as it has a greater impact on the effect of the synthetic pile dimensions in design.

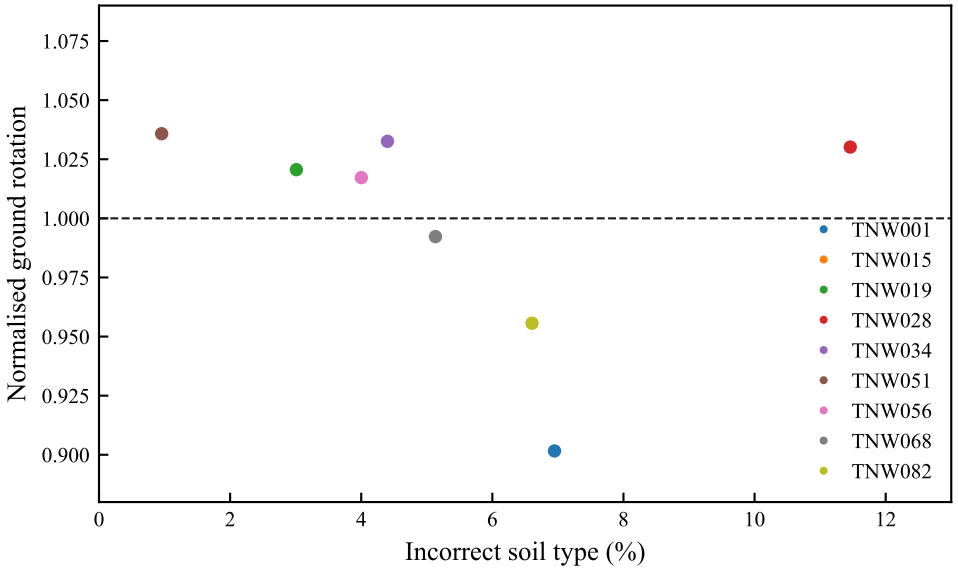

FIGURE 4.12: Normalised ground rotations under CPT-based design methods with incorrect soil type

Overall, the effect of installing a pile of synthetic dimensions into the in situ soil is minimal, with predicted pile ground rotations within 5 % of those for a pile of in situ dimensions, for seven of the nine CPTs, and within 9 % for eight.

4.8.4 Effect of using synthetic CPT

Whilst Section 4.8.3 looked at the effect of using synthetic pile dimensions in design, this Section moves on to address another normalisation scenario that focuses on the effect of using the synthetic CPT profile on predicted deflections. The pile of synthetic dimensions is inserted in the in situ geotechnical soil but is then divided by the same synthetic dimensions pile installed in the synthetic soil (*sDgCPT*/*sDsCPT*). Plotting first with discrepancy of the cone penetration resistance profiles produces Figure 4.13. The CPTs remain on the same side of the horizontal normalised ground rotation line of one as they did in Figure 4.11 for the *sDgCPT*/*gDgCPT* normalisation, but not by the same magnitude. TNW028 has the greatest shift from just over a normalised ground rotation of 1.025 in Figure 4.11 to a little over 1.075 in Figure 4.13. A value larger than one indicates that the pile of synthetic dimensions has deflected by a larger amount in the in situ soil than in the synthetic soil. Therefore, the strength of the soil from the synthetic CPT profile is greater than that of the in situ soil, so the overall result is that the synthetic profile overpredicts the actual soil conditions. For the CPTs that have a normalised ground rotation of less than one, the opposite is true, i.e., the synthetic CPT has underpredicted the in situ soil strength.

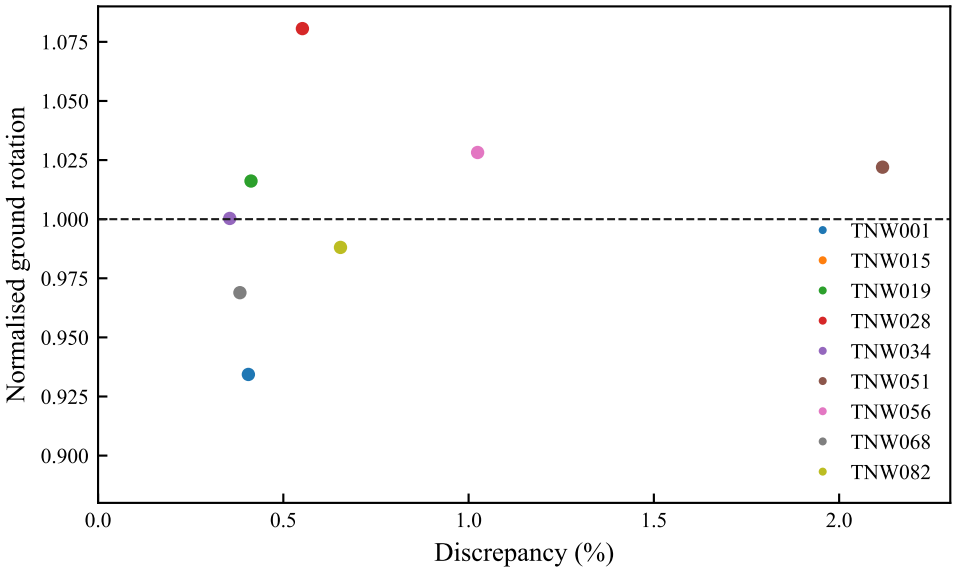

FIGURE 4.13: Effect of using synthetic CPT on normalised ground rotations with discrepancy

The predicted ground rotation for TNW034 is almost identical for the synthetic pile in both the in situ soil and synthetic soil, since the marker lies on the horizontal line of a normalisation of one. This implies that the synthetic CPT profile must accurately reflect that of the in situ geotechnical profile. As was portrayed in Figure 4.3 and is reiterated in Figure 4.13 by the TNW034 marker being plotted the furthest left, TNW034 exhibits the least discrepancy between its synthetic and in situ cone penetration resistance profiles: 0.4 %. The sleeve friction synthetic and in situ profiles for TNW034 in Figure 4.3 also demonstrate a close match with a discrepancy of 1.3 %, even though it is not quite the smallest observed.

Despite the CPT with the least discrepancy between the in situ and synthetic profiles showing no change in predicted normalised ground rotation, the other CPTs do not follow such a trend, nor is there a correlation linking the two measures. Figure 4.14 then plots the CPT normalised ground rotation in order of proportion of incorrect soil type. Ground rotation tends to decrease as the proportion of incorrect soil type in the synthetic CPT profile increases, although whether this is linear or at a similarly increasing rate to the curve in Figure 4.12, is less apparent.

Overall, the effect of using a synthetic CPT profile in design to predict lateral deflection, as opposed to an actual in situ CPT profile, is not significant, since variations in predicted ground rotations are very small: well within 10 % for eight of the nine CPTs tested.

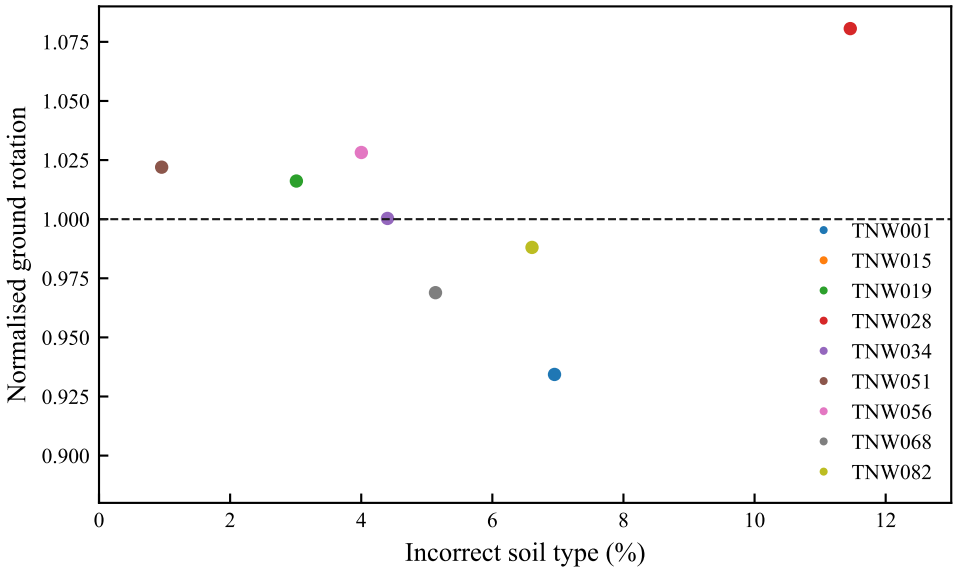

FIGURE 4.14: Effect of using synthetic CPT on normalised ground rotations with incorrect soil type

4.9 Summary

This chapter has built upon the work carried out in Chapter 3 by extending the analysis of the effect of reduced resolution CPT profiles on pile design, to that of synthetic CPTs. The availability of co-located geotechnical in situ CPT profiles to those of synthetic profiles at the TNW site enabled an extensive comparison to be performed, from discrepancies in their profiles to the effect on minimum pile dimensions of monopiles for offshore wind turbines, in accordance with **RO2**.

Synthetic CPTs demonstrated good prediction of the in situ geotechnical cone penetration resistance profiles, generally within 1 %, but with a maximum discrepancy of just over 2 % (Figure 4.3). The synthetic CPT profiles were able to capture the trends of the in situ CPTs, although lacked the extent of the vertical resolution, having an estimated resolution of 1 m, as opposed to the 0.02 m resolution of the in situ CPTs. In terms of ability to predict soil type, accurate soil classification was achieved with the synthetic CPTs, with the percentage of incorrect soil for the majority of CPTs being less than 10 %. However, no correlation between the cone penetration discrepancy and the proportion of incorrect soil was evident.

Similar to the the effect of artificially reduced resolution CPT profiles on optimal pile design at the Burbo Bank Extension wind farm site in Chapter 3, artificially reducing the in situ CPT profile resolution of the selected CPTs at the TNW offshore wind farm site through the double averaging interval method led to an overall decrease in minimum pile volume (Figure 4.5). In comparison, the synthetic CPTs showed both a decrease and increase in predicted pile volume within 3 % of the in situ design. This

translated to a decreasing trend in pile capacity with artificial reducing resolution (Figure 4.6), although to a greater degree, further emphasising the non one-to-one relationship between pile volume and capacity. Additionally, the synthetic CPTs demonstrated either an increase or decrease in pile capacity, in correlation to that of pile volume, but to a larger extent: within 7 %.

An important finding was the fact that pile volume, and therefore capacity, exhibited a positive correlation with the percentage of incorrect soil type (Figure 4.8), rather than the discrepancy of cone penetration resistance (Figure 4.7) between the in situ and synthetic CPTs. That is, pile volume and capacity were predicted to increase with the proportion of incorrect soil type in the synthetic profile.

As an ULS case scenario has been implemented to derive minimum pile dimensions, it was also insightful to assess the influence of synthetic CPTs in terms of SLS design. Firstly, the expected change in deformations due to the change in pile dimensions resulting from ULS design by synthetic CPT was considered. Secondly, the change in predicted deformations when employing either the synthetic or geotechnical CPT was calculated. Deformations were quantified in terms of both ground displacements and rotations, however, little variation was observed between the two. Two different design approaches were also implemented: CPT-based and PISA. While the magnitude of the predicted deformations with each method were different, the results indicated that the use of synthetic CPTs in the calculation method had a similar impact on the predicted SLS behaviour. Therefore, running the analysis for ground rotations under CPT-based design, revealed that in both concepts, variations in predicted rotations remain minimal, well within 10 %, but show an overall decrease as incorrect soil type increases.

It is possible that with different seabed conditions, synthetic CPT algorithms, and foundation or anchor types, outcomes may differ, and further research is required. Nonetheless, this chapter has demonstrated that synthetic CPTs with a certain level of resolution, in this case study 1 m, can be used in the design of offshore wind turbine monopile foundations with little impact on the design outcome, highlighting their potential as an innovative site investigation tool.

Chapter 5

Effect of complexity of CPT profile on design outcome

5.1 Introduction

This chapter applies mathematical complexity measures developed for time series analysis to CPT profiles in an effort to describe the complexity of a CPT profile with a quantitative index. The motivation is to provide guidance on the minimum resolution of a synthetic CPT as a function of the complexity of the real ground profile. Complexity can be measured from different approaches, depending on the specific characteristics of a time series complexity is assessed through. Therefore, a range of methods are implemented in this analysis. These methods are first applied to simplified CPT profiles (Section 5.5) with known levels of complexity to assess the suitability of the complexity measure to soil data, before actual CPTs at the Burbo Bank Extension offshore wind farm site (Section 5.8). A geotechnically informed measure of complexity is derived to provide a benchmark to compare the ability of the mathematical complexity measures in capturing complexity of the soil.

5.2 Methodology: Applying measures of complexity

A range of complexity measures of time series data were selected to cover the different ways in which complexity can be quantified (see Section 2.6.3) but to also be applicable to depth series CPT profiles. In the following sections, a time series, X, can be expressed in the form $X = X_1, X_2, X_3, \ldots, X_n$.

5.2.1 Statistical measures

Statistical measures quantify specific properties of a time series, such as its central tendency, variability, and range. These include the mean (μ) (Equation 5.1), standard deviation (S) (Equation 5.2) and range (R) (Equation 5.3).

$$\mu = \frac{1}{n}\sum_{i=1}^{n} X_i \tag{5.1}$$

$$S = \sqrt{\frac{1}{n}\sum_{i=1}^{n}(X_i - \mu)^2} \tag{5.2}$$

$$R = \max(X_i) \; - \; \min(X_i) \tag{5.3}$$

where n is number of terms in time series and X_i is value in time series at position i for $i = 1, 2, 3, \ldots, n$.

5.2.2 Long-term correlations

5.2.2.1 Rescaled range

The rescaled range (R/S) is based on the concept that the range follows a scaling law (Kristoufek, 2010). It measures the cumulative differences from the mean, divided by the standard deviation for different periods of time. In this way, it can assess the scaling behaviour of a time series in terms of the Hurst exponent, which was introduced in Section 2.6.3.1. Depending on the value of the Hurst exponent, the long-term memory of a time series can be evaluated (Raubitzek and Neubauer, 2021). A Hurst exponent of 0.5 indicates a random system with no memorability or self-similarity. For values greater than 0.5, the time series demonstrates positive correlation (persistence), which means increases are more likely to be followed by increases at all lengths. A time series of negative correlation (anti-persistence), when increases are more likely followed by decreases at all lengths, is given by values of less than 0.5 (Bassingthwaighte and Raymond, 1994). The Hurst exponent is sensitive to the long-range statistical dependence in a signal, enabling the rescaled range analysis to distinguish between time series that are correlated, those that are not, and those that exhibit long-run correlations in random processes (Di Matteo, 2007). R/S has continued to be implemented over the years, providing better results for positively correlated time series, but does tend to overestimate the Hurst exponent. The segment lengths over which the rescaled range are calculated must be chosen carefully to avoid bias. Too small scales mean the standard deviations are based on only a few observations, whilst too large scales can cause outliers or extreme values not to be averaged out (Kristoufek, 2010).

1. Let a value in the time series of length n be defined as X_i where i denotes the position in the times series and has values $1 \leq i \leq n$.

2. Select a range of segment lengths to be tested. For each segment length, n_τ,split the time series into B $(= n/n_\tau)$ number of non-overlapping segments of length n_τ. Each segment is represented by τ_k where k indicates the segment number and has values $1 \leq k \leq B$. The values of the time series that are included in each segment can be expressed according to their original position i in the time series and the specified segment length: $\tau_k = \{X_i....\}$ for values $(k-1)n_\tau + 1 \leq i \leq kn_\tau$

   For each segment τ_k:

   (a) Calculate the mean μ_k using Equation 5.1 for the segment length n_τ.

   (b) Calculate the standard deviation S_k using Equation 5.2 for the segment length n_τ and segment mean μ_k.

   (c) Find the difference between each value in the segment X_i and the mean of its segment μ_k. The resulting values in this new series can be labelled Y_i:

   $$Y_i = X_i - \mu_k \tag{5.4}$$

   (d) Calculate the cumulative sum of the differences found in the previous step, calling the values in this new series Z_i starting at $i_{0,k} = (k-1)n_\tau + 1$:

   $$Z_i = \sum_{i=i_{0,k}}^{kn_\tau} Y_i \tag{5.5}$$

   (e) Calculate the range R_k using Equation 5.3 for the values Z_i.

   (f) Divide the range R_k by the standard deviation S_k to obtain the rescaled range R_k/S_k.

3. For each segment length, n_τ, calculate the average rescaled range over all the segments as follows:

   $$\frac{R}{S} = \frac{1}{B}\sum_{k=1}^{B}\frac{R_k}{S_k} \tag{5.6}$$

   This uses the same calculation in Equation 5.1 but has been repeated to demonstrate the different parameters implemented.

4. Fit (using least-squares regression) a power-law relationship between the average rescaled ranges and the segment lengths:

   $$\frac{R}{S} \propto n_\tau^{H_e} \tag{5.7}$$

H_e is the Hurst exponent.

5. Determine the value of the Hurst exponent by taking logarithms of both sides in Equation 5.7 and using linear regression to find the slope of plot:

$$\log\left(\frac{R}{S}\right) = H_e \log n_\tau \tag{5.8}$$

In this work, a logarithmically spaced set of segment sizes was selected, with minimum size of four and maximum size equal to the integer when the number of data points in the time series is divided by four (Alvarez-Ramirez et al., 2009; Peng et al., 1994). At segment sizes of less than four, detrending no longer works (Hardstone et al., 2012), whereas, segment sizes greater than the maximum value of $n/4$ are statistically unreliable because the number of segments to average over becomes too few (Kantelhardt et al., 2002). Using a logarithmic scale gives equal weight to all time scales when plotting the log-log plot of these measures and fitting the line through linear regression (Hardstone et al., 2012).

5.2.2.2 Detrended fluctuation analysis

Detrended fluctuation analysis (*DFA*) enables the detection of long-range correlations of the intrinsic structure within a patchy system, without the detection of false long-range correlations (Kantelhardt et al., 2001; Peng et al., 1994). In this context, patchiness refers to the irregular clustering of patterns in a time series, which can often be mistaken for long-range correlations (Peng et al., 1994). *DFA* prevents the detection of false long-range correlations by implementing a detrending approach. This involves locally fitting a polynomial to segments of the time series and then subtracting this polynomial (Bryce and Sprague, 2012). The polynomial used was originally linear (Peng et al., 1994) and that is still often the case (Bryce and Sprague, 2012), however, higher order quadratic and cubic polynomials can be used (Kantelhardt et al., 2001). *DFA* determines long-range correlations through the *DFA* exponent (Hardstone et al., 2012). This is similar to the Hurst exponent, calculated through *R/S* analysis in Section 5.2.2.1, for stationary time series but is able to accommodate nonstationary time series and therefore can be considered an improvement (Bryce and Sprague, 2012).

1. Let a value in the time series of length n be defined as X_i where i denotes the position in the times series and has values $1 \leq i \leq n$.

2. Calculate the mean μ of the time series using Equation 5.1.

3. Calculate the cumulative sum of the time series and call it Y_i:

$$Y_i = \sum_{i=0}^{n} (X_i - \mu) \tag{5.9}$$

This removes the global trend from the time series (Hardstone et al., 2012).

4. Select a range of segment lengths to be tested. For each segment length, n_τ, split the time series into B ($= n/n_\tau$) number of non-overlapping segments of length n_τ. Each segment is represented by τ_k where k indicates the segment number and has values $1 \leq k \leq B$. The values of the time series that are included in each segment can be expressed according to their original position i in the time series Y_i and the specified segment length: $\tau_k = \{Y_i ....\}$ for values $(k-1)n_\tau + 1 \leq i \leq kn_\tau$

   For each segment τ_k:

   (a) Fit a polynomial P_k to the segment trend.

   (b) Subtract the fitted polynomial from the segment to calculate the detrended fluctuation of the segment W_k.

$$W_k = \tau_k - P_k \tag{5.10}$$

   (c) Calculate the standard deviation of the detrended segment using Equation 5.11. This is the fluctuation function of the segment F_k.

$$F_k = \sqrt{\frac{1}{n_\tau} \sum_{k=1}^{B} W_k^2} \tag{5.11}$$

5. Calculate the mean of all segment standard deviations using Equation 5.12 This is the average fluctuation function F.

$$F = \frac{1}{B} \sum_{k=1}^{B} F_k \tag{5.12}$$

6. Repeat for different segment lengths.

7. Fit (using least-squares regression) a power-law relationship between the fluctuation functions and the segment lengths:

$$F \propto n_\tau^{\alpha_{DFA}} \tag{5.13}$$

α_{DFA} is the *DFA* exponent.

8. Determine the value of the *DFA* exponent by taking logarithms of both sides in Equation 5.13 and using linear regression to find the slope of plot:

$$\log(F) = \alpha_{DFA} \log n_\tau \tag{5.14}$$

In this work, a logarithmically spaced set of segment sizes was selected, with minimum size of four and maximum size equal to the integer when the number of data points in the time series is divided by four (Alvarez-Ramirez et al., 2009; Peng et al., 1994). This is the same set of segment sizes used in the *R/S* analysis in Section 5.2.2.1. An additional input parameter for *DFA* is the order of the detrending polynomial. In this work, the simplest case of a linear order was selected.

5.2.2.3 Multifractal detrended fluctuation analysis

Multifractal detrended fluctuation analysis (*MF-DFA*) is based on *DFA*, as described in Section 5.2.2.2. It takes *DFA* further by calculating the fluctuation function for different orders so it can assess the extent to which a certain segment size affects the fluctuations of a time series (Seo et al., 2012). In this way, *MF-DFA* allows for multifractal behaviour. This was introduced in Section 2.6.3.1 and is when the scaling behaviour of a time series cannot be characterised by a single scaling exponent (Ihlen, 2012). *MF-DFA* measures long-range correlations for a range of scaling exponents through the different orders of the fluctuation function. A fluctuation function of order two is equivalent to the *DFA* method. Both negative and positive orders are usually tested to describe the scaling behaviour of segments with small and large fluctuations, respectively (Kantelhardt et al., 2002). In the same way as *R/S* analysis and *DFA*, the *MF-DFA* exponent is a measure of the long-range correlations, but is instead labelled as generalised to allow for the various orders of the fluctuation function. Whilst each value of the generalised *MF-DFA* exponent provides information on the long-range correlations for that order, how the generalised *MF-DFA* exponent varies with order reveals the correlations for small and large fluctuations. If the generalised *MF-DFA* exponent increases with order, large fluctuations demonstrate more long-term persistence than small fluctuations, taking order as a vector so that negative values are smaller. If the time series only demonstrates monofractal behaviour, the generalised *MF-DFA* exponent will not change for different fluctuation function orders (Kantelhardt et al., 2002).

In this work, a single value of the complexity of a CPT profile is desired, therefore, the general exponents acquired through *MF-DFA* are not necessary and the monofractal approach of *DFA* is deemed sufficient.

5.2.3 EntropyHub functions

In order to compare a large range of complexity measures, the python library 'EntropyHub' (Flood, 2024) was employed to implement a number of complexity measures related to entropy. This section details the methods from the EntropyHub library to obtain the complexity of a time series (Flood, 2024). For the purpose of this work, where an initial assessment of the complexity of CPT profiles has been investigated, input parameters besides the time series have been kept at default values.

5.2.3.1 Kolmogorov entropy

Kolmogorov entropy (*K2En*) studies the chaotic behaviour of a system by measuring how quickly information about its state is lost over time (Gao et al., 2013; Grassberger and Procaccia, 1983). Since it is based on chaoticity principles (see Section 2.6.3.2), this measure can be classified under methods derived from nonlinear systems (Tang et al., 2015), however, the fact that it quantifies the rate of information production also aligns it with entropy-based approaches. As such, it has been included within the EntropyHub library (Flood, 2024), highlighting the strong overlap between nonlinear dynamical analysis and entropy-based complexity measures in time series analysis.

K2En estimates how unpredictable a system becomes over time by measuring how quickly nearby states in a time series diverge (Grassberger and Procaccia, 1983). To do this, it reconstructs the system's dynamics using time-delay embedding: a method that creates multi-dimensional vectors from a single observed variable, representing the system's state at different time steps. In the system's phase space, i.e. a mathematical space representing all possible states, two trajectories that start very close together may eventually move apart. *K2En* quantifies the rate at which this divergence occurs, reflecting how rapidly information about the system's initial state is lost and how difficult it becomes to predict its future (Grassberger and Procaccia, 1983). A value of zero indicates a regular system in which future behaviour is predictable. As *K2En* becomes infinitely large, the system is completely random and has no predictability. Between these two extremes, the system is considered to be chaotic, demonstrating dependence on initial conditions whilst still governed by deterministic behaviour.

Compared to other entropy measures, *K2En* is unique in that it focuses on the structure of the system's attractor, which is the set of states the system tends to evolve toward (Grassberger and Procaccia, 1983). It captures how predictability decreases along this attractor, rather than simply measuring randomness or variability. As an attractor invariant, *K2En* reflects a fundamental property of the system's dynamics that remains

consistent regardless of the specific observation method used. By quantifying this divergence, *K2En* provides a practical and theoretically grounded way to assess the complexity and chaoticity of time series data. However, *K2En* can become inaccurate for noisy, short datasets.

5.2.3.2 Approximate entropy

Approximate entropy (*ApEn*) is a statistical tool designed to measure how regular or predictable a time series is (Chen et al., 2009; Delgado-Bonal and Marshak, 2019; Pincus, 1991; Richman and Moorman, 2000). It was developed to be applicable to noisy and medium-sized datasets, typical of signals in practice (Pincus, 1991). *ApEn* works by comparing patterns through an embedding dimension and assessing how likely similar patterns are to remain similar over time, within a specified level of tolerance (Richman and Moorman, 2000). The embedding dimension relates to the number of consecutive data points used to form a vector representation of the time series.

ApEn is based on the Heaviside function as a two-state classifier, through the distance between the two vectors and a tolerance (Chen et al., 2009). This conveys the rigid boundary of the Heaviside function. Data points are compared to the original point and are only deemed similar enough if it is within the tolerance (Richman and Moorman, 2000). If this is the case, the data point becomes a member and will be assessed in the complexity measure. All members are given an equal contribution. Data points outside the boundary are left out, regardless of how close they are to the border and other data points. Therefore, contribution of data points through the Heaviside function is completely dependent on the tolerance, indicating a high sensitivity to changes in tolerance or data position. The potential significant variations in *ApEn* as a result, may even lead to discontinuities (Chen et al., 2009). *ApEn* tends to be biased due to the fact that it includes self-matches, which are always going to be counted as similar.

As an example of how these types of methods are implemented, the following steps can be followed to calculate the *ApEn* of a time series:

1. Let a value in the time series of length n be defined as X_i where i denotes the position in the times series and has values $1 \leq i \leq n$.
2. Select an embedding dimension m and tolerance r. m relates to the number of consecutive data points used to form a vector representation of the time series.
3. Form vector sequences from $\mathbf{X}_1$ to $\mathbf{X}_{n-m+1}$ of length m for $i = 1, \ldots, n-m+1$:

$$\mathbf{X}_i = \{ X_i, X_{i+1}, \ldots, X_{i+m-1} \} \tag{5.15}$$

4. For each vector $\mathbf{X}_i$, count the number of vectors $\mathbf{X}_j$ such that the maximum absolute difference between corresponding elements is less than or equal to r:

$$d(\mathbf{X}_i, \mathbf{X}_j) = \max_{k=1,\ldots,m} |X_{i+k-1} - X_{j+k-1}| \leq r \tag{5.16}$$

5. Compute the similarity ratio for each i:

$$C_i^m(r) = \frac{\text{number of matches}}{n-m+1} \tag{5.17}$$

6. Calculate the average similarity:

$$\Phi^m(r) = \frac{1}{n-m+1} \sum_{i=1}^{n-m+1} \ln C_i^m(r) \tag{5.18}$$

7. Repeat steps 3–6 for embedding dimension $m+1$ to obtain $\Phi^{m+1}(r)$.

8. Compute the Approximate Entropy:

$$\text{ApEn}(m, r) = \Phi^m(r) - \Phi^{m+1}(r) \tag{5.19}$$

5.2.3.3 Sample entropy

Sample entropy (*SampEn*) is a refinement of *ApEn* (see Section 5.2.3.2), developed to provide a more consistent and less biased measure of complexity of a time series data (Chen et al., 2009; Delgado-Bonal and Marshak, 2019; Lake et al., 2002; Richman and Moorman, 2000; Zhou et al., 2017). In the same way as *ApEn*, *SampEn* quantifies unpredictability and irregularity of a time series by measuring how often similar patterns of data remain similar over time (Chen et al., 2009; Delgado-Bonal and Marshak, 2019; Lake et al., 2002; Richman and Moorman, 2000; Zhou et al., 2017). Tolerance, in which a pattern is taken to be similar, is once again based on the Heaviside function (Section 5.2.3.2). However, *SampEn* does not count self-matches, removing the bias observed in *ApEn*. Furthermore, *SampEn* is simpler and so requires about half as much time to calculate, is largely independent of length, and displays relative consistency where *ApEn* does not (Chen et al., 2009).

5.2.3.4 Fuzzy entropy

Fuzzy entropy (*FuzzEn*) was introduced to mitigate the limitations associated with *ApEn* and *SampEn* by using fuzzy logic rather than hard thresholds of tolerance, whilst still measuring the regularity and predictability of a time series through the concept that similar patterns will remain similar over time (Azami et al., 2019; Chen et al., 2007,

2009). This is becasue the rigid boundary demonstrated in the Heaviside function, implemented in both *ApEn* and *SampEn*, is not representative of boundaries within the real physical world, which tend to be ambiguous. Furthermore, membership of an input pattern to a given class is always imprecise and uncertain (Chen et al., 2009). *FuzzEn*, based on the concept of fuzzy sets, uses a fuzzy membership function: the exponential function, in place of the Heaviside function so that there is now a fuzzy boundary (Chen et al., 2007). *FuzzEn* consists of the same input parameters as those for *ApEn* and *SampEn*, but with the addition of the gradient of the boundary of the exponential function, which remains fixed for each *FuzzEn* calculation. This acts as the weight of the vector's similarity. Values greater than one weights the similarity degree of the close vectors and unweights that of the far ones, whereas values less than one do the opposite. In summary, the larger the gradient of the boundary of the exponential function, the more the closer vectors and the less the further vectors are weighted. However, as this parameter gets larger, detailed information is lost so that on tending to infinity, the exponential function becomes reduced to the Heaviside function. For the preservation of detailed information, it is recommended that the gradient of the boundary of the exponential function should be a small integer greater than one. The combination of the gradient of the boundary of the exponential function with the tolerance and data position to determine a vector's similarity is what increases the accuracy of *FuzzEn* (Chen et al., 2007). The exponential function is not as sensitive to changes in tolerance or data position, not changing drastically but also remaining continuous (Chen et al., 2009). Overall, *FuzzEn* has a stronger relative consistency and less dependence on data length, which means less bias. It also achieves continuity, freer parameter selections and more robustness to noise (Chen et al., 2009).

5.2.3.5 Spectral entropy

Spectral entropy (*SpecEn*) takes a different approach to the other entropy measures, quantifying the complexity of a time series through the distribution of the frequency components (Powell and Percival, 1979). *SpecEn* first requires the observed data to be transformed from the time domain to the frequency domain using methods such as the Fast Fourier Transform. In this way, the power spectral density of the signal, which is the distribution of the signal's energy across different frequencies, can be obtained and is normalised so that the total power is equal to one. If most of the energy is concentrated in just a few frequencies, *SpecEn* is low, meaning the time series is more regular and structured. However, if the energy is spread out across many frequencies, the *SpecEn* is high, indicating the time series is more random (Inouye et al., 1991).

5.2.3.6 Permutation entropy

Permutation entropy (*PermEn*) can also be considered an improvement to *ApEn* and *SpecEn* but does so in a different way to *FuzzEn*. Whilst *FuzzEn* softens the similarity criterion using fuzzy logic instead of using the Heaviside function, *PermEn* focusses on the ordinal patterns within a time series (Bandt and Pompe, 2002; Riedl et al., 2013), removing the need for a distance threshold. It works on the same basis that similar patterns will remain similar over time, but that similarity is defined through the order of values rather than their actual magnitudes (Bandt and Pompe, 2002). *PermEn* captures how the values in a time series are arranged over time, concentrating on the patterns formed by their relative positions. In this way, *PermEn* is robust to noise, scaling and shifts in amplitude (Bandt and Pompe, 2002).

5.3 Properties of selected complexity measures

In order to apply the complexity measures to CPT profiles, the features of such measures and their limitations in a geotechnical context must be evaluated. This includes the type of time series data the measures are applicable to, as well as the meaning of the output measure of complexity. Some complexity measures, such as *R/S* analysis, are only designed for stationary time series, whereas *DFA* was, in particular, derived for nonstationary time series. Other measures, like *ApEn*, can handle both stationary and non-stationary data.

To compare the complexity measures to each other, some rescaling of the output values may be necessary, since the measures use different characteristics of time series data. For example, *R/S* analysis estimates the Hurst exponent as a means of assessing the long-term correlations. A value of 0.5 portrays a random system with no long-term correlations, but values either side of 0.5, heading towards zero and one, demonstrate increasing long-term correlations of anti-persistence and persistence, respectively (see Section 5.2.2.1). In comparison, entropy methods give an output of zero for regular time series, as they have minimal disorder. The output value of complexity then increases with increasing complexity to a practical limit equivalent to a completely random system. This limiting value depends on the particular entropy measure, and will therefore even need to be normalised before comparison with other entropy measures.

In this work, a minimum complexity value of zero is desired for a regular system, in which a CPT profile follows a clear trend that can be predicted from a low resolution. The maximum complexity value is that for a random system, since reducing the resolution will have the greatest effect on the profile shape, as peaks and troughs will be

omitted from the profile if data is not recorded for these depths. Therefore, the maximum complexity for each complexity measure can be found by simulating a random time series.

5.4 Modelling white noise

White noise is a random time series which can be used to determine the maximum limits of the complexity measures in practice. White noise can be modelled as a Gaussian distribution of zero mean and constant standard deviation. To generate the exact same random profile, a random seed was set in python. The resulting time series can be seen in Figure 5.1. The complexity value for each of the selected complexity measures can be determined for this white noise distribution. This was repeated for 100 different random noise time series, from which the mean complexity value and standard deviation of each measure were obtained. An upper bound for the maximum complexity under each measure was derived by adding two times the standard deviation to the mean. This is because a random system, such as white noise, should have the greatest value of complexity. Table 5.1 shows the complexity values for the particular time series in Figure 5.1, along with the mean and standard deviation of the 100 profiles, and the subsequent upper bounds. For *R/S* and *DFA*, the values correspond to the exponents of these measures.

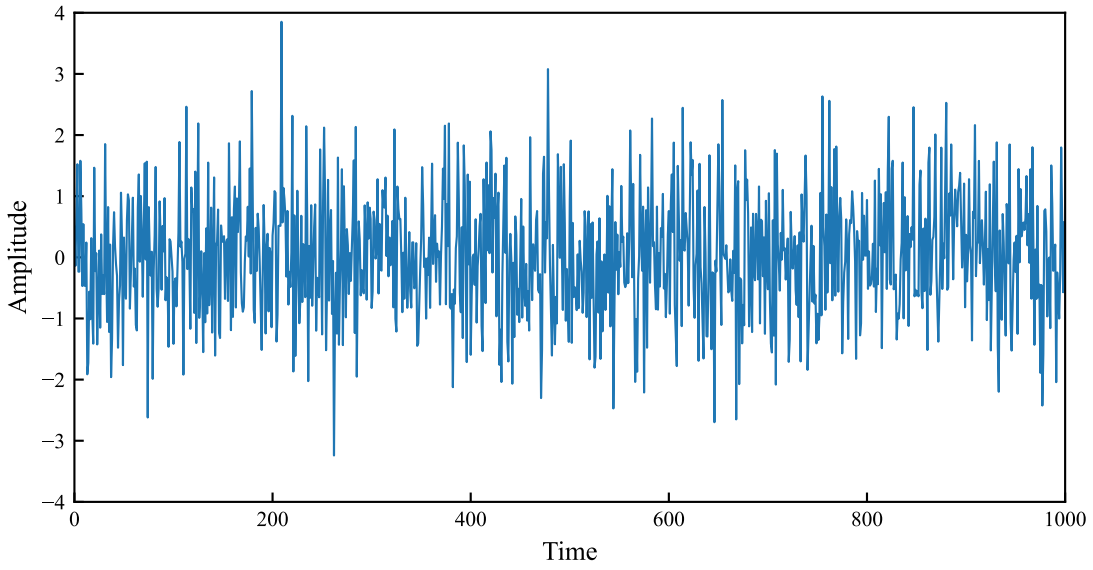

FIGURE 5.1: White noise

5.4.1 Rescaling of complexity measures

The need for comparison between complexity measures was highlighted in Section 5.3. This was achieved for *R/S* analysis and *DFA* by assessing the output limits explained

TABLE 5.1: Complexity values of white noise for selected complexity measures

Complexity Measure	Complexity of 1 Profile	μ of 100 Profiles	S of 100 Profiles	CoV of 100 Profiles	Maximum Complexity
R/S	0.575	0.579	0.043	0.074	0.664
DFA	0.504	0.502	0.054	0.108	0.611
K2En	2.525	2.591	0.057	0.022	2.706
SpecEn	0.942	0.939	0.003	0.003	0.944
PermEn	2.584	2.582	0.002	0.001	2.586
ApEn	1.637	1.663	0.020	0.012	1.703
SampEn	2.154	2.189	0.042	0.019	2.273
FuzzEn	1.372	1.377	0.026	0.019	1.430

in Sections 5.2.2.1 and 5.2.2.2, respectively. Since CPT data is unlikely to demonstrate anti-persistent correlations, due to the overburden of the soil, the rescaling process was simplified by eliminating values of less than 0.5. Therefore, the normalised parameter could be calculated by subtracting from the maximum value and dividing by the difference between the minimum and maximum values for that measure. *R/S* analysis has an upper theoretical limit of one and, ignoring anti-persistence, a minimum value of 0.5 for random noise. For *DFA*, the maximum observed value tends to be two, with the minimum equal to that in *R/S* analysis, applying the same reasoning. These upper limits of one and two for *R/S* and *DFA*, respectively, only apply to nonstationary data series. The equations are depicted in Table 5.2.

Having converted both the correlation measures of complexity, *R/S* analysis and *DFA*, to the same domain as the other measures via the corresponding normalisation functions in Table 5.2, the remaining six measures must also be normalised. This simply required dividing each complexity value by its maximum value observed for white noise, as recorded in Table 5.1, since minimum complexity is zero. These normalisation functions are also included in Table 5.2.

5.5 Simplified CPT profiles

With the eight complexity measures rescaled and normalised through Section 5.4.1, it was possible to apply them to some simple scenarios and assess their behaviour. Four functions were chosen to represent the simplified profiles:

- Linearly increasing (Section 5.5.1)
- Square root (Section 5.5.2)
- Step (Section 5.5.3)

- Sine wave (Section 5.5.4)

TABLE 5.2: Normalisation functions for rescaling complexity measures

Complexity Measure	**Normalisation Function**	**Method**
R/S	$\overline{\text{R/S}} = \frac{1 - \text{R/S}}{0.5}$	Subtract from maximum limit and divide by difference between limits, excluding anti-persistence
DFA	$\overline{\text{DFA}} = \frac{2 - \text{DFA}}{1.5}$	Subtract from maximum limit and divide by difference between limits, excluding anti-persistence
K2En	$\overline{\text{K2En}} = \frac{\text{K2En}}{2.71}$	Divide by maximum complexity from Table 5.1
SpecEn	$\overline{\text{SpecEn}} = \frac{\text{SpecEn}}{0.94}$	Divide by maximum complexity from Table 5.1
PermEn	$\overline{\text{PermEn}} = \frac{\text{PermEn}}{2.59}$	Divide by maximum complexity from Table 5.1
ApEn	$\overline{\text{ApEn}} = \frac{\text{ApEn}}{1.70}$	Divide by maximum complexity from Table 5.1
SampEn	$\overline{\text{SampEn}} = \frac{\text{SampEn}}{2.27}$	Divide by maximum complexity from Table 5.1
FuzzEn	$\overline{\text{FuzzEn}} = \frac{\text{FuzzEn}}{1.43}$	Divide by maximum complexity from Table 5.1

This enabled the complexity values of the selected measures to be compared against CPT profiles of known complexity and an assessment of the effect of certain parameters on the complexity to be performed. The corrected cone penetration resistance was normalised by dividing by the maximum corrected cone penetration resistance in the profile so that the actual corrected cone penetration values would not influence the results. Each simplified CPT profile was a function of the starting corrected cone penetration resistance, as a proportion of the maximum observed value. Both the step and sine wave functions were also functions of additional parameters. The step function profile, which represented a two type soil, therefore depended on the depth at which the soil changed (z_r). For the sine wave, the function had to be defined in terms of the mean, amplitude and time period. The mean was taken to be the same as the starting corrected cone penetration resistance and the amplitude was expressed in terms of the

mean, leaving the time period as a separate parameter to be investigated. By evaluating the effect of varying these different parameters on the complexity output, it was possible to determine their influence on the measures of complexity to help define the requirements of the complexity measure for use in soil data.

5.5.1 Linearly increasing function

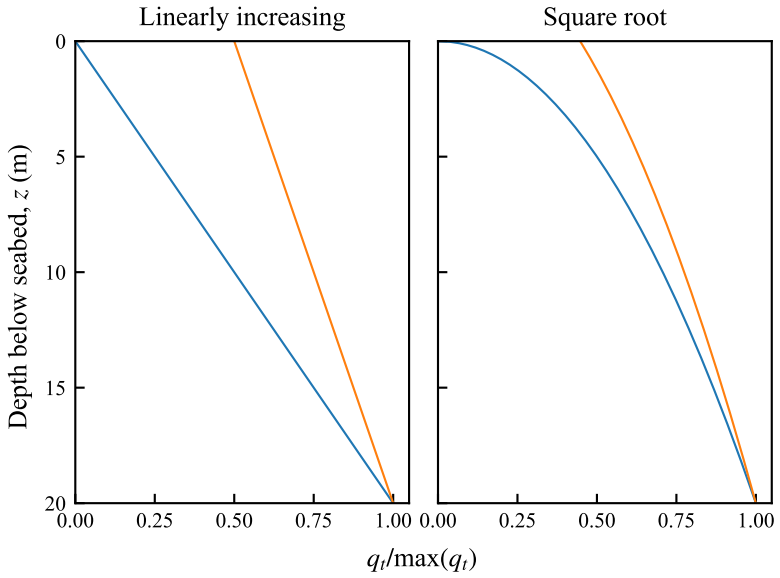

FIGURE 5.2: Linearly increasing and square root CPT profile with depth for different starting q_t

5.5.1.1 Effect of starting corrected cone penetration resistance

The results for the linearly increasing function are displayed in Table 5.3 for normalised corrected cone penetration resistance values from 0 to 0.8. It can be seen that only *SpecEn* varies with increasing starting corrected cone penetration resistance, however, the slight decrease in complexity is minimal. Although *SpecEn* provides the greatest value of complexity, it is still consistent with the other measures: the complexity of a linearly increasing function is essentially zero.

Any negative values are an artifact of the normalisation functions (from Table 5.2) applied to the complexity measures. When strongly non-stationary data is subjected to *R/S* and *DFA* analyses, the resulting exponents may exceed the conventional upper limits for stationary data, namely one and two, respectively. In particular, a *DFA* exponent greater than two indicates that the detrending process is insufficient and fails to remove non-stationary components effectively. For the other measures, negative values may occur due to the statistical analysis involved in selecting a practical upper limit of complexity. Neither of these should pose an issue in assessing the complexity of CPT profiles.

TABLE 5.3: Effect of starting q_t on complexity value for complexity measures

Starting q_t	**0.00**	**0.20**	**0.40**	**0.60**	**0.80**
$\overline{\text{R/S}}$	-0.021	-0.021	-0.021	-0.021	-0.021
$\overline{\text{DFA}}$	-0.004	-0.004	-0.004	-0.004	-0.004
$\overline{\text{K2En}}$	0.074	0.074	0.074	0.074	0.074
$\overline{\text{SpecEn}}$	0.185	0.162	0.146	0.137	0.132
$\overline{\text{PermEn}}$	-0.000	-0.000	-0.000	-0.000	-0.000
$\overline{\text{ApEn}}$	-0.000	-0.000	-0.000	-0.000	-0.000
$\overline{\text{SampEn}}$	-0.000	-0.000	-0.000	-0.000	-0.000
$\overline{\text{FuzzEn}}$	0.000	0.000	0.000	0.000	0.000

5.5.2 Square root function

The plot showing the square root function with depth for different starting corrected cone penetration resistances has been included in Figure 5.2, alongside the linearly increasing function.

5.5.2.1 Effect of starting corrected cone penetration resistance

The complexity measures behave similarly to how they did for the linearly increasing function, when applied to the square root function. All values in Table 5.4 remain either zero or are very close to a complexity of zero, regardless of the starting corrected cone penetration resistance. Once again, *SpecEn* gives the largest value of complexity, although less than that for the linearly increasing function, and decreases with starting corrected cone penetration resistance. A few fluctuations in the complexity value under *R/S* analysis, *DFA*, and *K2En* can be observed, but overall remain fairly consistent.

TABLE 5.4: Effect of starting q_t on complexity value for complexity measures

Starting q_t	**0.00**	**0.20**	**0.40**	**0.60**	**0.80**
$\overline{\text{R/S}}$	-0.016	-0.021	-0.021	-0.021	-0.021
$\overline{\text{DFA}}$	0.051	-0.008	-0.007	-0.006	-0.005
$\overline{\text{K2En}}$	0.073	0.074	0.074	0.074	0.074
$\overline{\text{SpecEn}}$	0.151	0.140	0.134	0.132	0.130
$\overline{\text{PermEn}}$	-0.000	-0.000	-0.000	-0.000	-0.000
$\overline{\text{ApEn}}$	-0.000	-0.000	-0.000	-0.000	-0.000
$\overline{\text{SampEn}}$	-0.000	-0.000	-0.000	-0.000	-0.000
$\overline{\text{FuzzEn}}$	0.000	0.000	0.000	0.000	0.000

5.5.3 Step function

Similarly to the previous two functions, the step function has been plotted with depth for different starting corrected cone penetration resistances. In addition to this, there is the variability in the depth at which the soil changes, as portrayed in Figure 5.3.

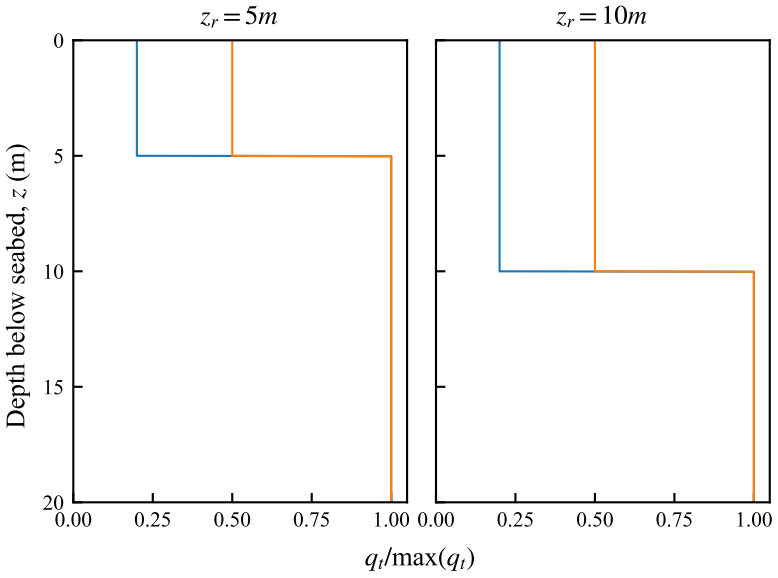

FIGURE 5.3: Two soil type (step) CPT profile with depth for different starting q_t and different depth of soil change (z_r)

5.5.3.1 Effect of starting corrected cone penetration resistance

Evaluating the values of complexity for the step function (Table 5.5) under varying starting corrected cone penetration resistances did not reveal significant changes. However, specific measures did perform differently to this function. *K2En* has a value of zero, suggesting it could not detect the change in soil, whereas, *ApEn* and *FuzzEn* displayed values just above zero for the first time. As the starting corrected cone penetration resistance increases, there tends to be a trend that the complexity value decreases, most evident for *SpecEn*, in accordance with the difference between the resistance of the two soils becoming smaller. This trend is absent for both *R/S* analysis and *DFA*, where *R/S* analysis generates values that jump around, either side of zero, whilst *DFA* is more consistent but also more negative, due to the detrending process.

5.5.3.2 Effect of depth of change in soil

The effect of the depth at which the soil changes on the complexity values of the step function were assessed for three different scenarios, as laid out in Table 5.6. The only complexity measure that seemed somewhat influenced by the soil change occurring at

TABLE 5.5: Effect of starting q_t on complexity value for complexity measures

Starting q_t	**0.00**	**0.20**	**0.40**	**0.60**	**0.80**
$\overline{\text{R/S}}$	0.057	0.251	0.251	-0.030	0.251
$\overline{\text{DFA}}$	-0.771	-0.770	-0.773	-0.769	-0.770
$\overline{\text{K2En}}$	0.000	0.000	0.000	0.000	0.000
$\overline{\text{SpecEn}}$	0.221	0.193	0.167	0.146	0.134
$\overline{\text{PermEn}}$	-0.000	-0.000	-0.000	-0.000	-0.000
$\overline{\text{ApEn}}$	0.002	0.002	0.002	0.002	0.002
$\overline{\text{SampEn}}$	0.000	0.000	0.000	0.000	0.000
$\overline{\text{FuzzEn}}$	0.001	0.001	0.001	0.000	0.000

a different depth is *SpecEn*. As the change in soil gets deeper, the complexity increases, although this is still by only a small amount. The zero value of *K2En*, further reiterates the fact that it is not sensitive to a step function, which can also be assumed to be the case for the other entropy measures.

TABLE 5.6: Effect of depth of change in soil z_r on complexity value for complexity measures

Depth of change in soil, z_r	**5.00**	**10.00**	**15.00**
$\overline{\text{R/S}}$	0.096	0.019	-0.004
$\overline{\text{DFA}}$	-0.264	-0.771	-0.836
$\overline{\text{K2En}}$	0.000	0.000	0.000
$\overline{\text{SpecEn}}$	0.146	0.179	0.227
$\overline{\text{PermEn}}$	-0.000	-0.000	-0.000
$\overline{\text{ApEn}}$	0.002	0.002	0.002
$\overline{\text{SampEn}}$	0.000	0.000	0.001
$\overline{\text{FuzzEn}}$	0.001	0.001	0.001

5.5.4 Sine wave function

The final function assessed of the four simplified CPT profiles was the sine wave. This has different properties to the other three functions and, as mentioned in the overview of the section (Section 5.5), is governed by mean, amplitude and time period. Combining mean and amplitude into the starting corrected cone penetration resistance parameter, the same analysis as the other three functions could be performed, along with a separate one for the effect of time period.

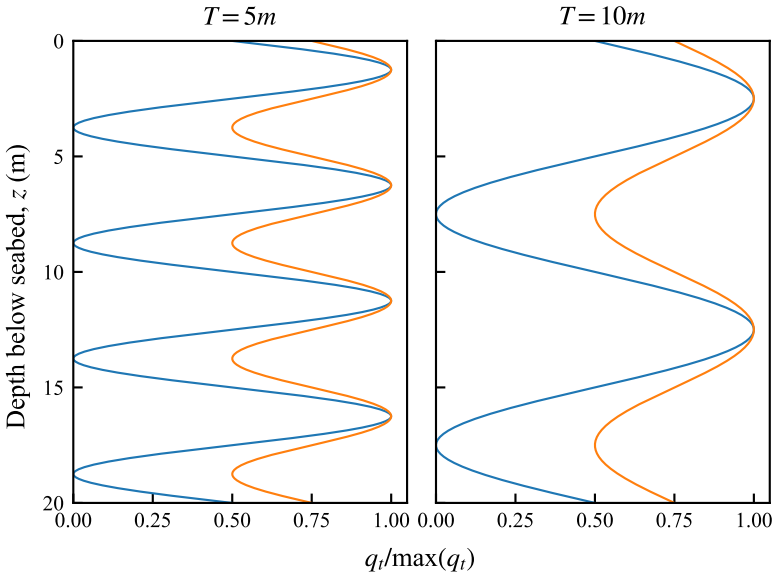

FIGURE 5.4: Sine wave CPT profile with depth for different starting q_t and different time period (T)

5.5.4.1 Effect of starting corrected cone penetration resistance

The normalised corrected cone penetration resistances for the sine wave ranged from starting corrected cone penetration resistance values of 0.5 to 0.9. This was due to the shape of the graph and preventing the profile from becoming negative, since the sine wave was assumed to have its mean value at the seafloor, therefore equal to the normalised starting corrected cone penetration resistance, and an amplitude of one. Figure 5.4 demonstrates this for a constant time period. Applying the complexity measures to a sine function with time period 5 m, gave the results in Table 5.7.

The *DFA* appears to behave more appropriately under the sine wave than the other functions, probably because the linear polynomial is adequate to detrend the data. The near zero constant value implies that it is able to detect the regularity of the sine wave profile for all starting corrected cone penetration resistances. Only *SpecEn* experiences its usual decrease in complexity with increasing starting corrected cone penetration resistances. Another measure to note is *PermEn*, in which the value of complexity is no longer zero but 0.4. This relatively high measure of complexity conveys a system that is almost halfway as complex as random noise. However, the other complexity measures are in agreement, with the sine wave of constant time period being of almost zero complexity.

5.5.4.2 Effect of time period

The effect of time period of the sine wave function on the complexity was investigated by increasing the time period from 1 to 10 m in intervals of 0.5 m. Since the results

TABLE 5.7: Effect of starting q_t on complexity value for complexity measures

Starting q_t	**0.50**	**0.60**	**0.70**	**0.80**	**0.90**
$\overline{\text{R/S}}$	-0.040	-0.040	-0.040	-0.040	-0.040
$\overline{\text{DFA}}$	0.083	0.083	0.083	0.083	0.083
$\overline{\text{K2En}}$	0.063	0.063	0.063	0.063	0.063
$\overline{\text{SpecEn}}$	0.213	0.183	0.159	0.142	0.133
$\overline{\text{PermEn}}$	0.401	0.401	0.401	0.401	0.401
$\overline{\text{ApEn}}$	0.019	0.019	0.019	0.019	0.019
$\overline{\text{SampEn}}$	0.012	0.012	0.012	0.012	0.012
$\overline{\text{FuzzEn}}$	0.000	0.000	0.000	0.000	0.000

portrayed in Table 5.8 exhibited much more variation than in any of the other analyses, they were plotted to form Figure 5.5. The general trend is that complexity decreases with increasing time period, as the number of sine waves within a given depth reduces. Two wavelengths of time period 10 m fit in a 20 m depth. In comparison, 20 wavelengths of time period 1 m fit in 20 m. Having more sine waves in a profile, therefore, agrees with the concept of being more complex. The decrease in complexity is most evident for *R/S* analysis and *DFA*. They both start at a relatively high complexity of almost 0.8 for a time period of 1 m, before rapidly decreasing to their plateau levels of zero and 0.1 complexity at time periods of 3 and 5 m for *R/S* analysis and *DFA*, respectively. The time period of the sine wave does not appear to effect the complexity for *SpecEn*, *PermEn* and *FuzzEn* as all three remain approximately constant horizontal lines. Whilst *PermEn* has a middling complexity of a little above 0.4, *SpecEn* has a fairly low complexity of just under 0.2, whereas *FuzzEn* assumes zero complexity. The remaining measures begin at a complexity between 0.05 and 0.15 at a time period of one, decreasing slightly as time period increases until levelling off. *K2En* reaches the same minimum complexity as *DFA*, whereas both *ApEn* and *SampEn* reduce to a complexity of zero, joining *FuzzEn* for the time periods greater than 6 m.

TABLE 5.8: Effect of starting q_t on complexity value for complexity measures

Time period, T	**1.00**	**2.50**	**4.00**	**5.50**	**7.00**	**8.50**	**10.00**
$\overline{\text{R/S}}$	0.756	0.114	-0.045	-0.035	-0.027	-0.021	-0.018
$\overline{\text{DFA}}$	0.732	0.289	0.121	0.081	0.058	0.059	0.044
$\overline{\text{K2En}}$	0.125	0.068	0.064	0.063	0.061	0.060	0.061
$\overline{\text{SpecEn}}$	0.172	0.170	0.168	0.165	0.161	0.173	0.161
$\overline{\text{PermEn}}$	0.448	0.413	0.404	0.399	0.397	0.395	0.395
$\overline{\text{ApEn}}$	0.118	0.041	0.023	0.017	0.013	0.010	0.009
$\overline{\text{SampEn}}$	0.072	0.026	0.015	0.011	0.008	0.006	0.006
$\overline{\text{FuzzEn}}$	0.001	0.000	0.000	0.000	0.000	0.000	0.000

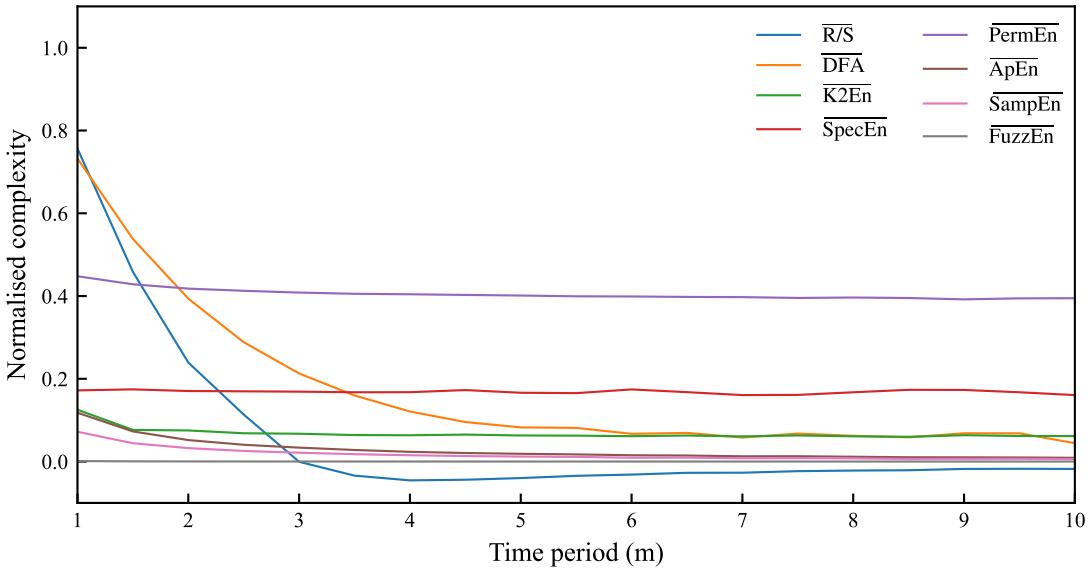

FIGURE 5.5: Effect of time period of sine wave on complexity measure value

5.6 Applying noise to simplified CPT profiles

CPTs can contain noise, which could potentially increase the complexity of the profile if it is beyond a certain value. To determine this limit for the eight complexity measures and ascertain their sensitivity to noise, noise was artificially added to the two simplified CPT profiles for the linearly increasing and sine wave functions. Noise was modelled as a random variable with Gaussian distribution of zero mean and constant standard deviation, in the same way as the white noise in Section 5.4, except it was trialled for varying levels of standard deviation, ranging from 0 to 0.1 in intervals of 0.02. The noise was then applied to the function in two different ways, through:

- addition of the noise value ($q_t(z) + \text{noise}$)
- multiplication by 10 to the power of the noise value ($q_t(z) * 10^{\text{noise}}$)

at a given data point to the corresponding corrected cone penetration resistance at that depth. In this way, the methods of applying noise could be compared and the effect on complexity evaluated.

5.6.1 Linearly increasing function

First noise was applied to the linearly increasing function from Section 5.5.1. Figure 5.6 demonstrates the influence of noise of varying standard deviations on the function through addition and multiplication. The central blue line, depicting a standard deviation of zero, is equivalent to the straight line of the linearly increasing function. As

the standard deviation of the noise increases, the further the points become from the original line. A normalised starting corrected cone penetration resistance of 0.5 was used in the analysis to ensure that the profile always remained greater than zero even for negative values of noise. This was only necessary for the addition of noise because when multiplying, negative noise values result in rescaling of the profile towards a limit of zero. On the other hand, the effect of multiplication of noise for positive values exponentially increases the profile. It should be noted that the normalisation of the corrected cone penetration resistance has been performed for the original linearly increasing profile that has zero standard deviation.

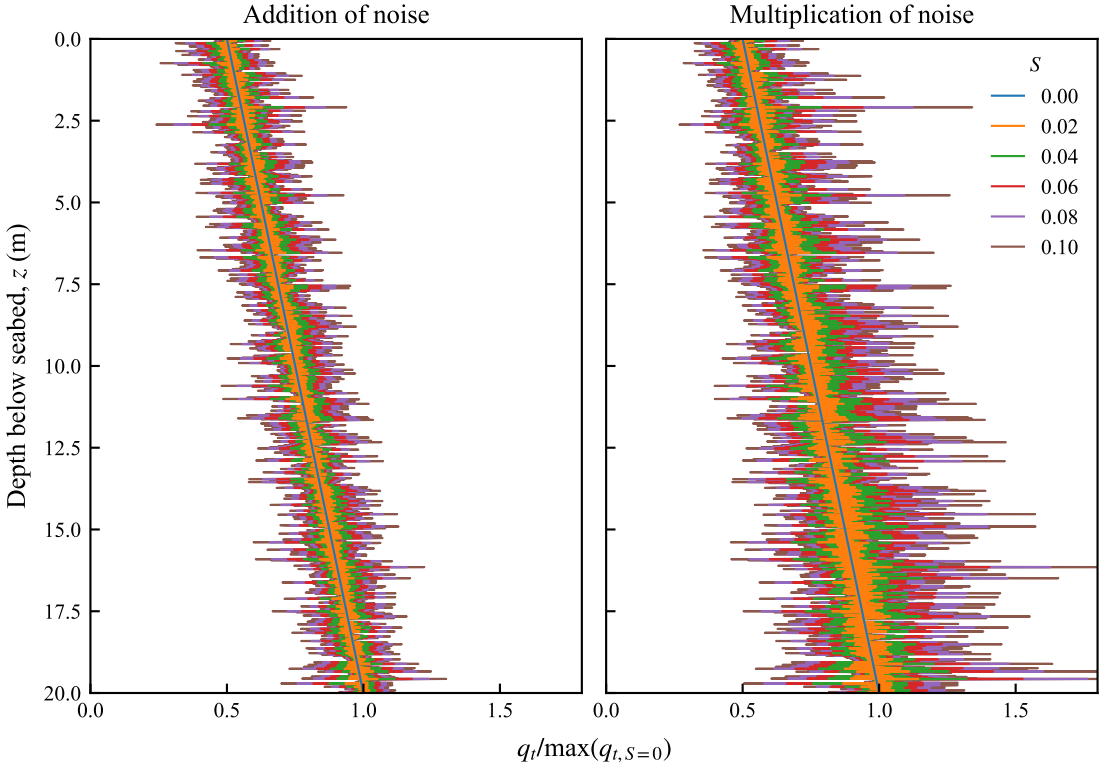

FIGURE 5.6: Linearly increasing CPT profile with addition and multiplication of noise of distribution $N(0, S)$

Running the complexity measures for different standard deviations of the noise applied to the linearly increasing function, produced the results displayed in Tables 5.9 and 5.10 for addition and multiplication of noise, respectively. The data was then transformed into the graphs in Figure 5.7. It can be seen that, for the majority of measures, complexity increases with increasing standard deviation up to a certain point. *PermEn* reaches a maximum complexity at a standard deviation of 0.02, whereas for other methods, including *ApEn*, *SampEn*, *K2En* and *DFA*, the complexity increases at a decreasing rate, highlighting the transition between a regular linearly increasing function with a bit of inconsequential noise, and the noise becoming large enough that it overpowers the trend and approaches the complexity of a random noise time series. Meanwhile, *SpecEn* does not appear to be affected by increasing the standard deviation of the noise as it remains almost horizontal. *FuzzEn*, on the other hand, demonstrates the greatest

resistance to noise whilst still being able to detect its presence at larger standard deviations. This is portrayed by the slight upwards curve of the grey line at a standard deviation of 0.04 and 0.06, for addition and multiplication of noise, respectively. The initial decrease observed in the complexity for *R/S* can be attributed to the limitations of the method in strongly correlated time series, rather than becoming less complex. Overall, multiplication of noise resembles that in the addition but shows increased sensitivity to standard deviation.

TABLE 5.9: Effect of standard deviation of addition of noise on complexity value for complexity measures

Standard deviation, S	**0.00**	**0.02**	**0.04**	**0.06**	**0.08**	**0.10**
$\overline{\text{R/S}}$	-0.021	-0.396	-0.181	0.018	0.171	0.286
$\overline{\text{DFA}}$	-0.004	0.376	0.525	0.616	0.681	0.728
$\overline{\text{K2En}}$	0.074	0.324	0.542	0.668	0.749	0.808
$\overline{\text{SpecEn}}$	0.141	0.142	0.144	0.147	0.152	0.158
$\overline{\text{PermEn}}$	-0.000	0.999	0.999	0.999	0.999	0.999
$\overline{\text{ApEn}}$	-0.000	0.348	0.676	0.849	0.942	1.005
$\overline{\text{SampEn}}$	-0.000	0.241	0.477	0.624	0.717	0.785
$\overline{\text{FuzzEn}}$	0.000	0.002	0.008	0.017	0.030	0.046

TABLE 5.10: Effect of standard deviation of multiplication of noise on complexity value for complexity measures

Standard deviation, S	**0.00**	**0.02**	**0.04**	**0.06**	**0.08**	**0.10**
$\overline{\text{R/S}}$	-0.021	-0.256	0.066	0.275	0.410	0.502
$\overline{\text{DFA}}$	-0.004	0.497	0.655	0.744	0.802	0.842
$\overline{\text{K2En}}$	0.074	0.469	0.678	0.777	0.830	0.863
$\overline{\text{SpecEn}}$	0.141	0.143	0.150	0.160	0.174	0.190
$\overline{\text{PermEn}}$	-0.000	0.999	0.999	0.999	0.999	0.999
$\overline{\text{ApEn}}$	-0.000	0.598	0.878	0.987	1.039	1.067
$\overline{\text{SampEn}}$	-0.000	0.400	0.632	0.755	0.817	0.847
$\overline{\text{FuzzEn}}$	0.000	0.006	0.024	0.053	0.090	0.134

5.6.2 Sine wave function

Applying both the addition and multiplication of noise to the sine wave function was performed in a similar way to the linearly increasing function in Section 5.6.1. The graphs for a starting normalised corrected cone penetration resistance of 0.5 and time period of 5 m can be seen in Figure 5.8. Increasing the standard deviation of the noise,

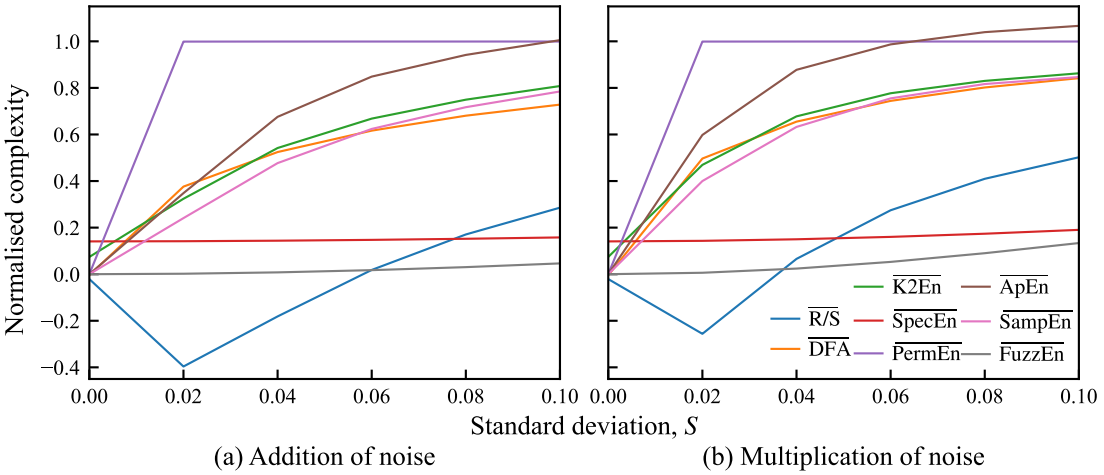

FIGURE 5.7: Effect of standard deviation of noise to linearly increasing CPT profile on complexity measure value

once again, increases the possible range of corrected cone penetration resistances from the zero standard deviation sine wave curve in blue. Furthermore, multiplication of noise results in scaling of the values towards zero or exponentially large, preventing the cone penetration resistances from becoming negative. The exponential effect is emphasised by the increased variation within the larger standard deviation curves (red, purple and brown).

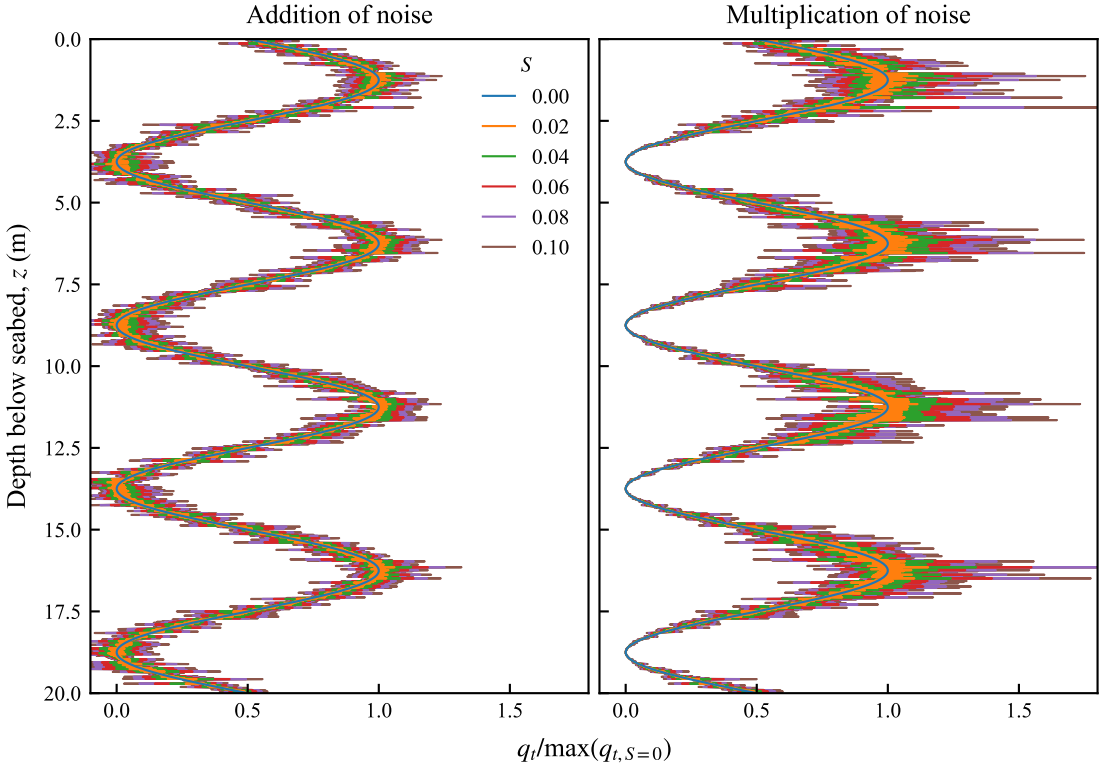

FIGURE 5.8: Sine wave CPT profile with addition and multiplication of noise of distribution $N(0, S)$

The complexity measures were run on the sine wave function under a range of standard deviations, the results of which are presented in Tables 5.11 and 5.12 for the addition and multiplication of noise, respectively. Figure 5.9 portrays this data graphically. Whilst most complexity measures have zero complexity at a zero standard deviation, *PermEn* begins at a relatively high complexity of 0.4, consistent with that observed for the standard sine wave function in Section 5.5.4. The overall trend that normalised complexity increases with standard deviation, as the fluctuations of noise begin to be detected within the sine wave. However, beyond a certain threshold of around 0.03, increasing the standard deviation further does not significantly affect the complexity, despite it still increasing. The curves tend to plateau at a lower complexity in the multiplication of noise, exhibiting a slightly more gentle increase in complexity at a decreasing rate, as standard deviation increases.

TABLE 5.11: Effect of standard deviation of addition of noise on complexity value for complexity measures

Standard deviation, S	**0.00**	**0.02**	**0.04**	**0.06**	**0.08**	**0.10**
$\overline{\text{R/S}}$	-0.040	-0.147	-0.230	-0.288	-0.330	-0.358
$\overline{\text{DFA}}$	0.083	0.126	0.168	0.203	0.233	0.260
$\overline{\text{K2En}}$	0.063	0.106	0.251	0.371	0.463	0.537
$\overline{\text{SpecEn}}$	0.213	0.214	0.218	0.223	0.231	0.239
$\overline{\text{PermEn}}$	0.401	0.999	0.999	0.999	0.999	0.999
$\overline{\text{ApEn}}$	0.019	0.087	0.260	0.439	0.578	0.683
$\overline{\text{SampEn}}$	0.012	0.060	0.174	0.293	0.392	0.473
$\overline{\text{FuzzEn}}$	0.000	0.002	0.008	0.017	0.030	0.046

TABLE 5.12: Effect of standard deviation of multiplication of noise on complexity value for complexity measures

Standard deviation, S	**0.00**	**0.02**	**0.04**	**0.06**	**0.08**	**0.10**
$\overline{\text{R/S}}$	-0.040	-0.135	-0.189	-0.220	-0.236	-0.242
$\overline{\text{DFA}}$	0.083	0.144	0.197	0.239	0.274	0.306
$\overline{\text{K2En}}$	0.063	0.128	0.149	0.152	0.153	0.155
$\overline{\text{SpecEn}}$	0.213	0.216	0.223	0.234	0.249	0.267
$\overline{\text{PermEn}}$	0.401	0.984	0.994	0.997	0.997	0.998
$\overline{\text{ApEn}}$	0.019	0.145	0.324	0.446	0.532	0.588
$\overline{\text{SampEn}}$	0.012	0.073	0.105	0.115	0.122	0.128
$\overline{\text{FuzzEn}}$	0.000	0.004	0.016	0.035	0.059	0.086

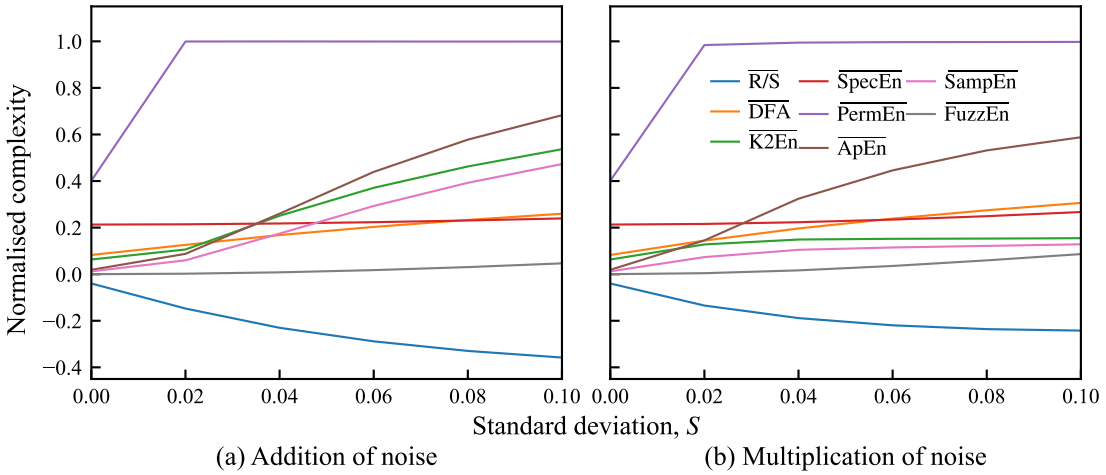

FIGURE 5.9: Effect of standard deviation of noise to sine wave CPT profile on complexity measure value

5.7 Requirements of complexity measure

Sections 5.5 and 5.6 have provided useful information on the behaviour of the eight complexity measures under simple soil profiles. The variation in normalised cone penetration resistance experienced within a profile tends to not greatly influence complexity; neither does a single change in soil. On the other hand, the time period of the profile, relating to the number of changes in direction, does affect the normalised complexity of most measures. It is important for the complexity measures to be able to identify between time period and noise, since a large enough level of noise will be interpreted as an increased time period, and therefore, lead to an increased complexity. Assessing the sensitivity to noise through Sections 5.6.1 and 5.6.2 has demonstrated that, except for the unexpected output of *R/S* analysis, the complexity measures appear to have a threshold (approximately 0.02 standard deviations) below which they are not overly sensitive to noise.

5.8 CPT profiles from Burbo Bank Extension case study site

The nine CPTs from the Burbo Bank Extension offshore wind farm site that were introduced in Section 3.2 and used in the resolution analysis in Chapter 3, were re-evaluated in terms of their complexity. A further two CPTs (CPT115 and CPT116) were added to the selection, chosen due to their 'similar' profiles to each other, and to that of CPT117. These have been presented in Figure 5.10. All three corrected cone penetration resistance profiles exhibit increased resistance at the same depths, especially between 10 and 18 m. The purpose of including 'similar' CPTs in the dataset was because these profiles were assumed to have close values of complexity. When applying the chosen complexity measures from Section 5.2 to these Burbo Bank Extension CPT profiles, comparing

the complexity values of the 'similar' profiles added another level of analysis, enabling the assessment of the capability of the complexity measures.

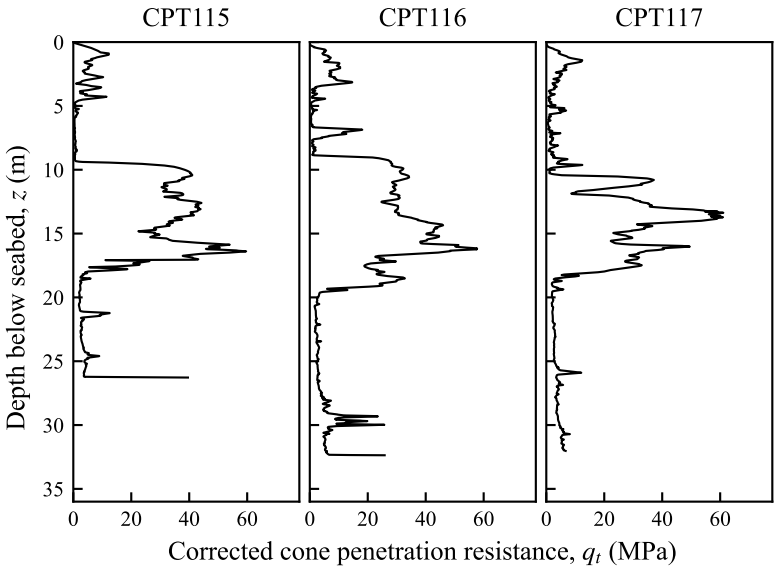

FIGURE 5.10: 'Similar' CPT profiles of corrected cone penetration resistance (q_t) with depth

In the same way that the eight complexity measures (Section 5.2) were carried out on the simplified CPT profiles, laid out in Section 5.5, they were performed on the now eleven CPTs at the Burbo Bank Extension. For comparison, all the complexity measures were normalised by dividing by their respective maximum values, in accordance with Table 5.2. The complexity of the CPT profiles is dependent on several factors that could not be tested all at once, including the type of CPT profile and the length. In this work, corrected cone penetration resistance was selected as the CPT profile from which complexity was measured, as was the case in the simplified CPT profiles. However, the complexity measures could equally be applied to CPT profiles of sleeve friction or other derived parameters such as normalised cone resistance or soil classification index (see Sections 2.4 and 2.4.2).

The value of complexity of the profile is affected by the length of the profile assessed. Furthermore, CPTs are performed to different lengths, so using the full profile of each CPT would prevent a clear comparison of complexity values. Due to the method in which the measured data was processed, the final depth readings were usually at a smaller interval to the rest, making them unsuitable for the complexity measures of a time series. This issue is exacerbated in the reduced resolution profiles. It was shown that the optimal pile lengths determined in Chapter 3 were all much less than the depth of the full CPT profile. This could result in the complexity measure of a CPT unreliably predicting the complexity value based on sections of the profile that did not even govern the design of the monopile. Another option was to calculate the complexity of a

CPT profile up to its corresponding optimal pile length under static, lateral, ULS design. Although this would also result in different profile lengths between CPTs, the profile length would incorporate the varying soil strengths so that the total resistance remained consistent. However, such a process would require the optimal pile lengths for each CPT profile to be known in advance of the complexity assessment. Therefore, a pile length of 20 m was selected for all CPTs as an initial test, since this still captured most of the optimal pile lengths for the Burbo Bank Extension site without being excessively long.

5.8.1 Complexity results

Running the eleven full resolution CPT profiles (data interval of 0.01 m) of corrected cone penetration resistance over a depth of 20 m, for the eight normalised complexity measures, generated the complexity values in Table 5.13. To ensure that the eleven CPTs were representative of the whole Burbo Bank Extension site, the complexity of all the 41 CPTs performed was also calculated and plotted, alongside the eleven specified CPTs, as box and whisker plots in Figure 5.11. The length of the box and whisker plots demonstrate the range of the complexity values for that complexity measure across the Burbo Bank Extension site. The coloured dots indicate the complexity value for each of the eleven CPTs. The dots tend to spread along most of the box and whisker plots, meaning the selected CPTs suitably represent the range of complexity values observed across the site. However, some measures can be seen to not fluctuate greatly between the CPT profiles. These include *K2En*, *PermEn*, *ApEn* and *SampEn*. Furthermore, none of the complexity measures give a normalised complexity value of one and are generally towards the lower half of the plot. This means they do not resemble random time series but have some sort of correlation and regularity, especially for those values that approach zero.

5.8.2 Relative complexity

The vertical ordering of the coloured dots also changes throughout the different complexity measures. This can be more clearly evaluated by plotting the relative complexity, obtained through Equation 5.20 for the full 41 CPT profiles, using *R/S* analysis as an example, and portrayed in Figure 5.12. The relative complexity demonstrates the ranking of complexity of CPTs whilst revealing how much they differ from each other. There does not appear to be a trend in the ordering of the CPTs under the various complexity measures, although CPT109 (orange marker) seems to be the most consistently highly ranked. On the other hand, the greatest discrepancy between complexity measures occurs for CPT110 (green marker), in which it is either ranked the most complex or least. The difference between the complexity values for *R/S* analysis and *DFA*

TABLE 5.13: Normalised complexity of eleven CPT profiles at Burbo Bank Extension offshore wind farm under eight selected complexity measures

CPT	$\overline{\text{R/S}}$	$\overline{\text{DFA}}$	$\overline{\text{K2En}}$	$\overline{\text{SpecEn}}$	$\overline{\text{PermEn}}$	$\overline{\text{ApEn}}$	$\overline{\text{SampEn}}$	$\overline{\text{FuzzEn}}$
101	-0.012	0.430	0.085	0.281	0.621	0.101	0.037	0.281
109	0.136	0.487	0.095	0.242	0.605	0.092	0.052	0.252
110	0.152	0.256	0.056	0.280	0.656	0.015	0.003	0.097
115	0.104	0.308	0.055	0.245	0.590	0.033	0.012	0.177
116	0.057	0.351	0.053	0.212	0.615	0.030	0.014	0.159
117	0.079	0.318	0.054	0.263	0.593	0.034	0.012	0.205
203	0.020	0.392	0.077	0.241	0.643	0.074	0.030	0.288
205	0.028	0.327	0.074	0.273	0.610	0.082	0.041	0.232
308	0.039	0.341	0.074	0.232	0.620	0.056	0.029	0.168
318	0.128	0.513	0.040	0.260	0.622	0.071	0.019	0.140
323	0.057	0.287	0.071	0.331	0.629	0.042	0.019	0.172

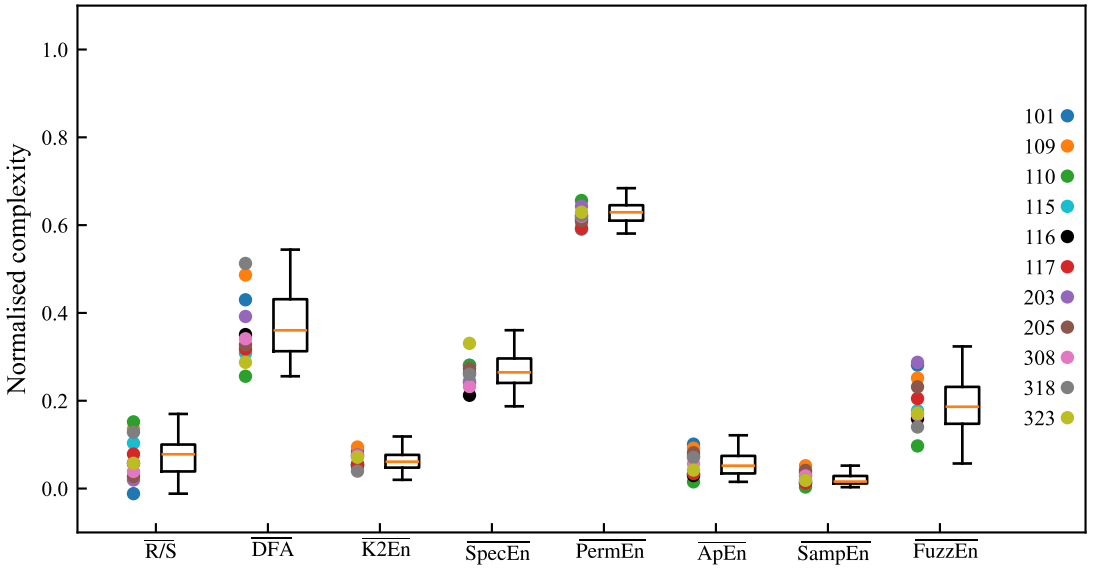

FIGURE 5.11: Distribution of normalised complexity for all 41 CPTs within the Burbo Bank Extension offshore wind farm site, with actual values of the eleven selected CPTs plotted alongside

could be attributed to the fact that CPT110 has some structured trends or nonstationary components, which would result in long-term persistence for *R/S* analysis. Meanwhile, *DFA* is able to identify and remove trends within a time series before calculating the long-term persistence, as well as being able to handle nonstationary data. In terms of the difference in entropy measures between *PermEn* and the similar methods of *ApEn*, *SampEn* and *FuzzEn*, CPT110 must exhibit short-term predictability but small up and down fluctuations which remove order patterns from the signal. The shape of CPT110 can verify this, since it features two consistent sections from 0 to 9 m and 15 to 25 m, with a distinct change of soil between 9 and 15 m. The fact that CPT profiles generally show low but frequent fluctuations, which could be noise from the equipment, means that even consistent sections are going to have few temporal patterns, giving a higher value of *PermEn*. The sensitivity of *PermEn* to noise was highlighted back in Figure 5.9. Once the threshold of detectable noise is exceeded, in this case a standard deviation of 0.02, *PermEn* increases sharply and gives maximum complexity. Therefore, *PermEn*, is a less appropriate measure of complexity for CPT data. Furthermore, with the unreliability of *R/S* analysis in trended and nonstationary data, it can be assumed that CPT110 is more likely to have a low complexity.

$$\widetilde{\mathrm{R/S}} = \frac{\overline{\mathrm{R/S}} - \min(\overline{\mathrm{R/S}})}{\max(\overline{\mathrm{R/S}}) - \min(\overline{\mathrm{R/S}})} \tag{5.20}$$

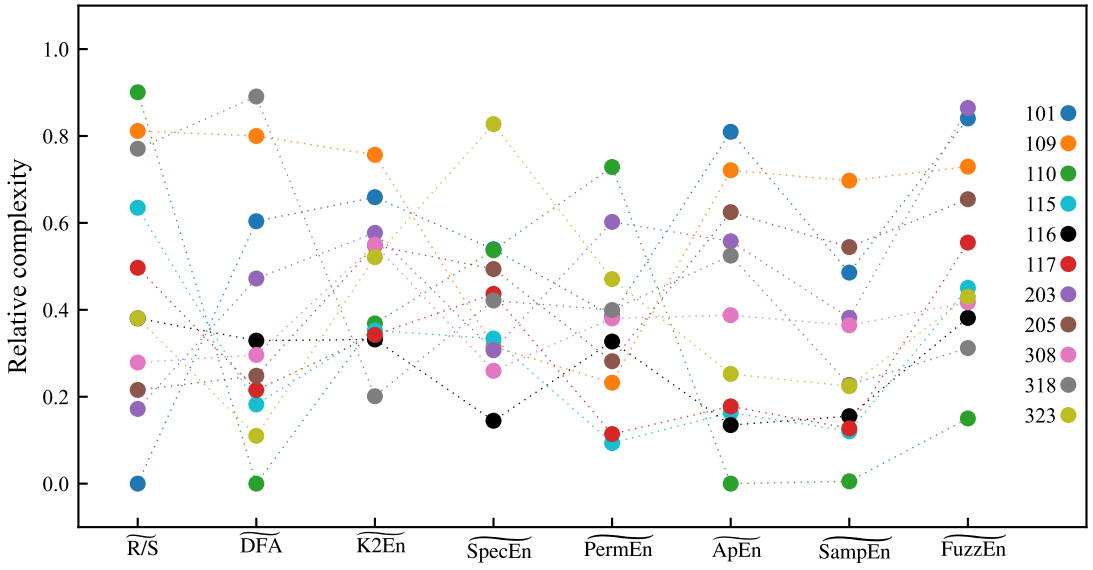

FIGURE 5.12: Relative complexity of the eleven selected CPTs within the Burbo Bank offshore wind farm site compared to the total 41 CPTs

The 'similar' CPTs of 115, 116 and 117, from Section 5.5, were identified in Figure 5.12 and have been highlighted in the reproduced plot in Figure 5.13. For *K2En*, *ApEn* and

SampEn, these three CPTs have almost equal complexity to each other, whilst the complexity of the other CPTs remains distributed across the range. Even for the other complexity measures, CPTs 115, 116 and 117 are reasonably close, suggesting that the measures are detecting some similarity between these CPTs compared to most of the rest.

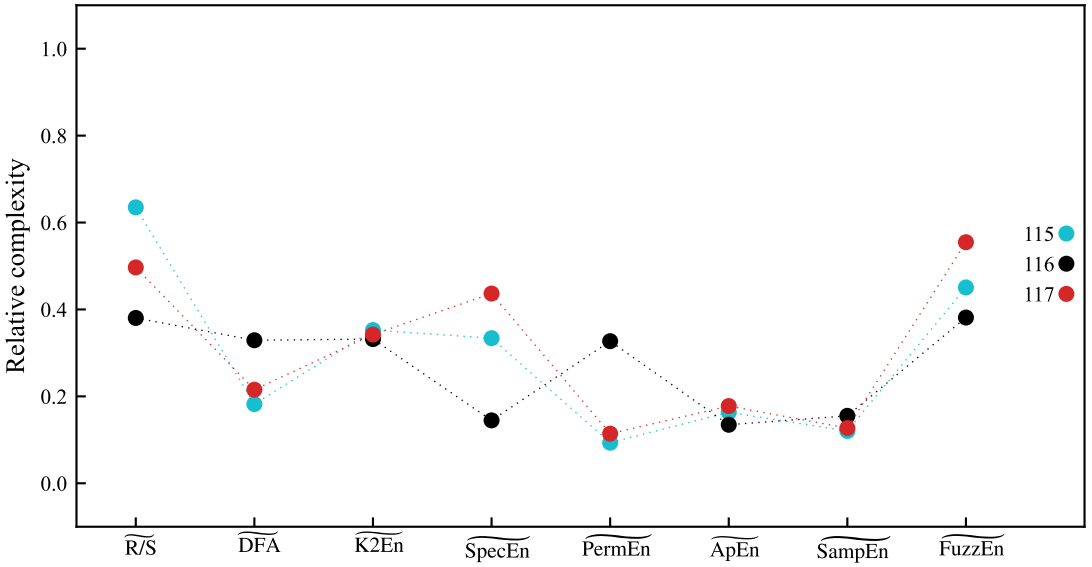

FIGURE 5.13: Relative complexity of the three similar CPTs (CPTs 115, 116 and 117) within the Burbo Bank offshore wind farm site compared to the total 41 CPTs

5.8.3 Reducing resolution

The next step was to evaluate how the eight complexity measures responded to profiles of reduced resolution. The full resolution profiles of the eleven CPTs were artificially reduced by increasing the data interval between CPT readings under the double averaging interval method, detailed in Section 3.5.3, from a data interval of 0.1 m (maximum reduced resolution) to 2.5 m (minimum resolution) at intervals of 0.1 m, as was tested in Section 3.5. In order for an equal comparison across CPTs with data points up to the same depth, the data was cut off at a depth of 25 m, incorporating the whole profile used to determine minimum pile dimensions and to match the dimensions used later in Section 5.10. Furthermore, this removed the issue of the smaller data interval at the bottom of the profiles, which would be exacerbated by reducing the resolution, with values also being plotted at the midpoint of such intervals. As reducing the resolution of the CPT profiles was achieved through increasing the data interval between readings, lower resolutions would have significantly fewer data points. This posed a problem for the complexity measures, which often required a certain length of time series data in order to both work and provide meaningful results. For example, entropy measures, such as *SampEn*, *ApEn* and *FuzzEn* had to have a minimum length of ten, equating to a maximum data interval of just under 1.5 m. However, even when this data interval

was maintained, so that the analysis could actually be completed, the output complexity behaved incoherently. Therefore, the sampling rate of the full resolution at constant depth intervals of 0.01 *m* had to be maintained for the reduced resolution profiles. This meant linear interpolation was performed between the reduced resolution data points.

The results for running the complexity measures on CPT101 for the range of data intervals has been displayed graphically in Figure 5.14. All measures follow the predicted trend: a decrease in complexity as data interval increases, although to varying extents. *PermEn* has the greatest level of normalised complexity at full resolution, but still maintains a relatively high level at reduced resolutions. Both *DFA* and *FuzzEn* show a noticeable drop in complexity at data intervals of less than 0.5 *m*, before plateauing at a complexity approaching zero as the data interval increases beyond 1.5 *m*. This change in complexity value between the full resolution CPT profile and that of lower resolutions is what is desired in being able to identify the minimum resolution that adequately captures soil variability for that location and ensures an essentially unchanged pile design compared to the full resolution CPT.

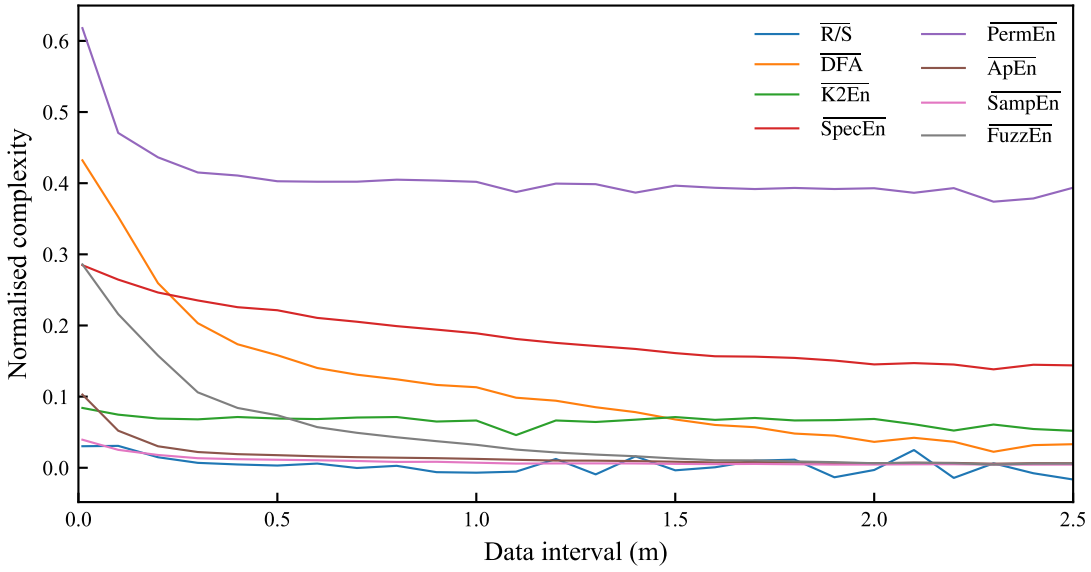

FIGURE 5.14: Effect of CPT profile resolution on normalised complexity for CPT101 within the Burbo Bank Extension offshore wind farm

Another important feature of a complexity measure for CPT profiles, is the sensitivity of complexity to resolution. This can be found from Figure 5.14 as the rate at which the curve plateaus. To assess this rate of decrease further, a re-normalisation of the normalised complexity was plotted, as seen in Figure 5.15. The measures that fall by the largest amount are those that are most sensitive to resolution. These are *DFA*, *ApEn*, *SampEn* and *FuzzEn*. The erratic behaviour of *R/S* analysis has been emphasised, making it an unsuitable measure of complexity.

To ensure that CPT101 was not erroneous in the way it caused the complexity measures to behave, the analysis was also performed on the other ten CPT profiles. Whilst *R/S*

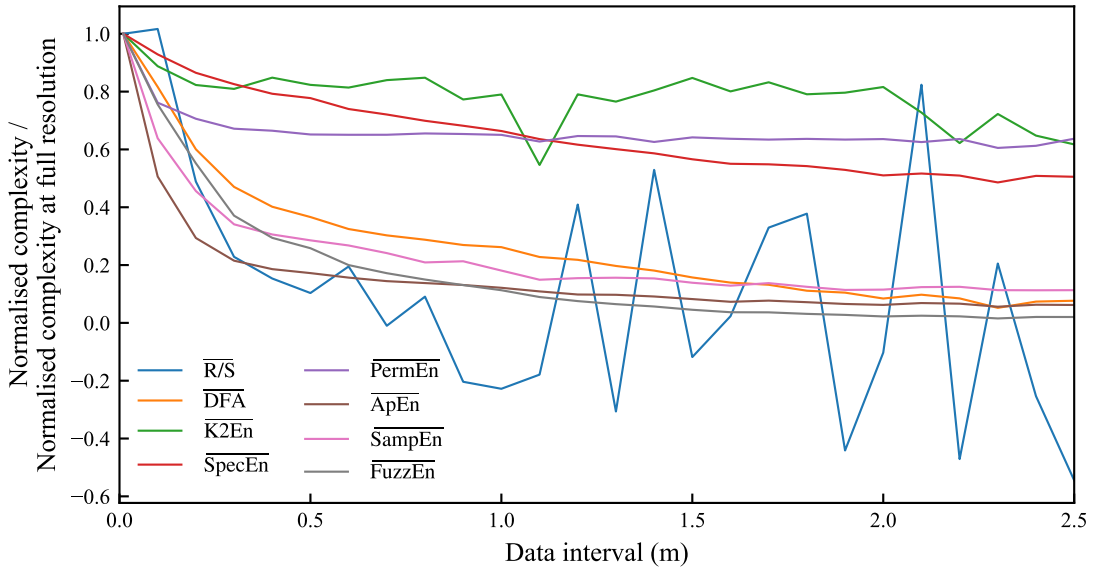

FIGURE 5.15: Effect of CPT profile resolution on re-normalised normalised complexity for CPT101 within the Burbo Bank Extension offshore wind farm

analysis maintained inconsistency and *K2En* demonstrated some variability between CPTS, the remaining complexity measures exhibited the same trends. Therefore, in this analysis, *DFA* and *FuzzEn* were deemed the most suitable, as they exhibit the greatest spread in Figure 5.11 while maintaining sufficient sensitivity to resolution.

5.9 Most suitable complexity measures

Having identified the two most suitable complexity measures in Section 5.8.3 as *DFA* and *FuzzEn*, these were applied to all eleven CPTs for the full range of data intervals. This generated the plots shown in Figures 5.16 and 5.17 for *DFA* and *FuzzEn*, respectively. The length of CPT profile assessed was kept constant at 25 m. Normalised complexity decreases at a decreasing rate towards zero as data interval increases, for all CPTs under both complexity measures. *FuzzEn* reaches its plateau at a smaller data interval of 1.0 m, compared to *DFA*, which does not happen until a 2.0 m data interval. However, the starting normalised complexity for *DFA* is consistently higher than that for *FuzzEn*.

To observe the rate of decrease in complexity with decreasing CPT profile resolution, the re-normalised complexity was also plotted in the same way as in Section 5.8.3. This can be seen in Figures 5.18 and 5.19 for *DFA* and *FuzzEn*, respectively. Overall, the rate of decrease is greatest for *FuzzEn*, suggesting it is more sensitive to resolution, however, the compaction of all the curves in both graphs do not give much indication to the CPT that is most affected by resolution.

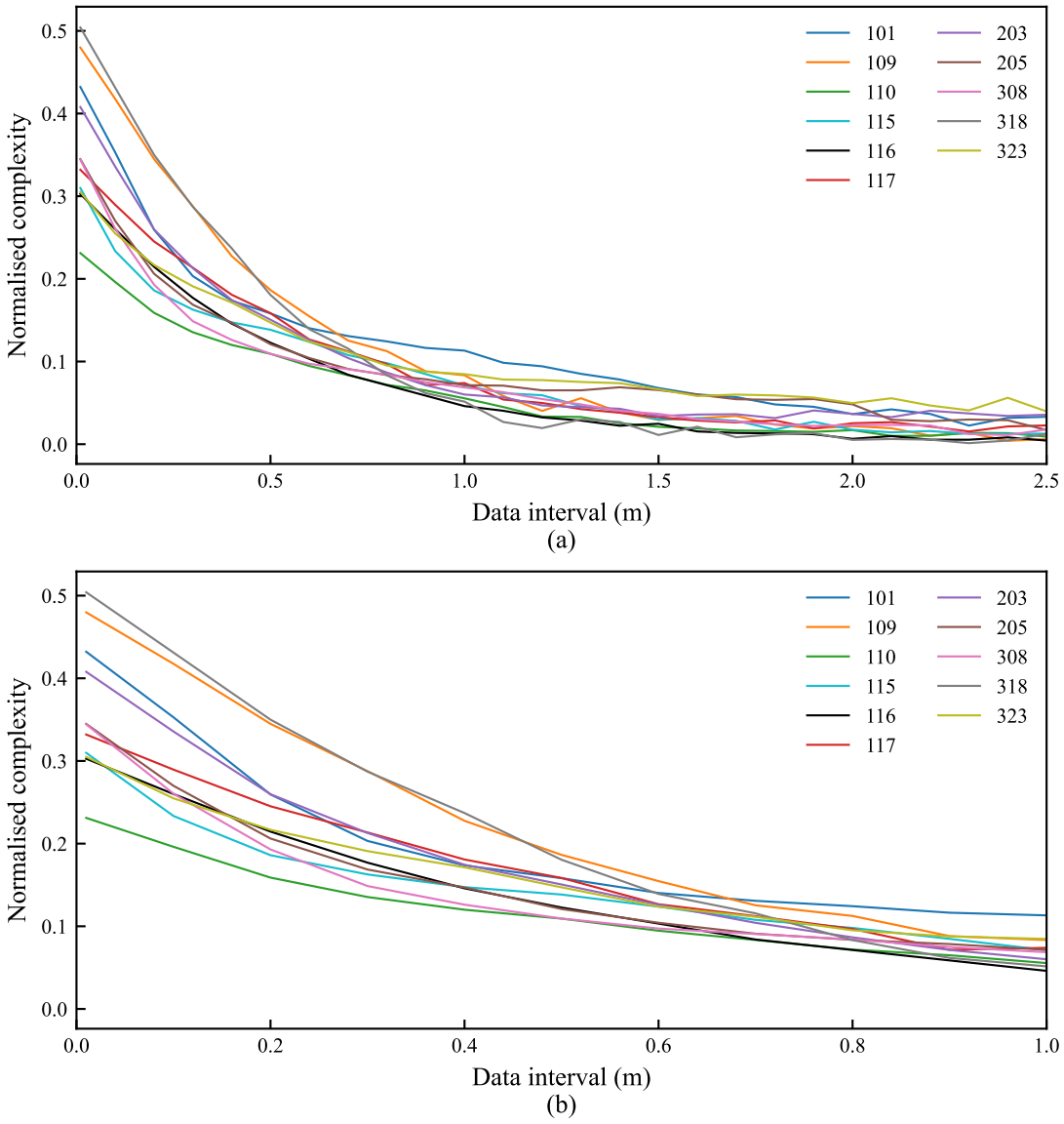

FIGURE 5.16: Effect of CPT profile resolution on normalised *DFA* complexity for CPTs within the Burbo Bank Extension offshore wind farm

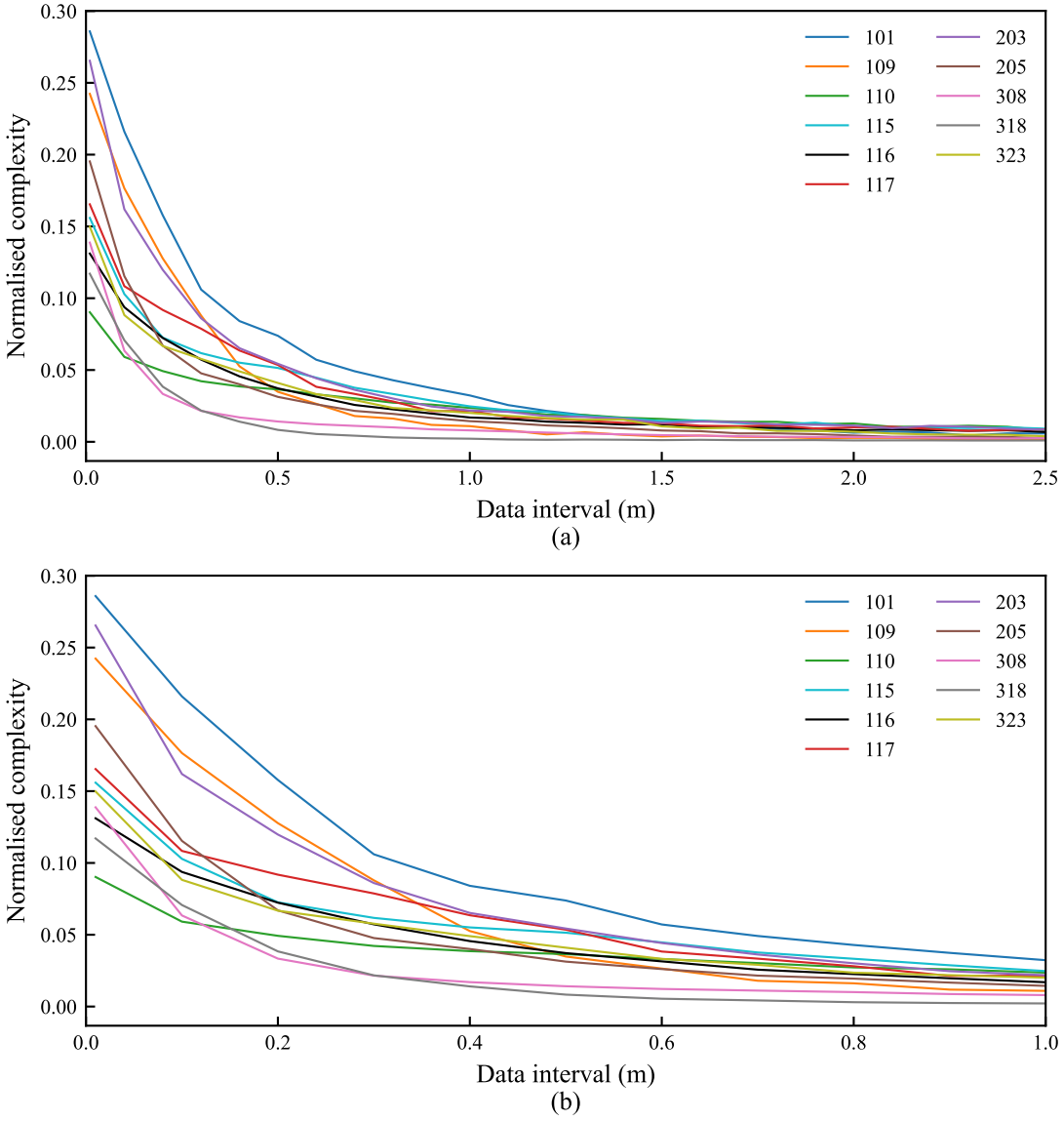

FIGURE 5.17: Effect of CPT profile resolution on normalised *FuzzEn* complexity for CPTs within the Burbo Bank Extension offshore wind farm

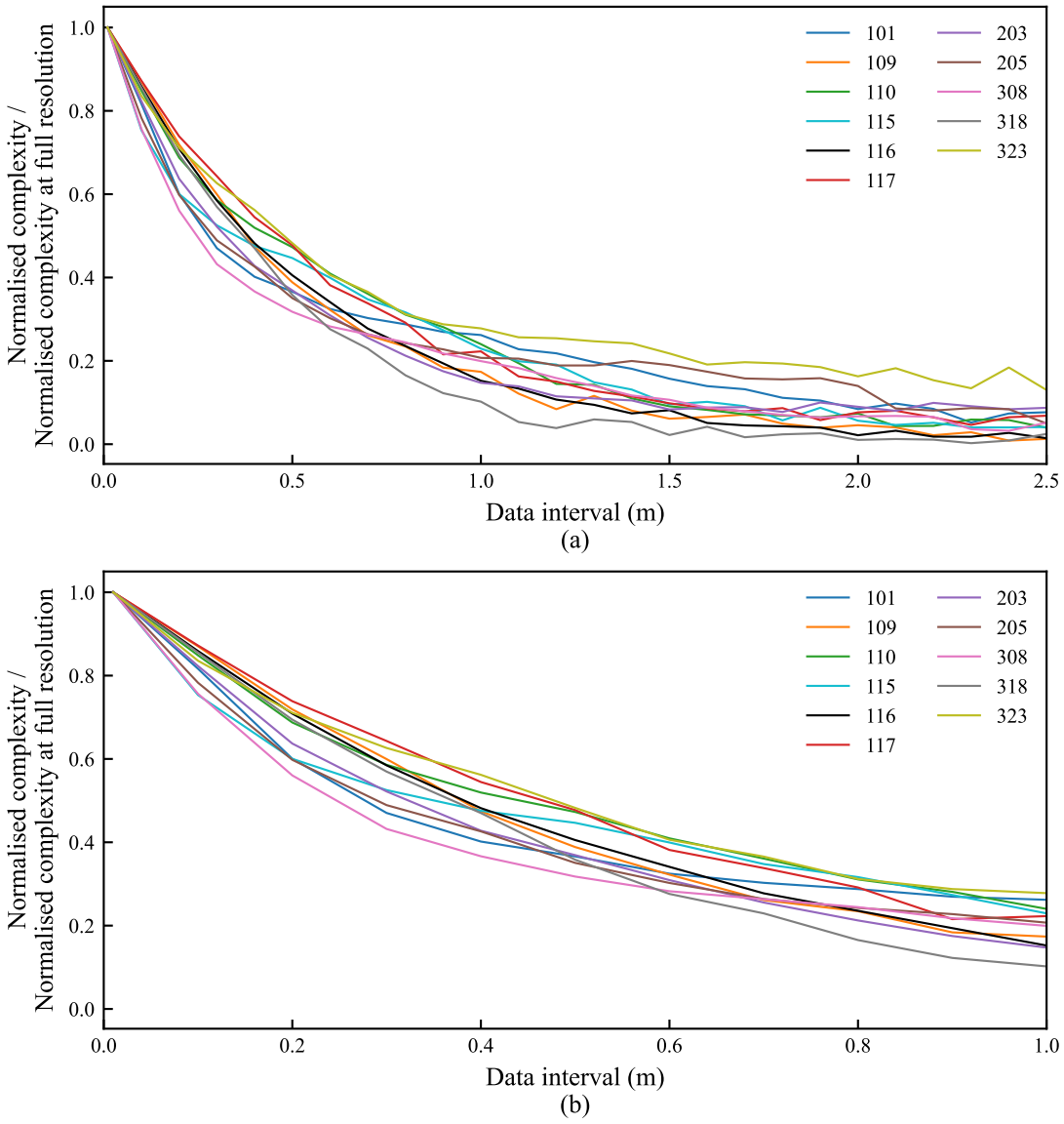

FIGURE 5.18: Effect of CPT profile resolution on re-normalised *DFA* complexity for CPTs within the Burbo Bank Extension offshore wind farm

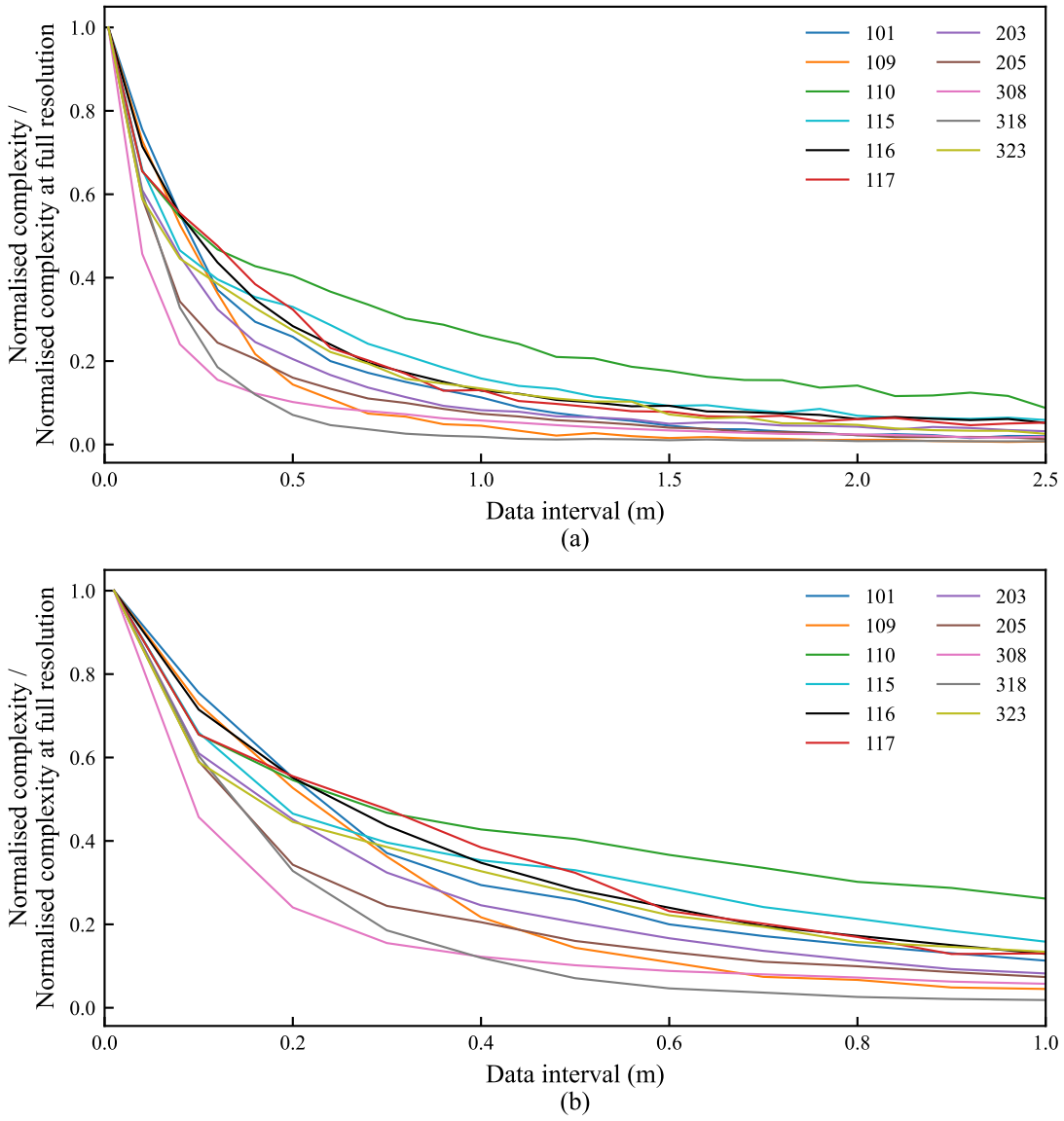

FIGURE 5.19: Effect of CPT profile resolution on re-normalised *FuzzEn* complexity for CPTs within the Burbo Bank Extension offshore wind farm

5.10 Resolution-induced pile design error

A resolution-induced pile design error (RPDE) was established for comparison to the time series complexity measures of *DFA* and *FuzzEn*. This measure was derived from the capacity of a monopile in the reduced resolution CPT soil profile in comparison to that in the actual full resolution soil profile. It is important to note that this normalised pile capacity is calculated in a different way to that in previous chapters. As the reduced resolution CPT profiles generally overestimated soil strength so that piles were generated with smaller dimensions (see Chapter 3), for a given monopile size, this normalised capacity (reduced resolution capacity divided by full resolution capacity) utilises the proportion of overdesign of a monopile. Since optimal pile dimensions are not necessarily known, a pile of length 25 m and diameter 10 m were selected. Whilst this diameter is representative of the optimal diameters predicted in Chapter 3, an assessment of other diameters proved to not significantly affect the results of the RPDE. In this way, the maximum horizontal lateral resistance of the 10 m diameter, 25 m length pile in a range of reducing resolution soil conditions was determined to produce normalised capacities, for each of the eleven CPTs at the Burbo Bank Extension offshore wind farm site, as portrayed in Figure 5.20. The area between a particular curve in Figure 5.20 and the horizontal line at a normalised capacity of one, up to a specified resolution, could then be obtained to convert the capacity into a measure of complexity.

A specified resolution of 2.5 m was taken, including the whole graph in the analysis. The values obtained through the RPDE have been plotted in Figure 5.21(a) in accordance with the CPT ranking, identifying CPT203 as the least complex and CPT323 as the most. Relative RPDE has also been plotted in Figure 5.21(b) to enable comparison to relative *DFA* and *FuzzEn*, which is demonstrated in Figure 5.22. There is no clear relationship between relative RPDE and the relative complexity of *DFA* and *FuzzEn*. However, this could be due to the fact that the RPDE is much more sensitive to a range of geotechnical properties. This includes the chosen pile dimensions, especially pile length which tends to govern design, as well as distance to pivot. The large possibility in selecting a soil profile with depth adds to the vast unknowns, therefore, corrected cone penetration resistance may not be the most appropriate measure to apply the complexity measures to. Perhaps the Burbo Bank Extension site in particular is not a good example in demonstrating the influence of resolution on complexity. Despite a lack of trend connecting the times series measures of complexity to the RPDE, this work has demonstrated the potential of *DFA* and *FuzzEn* in determining the resolution required of synthetic CPTs.

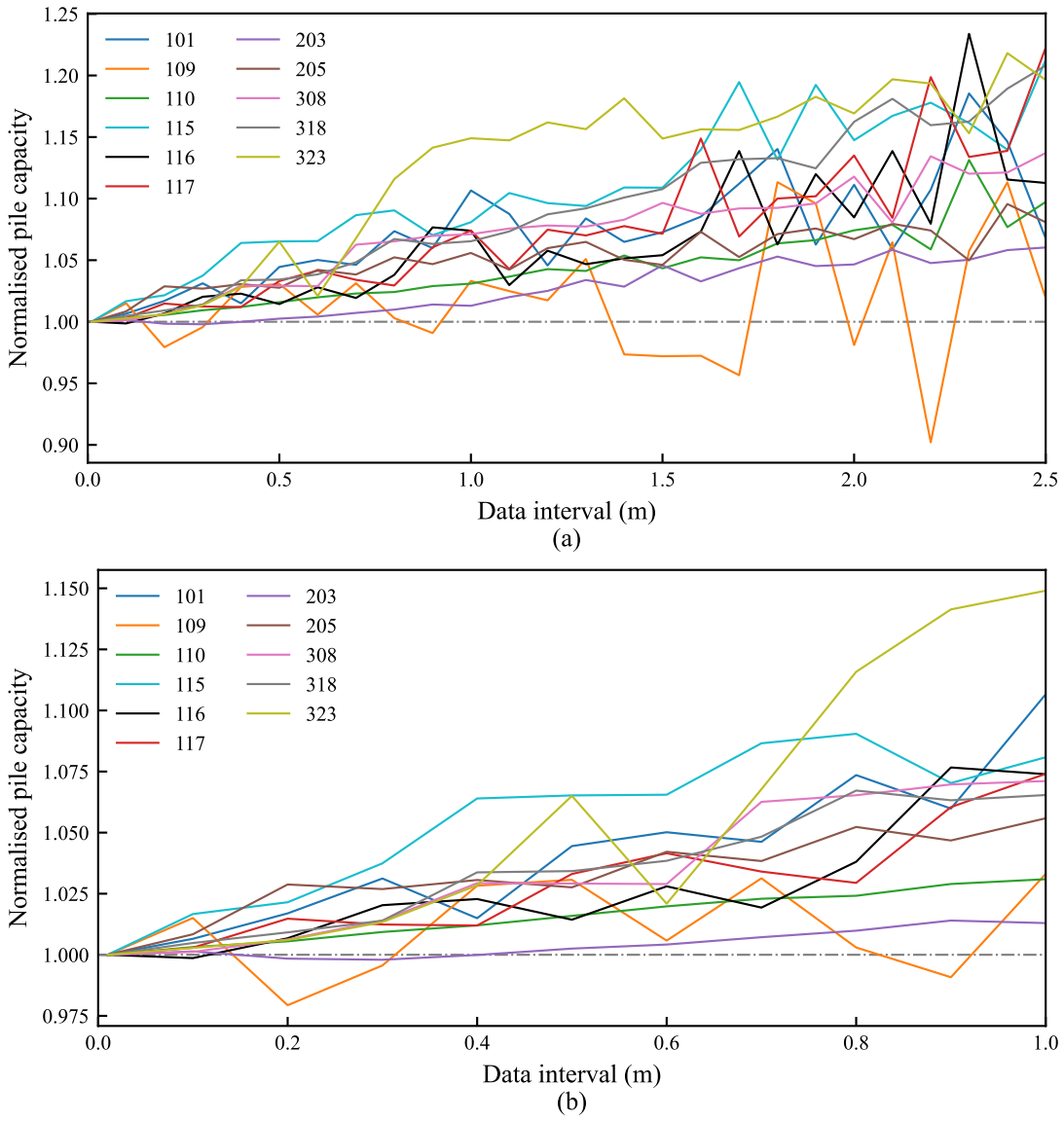

FIGURE 5.20: Effect of CPT profile resolution on pile capacity for selected CPTs within the Burbo Bank Extension offshore wind farm

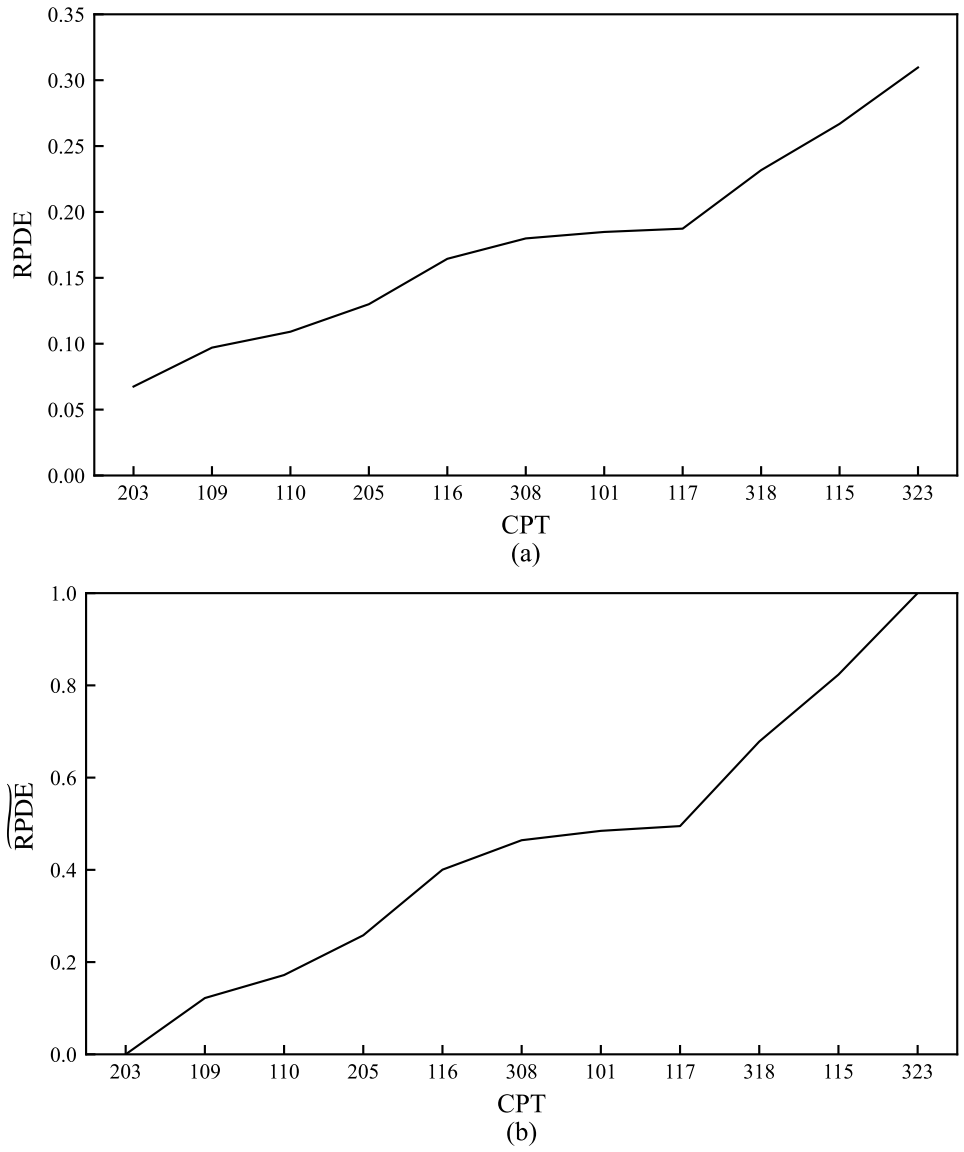

FIGURE 5.21: RPDE and relative RPDE of the selected CPTs within the Burbo Bank Extension offshore wind farm

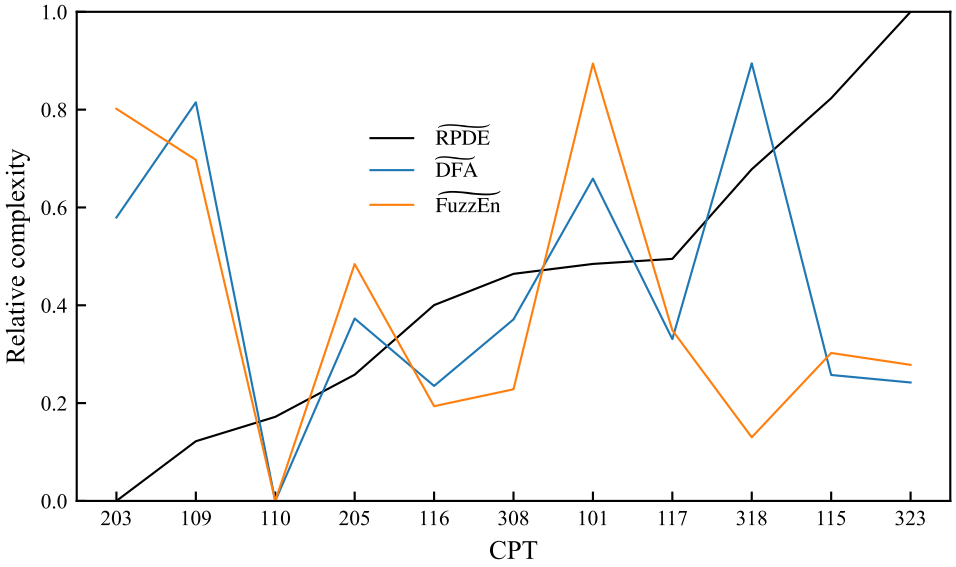

FIGURE 5.22: Relative RPDE compared to relative *DFA* and *FuzzEn* of the selected CPTs within the Burbo Bank Extension offshore wind farm

5.11 Summary

This chapter has utilised the consistent sampling nature in which CPTs are performed that enable the collection of constant profiles of cone penetration resistance with depth. As such, CPT profiles resemble time series data, opening up a whole field of measures in the ways CPT profiles can be quantified. This work focussed on complexity measures, as a means of assessing the required resolution of a synthetic CPT in order for it to be acceptable in pile design. In this way, the effect of CPT profile complexity on the design of monopile foundations for offshore wind turbines was investigated in accordance with **RO3**.

Eight complexity measures were identified as suitable in the context of this work which covered different approaches of complexity through long-term correlations and entropy features. Rescaling and normalisation of these complexity measures had to first be carried out in order to enable comparison between them. This involved the computation of a practical upper limit of each measure based on a time series of maximum complexity. For the purpose of this work, a completely random time series was taken to have maximum complexity, and therefore modelled through white noise (Figure 5.1). The maximum values of each complexity measure under white noise were then used for normalisation through the functions in Table 5.2 so that an output of zero implied zero complexity, and a value of one denoted a completely random system, such as white noise.

The behaviour of the eight selected complexity measures was assessed under simple functions with depth, with the purpose of simulating simplified CPT profiles for which

the complexity was known (see Section 5.5). The sensitivity of these complexity measures to noise was also investigated through both addition and multiplication of noise to two of the simple functions (see Section 5.6). From these analyses, it was found that all eight measures behaved as desired: the starting cone penetration resistance and a single change in soil type did not effect the complexity of the profile, whereas the number of changes in direction did (increased time period in the sine wave function), with an increasing number generating a higher output complexity. Furthermore, the majority of complexity measures were tolerant of small levels of noise, demonstrating a gentle transition between this level and the point at which it begins to be detected, increasing the overall complexity of the profile.

The eight complexity measures were then applied to actual CPT profiles of cone penetration resistance from the Burbo Bank Extension offshore wind farm site. Only the top 20 m of the CPT were considered as this is the section which influences pile design. The complexity of a CPT profile and the range of values exhibited across the site were shown to be dependent on the type of complexity measure (Figure 5.11). The ordering of the complexity of eleven selected CPT locations, representative of those across the whole site, showed some similarities, especially between complexity measures derived from the same theory (e.g. *ApEn*, *SampEn* and *FuzzEn*), but clear trends in terms of the least and most complex CPT profiles were difficult to identify (Figure 5.12).

Artificially reducing the resolution of the eleven selected CPT locations, in accordance with the method of the double averaging interval approach from Chapter 3, and running the eight complexity measures demonstrated a decrease in complexity with reducing resolution (Figure 5.14). This was to be expected as a larger data interval between consecutive readings would simplify the overall shape of the CPT profile. The sensitivity to resolution was obtained through the rate at which complexity decreased with increasing resolution and the extent of such a decrease. The two complexity measures with the greatest sensitivity to resolution were identified to be *DFA* and *FuzzEn* (Figure 5.15).

To evaluate the suitability of *DFA* and *FuzzEn* in geotechnical data, a resolution-induced pile design error (RPDE) was established using the capacity of a given sized monopile, in this case 10 m diameter and 25 m length. The ranking of CPT profiles in terms of complexity under the RPDE was compared to the trends of complexity with reducing resolution for *DFA* and *FuzzEn*. However, the compaction of all eleven CPT profile curves in both *DFA* and *FuzzEn* graphs did not give much indication to the CPT that was most affected by resolution. As a result, a possible conclusion was that the Burbo Bank Extension wind farm site did not include CPTs that were very sensitive to complexity, since a relatively large data interval was still proven to be acceptable.

Furthermore, the degree of geotechnical parameters that influence design was potentially deemed to be too great, in which *DFA* and *FuzzEn* were unable to capture. In

combination with the results from Chapter 4 that showed soil type played a larger role in the effect on pile outcomes than the cone penetration resistance profile, it was also surmised that resolution may not be the driving factor behind complexity. As such, further research into the relationship between soil type classification and complexity should be investigated.

Chapter 6

Conclusions and guidance in design

6.1 Conclusions

The aim of this thesis was to advance the implementation of synthetic CPTs in the design of offshore wind turbine monopile foundations, which has been demonstrated through the exploration of the implications of in situ geotechnical reduced resolution CPT profiles, synthetic CPT profiles, and the complexity of CPT profiles, on the design of offshore wind turbine monopile foundations under lateral loading ultimate limit state design, through **RO1**, **RO2**, and **RO3**, respectively. Together, these investigations have contributed to narrowing the gap between theoretical developments in synthetic CPT generation and their practical application in the geotechnical design of monopile foundations for offshore wind turbines under lateral loading.

The impact of reducing CPT profile resolution was assessed through geotechnical CPTs at the Burbo Bank Extension wind farm site. It was shown that artificially reducing CPT profile resolution through a double averaging interval method, led to more consistent design outcomes by mitigating randomness and dependency on profile starting depth. This method also aligned with sampling theory principles, ensuring no aliasing occurred. The reduction in resolution generally resulted in decreased minimum pile volumes, attributed to the omission of weaker soil layers and an apparent increase in lateral soil resistance. The relationship between pile volume and capacity was found to be non-linear, with reductions in pile capacity not directly proportional to reductions in pile volume. Furthermore, reduced resolution profiles improved the accuracy of soil properties between CPT locations, compared to standard linear interpolation, highlighting the benefit of synthetic CPTs in site characterisation.

The analysis was extended to involve the comparison of geotechnical in situ CPTs with co-located synthetic CPTs at the TNW offshore wind farm site. Synthetic CPTs were found to replicate the general trends of in situ profiles with reasonable accuracy, despite having lower vertical resolution. Soil classification from synthetic profiles was

also largely accurate, though discrepancies in soil type were more influential on design outcomes than differences in cone penetration resistance profiles. The synthetic profiles led to both increases and decreases in predicted pile volumes and capacities, again reinforcing the non-linear relationship between these parameters. Furthermore, the percentage of incorrect soil classification was positively correlated with increases in pile volume and capacity, highlighting the sensitivity of design to soil type prediction. In terms of serviceability limit state design, the effect on lateral deformations of the ULS designed pile from the synthetic CPT was compared to that of the geotechnical CPT. Furthermore, the predicted lateral deformations of the ULS designed pile from the synthetic CPT was compared when implemented into the in situ and synthetic soils. In both scenarios, variations in the deformations were minimal and tended to decrease as the proportion of incorrect soil type increased.

The complexity of a CPT profile was assessed through the application of time series complexity measures to the depth series of CPT profiles. Eight complexity measures were selected, including correlation and entropy-based approaches. These were normalised using a white noise benchmark to allow meaningful comparison. The behaviour of these measures was validated using simplified CPT functions and noise sensitivity tests, confirming their ability to detect meaningful structural changes while remaining tolerant to low levels of noise. Application of these measures to actual CPT profiles from the Burbo Bank Extension site revealed that complexity varied across the site and was dependent on the chosen measure. Whilst some consistency was observed among measures derived from similar theoretical bases, identifying clear trends in profile complexity proved challenging. Resolution reduction led to an expected decrease in complexity, with *DFA* and *FuzzEn* showing the greatest sensitivity. However, when compared to a geotechnically informed ranking based on pile capacity, *DFA* and *FuzzEn* did not clearly identify profiles most affected by resolution, suggesting that the site may not contain CPTs highly sensitive to complexity. It was also proposed that the influence of geotechnical parameters on design may outweigh the role of complexity, and that soil type classification may be a more critical factor. This aligns with findings from synthetic CPTs and points to the need for further research into the relationship between soil classification and complexity.

6.2 Guidance in design

The conclusions of this thesis can be used to inform on guidance in the ultimate limit state design of monopile foundations for offshore wind turbines under lateral loading. In particular, the following results can give confidence in the use of synthetic CPTs on sites with similar geology to Burbo Bank Extension or TNW offshore wind farm sites, as well as help calibrate any modifications to partial factors.

- For reduced resolution CPT profiles with a data interval no greater than 0.5 m, pile volume is underpredicted by no more than 3 %, with capacity underpredicted by no more than 7 %.
- For synthetic CPT profiles with a data interval no greater than 1 m, predicted pile volume is within 3 %, with predicted capacity within 7 %.
- Using synthetic CPT profiles to predict rotations has minimal impact, with results remaining well within 10 % of prediction carried out with geotechnical CPTs.

It should be noted that the largest discrepancies in predictions using synthetic CPTs occurred when incorrect soil types were identified. Therefore, it is recommended that designers focus on this aspect of CPT interpretation and further development of synthetic CPTs aim to reduce the frequency at which this occurs.

For sites far from these case study locations, the results listed above give a starting point that can be used in lieu of additional information. This may be suitable if the geology and/or complexity of CPTs on the site are similar. Complexity of CPT profiles is best derived from time series complexity measures of *DFA* and *FuzzEn*. However, if the site is not similar, or an alternative foundation type is being considered, the approaches employed in Chapters 3 and 4 can be used to assess the sensitivity of a design to the use of synthetic CPTs.

6.3 Further work

The workflows and methodologies developed in this work serve as proof-of-concept approaches for monopile foundations of offshore wind turbines in soils consisting of interbedded sands and lightly overconsolidated, low plasticity clay that are highly heterogenous with depth and laterally, such as at the Burbo Bank Extension and TNW offshore wind farm sites. Further research should involve the application to a broader range of foundation and anchor types, loading conditions, limit states, and seabed environments, as well as assessing the effect on different methods of generating synthetic CPTs of varying quality. Some specific analyses include:

- Comparing soil type classification approaches, such as through direct interpretation of geophysical data, as opposed to using both synthetic cone penetration resistance and synthetic sleeve friction data to derive normalised parameters and obtain the Soil Behaviour Type Index (Equation 2.10).
- Use synthetic pore water pressure profiles to calculate excess pore water pressure ratio to plot on $Q_t - B_q$ Robertson chart (Figure 2.12) for confirmation of soil type.

- Test classified CPT profiles, i.e. synthetic CPT profiles that exhibit a range of possible values rather than a single estimation at each depth increment. Therefore, run the analysis for both the upper and lower bounds and determine whether they give the same soil type and pile dimensions. This approach allows for uncertainties in exact synthetic CPT parameters.
- Assess the impact of modifying parameters of the different complexity functions employed in this work.
- Measure complexity of CPT sleeve friction or other derived parameters such as normalised cone resistance or soil classification index, rather than cone penetration resistance.
- Assess how complexity measures are sensitive to the length of the CPT profile.

References

Ahayan, S., Kotronis, P., Yin, Z.-Y., Cerfontaine, B., & Collin, F. (2019). Study of the Behavior of Offshore Wind Turbine Monopiles under Monotonic and Cyclic Lateral Loading. In P. Kotronis (Ed.), *Risk Evaluation and Climate Change Adaptation of Civil Engineering Infrastructures and Buildings* (pp. 57–83). Wiley, 1 edition. https://doi.org/10.1002/9781119671428.ch2.

Alexander, N. A. & Bhattacharya, S. (2011). The dynamics of monopile-supported Wind Turbines in nonlinear soil. In *Proceedings of the 8th International Conference on Structural Dynamics, EURODYN 2011*, number January (pp. 3416–3422). Leuven, Belgium.

Alvarez-Ramirez, J., Rodriguez, E., & Carlos Echeverria, J. (2009). A DFA approach for assessing asymmetric correlations. *Physica A: Statistical Mechanics and its Applications*, *388*(12), 2263–2270, https://doi.org/10.1016/j.physa.2009.03.007.

American Institute of Steel Construction (2017). *Steel Construction Manual*. United States of America: American Institute of Steel Construction, 15 edition.

Anastassopoulos, C., Charles, J., Crispin, J., Henstock, T., Vardy, M., & Gourvenec, S. (2025a). Understanding the effect of CPT resolution on calculated lateral pile resistance to assist adoption of synthetic CPTs in geotechnical design. *Geoenergy*, https://doi.org/10.1144/geoenergy2025-022.

Anastassopoulos, C., Charles, J., & Gourvenec, S. (2023). Effect of CPT profile resolution on minimum required size of monopile for ultimate limit state design. In *9th International SUT Offshore Site Investigation Geotechnics Conference Proceedings* (pp. 393–400).: Society of Underwater Technology. https://doi.org/10.3723/IPLP6449.

Anastassopoulos, C., Crispin, J., Vardy, M., Henstock, T., & Gourvenec, S. (2025b). Assessment of Synthetic CPTs in Monopile Design for Offshore Wind Turbines: A Case Study. In *Sixth EAGE Global Energy Transition Conference & Exhibition (GET 2025)* (pp. 1–5). Rotterdam, Netherlands,: European Association of Geoscientists & Engineers. https://doi.org/10.3997/2214-4609.202521144.

Andrew, R. M. & Peters, G. P. (2021). The Global Carbon Project's fossil CO2 emissions dataset. *Zenodo*, https://doi.org/10.5281/zenodo.5569235.

Arany, L., Bhattacharya, S., Macdonald, J., & Hogan, S. (2017). Design of monopiles for offshore wind turbines in 10 steps. *Soil Dynamics and Earthquake Engineering*, *92*, 126–152, https://doi.org/10.1016/j.soildyn.2016.09.024.

Atkinson, J. (2007). *The Mechanics of Soils and Foundations, Second Edition*. CRC Press.

Audibert, J. M. & Huang, J. (2005). Geophysical and Geotechnical Design. In *Handbook of Offshore Engineering* (pp. 1145–1268). Elsevier. https://doi.org/10.1016/B978-0-08-044381-2.50023-0.

Azami, H., Li, P., Arnold, S. E., Escudero, J., & Humeau-Heurtier, A. (2019). Fuzzy Entropy Metrics for the Analysis of Biomedical Signals: Assessment and Comparison. *IEEE Access*, *7*, 104833–104847, https://doi.org/10.1109/ACCESS.2019.2930625.

Bai, Y. & Bai, Q. (2019). Subsea Surveying, Positioning, and Foundation. In *Subsea Engineering Handbook* (pp. 81–121). Elsevier. https://doi.org/10.1016/B978-0-12-812622-6.00004-X.

Bandt, C. & Pompe, B. (2002). Permutation Entropy: A Natural Complexity Measure for Time Series. *Physical Review Letters*, *88*(17), 174102, https://doi.org/10.1103/PhysRevLett.88.174102.

Bassingthwaighte, J. B. & Raymond, G. M. (1994). Evaluating rescaled range analysis for time series. *Annals of Biomedical Engineering*, *22*(4), 432–444, https://doi.org/10.1007/BF02368250.

Bhattacharya, S. (2014). Challenges in Design of Foundations for Offshore Wind Turbines. *Engineering & Technology Reference*, https://doi.org/10.1049/etr.2014.0041.

Bhattacharya, S. (2019). *Design of Foundations for Offshore Wind Turbines*. Wiley, 1 edition.

Bolève, A., Eddies, R., Staring, M., Benboudiaf, Y., Pournaki, H., & Nepveaux, M. (2025). Innovative cone resistance and sleeve friction prediction from geophysics based on a coupled geo-statistical and machine learning process. *Artificial Intelligence in Geosciences*, *6*(1), https://doi.org/10.1016/j.aiig.2025.100110.

Box, G. E. P., Jenkins, G. M., Reinsel, G. C., & Ljung, G. M. (2015). *Time Series Analysis: Forecasting and Control*. Wiley Series in Probability and Statistics. Hoboken, New Jersey: Wiley, fifth edition edition.

Briaud, J.-L. (2013). *Geotechnical Engineering: Unsaturated and Saturated Soils*. Wiley, 1 edition.

Brockwell, P. J. & Davis, R. A. (2016). *Introduction to Time Series and Forecasting*. Springer Texts in Statistics. Cham: Springer International Publishing, 3 edition.

Bryce, R. M. & Sprague, K. B. (2012). Revisiting detrended fluctuation analysis. *Scientific Reports*, *2*(1), 315, https://doi.org/10.1038/srep00315.

Burd, H. J., et al. (2020). PISA design model for monopiles for offshore wind turbines: Application to a marine sand. *Géotechnique*, *70*(11), 1048–1066, https://doi.org/10.1680/jgeot.18.P.277.

Byrne, B., et al. (2015). New design methods for large diameter piles under lateral loading for offshore wind applications. In *Proceedings of the 3rd International Symposium on Frontiers in Offshore Geotechnics* (pp. 705–710). Oslo, Norway. https://doi.org/10.1201/b18442-96.

Byrne, B. W., et al. (2019). PISA Design Methods for Offshore Wind Turbine Monopiles. In *Offshore Technology Conference* (pp. D011S005R002). Houston, Texas: OTC. https://doi.org/10.4043/29373-MS.

Byrne, B. W. & Houlsby, G. T. (2003). Foundations for offshore wind turbines. *Philosophical Transactions of the Royal Society of London. Series A: Mathematical, Physical and Engineering Sciences*, *361*(1813), 2909–2930, https://doi.org/10.1098/rsta.2003.1286.

Byrne, B. W., et al. (2020). PISA design model for monopiles for offshore wind turbines: Application to a stiff glacial clay till. *Géotechnique*, *70*(11), 1030–1047, https://doi.org/10.1680/jgeot.18.P.255.

Campanella, R. G., Gillespie, D., & Robertson, P. K. (1982). Pore pressures during cone penetration testing. In *2nd European Symposium on Penetration Testing* (pp. 507–512). Amsterdam, The Netherlands.

Carpentier, S., et al. (2021). Generating synthetic CPTs from marine seismic reflection data using a neural network approach. In *Second EAGE Workshop on Machine Learning* (pp. 1–3). Online,: European Association of Geoscientists & Engineers. https://doi.org/10.3997/2214-4609.202132008.

CCC (2021). *Progress in Reducing Emissions: 2021 Report to Parliament*. Technical Report June, Climate Change Committee.

Charles, J., Axtell, D., & Gourvenec, S. (2023). Quantitative analysis approach to assess variability in seabed conditions across a large offshore windfarm site. In *9th International SUT Offshore Site Investigation Geotechnics Conference Proceedings* (pp. 216–223).: Society of Underwater Technology. https://doi.org/10.3723/GNIE4326.

Chatfield, C., Ed. (2003). *The Analysis of Time Series: An Introduction*. Chapman & Hall/CRC Texts in Statistical Science Series. Boca Raton: Chapman & Hall/CRC, 6. ed edition.

Chen, J., Vissinga, M., Shen, Y., Hu, S., Beal, E., & Newlin, J. (2021). Machine Learning–Based Digital Integration of Geotechnical and Ultrahigh–Frequency Geophysical

Data for Offshore Site Characterizations. *Journal of Geotechnical and Geoenvironmental Engineering*, *147*(12), https://doi.org/10.1061/(ASCE)GT.1943-5606.0002702.

Chen, W., Wang, Z., Xie, H., & Yu, W. (2007). Characterization of Surface EMG Signal Based on Fuzzy Entropy. *IEEE Transactions on Neural Systems and Rehabilitation Engineering*, *15*(2), 266–272, https://doi.org/10.1109/TNSRE.2007.897025.

Chen, W., Zhuang, J., Yu, W., & Wang, Z. (2009). Measuring complexity using FuzzyEn, ApEn, and SampEn. *Medical Engineering & Physics*, *31*(1), 61–68, https://doi.org/10.1016/j.medengphy.2008.04.005.

COP (2015). *COP21 The Paris Agreement*. Technical report, United Nations Climate Change.

COP (2021). *COP26 The Glasgow Climate Pact*. Technical report, United Nations Climate Change.

CORE (2015). *Building Offshore Wind in England*. Technical report, Centres for Offshore Renewable Engineering.

Cox, P., et al. (2024). Nederwiek Zuid (NL) Integrated Ground Model: AVO-Compliant UHRS Processing for Elastic Pre-Stack Inversion. In *First EAGE/SUT Workshop on Integrated Site Characterization for Offshore Renewable Energy*, volume 2024 (pp. 1–6). Boston, Massachusetts, United States: European Association of Geoscientists & Engineers. https://doi.org/10.3997/2214-4609.202480019.

Delgado-Bonal, A. & Marshak, A. (2019). Approximate Entropy and Sample Entropy: A Comprehensive Tutorial. *Entropy*, *21*(6), 541, https://doi.org/10.3390/e21060541.

Di Matteo, T. (2007). Multi-scaling in finance. *Quantitative Finance*, *7*(1), 21–36, https://doi.org/10.1080/14697680600969727.

Doherty, J. P. (2020). Lateral Analysis of Piles User Manual.

Doherty, P. & Gavin, K. (2012). Laterally loaded monopile design for offshore wind farms. *Proceedings of the Institution of Civil Engineers - Energy*, *165*(1), 7–17, https://doi.org/10.1680/ener.11.00003.

DONG Energy (2013). *Burbo Bank Extension Offshore Wind Farm (BBW02) Substations SSC , Geotechnical Site Investigation*. Technical Report June, DONG Energy.

DONG Energy (2014). *Burbo Bank Extension Offshore Wind Farm (BBW02) Geotechnical Site Investigation (2014), Geotechnical Site Investigation Fieldwork Report, Part B – Geotechnical Data*. Technical Report June, DONG Energy.

Flood, M. W. (2024). The EntropyHub Guide: A user manual for the EntropyHub toolkit.

Forsberg, C. F., Lunne, T., Vanneste, M., James, L., Tjelta, T. I., Barwise, A., & Duffy, C. (2017). Synthetic Cpts from Intelligent Ground Models Based on the Integration of Geology, Geotechnics and Geophysics as a Tool for Conceptual Foundation Design and Soil Investigation Planning. In *8th International SUT Offshore Site Investigation Geotechnics Conference* (pp. 1254–1259). London, UK: Society for Underwater Technology. https://doi.org/10.3723/OSIG17.1254.

Friedlingstein, P., et al. (2022). Global Carbon Budget 2021. *Earth System Science Data*, *14*(4), 1917–2005, https://doi.org/10.5194/essd-14-1917-2022.

Fugro (2020). *Geotechnical Survey - Seafloor In Situ Test Locations Report: Ten Noorden van de Waddeneilanden Wind Farm Zone*. Technical report, Netherlands Enterprise Agency.

Gao, L., Wang, J., & Chen, L. (2013). Event-related desynchronization and synchronization quantification in motor-related EEG by Kolmogorov entropy. *Journal of Neural Engineering*, *10*(3), 036023, https://doi.org/10.1088/1741-2560/10/3/036023.

Ge, M. & Friedrich, J. (2024). Climate Watch Country Greenhouse Gas Emissions Data and Methodology. *World Resources Institute*, https://doi.org/10.46830/writn.20.00105.

Gneiting, T., Ševčíková, H., & Percival, D. B. (2012). Estimators of Fractal Dimension: Assessing the Roughness of Time Series and Spatial Data. *Statistical Science*, *27*(2), 247–277, https://doi.org/10.1214/11-STS370.

Gourvenec, S. (2024). Offshore geotechnical challenges of the energy transition. *Geomechanics for Energy and the Environment*, *39*, https://doi.org/10.1016/j.gete.2024.100584.

Grassberger, P. & Procaccia, I. (1983). Estimation of the Kolmogorov entropy from a chaotic signal. *Physical Review A*, *28*(4), 2591–2593, https://doi.org/10.1103/PhysRevA.28.2591.

Guo, F., Lehane, B., & Ju, J. (2014). Experimentally derived CPT-based p-y curves for soft clay. In *Third International Symposium on Cone Penetration Testing* (pp. 1021–1028).

GWEC (2022). *Global Wind Report 2022*. Technical report, Global Wind Energy Council.

GWEC (2024). *Global Offshore Wind Report 2024*. Technical report, Global Wind Energy Council, Brussels.

Hardstone, R., Poil, S.-S., Schiavone, G., Jansen, R., Nikulin, V. V., Mansvelder, H. D., & Linkenkaer-Hansen, K. (2012). Detrended Fluctuation Analysis: A Scale-Free View on Neuronal Oscillations. *Frontiers in Physiology*, *3*, https://doi.org/10.3389/fphys.2012.00450.

HM Government (2022). *British Energy Security Strategy*. Technical Report April, HM Government.

Houlsby, G. T. (2016). Interactions in offshore foundation design. *Géotechnique*, *66*(10), 791–825, https://doi.org/10.1680/jgeot.15.RL.001.

Ihlen, E. A. F. (2012). Introduction to Multifractal Detrended Fluctuation Analysis in Matlab. *Frontiers in Physiology*, *3*, https://doi.org/10.3389/fphys.2012.00141.

Inouye, T., et al. (1991). Quantification of EEG irregularity by use of the entropy of the power spectrum. *Electroencephalography and Clinical Neurophysiology*, *79*(3), 204–210, https://doi.org/10.1016/0013-4694(91)90138-T.

IPCC (2014). *Impacts, Adaption, and Vulnerability - Part A: Global and Sectoral Aspects*. Technical report, Intergovernmental Panel on Climate Change.

IPCC (2023). *Synthesis Report of the IPPC Sixth Assessment Report (AR6): Summary for Policymakers*. Technical report, Intergovernmental Panel on Climate Change, Geneva, Switzerland. https://doi.org/10.59327/IPCC/AR6-9789291691647.

IRENA & GWEC (2021). *A next Decade Action Agenda to Advance SDG7 on Sustainable Energy for All, in Line with the Goals of the Paris Agreement on Climate Change*. Technical report, International Renewable Energy Agency and Global Wind Energy Council.

Jamiolkowski, M., Lo Presti, D. C. F., & Manassero, M. (2003). Evaluation of Relative Density and Shear Strength of Sands from CPT and DMT. In *Soil Behavior and Soft Ground Construction* (pp. 201–238). Cambridge, Massachusetts, United States: American Society of Civil Engineers. https://doi.org/10.1061/40659(2003)7.

Jefferies, M. & Davies, M. (1993). Use of CPTu to Estimate Equivalent SPT *N* 60. *Geotechnical Testing Journal*, *16*(4), 458–468, https://doi.org/10.1520/GTJ10286J.

Kallehave, D., Byrne, B. W., LeBlanc Thilsted, C., & Mikkelsen, K. K. (2015). Optimization of monopiles for offshore wind turbines. *Philosophical Transactions of the Royal Society A: Mathematical, Physical and Engineering Sciences*, *373*(2035), 20140100, https://doi.org/10.1098/rsta.2014.0100.

Kantelhardt, J. W., Koscielny-Bunde, E., Rego, H. H., Havlin, S., & Bunde, A. (2001). Detecting long-range correlations with detrended fluctuation analysis. *Physica A: Statistical Mechanics and its Applications*, *295*(3-4), 441–454, https://doi.org/10.1016/S0378-4371(01)00144-3.

Kantelhardt, J. W., Zschiegner, S. A., Koscielny-Bunde, E., Havlin, S., Bunde, A., & Stanley, H. (2002). Multifractal detrended fluctuation analysis of nonstationary time series. *Physica A: Statistical Mechanics and its Applications*, *316*(1-4), 87–114, https://doi.org/10.1016/S0378-4371(02)01383-3.

Keaveny, J. (1985). *In-Situ Determination of Drained and Undrained Soil Strength Using the Cone Penetration Test*. PhD thesis, University of California, Berkeley, Berkeley, CA, USA.

Klinkvort, R., Sauvin, G., Dujardin, J., Griffiths, L., Vardy, M., & Vanneste, M. (2024). Cone Penetration Testing Prediction Using Seismo-Acoustic Data. In *85th EAGE Annual Conference & Exhibition* (pp. 1–5). Oslo, Norway: European Association of Geoscientists & Engineers. https://doi.org/10.3997/2214-4609.2024101434.

Knappett, J. A. & Craig, R. F. (2020). *Craig's Soil Mechanics*. Boca Raton London New York: CRC Press, Taylor & Francis Group, ninth edition edition.

Kristoufek, L. (2010). Rescaled Range Analysis and Detrended Fluctuation Analysis: Finite Sample Properties and Confidence Intervals. *Czech Economic Review*, *4*, 236–250.

Lacis, A. A., Schmidt, G. A., Rind, D., & Ruedy, R. A. (2010). Atmospheric CO_2 : Principal Control Knob Governing Earth's Temperature. *Science*, *330*(6002), 356–359, https://doi.org/10.1126/science.1190653.

Lake, D. E., Richman, J. S., Griffin, M. P., & Moorman, J. R. (2002). Sample entropy analysis of neonatal heart rate variability. *American Journal of Physiology-Regulatory, Integrative and Comparative Physiology*, *283*(3), R789–R797, https://doi.org/10.1152/ajpregu.00069.2002.

Lan, X., Tans, P., & Thoning, K. (2025). Trends in globally-averaged CO2 determined from NOAA Global Monitoring Laboratory measurements. https://doi.org/10.15138/9N0H-ZH07.

Leblanc, C., Houlsby, G., & Byrne, B. (2010). Response of stiff piles in sand to long-term cyclic lateral loading. *Géotechnique*, *60*(2), 79–90, https://doi.org/10.1680/geot.7.00196.

Lehane, B. M. (2019). E.H. Davis Memorial Lecture (2017): CPT-based design of foundations. *Australian Geomechanics*, *54*(4), 23–48.

Lesny, K. & Wiemann, J. (2005). Design aspects of monopiles in German offshore wind farms. In *Proceedings of the 1st International Symposium on Frontiers in Offshore Geotechnics* (pp. 383–389). https://doi.org/10.1201/NOE0415390637.ch37.

Li, T.-Y. & Yorke, J. A. (1975). Period Three Implies Chaos. *The American Mathematical Monthly*, *82*(10), 985–992, https://doi.org/10.1080/00029890.1975.11994008.

Lipsitz, L. A. & Goldberger, A. L. (1992). Loss of 'Complexity' and Aging: Potential Applications of Fractals and Chaos Theory to Senescence. *JAMA*, *267*(13), 1806–1809.

Lopes, R. & Betrouni, N. (2009). Fractal and multifractal analysis: A review. *Medical Image Analysis*, *13*(4), 634–649, https://doi.org/10.1016/j.media.2009.05.003.

Malhotra, S. (2009). Design and Construction Considerations for Cffshore Wind Turbine Foundations in North America. *Civil Engineering Practice: Journal of the Boston Society of Civil Engineers Section/ASCE*, *Spring/Sum*, 6–42.

Mandelbrot, B. B. (1977). *Fractals: Form, Chance, and Dimension*. San Francisco: W.H. Freeman.

Marine Data Exchange (2014). 2014, Fugro Engineering Services, Burbo Bank Extension Offshore Wind Farm, Geotechnical Site Investigation.

Matlock, H. (1970). Correlation for Design of Laterally Loaded Piles in Soft Clay. In *Proceedings of the Offshore Technology Conference* (pp. OTC–1204–MS). Houston, Texas: OTC. https://doi.org/10.4043/1204-MS.

Mayne, P. W. (2007). *Cone Penetration Testing State-of-Practice*. Technical Report NCHRP Project 20-05.

Mayne, P. W. & Rix, G. J. (1993). *G* max-*qc* Relationships for Clays. *Geotechnical Testing Journal*, *16*(1), 54–60, https://doi.org/10.1520/GTJ10267J.

Micallef, A. (2011). Marine Geomorphology: Geomorphological Mapping and the Study of Submarine Landslides. In *Developments in Earth Surface Processes*, volume 15 (pp. 377–395). Elsevier. https://doi.org/10.1016/B978-0-444-53446-0.00013-6.

MMT (2020). *3D Geophysical Ultra High Resolution Survey (UHRS) Report: Ten Noorden van de Waddeneilanden Wind Farm Zone*. Technical report, Netherlands Enterprise Agency.

Moshfeghi, S. & Eslami, A. (2016). Study on pile ultimate capacity criteria and CPT-based direct methods. *International Journal of Geotechnical Engineering*, *12*(1), 28–39, https://doi.org/10.1080/19386362.2016.1244150.

Murff, J. D. & Hamilton, J. M. (1993). *P*-Ultimate for Undrained Analysis of Laterally Loaded Piles. *Journal of Geotechnical Engineering*, *119*(1), 91–107, https://doi.org/10.1061/(ASCE)0733-9410(1993)119:1(91).

Myers, D. E. (1984). Co-Kriging — New Developments. In *Geostatistics for Natural Resources Characterization* (pp. 295–305). Dordrecht: Springer Netherlands. https://doi.org/10.1007/978-94-009-3699-7_18.

National Grid ESO (2021). *Future Energy Scenarios*. Technical Report July, National Grid ESO.

NGI (2022). *Ten Noorden van de Waddeneilanden Wind Farm Zone Integrated Ground Model*. Client RVO 20190798-04-R, Norwegian Geotechnical Institute.

O'Kelly, B. & Arshad, M. (2016). Offshore wind turbine foundations – analysis and design. In *Offshore Wind Farms* (pp. 589–610). Elsevier. https://doi.org/10.1016/B978-0-08-100779-2.00020-9.

Onajite, E. (2014). Understanding Seismic Interpretation Methodology. In *Seismic Data Analysis Techniques in Hydrocarbon Exploration* (pp. 177–211). Elsevier. https://doi.org/10.1016/B978-0-12-420023-4.00013-7.

Ørsted (2020). *Burbo Bank Extension Offshore Wind Farm*. Technical report, Ørsted.

Patel, A. (2019). Geotechnical investigation. In *Geotechnical Investigations and Improvement of Ground Conditions* (pp. 87–155). Elsevier. https://doi.org/10.1016/B978-0-12-817048-9.00009-3.

Peng, C.-K., Buldyrev, S. V., Havlin, S., Simons, M., Stanley, H. E., & Goldberger, A. L. (1994). Mosaic organization of DNA nucleotides. *Physical Review E*, *49*(2), 1685–1689, https://doi.org/10.1103/PhysRevE.49.1685.

Peuchen, J., Kaltekis, K., Klein, M., Murali, M., van Erp, F., & Hicks, M. (2022a). Characteristic Values for Geotechnical Design of Offshore Monopiles in Sandy Soils - Case Study. In *Proceedings of the 4th International Symposium Frontiers in Offshore Geotechnics* (pp. 1892–1901). Austin, Texas, USA.

Peuchen, J., Van Kesteren, W., Vandeweijer, V., Carpentier, S., & Van Erp, F. (2022b). *Upscaling 1 500 000 Synthetic CPTs to Voxel CPT Models of Offshore Sites*, (pp. 641–645). CRC Press: London, 1 edition. https://doi.org/10.1201/9781003308829-93.

Pincus, S. M. (1991). Approximate entropy as a measure of system complexity. *Proceedings of the National Academy of Sciences*, *88*(6), 2297–2301, https://doi.org/10.1073/pnas.88.6.2297.

Powell, G. E. & Percival, I. C. (1979). A spectral entropy method for distinguishing regular and irregular motion of Hamiltonian systems. *Journal of Physics A: Mathematical and General*, *12*(11), 2053–2071, https://doi.org/10.1088/0305-4470/12/11/017.

Provenzano, G., Vardy, M. E., & Henstock, T. J. (2017). Pre-stack full waveform inversion of ultra-high-frequency marine seismic reflection data. *Geophysical Journal International*, *209*(3), 1593–1611, https://doi.org/10.1093/gji/ggx114.

Provenzano, G., Vardy, M. E., & Henstock, T. J. (2018). Decimetric-resolution stochastic inversion of shallow marine seismic reflection data: Dedicated strategy and application to a geohazard case study. *Geophysical Journal International*, *214*(3), 1683–1700, https://doi.org/10.1093/gji/ggy221.

Putuhena, H., White, D., Gourvenec, S., & Sturt, F. (2023a). Finding space for offshore wind to support net zero: A methodology to assess spatial constraints and future scenarios, illustrated by a UK case study. *Renewable and Sustainable Energy Reviews*, *182*, 113358, https://doi.org/10.1016/j.rser.2023.113358.

Putuhena, H., White, D., Gourvenec, S., & Sturt, F. (2023b). Geospatial assessment of future floating offshore wind challenges: UK case study exploring drag anchor

suitability and requirements. In *9th International SUT Offshore Site Investigation Geotechnics Conference Proceedings* (pp. 257–264).: Society of Underwater Technology. https://doi.org/10.3723/HJMJ5655.

Randolph, M. & Gourvenec, S. (2011). *Offshore Geotechnical Engineering*. London: CRC Press, 1st edition.

Raubitzek, S. & Neubauer, T. (2021). Combining Measures of Signal Complexity and Machine Learning for Time Series Analyis: A Review. *Entropy*, *23*(12), 1672, https://doi.org/10.3390/e23121672.

Reese, L. C., Cox, W. R., & Koop, F. D. (1974). Analysis of Laterally Loaded Piles in Sand. In *Offshore Technology Conference* (pp. OTC–2080–MS). Houston, Texas: OTC. https://doi.org/10.4043/2080-MS.

Richman, J. S. & Moorman, J. R. (2000). Physiological time-series analysis using approximate entropy and sample entropy. *American Journal of Physiology-Heart and Circulatory Physiology*, *278*(6), H2039–H2049, https://doi.org/10.1152/ajpheart.2000.278.6.H2039.

Riedl, M., Müller, A., & Wessel, N. (2013). Practical considerations of permutation entropy. *The European Physical Journal Special Topics*, *222*(2), 249–262, https://doi.org/10.1140/epjst/e2013-01862-7.

Ritchie, H., Rosado, P., & Roser, M. (2023). CO2 and Greenhouse Gas Emissions. *Our World in Data*.

Rix, G. & Stokoe, K. (1991). Correlation of initial tangent modulus and cone penetration resistance. In *Proceedings of the Calibration Chamber Testing* (pp. 351–362). New York, USA: Elsevier.

Robertson, P., Campanella, R., Gillespie, D., & Greig, J. (1986). Use of Piezometer Cone Data. In *Proceedings of American Society of Civil Engineers, ASCE, In-Situ 86 Specialty Conference* (pp. 1263–1280). Blacksburg, Virginia, USA: ASCE.

Robertson, P. K. (1990). Soil classification using the cone penetration test. *Canadian Geotechnical Journal*, *27*(1), 151–158, https://doi.org/10.1139/t90-014.

Robertson, P. K. (2009a). Interpretation of cone penetration tests - A unified approach. *Canadian Geotechnical Journal*, *46*(11), 1337–1355, https://doi.org/10.1139/T09-065.

Robertson, P. K. (2009b). Performance based earthquake design using the CPT. In *Proceedings of the International Conference on Performance-Based Design in Earthquake Geotechnical Engineering* (pp. 3–20). Tokyo, Japan. https://doi.org/10.1201/NOE0415556149.ch1.

Robertson, P. K. (2010). Soil Behaviour Type from the CPT: An update. In *2nd International Symposium on Cone Penetration Testing*.

Robertson, P. K. & Cabal, K. (2015). *Guide to Cone Penetration Testing*. Gregg Drilling and Testing, Inc., 6 edition.

Robertson, P. K. & Campanella, R. G. (1983). Interpretation of cone penetration tests. Part I: Sand. *Canadian Geotechnical Journal*, *20*(4), 718–733, https://doi.org/10.1139/t83-078.

Robertson, P. K. & Wride, C. (1998). Evaluating cyclic liquefaction potential using the cone penetration test. *Canadian Geotechnical Journal*, *35*(3), 442–459, https://doi.org/10.1139/t98-017.

Sauvin, G., Vanneste, M., Vardy, M., Klinkvort, R. T., Forsberg, C. F., & Kort, D. A. (2024). Integration of Geoscience Data – The TNW Offshore Wind Farm Case Study. In *Offshore Technology Conference* Houston, Texas, USA: OTC. https://doi.org/10.4043/35476-MS.

Sauvin, G., Vanneste, M., Vardy, M. E., Klinkvort, R. T., & Forsberg, C. F. (2019). Machine Learning and Quantitative Ground Models for Improving Offshore Wind Site Characterization. In *Offshore Technology Conference* Houston, Texas: OTC. https://doi.org/10.4043/29351-MS.

Sauvin, G., Vardy, M., Klinkvort, R., Vanneste, M., Forsberg, C., & Kort, A. (2022). State-of-the-Art Ground Model Development for Offshore Renewables – TNW Case Study. In *3rd EAGE Global Energy Transition Conference & Exhibition* (pp. 1–5). The Hague, Netherlands,: European Association of Geoscientists & Engineers. https://doi.org/10.3997/2214-4609.202221109.

Seo, S. K., Kim, K., Chang, K.-H., Choi, Y.-J., Song, K., & Park, J.-K. (2012). Determination of the dynamical behavior of rainfalls by using a multifractal detrended fluctuation analysis. *Journal of the Korean Physical Society*, *61*(4), 658–661, https://doi.org/10.3938/jkps.61.658.

Sharma, V. (2009). Deterministic Chaos and Fractal Complexity in the Dynamics of Cardiovascular Behavior: Perspectives on a New Frontier. *The Open Cardiovascular Medicine Journal*, *3*(1), 110–123, https://doi.org/10.2174/1874192400903010110.

Shoukat, G., Michel, G., Coughlan, M., Malekjafarian, A., Thusyanthan, I., Desmond, C., & Pakrashi, V. (2023). Generation of Synthetic CPTs with Access to Limited Geotechnical Data for Offshore Sites. *Energies*, *16*(9), 3817, https://doi.org/10.3390/en16093817.

Siemann, L., et al. (2024). Comparison of Different Prediction Methods to Derive Synthetic CPT Profiles - An Offshore Wind Farm Case Study from the German North

Sea. In *7th International Conference on Geotechnical and Geophysical Site Characterization*: CIMNE. https://doi.org/10.23967/isc.2024.233.

Silva, S. A., Da Silva, S. L. E. F., De Souza, R. F., Marinho, A. A., De Araújo, J. M., & Bezerra, C. G. (2021). Improving Seismic Inversion Robustness via Deformed Jackson Gaussian. *Entropy*, *23*(8), 1081, https://doi.org/10.3390/e23081081.

Sokolov, A., Schulte, B., Shalaby, H., & Molen, M. V. D. (2021). Seismic inversion for reservoir characterization. In *Applied Techniques to Integrated Oil and Gas Reservoir Characterization* (pp. 329–351). Elsevier. https://doi.org/10.1016/B978-0-12-817236-0.00013-3.

Song, C., Havlin, S., & Makse, H. A. (2005). Self-similarity of complex networks. *Nature*, *433*(7024), 392–395, https://doi.org/10.1038/nature03248.

Stuyts, B. (2024). PLENARY LECTURE - Machine learning tools for the treatment of offshore site investigations. In *7th International Conference on Geotechnical and Geophysical Site Characterization*: CIMNE. https://doi.org/10.23967/isc.2024.308.

Sun, W., Xu, G., Gong, P., & Liang, S. (2006). Fractal analysis of remotely sensed images: A review of methods and applications. *International Journal of Remote Sensing*, *27*(22), 4963–4990, https://doi.org/10.1080/01431160600676695.

Supergen ORE (2021). *Delivering Net Zero: The Role of Offshore Renewable Energy A COP26 Briefing Note Prepared by the Supergen Offshore Renewable Energy Hub*. Technical report, Engineering and Physical Sciences Research Council.

Suryasentana, S. & Lehane, B. (2014). Numerical derivation of CPT-based p-y curves for piles in sand. *Géotechnique*, *64*(3), 186–194, https://doi.org/10.1680/geot.13.P.026.

SUT (2022). *Guidance Notes for the Planning and Execution of Geophysical and Geotechnical Ground Investigations for Offshore Renewable Energy Developments*. Technical report, Society for Underwater Technology.

Tang, L., Lv, H., Yang, F., & Yu, L. (2015). Complexity testing techniques for time series data: A comprehensive literature review. *Chaos, Solitons & Fractals*, *81*, 117–135, https://doi.org/10.1016/j.chaos.2015.09.002.

Tapoglou, E., et al. (2023). *Clean Energy Technology Observatory: Wind Energy in the European Union - 2023 Status Report on Technology Development, Trends, Value Chains and Markets*. Technical report, Publications Office of the European Union, Luxembourg, Luxembourg. https://doi.org/10.2760/618644.

Truong, P. & Lehane, B. (2014). Numerically derived CPT-based p-y curves for a soft clay modeled as an elastic perfectly plastic material. In *Proceedings of 3rd International Conference on Cone Penetration Testing* (pp. 975–982). Las Vegas: International Symposium on Cone Penetration Testing.

Tyler, S., Vanneste, M., & Butler, D. (2017). Geophysical Techniques for Offshore Site Investigation. In J. Carlton, P. Jukes, & Y. S. Choo (Eds.), *Encyclopedia of Maritime and Offshore Engineering* (pp. 1–12). Wiley, 1 edition. https://doi.org/10.1002/9781118476406.emoe525.

UNEP (2022). *Emissions Gap Report 2022: The Closing Window - Climate Crisis Calls for Rapid Transformation of Societies*. Technical report, United Nations Environment Programme, Nairobi, Kenya.

Vanneste, M., Sauvin, G., Dujardin, J.-R., Forsberg, C. F., Klinkvort, R. T., Forsberg, C. S., & Hansen, R. C. (2022). Data-Driven Ground Models: The Road to Fully-Integrated Site Characterization and Design. In D. V. K. Huynh, A. M. Tang, D. H. Doan, & P. Watson (Eds.), *Proceedings of the 2nd Vietnam Symposium on Advances in Offshore Engineering*, volume 208 (pp. 3–21). Singapore: Springer Singapore. https://doi.org/10.1007/978-981-16-7735-9_1.

Vardy, M. & Pinson, L. (2018). Seismic Attenuation - Friend or Foe. In *3rd Applied Shallow Marine Geophysics Conference* (pp. 1–5). Porto, Portugal: European Association of Geoscientists & Engineers. https://doi.org/10.3997/2214-4609.201802658.

Vardy, M., Sauvin, G., Klinkvort, R. T., Vanneste, M., Kort, A., & Forsberg, C. F. (2023a). Capturing Uncertainty in Quantitative Ground Models. In *9th International SUT Offshore Site Investigation Geotechnics Conference Proceedings "Innovative Geotechnologies for Energy Transition"*: Society for Underwater Technology. https://doi.org/10.3723/QIUW9196.

Vardy, M. E., Clare, M. A., Vanneste, M., Forsberg, C. F., & Dix, J. K. (2018). Seismic Inversion for Site Characterization: When, Where and Why Should We Use It? In *Offshore Technology Conference* Houston, Texas, USA: OTC. https://doi.org/10.4043/28730-MS.

Vardy, M. E., Hill, A. W., & Campbell, K. J. (2017). An emerging tool in the site investigation toolbox. *Sea Technology*, *58*(9), 10–14.

Vardy, M. E., Sauvin, G., Vanneste, M., Klinkvort, R. T., & Dyer, N. J. (2023b). How many CPTs does it take to make a synthetic CPT? In *9th International SUT Offshore Site Investigation Geotechnics Conference Proceedings "Innovative Geotechnologies for Energy Transition"* (pp. 385–392).: Society of Underwater Technology. https://doi.org/10.3723/WASQ1942.

Vardy, M. E., Vanneste, M., Henstock, T. J., Morgan, E., & Pinson, L. J. (2015). Can high-resolution marine geophysical data be inverted for soil properties? In *Institute of Acoustics*, volume 37 (pp. 149–156). Bath: Institute of Acoustics. https://doi.org/10.25144/16060.

Wang, H., Lehane, B. M., Bransby, M. F., Wang, L. Z., & Hong, Y. (2022). Field and numerical study of the lateral response of rigid piles in sand. *Acta Geotechnica*, *17*(12), 5573–5584, https://doi.org/10.1007/s11440-022-01532-6.

Wu, X., et al. (2019). Foundations of offshore wind turbines: A review. *Renewable and Sustainable Energy Reviews*, *104*, 379–393, https://doi.org/10.1016/j.rser.2019.01.012.

Zhou, R., Yang, C., Wan, J., Zhang, W., Guan, B., & Xiong, N. (2017). Measuring Complexity and Predictability of Time Series with Flexible Multiscale Entropy for Sensor Networks. *Sensors*, *17*(4), 787, https://doi.org/10.3390/s17040787.